X-Ray Studies of Galaxy Clusters and Groups

Gas Properties in the Exceptional Cases of Faint Outskirts, High Redshift and a Merging Event

Dissertation
zur
Erlangung des Doktorgrades (Dr. rer. nat.)
der
Mathematisch-Naturwissenschaftlichen Fakultät
der
Rheinischen Friedrich-Wilhelms-Universität Bonn

von
Sophia Thölken
aus
Heidelberg

Bonn, 2017

Dieser Forschungsbericht wurde als Dissertation von der Mathematisch-Naturwissenschaftlichen Fakultät der Universität Bonn angenommen und ist auf dem Hochschulschriftenserver der ULB Bonn `http://hss.ulb.uni-bonn.de/diss_online` elektronisch publiziert.

1. Gutachter:	Prof. Dr. Thomas H. Reiprich
2. Gutachter:	Prof. Dr. Peter Schneider
Tag der Promotion:	08.12.2017
Erscheinungsjahr:	2018

Für meine Eltern.

Abstract

The history and evolution of the universe, the understanding of the formation of structures and the investigation of a wealth of astrophysical phenomena are the topical subjects in present-day galaxy cluster physics and cosmology. Galaxy clusters are important laboratories as they are the largest distinct building blocks in the universe and embedded in the cosmological large-scale structure. In common concepts, clusters and groups evolved from tiny overdensities in the early universe and grow at the node points of the filaments through the merging of substructures and accretion of material. They are thus direct probes of structure formation theories and the cosmological standard model as well as essential objects to study astrophysical imprints of these formation processes in the hot intracluster medium (ICM) which is the largest baryonic component in clusters. X-ray observations are excellent tools to analyze the ICM properties in great detail which is the main focus of this work.

In the first project, which was published in *Astronomy & Astrophysics* (Thölken et al., 2016), the gas properties of the galaxy group UGC 03957 are investigated out to very large radii ($1.4\,R_{200}$) with the Suzaku satellite. Due to the low surface brightness of groups and instrumental limitations, the outskirts of these objects are much less studied than galaxy clusters outskirts. However, Suzaku is able to reach these faint outer regions that are potentially influenced by structure formation effects. Previous analyses of cluster outskirts revealed interesting astrophysical effects such as gas clumping and non-equilibrium states. Here, the temperature, metal abundance, entropy and gas mass fraction profiles of the ICM are investigated and the following results are obtained. The metal abundance profile suggests a primary ICM enrichment by galactic winds and the abundance pattern yields a relative enrichment contribution for core-collapse supernovae of 80% – 100%. The temperature drops by a factor of three from the center to the outskirts which is consistent with findings for galaxy clusters. The latter often show a drop or flattening of the entropy profile at large radii and in some cases an excess in the gas mass fraction profile compared to the cosmic mean. Such an entropy drop is not observed in UGC 03957 and the gas mass fraction profile stays below the cosmic mean value up to $\sim R_{200}$ which points to a possible difference between clusters and groups.

The second project of this work addresses galaxy clusters as cosmological probes and was submitted to *Astronomy & Astrophysics* in April 2017. Relaxed distant clusters are essential for tests of the cosmological standard model using the gas mass fraction. Therefore, the dynamical status is crucial and X-ray observations of the ICM are the prime tool to investigate the hydrodynamical properties. Here, the extremely X-ray luminous high redshift cluster Cl $J120958.9{+}495352$ ($z = 0.902$) is studied with the XMM-Newton satellite and the Hubble Space Telescope. The results show that this object is one of the most luminous clusters known with $L_X = (18.7^{+1.3}_{-1.2}) \times 10^{44}\,\mathrm{erg/s}$ in the $0.1 - 2.4\,\mathrm{keV}$ band. Additionally, strong indications for the presence of a cool core are found from the temperature profile and the central cooling time which makes this rare cluster a valuable object for cosmological probes. A gas mass fraction of $f_{\mathrm{gas},2500} = 0.11^{+0.06}_{-0.03}$ is obtained in good agreement with previous findings and the standard ΛCDM cosmology.

In the last project, the imprints of structure formation in the ICM are studied in detail for the disturbed cluster A2163 with the Suzaku satellite. A2163 likely underwent one or several merging processes in the recent past and the work at hand reveals several shock fronts in the ICM. So far, only relatively few shocks have been detected and studied in detail in X-rays. In this work, the gas properties in two azimuthal directions are investigated yielding significant differences with higher surface brightness and emission measure profiles in north-east (NE) and a lower temperature in south-west (SW) direction. In both directions, a shock front at $R \sim 1.3\,\mathrm{Mpc}$ is found, visible as distinct jumps in the temperature profiles with Mach numbers of $M = 1.5^{+0.2}_{-0.1}$ and $M = 3.3^{+0.8}_{-0.7}$ and shock velocities of $v = (1.2^{+0.2}_{-0.1}) \times 10^3\,\mathrm{km/s}$ and $v = 4.1^{+1.0}_{-0.9} \times 10^3\,\mathrm{km/s}$, for the NE and SW direction, respectively. The former is a typical value for X-ray detected merging shocks while the latter is comparable to one of the strongest known shocks, measured in the Bullet cluster. The SW density and temperature profile exhibit evidence for a second shock front at $R \sim 700\,\mathrm{kpc}$ with $M = 1.8^{+1.7}_{-0.7}$, coinciding with a steepening of the surface brightness profile and spatially close to a cool core "bullet". Additionally, spatial correlation to radio emission is found, in particular a coinciding of the NE shock front with a radio relic which hints at a causal connection of these phenomena, likely due to relativistic electrons which are accelerated in the shock.

Contents

Preface

Towards the end of the 18th century, Charles Messier (*26 June 1730; †12 April 1817) and his friend Pierre Méchain (*16 August 1744; †20 September 1804), two French astronomers, were hunting for undiscovered comets. During their search, they came across several diffuse, distracting objects which could be falsely identified as comets. To avoid misinterpretations, C. Messier mapped all these "Nebulae" – that are known today as Messier objects – and collected them in a catalog. In 1784, he added the following note to this catalog

> *"The constellation of Virgo, & especially the northern Wing is one of the constellations which encloses the most Nebulae [...]. All these nebulae appear to be without stars: one can see them only in a very good sky, & near their meridian passage. Most of these nebulae have been pointed to me by M. Méchain."*
>
> *Charles Messier in* Connoissance des Temps*, 1784*[1]

This note documents that, without knowing, C. Messier and P. Méchain were probably the first persons to discover a galaxy cluster, i.e. a cumulation of diffuse Nebulae at first sight. Long after the time of Messier and Méchain, 16 of those Nebulae were identified as galaxies belonging to the Virgo galaxy cluster.

Today, it is known that galaxy clusters consist of much more ingredients than just the member galaxies, which actually only account for a few percent of the total cluster mass. To identify all of them, multi-wavelength observations are needed which in the recent past dramatically improved the understanding of galaxy clusters as the largest distinct building blocks in the universe.

This work is based on X-ray observations which in the 1960's first revealed a diffuse gaseous component in galaxy clusters (not to be confused with the Nebulae seen by Messier) called the intracluster medium (ICM). Since then, large surveys as e.g. the ROSAT All-Sky-Survey mapped the soft X-ray emission across the entire sky and many galaxy clusters could be identified in these observations. Later missions as Suzaku, XMM-Newton and Chandra brought up the opportunity to study the ICM in great detail with respect to spatial and spectral resolution. And still the field of galaxy cluster X-ray astronomy enjoys great attention and is open to new discoveries as e.g. expected from the upcoming eROSITA telescope which will detect about 100.000 galaxy clusters and the Athena mission which was selected as the second large mission in the ESA's Cosmic Vision 2015–2025 plan.

In this work, three particularly fascinating objects are studied in great detail and cover the variety of interesting topics coming up in X-ray analyses of galaxy clusters from astrophysical phenomena in the hot ICM to galaxy clusters as probes of the cosmological standard model. A detailed introduction to those topics is given in chapter 1 and 2 and the instruments used in this work are presented in chapter 3.

[1] `http://messier.seds.org/xtra/history/m-cat.html`

Each of the three projects in this work addresses galaxy clusters in the global context of structure formation with respect to the gas properties and the dynamical status and faces different observational and analytical challenges. The first project, presented in chapter 4, focuses on the X-ray properties of a galaxy group and possible differences compared to the larger galaxy clusters. The content of this chapter has been published in *Astronomy & Astrophysics* in July 2016 as Thölken et al. (2016) (DOI: 10.1051/0004-6361/201527608). In current structure formation theories, clusters and groups should be just scaled versions of each other. This is e.g. important for the above mentioned upcoming large surveys as the analyses of their data will largely rely on scaling relations that might differ for groups and clusters. So far, only few detailed studies of galaxy groups exist and this work investigates the ICM properties up to large radii. This is challenging due to the low surface brightness in the outskirts which requires a well suited instrument with a low background level such as the Suzaku satellite and a rigorous treatment of the fore- and background components.

The second project of this work addresses galaxy clusters in the context of cosmological probes. The content of this chapter was submitted to *Astronomy & Astrophysics* in April 2017. The parameters of the standard model of cosmology, which describes the history and evolution of the universe, can be estimated using galaxy clusters and in particular very distant, massive objects provide important constraints. However, structure formation theories predicts such objects to be extremely rare and thus each individual object is of great interest and value for cosmology. X-ray observations of the ICM are a prime tool to access the gas properties and judge whether the object is suited for cosmological tests. However, analyses of these distant objects are challenging as their extent on the sky is small and the photon rate is low. One of these rare objects, the cluster Cl $J120958.9{+}495352$, is studied in detail in this work with the XMM-Newton satellite as documented in chapter 5.

The third project studies the effects of structure formation in the ICM. Galaxy clusters evolve through the merging of substructures that are the most energetic events in the universe. As the ICM interacts, imprints of these mergers are visible e.g. in shocks that crucially affect the gas properties. Despite prominent examples as for instance the merging Bullet cluster, relatively few shocks have been identified and studied in detail in X-rays. The cluster Abell 2163 is a morphologically irregular system hosting one of the largest known radio halos and is thus a promising candidate to find shocks evolving from structure formation. The analyses of the ICM properties and the investigation of the shock fronts using data from the Suzaku satellite is subject to the last project of this work introduced in chapter 6. The content of this chapter is being prepared for submission to *Astronomy & Astrophysics*. Chapter 7 gives a brief summary of the main conclusions of all projects and future prospects.

CHAPTER 1

Cosmological framework

The evolution of galaxy clusters as the largest building blocks in the universe depends on the history and evolution of the universe itself, which is described by the cosmological model. Hence, the cosmological context is essential when studying galaxy clusters. This, on the one hand, makes clusters a valuable probe to test cosmological models. On the other hand, the physical properties acting in the clusters themselves – and are the main subject of this work – are influenced by the growth of structures that is described by the cosmological structure formation theory.

The standard model of cosmology is introduced in Sec. 1.1 and structure formation as well as the thermal history of the universe are summarized in Sec. 1.2. The content of this chapter is based on standard literature on cosmology, i.e. Schneider (2015), Schneider (2009), Peacock (1999), Dodelson (2003), Peebles (1993) and Bertschinger (1995).

1.1 The standard model of cosmology

Homogeneity and isotropy – these two fundamental characterizations of the universe together are called the *cosmological principal*. However, on scales of our planetary system or galaxies, the universe does neither look homogeneous nor isotropic. Therefore, only in the late 20^{th} century, this concept strengthened due to advanced computing power, extended theoretical models and especially observations of the cosmic microwave background (cf. Sec. 1.2). The 2dF galaxy redshift survey was one of the first large surveys mapping the large-scale distribution of galaxies. Their findings support the cosmological principle on large scales ($\gg$100 Mpc), as shown in Fig. 1.1, while on smaller scales matter is structured.

But a fundamental problem arises if the cosmological principle and, as it was a common concept until the early 20^{th} century, an infinite extent of the universe in space and time is assumed. Heinrich Wilhelm Olbers formulated this problem already in 1823: An infinite universe is populated by an infinite number of stars whose light reaches the earth from all directions. Hence, the night sky should be bright. In current concepts, this *steady-state universe* is ruled out and replaced by the so-called ΛCDM model which solves the Olber's paradox because it assumes a temporal evolving and expanding universe, starting with the Big Bang, and thus a finite extent of the visible universe.

The ΛCDM model is currently the most accepted model. CDM stands for *cold dark matter* (this nomenclature is explained in Sec. 1.2) and Λ is associated with *dark energy*, which drives the expansion of the universe. Up to now, very little is known about the nature of dark energy, however, the ΛCDM model is able to reproduce and explain observations to a large

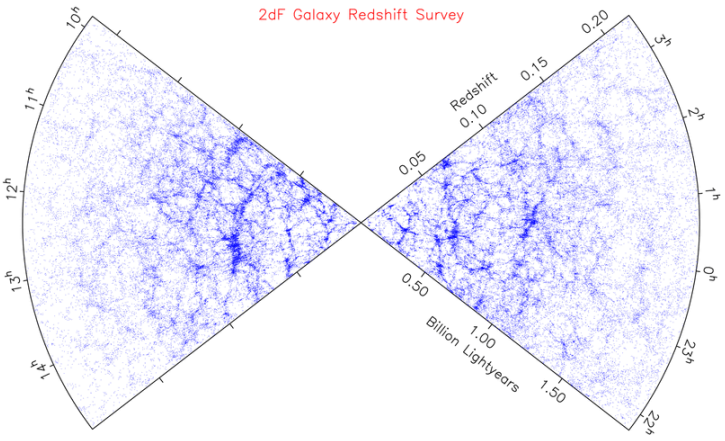

Figure 1.1: Projected galaxy distribution in the 2dF galaxy redshift survey as a function of right ascension and redshift. The distribution confirms the cosmological principle on large scales. Credit: Matthew Colless (2003).

extent. Several of these observations will be addressed in the following sections. Notably, already Einstein postulated a *cosmological constant* as an addition to his formulation of General Relativity in 1917. In his theory, this constant acts as "anti-gravity", to achieve a static universe. Even if this idea is now rejected – and was already rejected by Einstein himself in 1929 after Hubble's discovery of an expanding universe – the cosmological constant is still the simplest form of dark energy.

Measurements show that dark energy makes up the largest component in the current energy budget of the universe with about 69% (Planck Collaboration et al., 2016), followed by matter (including dark matter) with 31% while radiation is negligible. Constraining these so-called *cosmological parameters* is the main subject to observational cosmology and galaxy clusters provide an independent constraint on these parameters (cf. Sec. 2.4) as well as an important cross check to other methods like e.g. the cosmic microwave background. For a full list of the current values of the cosmological parameters see Appendix A.

The formal description of the standard model of cosmology, the cosmological parameters and the evolution of the universe is given in the following paragraphs which are mainly based on Schneider (2009) and Bertschinger (1995).

Newtonian description The expansion rate of the universe is described by the time dependent Hubble parameter $H(t)$:

$$H(t) = \frac{\dot{a}}{a}, \tag{1.1}$$

where a is the *scale factor* given by

$$a = \frac{1}{(1+z)} \tag{1.2}$$

with the redshift z

$$z = \frac{\lambda_{\mathrm{obs}} - \lambda_0}{\lambda_0}. \tag{1.3}$$

λ_{obs} is the observed wavelength of a source while λ_0 is the emitted wavelength. The scale factor is one at the present time and $H_0 = H(t=0)$. As the universe expands, the so-called comoving

coordinates for a particle at position $\boldsymbol{x}$ are defined as

$$\boldsymbol{r}(t) = a(t)\boldsymbol{x}. \tag{1.4}$$

where $\boldsymbol{r}(t)$ is the changed position after time t due to the expansion. To understand the dynamics of the expansion, the surface of an expanding sphere with radius $x = r(t)/a(t)$ can be considered for which the mass is given by

$$M(x) = \frac{4\pi}{3}\rho(t)r^3(t) = \frac{4\pi}{3}\rho(t)a^3(t)x^3 \tag{1.5}$$

with $\rho(t)$ being the time-dependent mass density of the sphere. Using the gravitational force (with gravitational constant G), Eq. 1.4 and Eq. 1.5, the equation of motion is given by

$$\ddot{r}(t) = -\frac{GM(x)}{r^2} \Leftrightarrow \ddot{a}(t) = -\frac{4\pi G}{3}\rho(t)a(t). \tag{1.6}$$

Integrating this equation yields

$$\dot{a}^2 = \frac{8\pi G}{3}\rho(t)a^2(t) - Kc^2, \tag{1.7}$$

where Kc^2 is an integration constant. This is the first *Friedmann equation* which is one of the most important equations describing the evolution of the universe. The value of K has great impact on the cosmic evolution, under the assumption that the cosmological constant is zero. In this case, for negative values of K, the time derivative of the scale factor is always positive, i.e. the universe expands forever. The same is true for $K = 0$, but in the limit $t \longrightarrow \infty$ the expansion velocity becomes 0. For positive K, Eq. 1.7 has a maximum, meaning that after a certain point the universe will contract again. For $K = 0$, the critical density ρ_{crit} in todays universe, which marks the critical line between the above cases, is given by

$$\rho_{\text{crit}} = \frac{3H_0^2}{8\pi G}. \tag{1.8}$$

However, for a non-zero positive cosmological constant and the current measured values of the cosmological parameters (cf. Appendix A), the universe is expected to expand forever.

As mentioned earlier, the energy content of the universe is composed of three main components (matter, including dark matter, radiation and dark energy, denoted by index m, r and Λ in the following). Thus, the total density is the sum over all of these three contributions:

$$\rho_{\text{tot}}(t) = \rho_{\text{m}}(t) + \rho_{\text{r}}(t) + \rho_{\Lambda}(t). \tag{1.9}$$

Using the first law of thermodynamics and introducing the so-called equation of state parameter $w = \frac{p}{\rho c^2}$ with pressure p yields the following general solution for the density of each component

$$\rho = \rho_0 a^{-3(1+w)}, \tag{1.10}$$

which is valid for all cosmic times and under the assumption of a timely constant w. From this and Eq. 1.7 it follows that

$$\dot{a} \propto \rho^{\frac{1}{2}} a \propto a^{1-\frac{3}{2}(1+w)} \tag{1.11}$$

and consequently

$$a \propto \begin{cases} t^{\frac{2}{3(1+w)}} & w > -1 \\ e^t & w = -1 \end{cases}. \tag{1.12}$$

The question is now: What is the value of w for matter, radiation and dark energy? Matter (baryons and dark matter) can be considered as non-relativistic and thus $w_\mathrm{m} = \frac{p_\mathrm{m}}{\rho_\mathrm{m} c^2} \approx 0$. Therefore,

$$\rho_\mathrm{m} = \rho_{\mathrm{m},0} a^{-3}. \tag{1.13}$$

For radiation the situation is less obvious. Qualitatively speaking, the following situation can be considered for this case: In a cavity where radiation is uniformly emitted in all directions, the pressure acting on one point of the wall of the cavity depends on the square of the cosine of the angle θ in which the radiation is hitting the wall. Averaging $\cos^2\theta$ over all solid angles gives a factor 1/3, yielding $p = \frac{1}{3}\rho c^2$ and thus $w = 1/3$. The density is then given by

$$\rho_\mathrm{r} = \rho_{\mathrm{r},0} a^{-4}. \tag{1.14}$$

From observations of supernovae Type Ia by Perlmutter et al. (1999) and Riess et al. (1998) – who were awarded with the Nobel Price for this discovery in 2011 – it is known that the expansion of the universe is accelerating, i.e. $\ddot{a} > 0$. This is achieved by any value of $w < -\frac{1}{3}$ (cf. Eq. 1.11). A special case is $w = w_\Lambda = -1$ in which the density is given by

$$\rho_\Lambda = \rho_{\Lambda,0}. \tag{1.15}$$

However, the exact value of w_Λ needs to be constrained from observations. Using Eq. 1.13 to 1.15 and $w_\Lambda = -1$, the total density (Eq. 1.9) is given by

$$\rho_\mathrm{tot} = \frac{\rho_{\mathrm{m},0}}{a^3} + \frac{\rho_{\mathrm{r},0}}{a^4} + \rho_\Lambda. \tag{1.16}$$

This implies that the evolution of the universe was dominated by radiation in early times, followed by a matter-dominated era and is now dominated by dark energy. From Eq. 1.12 the time dependence of the scale factor for the different eras is

$$a \propto \begin{cases} t^{\frac{2}{3}} & \text{matter-dominated} \\ t^{\frac{1}{2}} & \text{radiation-dominated} \\ e^t & \text{dark energy-dominated} \end{cases}. \tag{1.17}$$

The so-called *density parameters* of the ΛCDM model are defined as

$$\Omega_\mathrm{m} = \frac{\rho_{\mathrm{m},0}}{\rho_\mathrm{crit}};\ \ \Omega_\mathrm{r} = \frac{\rho_{\mathrm{r},0}}{\rho_\mathrm{crit}};\ \ \Omega_\Lambda = \frac{\rho_{\Lambda,0}}{\rho_\mathrm{crit}} = \frac{\Lambda c^2}{3H_0^2}, \tag{1.18}$$

where Λ is called the cosmological constant or vacuum energy, equivalent to the constant Einstein introduced in his field equations. For a flat universe, the sum of these density parameters, denoted by Ω_tot, is equal to one. Inserting this and Eq. 1.16 in Eq. 1.7 yields the following form of the Friedmann equation

$$\frac{H^2(t)}{H_0^2} = \frac{\Omega_\mathrm{r}}{a^4} + \frac{\Omega_\mathrm{m}}{a^3} - \frac{Kc^2}{a^2 H_0^2} + \Omega_\Lambda. \tag{1.19}$$

This overall formal description is solely based on the Newtonian theory. A brief description in the context of General Relativity (GR) is given in the following paragraph.

Robertson-Walker-Metric In General Relativity the distortion or curvature of the four-dimensional space-time is caused by matter, i.e. related to the energy and momentum. Gravity is thus a geometric property of the space-time and the description of the interaction between this gravitational field and matter is given by Einstein's field equations which he formulated in 1915. In this description, the metric for the four-dimensional space-time with the metric tensor $g_{\alpha\beta}$ can be written as

$$\mathrm{d}s^2 = g_{\alpha\beta}\mathrm{d}x^\alpha \mathrm{d}x^\beta \equiv \sum_{\alpha,\beta=0}^{3} g_{\alpha\beta}\mathrm{d}x^\alpha \mathrm{d}x^\beta \tag{1.20}$$

Based on the work of A. Friedmann, G. Lemaître, H. P. Robertson and A. G. Walker, a metric to describe a homogeneous isotropic universe can be formulated which is an exact solution to Einsteins field equations. This metric in hyperspherical coordinates is given by

$$\mathrm{d}s^2 = c^2\mathrm{d}t^2 - a^2(t)[\mathrm{d}\chi^2 + f_K^2(\chi)(\mathrm{d}\theta^2 + \sin^2\theta\,\mathrm{d}\varphi^2)]. \tag{1.21}$$

χ is the comoving radial coordinate, θ and φ are the angular coordinates and $f_K(\chi)$ is the comoving angular diameter distance depending on the curvature K. $f_K(\chi)$ is

$$f_K(\chi) = \begin{cases} K^{-1/2}\sin(K^{1/2}\,\chi) & \text{for } K > 0 \\ \chi & \text{for } K = 0 \\ (-K)^{-1/2}\sinh\left[(-K)^{1/2}\,\chi\right] & \text{for } K < 0 \end{cases} . \tag{1.22}$$

Distances The distance to a source is related to $f_K(\chi)$. Assuming the source has an angular diameter α, radius R and by setting $\alpha = \mathrm{d}\theta$ and $\mathrm{d}s = 2R$ in Eq. 1.21, the *angular diameter distance* is simply defined by trigonometry

$$D_\mathrm{A} = \frac{2R}{\alpha} = a(z) f_K(\chi). \tag{1.23}$$

However, the definition of distances is not unique as it can also be estimated from the luminosity L and flux F of a source by

$$D_\mathrm{L} = \sqrt{\frac{L}{4\pi F}}. \tag{1.24}$$

The two distance measures are related by $D_\mathrm{L} = (1+z)^2 D_\mathrm{A}$ and are thus the same for the present time but differ for high-redshift objects.

Extensions to the standard model As formulated previously, the cosmological principle is valid on large scales as e.g. shown through observations of the *cosmic microwave background* (CMB) with the Planck satellite (Planck Collaboration et al., 2014a) and WMAP (Bennett et al., 2003) and depicted in Fig. 1.2. The isotropy of the CMB temperature gives rise to a problem of the cosmological model as such a high level of isotropy is unexpected because regions on the sky, that are separated by more than about one degree, never have been in causal contact before the era of recombination due to the finite speed of light. This is known as the *horizon problem*. Another problem, the *flatness problem*, is related to the flat nature of the universe as

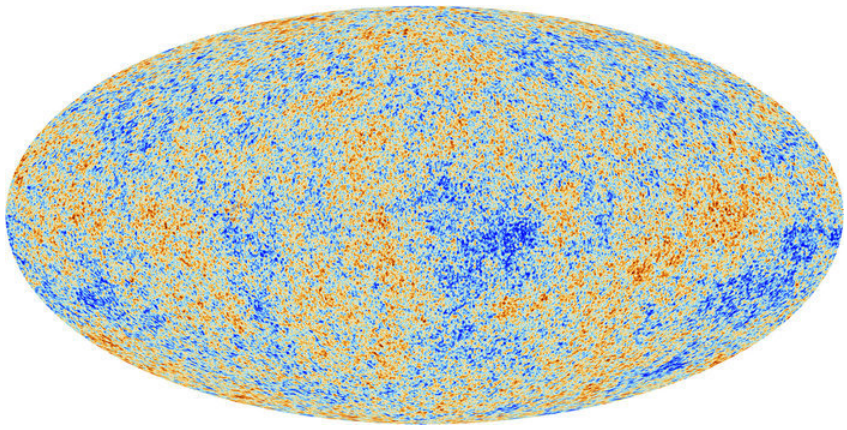

Figure 1.2: Map of the CMB temperature fluctuations observed by the Planck satellite. On large scales, the temperature distribution appears isotropic. On smaller scales, the primordial fluctuations with an amplitude of the order of 10^{-5} are measured. Higher temperatures are shown in blue. Credit: ESA and the Planck collaboration (2013).

e.g. inferred from the CMB. To achieve $\Omega_{\mathrm{tot}} \approx 1$ today, it had to be extremely close to one also in early times, i.e. a "fine-tuning" is necessary.

A solution to those problems has been first suggested by Alan Guth in 1980 under the name *Inflation*. In the epoch of inflation, the universe is expanding exponentially. This rapid expansion took place $\sim 10^{-34}$ s after the Big Bang and is a solution to both, the horizon and the flatness problem, because of the following considerations: During the inflationary time, the comoving horizon length, which sets the scale within the universe is in causal contact, can in principle become arbitrarily large and for this reason the CMB is isotropic. In addition, any curvature vanishes during inflation, so the universe is flat today. For these reasons, inflation is now a commonly accepted extension of the standard cosmological model and has great importance for the formation of structures as discussed in the next section.

1.2 Structure formation

From the formation of the first atoms in the early universe until now, structures on various scales from stars to galaxies and galaxy clusters evolved. These objects are embedded in the cosmological large-scale structure whose evolution as well as the thermal history is summarized in the following paragraphs, based on Schneider (2009) and Schneider (2015).

The early universe Tiny quantum fluctuations were magnified through inflation to macroscopic overdensities and afterwards evolved through self-gravity. Right after inflation, the cosmic evolution was dominated by radiation (cf. Eq. 1.19) and the baryon-photon fluid – tied together trough Thompson scattering – was gravitationally attracted by the dark-matter overdensities. Radiation pressure acted as a counter force to the gravitational attraction and the fluid underwent oscillations which are known as *baryonic acoustic oscillations* (BAO). The main energy contribution at this time came from relativistic electrons, neutrinos and photons. Energetic processes such as the production and annihilation of particle/anti-particle pairs could occur and stay in equilibrium as long as the reaction rate Γ of the interaction between particle 1 and 2 is

larger than the expansion rate H of the universe, i.e.

$$\Gamma(t) = n_2 \langle v\sigma \rangle \gg H = \frac{\dot{a}}{a}, \tag{1.25}$$

with n_2 being the density of particle species 2, v the relative velocity between particle 1 and particle 2 and σ the cross section of the process. As the universe expands, the density decreases as well as the temperature. This resulted in a so-called *freeze out* of several reactions at different times. The neutrinos froze out at temperatures of $T \lesssim 1.5\,\mathrm{MeV}$ which can be estimated from the weak interaction cross section. From this time on they have been traveling without interaction and should form a homogeneous background with a temperature of $T_\nu = 1.95\,\mathrm{K}$ today. However, due to the low interaction probability this background has not been detected so far.

Beside the relativistic particles, also the non-relativistic protons and neutrons as well as the weakly-interacting unknown dark matter particles were present in this early evolutionary phase. Whether dark matter was relativistic or non-relativistic depends on the mass of the dark matter particle. Current particle accelerators as the Large Hadron Collider (LHC) at CERN range up to $\sim$14 TeV in proton-proton collisions and its data is still being analyzed, however, even with the current knowledge, a potential dark matter particle has to have a mass larger than $\sim$400 GeV (Aaboud et al., 2016). Consequently, these particles were non-relativistic at freeze out, denoted as *cold dark matter*. The fact that dark matter is cold leads to the scenario that small structures form first and only later evolve to larger complexes as described in the next paragraph.

The further cooling of the universe caused the e^+e^- pair-production to become inefficient below $T\sim$0.5 MeV. However, the pair annihilation still took place and drastically reduced the number of $\mathrm{e^+e^-}$ pairs until almost all of them were gone. They dissipated their energy to the photon-gas which then had a higher temperature than the neutrino background because the latter already decoupled. Not all electrons vanished as it is known that the universe is neutral and thus some of them need to be left to form atoms.

For the expansion of the universe in the early radiation-dominated phase, the baryons can be neglected due to their low density. However, for the chemical composition these particles are important. They were in thermal equilibrium through electron captures of protons as well as beta and inverse-beta decays. As soon as the neutrinos froze out, the corresponding reactions stopped. At this time, the ratio of the number densities of protons and neutrons was $n_\mathrm{n}/n_\mathrm{p} \approx 1/3$ and only the decay of the free neutron could modify this ratio. As we see neutrons today, not all of them decayed. The reason for this was the formation of light atomic nuclei as e.g. Deuterium. Due to the Wien-tail of the Planck distribution of the photons, Deuterium was efficiently destroyed until the temperature dropped to $\sim$70 keV. From this point on, all neutrons got bound in Deuterium which then formed ^{4}He. From this considerations, the amount of ^{4}He in the universe is predicted to be 25% which is in perfect agreement with the measured amount of Helium in e.g. stars or nebulae of $25\% - 30\%$ (e.g. Izotov et al., 1994, Peimbert et al., 2000, Izotov et al., 2007) and thus one big achievement of the Big Bang model. The whole Big Bang Nucleosynthesis (BBN) took about three minutes and afterwards the universe contained photons, protons, Helium, traces of light elements, electrons, neutrinos and dark matter.

From BBN, a certain amount of baryons is expected to be present in the universe. Summing up all contributions from stars, gas, planets, etc. does not account for the expected amount of baryons (e.g. Nicastro et al., 2008, Shull et al., 2012) which is known as the *missing baryon problem*. A solution to this problem is likely the cosmological large-scale structure which will be addressed in the next paragraph.

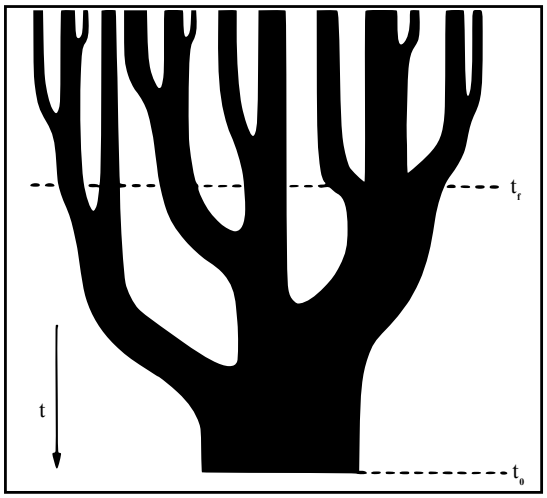

Figure 1.3: Schematic illustration of the merger tree. Small structures form first and through merging evolve to larger complexes as for instance galaxy clusters form through merging of the smaller galaxy groups. Credit: Lacey & Cole (1993).

Later in the cosmic evolution, at $z{\sim}3400$, the point of matter-radiation equality was reached, from which on matter started to dominate the cosmic evolution. After further cooling and expansion of the universe, at $z{\sim}1300$, neutral atoms started to form which is called the era of *recombination*. However, in the beginning they are destroyed by energetic photons and only at even lower temperatures of $T{\sim}3000\,\mathrm{K}$, the photo-dissociation became inefficient. As the electrons recombined, Thomson scattering was no longer possible and the photons decoupled from the baryons at the so-called *last scattering surface*. After recombination, all electrons were bound in atoms and (beside the decoupled CMB photons) only the 21 cm line of hydrogen is emitted in this so-called "dark ages". Observations of high-redshift sources (e.g. Fan et al., 2000, Becker et al., 2001) show that at some point the universe must have been reionized. The current understanding is that the first stars and AGNs between $6 < z < 20$ are responsible for the reionization and made the universe transparent again. However, the decoupled photons travel freely without interaction and are observed today as the cosmic microwave background.

The CMB was first detected by Arno Penzias and Robert Wilson in 1964 and is one of the most important confirmations of the cosmological standard model. The first CMB space mission COBE and later WMAP and Planck measured tiny fluctuations in the temperature of the CMB of the order of 10^{-5} (see Fig. 1.2). The most prominent fluctuations are the signatures of the BAOs and their power spectrum contains a wealth of information. It allows for the estimation of cosmological parameters and is one of the best arguments for the existence of cold dark matter.

After the decoupling of the photons, the baryon wave propagation stopped at a distance from the initial density perturbation which is known as the *sound horizon*. This distance marks a special scale in the two-point correlation function of the galaxy distribution and appears there as a peak at $\sim$150 Mpc (e.g. Eisenstein et al., 2005).

The hierarchical principle In the picture of a *hierarchical structure formation* the small structures evolved first, and with time larger objects were formed through merging of substructures (illustrated in Fig. 1.3) which is a consequence of the fact that dark matter is cold.

This *bottom-up* scenario has important implications for the formation of galaxy clusters. With the growth of structures, the so-called filamentary large-scale structure formed which consists of

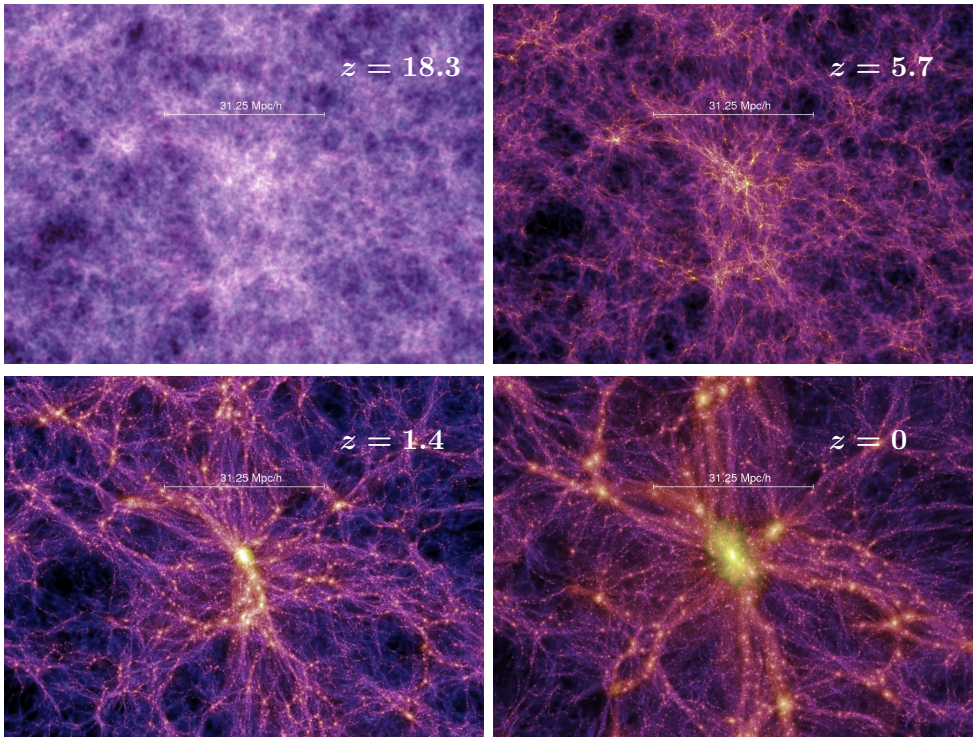

Figure 1.4: Snapshots of the Millennium Simulation at $z = 18.3, 5.7, 1.4, 0$. With time, structures become more pronounced and evolve to the filamentary large-scale structure until $z = 0$ with distinct node points where the galaxy clusters form. Credit: MPA (2005).

filaments and voids. At the node points of the filaments, galaxy clusters form and grow through the accretion of matter along the direction of the filaments and merging events. The evolution of the large-scale structure and the formation of the dark matter halos at the intersection points was e.g. simulated in the dark matter Millennium Simulation by Springel et al. (2005). Fig. 1.4 shows several snapshots of the simulation at different cosmic times and the emerging of the filaments and nodes where galaxy clusters are located. Already by qualitatively comparing the simulation snapshots to the large-scale galaxy distribution depicted in Fig. 1.1, it becomes clear that the models are able to reproduce the observations to a large extent. However, they also brought up the so-called *missing satellite problem* of the cosmological standard model. From the simulations, many more small dark matter halos are expected than are actually being observed e.g. satellite galaxies around the Milky Way (Moore et al., 1999, Klypin et al., 1999). Recently, Homma et al. (2016) discovered an extremely faint satellite dwarf galaxy which might suggest the presence of further ultra faint satellites that have not yet been found and can (partially) explain the missing satellite problem.

The large-scale structure is also the solution to the previously mentioned missing baryon problem. Simulations (e.g. Cen & Ostriker, 1999) predict, that a substantial fraction of the baryons is locked up in the warm-hot intergalactic medium (WHIM) of the filaments. Observational hints for these baryons can be found in X-ray observations, e.g. of superclusters as performed by Ren et al. (2014) and Fang et al. (2010) for the Hercules supercluster and the Sculptor supercluster, respectively. They detect evidence for X-ray absorption from the WHIM in the spectra of blazars. Also Finoguenov et al. (2003) found good indications for the presence of WHIM associated with the Coma cluster by detecting an excess soft X-ray emission from a $T{\sim}0.2\,\mathrm{keV}$ gas with about 0.1 solar metallicity.

The hierarchical picture of the formation of structures implies that galaxy groups are, in general, just scaled-down version of the larger galaxy clusters. This also means that the properties of clusters and groups should be *self-similar*. Consequently, scaling laws between different physical quantities (for instance relations between mass and luminosity or temperature of the clusters and groups) should behave in a similar way. As discussed in more detail in Sec. 2.4 and studied in chapter 4, this simplifying assumption does not always hold in reality.

In the 1970s, a different structure formation theory compared to the bottom-up scenario was popular, introduced by Zel'dovich (1970). He suggested a top-down scenario in which superclusters form first and with time fragment into smaller substructures. This is possible in so-called *hot dark matter* models where the dark matter particles are e.g. relativistic neutrinos. But nowadays this is found to be in disagreement with the observation, that galaxies already formed early in the cosmic evolution (as it can be inferred from the age of the stellar population in galaxies). Additionally, galaxy formation in hot dark matter models mainly takes place in superclusters where matter already locally collapsed as denoted in Frenk & White (2012). This is in disagreement with the observed large-scale galaxy distribution (cf. also Fig. 1.1).

Going back to the very beginning, the formation of all structures in cold dark matter models started with small initial density perturbations and the theory describing these perturbations is summarized in the following paragraphs.

Linear perturbation theory The linear ansatz to describe the formation of structure is a simplified method because the actual equations are non-linear and need to be solved numerically. However, the basic concept becomes clear in the linear regime of small perturbations, i.e. length scales much smaller than the horizon scale of the epoch, where a Newtonian description is appropriate. In this regime and at early times, matter can be described as a fluid which is, nevertheless, a crude approximation because dark matter is collisionless. The description of the perturbations with the dark matter density $\rho(\boldsymbol{x}, t)$ is given in the comoving coordinate frame (Eq. 1.4). The density contrast is defined as

$$\delta(\boldsymbol{x}, t) = \frac{\rho(\boldsymbol{x}, t) - \bar{\rho}(t)}{\bar{\rho}(t)} \tag{1.26}$$

with the mean density $\bar{\rho}(t)$. The velocity field $\boldsymbol{u}(\boldsymbol{r}, t)$ is the sum of the Hubble expansion (first term) and the peculiar velocity (second term)

$$\boldsymbol{u}(\boldsymbol{r}, t) = \dot{a}\boldsymbol{x} + \boldsymbol{v}(\boldsymbol{x}, t) = \frac{\dot{a}}{a}\boldsymbol{r} + \boldsymbol{v}\left(\frac{\boldsymbol{r}}{a(t)}, t\right). \tag{1.27}$$

The description of a fluid follows the Euler-, continuity- and the Poisson-equation. In the comoving description with the comoving gravitational potential Φ, they are given by

$$\frac{\partial \boldsymbol{v}}{\partial t} + \frac{\dot{a}}{a}\boldsymbol{v} + \frac{1}{a}(\boldsymbol{v} \cdot \boldsymbol{\nabla})\boldsymbol{v} = \boldsymbol{\nabla}\Phi \qquad \text{Euler equation} \tag{1.28}$$

$$\frac{\partial \delta}{\partial t} + \frac{1}{a}\boldsymbol{\nabla} \cdot [(1+\delta)\boldsymbol{v}] = 0 \qquad \text{Continuity equation} \tag{1.29}$$

$$\boldsymbol{\nabla}^2\Phi = \frac{3H_0^2\Omega_\mathrm{m}}{2a}\delta \qquad \text{Poisson equation.} \tag{1.30}$$

Combining the above equations gives a second-order differential equation for the density contrast

$$\ddot{\delta} + \frac{2\dot{a}}{a}\dot{\delta} - \frac{3H_0^2\Omega_\mathrm{m}}{2a^3}\delta = 0, \tag{1.31}$$

which is a linear damped acoustic wave equation. The general solution to this equation is given by

$$\delta(\boldsymbol{x}, t) = D_+(t)\Delta_+(\boldsymbol{x}) + D_-(t)\Delta_-(\boldsymbol{x}) \tag{1.32}$$

where D_+ represents the growing mode of the perturbation and D_- the decaying mode, however, for the formation of structure only the growing mode is relevant. In a special case of $\Omega_\mathrm{m} = 1$ and $\Omega_\Lambda = 0$ (called Einstein-de-Sitter, short EdS) universe this is

$$D_+ \propto t^{\frac{2}{3}} \propto a(t). \tag{1.33}$$

For radiation and ordinary baryonic matter, pressure is important. From General Relativity it is known that pressure acts as a source of gravity which is why the fluid equations derived from GR contain additional pressure terms that have to be considered for these cases. However, for the growth of the dark matter density contrast in the radiation dominated phase (where the dark matter perturbations are sub-dominant), the non-relativistic description of the fluid equations without pressure applies and yields that these perturbations grow as

$$\delta \propto \frac{a}{a_\mathrm{eq}} + \frac{2}{3},$$

where a_eq marks the point of matter-radiation equality. From this it can be seen that small matter perturbations in the radiation dominated phase will not grow until matter starts to dominate the evolution from when on they evolve as $\delta \propto a$.

For superhorizon scales, i.e. scales larger than the local comoving Hubble radius $d_\mathrm{H} = \frac{c}{aH(a)}$, a general relativistic treatment of the perturbation is necessary. But for the special case of spherical homogeneous perturbations, the situation simplifies and can be treated non-relativistic. This yields that the density contrast grows as $\delta \propto a^2(t)$ in the radiation dominated phase and as $\delta \propto a(t)$ for matter domination.

In summary, small perturbations evolve as

$$\delta_\mathrm{subhorizon} \propto \begin{cases} \text{const.} & \text{for } a \ll a_\mathrm{eq} \\ a & \text{for } a \gg a_\mathrm{eq} \end{cases}$$

and superhorizon perturbations as

$$\delta_\mathrm{superhorizon} \propto \begin{cases} a^2 & \text{for } a \ll a_\mathrm{eq} \\ a & \text{for } a \gg a_\mathrm{eq}. \end{cases}$$

As mentioned in the beginning, the above description only holds for several simplifying assumptions and the general non-relativistic evolution of perturbation can in detail only be solved numerically as e.g. done in the Millennium Simulation. However, the special situation of an idealized spherical overdensity evolving in a homogeneous universe, can be solved explicitly. This model is known as the *spherical collapse model* and described below.

Spherical collapse model The equation of motion for a spherical shell enclosing the mass M is

$$\ddot{r} = -\frac{GM}{r^2}. \tag{1.34}$$

Integrating this equation yields

$$\dot{r}^2 = \frac{2GM}{r} + C, \tag{1.35}$$

where C is an integration constant. This differential equation has the following parametrized solutions

$$r = A(1 - \cos\theta) \tag{1.36}$$

$$t = B(\theta - \sin\theta) \tag{1.37}$$

$$A^3 = GMB^2 \text{ and} \tag{1.38}$$

$$C = -\frac{A^2}{B^2} < 0, \tag{1.39}$$

where the latter equation expresses that the kinetic energy is smaller than the potential energy and the system is gravitationally bound. Starting at $t = 0$, the sphere expands up to a maximum turnaround radius of $r_{\rm max} = 2A$ for $t_{\rm max} = \pi B$ and collapses after $t_{\rm coll} = 2\pi B$. For early times ($t \longrightarrow 0$) the first order Taylor expansion of r and t yields

$$r^3 = \frac{9}{2}GMt^2 \quad \Rightarrow \quad a \propto t^{\frac{2}{3}} \tag{1.40}$$

as expected for a matter dominated universe.

In an ideal case, the sphere will collapse to a point, however, real overdensities always show deviations from exact spherical symmetry which is why the sphere will virialize at a certain radius $r_{\rm vir} = 0.5 r_{\rm max}$. In an EdS universe, the characteristic overdensity of the virialized sphere with the mean background density $\bar{\rho}_{\rm m} \propto r_{\rm EdS}^{-3}$ is

$$\frac{\rho_{\rm vir}}{\bar{\rho}_{\rm m}} = \frac{r_{\rm EdS}^3(t_{\rm vir})}{r_{\rm vir}^3} = 18\pi^2 \approx 178. \tag{1.41}$$

In chapter 2, where the properties of galaxy clusters are discussed, this overdensity plays an important role as many of these properties are given for specific radii corresponding to certain overdensities. For example, often the virial radius of a galaxy cluster or group (i.e. the radius within the cluster is virialized) is approximated by the radius where the density is 200 times the critical density because $178 \approx 200$ and is denoted by r_{200}. However, for different cosmologies this value changes, e.g. for $\Omega_{\rm m} = 0.3$ and $\Omega_\Lambda = 0.7$ and $z = 0$ the virial radius corresponds to an overdensity of $\sim$101 (Bryan & Norman, 1998).

CHAPTER 2

Galaxy clusters

In the last chapter, the cosmological context in which galaxy clusters form and evolve was summarized, while this chapter focuses on the properties of the galaxy clusters themselves. The basic characteristics are described in Sec. 2.1. This work is based on X-ray observations that trace the largest baryonic component in clusters – the intracluster medium. The underlying processes that lead to the X-ray emission are described in Sec. 2.2 as well as observations in other wavelengths that are often needed to understand the whole activity inside clusters. The characteristics of the intracluster medium are discussed in detail in Sec. 2.3. As mentioned in the previous chapter, clusters can be used as cosmological probes which is presented in Sec. 2.4. The main references for the content of this chapter are Reiprich et al. (2013), Schneider (2015), Schneider (2009), Schneider (2005) and Reiprich & Zhang (2012).

2.1 Basic properties

The largest objects in the universe, which are in virial equilibrium, are the galaxy clusters. They have masses from a few $10^{13}\,M_\odot$ for small groups up to $\sim 10^{15}\,M_\odot$ for the massive clusters. The extent of clusters lies between one and several Mpc and typical luminosities are about a few times 10^{44} ergs/s. Clusters are often characterized by their morphology and dynamical status into regular (relaxed) and irregular (disturbed) clusters. The former are spherically symmetric and in hydrostatic equilibrium while the latter show a perturbed morphology (e.g. due to merging events) and possibly deviations from equilibrium states. This discrimination is important and reasonable as the properties of these two types differ in many respects as will be discussed later in this chapter (Sec. 2.3). In general, galaxy clusters consist of four main constituents:

Galaxies Clusters contain about ∼100 up to ∼1000 member galaxies while the smaller galaxy groups host about $\lesssim 50$ galaxies. The number of cluster galaxies is called *richness*. In the process of cluster formation and due to higher galaxy densities in clusters compared to the field, cluster galaxies interact and merge frequently and form ellipses. For this reason, most of the cluster members are elliptical galaxies and only a small fraction of spirals is found in the outer parts of clusters (e.g. Dressler, 1984). Many clusters and groups contain a giant luminous elliptical galaxy (often a cD type galaxy with a diffuse extended halo) close to their spatial and kinematic center which is also called *brightest cluster galaxy* (BCG).

Gas Galaxy clusters and groups contain a hot diffuse gas – called the intracluster medium (ICM) – which has temperatures between $T_{\rm gas}{\sim}1-15\,{\rm keV}$. It is detectable in X-rays and was first observed by Boldt et al. (1966) for the Coma cluster with one of the first X-ray telescopes. The ICM accounts for about 10% of the total cluster mass with $M_{\rm gas}{\sim}10^{12}-10^{14}\,{\rm M}_{\odot}$. In general, its X-ray emission is also a tracer for the underlying dark matter distribution. The gas is optically thin and has densities of $n_{\rm gas}\lesssim 0.1\,{\rm particles/cm^3}$. The ICM provides one of the best tools to study the dynamical status of clusters and groups and can reveal imprints of structure formation such as gas clumping, shocks and non-equilibrium states. All three projects of this work focus on the ICM and a detailed description of this component can be found in Sec. 2.3.

Dark matter Dark matter is the largest component of galaxy clusters with about 80% of the total mass. Fritz Zwicky in 1933 was the first to find that galaxy clusters must contain an invisible component which he called dark matter. Zwicky studied the motion of the galaxies in the Coma cluster and compared the mass obtained from the virial theorem to the mass estimated from the galaxy luminosities. He found that the latter mass is too low by two orders of magnitude to form a gravitationally bound system and thus inferred that additional (dark) matter is needed. However, only poor knowledge of its exact nature and properties exist, despite from the fact that dark matter is cold (cf. Sec. 1.2) and likely made of *weakly-interacting massive particles* (WIMPs) which only interact though the weak force and gravity. A possible explanation is provided by an extension to the standard model of particle physics called *supersymmetry* (SUSY). The lightest SUSY particle – the neutralino – might be a good candidate for a dark matter particle and current accelerator experiments such as the LHC try to find those particles but, so far, without success.

Other kinds of dark matter as neutrinos (hot dark matter) or *Massive Astrophysical Compact Halo Objects* (MACHOS) are ruled out by current observations. The case of neutrinos has been discussed previously. MACHOS are compact objects that emit (almost) no light, e.g. black holes and brown dwarfs, and are thus hard to detect. However, through gravitational microlensing a constraint on their mass contribution can be estimated and yields that MACHOS can only account for about 20% of the mass of a dark matter halo (Alcock et al., 2000).

One of the strongest observational evidences for the existence of dark matter comes from X-ray and weak gravitational lensing analyses (cf. Sec. 2.2.3) of the famous merging Bullet cluster. In the merging process of the substructures, galaxies and dark matter particles act collisionless while the ICM acts collisional. Hence, an offset between the mass concentration and the X-ray emission (that traces the ICM distribution), is expected if the largest mass component in clusters is dark matter. Indeed, this offset is observed and thus strongly supports dark matter theories.

Relativistic particles A tiny fraction of the content of galaxy clusters consists of relativistic particles. These particles have velocities close to the speed of light and are accelerated e.g. in shocks or turbulences. They gyrate around the magnetic field lines (clusters can have magnetic fields at the order of a few μG) and emit synchrotron radiation. For the total mass they are negligible.

2.2 Observations of galaxy clusters

Observations of galaxy clusters in multiple wavelengths provide independent methods to detect clusters and, as it is e.g. obvious from the Bullet cluster, are essential to obtain a complete

picture of the cluster properties. This work is based on X-ray observations, hence, a special emphasis is put on these kinds of observations, however, also observations and measurements in other wavelengths will be briefly introduced in the following sections.

2.2.1 X-ray observations

X-ray observations offer the possibility to study the properties of the ICM – the largest baryonic component – in great detail. Additionally, these observations allow for an independent and complementary mass estimate of the full gravitational mass of the cluster compared to e.g. gravitational lensing. The ICM does only weakly suffer from projection effects, meaning that at the position of a clear extended accumulation of hot gas, most likely a cluster is located. This allows for extensive X-ray surveys to detect a large amount of clusters as, for instance, the previously mentioned upcoming eROSITA satellite is expected to detect about 100,000 clusters (Merloni et al., 2012). The following description is mainly based on Reiprich & Zhang (2012).

In general, the emissivity of the gas in clusters is given by

$$\epsilon = n_\mathrm{e} n_\mathrm{H} \Lambda(T_\mathrm{e}, A) \tag{2.1}$$

with the electron number density n_e and the hydrogen number density n_H and the cooling function $\Lambda(T_\mathrm{e}, A)$ which itself depends on the electron temperature T_e and the metallicity A.

The main X-ray emission from the ICM above energies of 2 keV is due to bremsstrahlung (or free-free emission, denoted by the index ff) where the electrons of the ICM get deflected or decelerated by the ions. In this case, the emissivity at frequency ν is

$$\epsilon_\nu^\mathrm{ff} \propto n_\mathrm{e} n_\mathrm{i} g_\mathrm{ff} T_\mathrm{e}^{-0.5} e^{-\frac{h\nu}{kT_\mathrm{e}}}, \tag{2.2}$$

with n_i being the ion number density, g_ff is the quantum mechanical Gaunt factor of the order of one and k is the Boltzmann constant. From this equation it becomes clear that one important characteristic of the ICM spectrum is the exponential cut-off whose position depends on the temperature is thus one prime feature to measure the ICM temperature. Typical cluster X-ray spectra for three different temperatures are illustrated in Fig. 2.1.

For a fully ionized plasma, the total bremsstrahlung emissivity is given by

$$\epsilon^\mathrm{ff} \propto n_\mathrm{e}^2 T_\mathrm{e}^{0.5}. \tag{2.3}$$

In addition to bremsstrahlung, also line emission shows up in the ICM spectra. Especially the iron line complexes at around 1 keV (L line complex) and 6 keV (K line complex) are further important spectral features to determine the temperature of the plasma. For plasma temperatures below $\sim$2 keV this component is even dominant and the total emissivity is then given by

$$\epsilon \propto n_\mathrm{e}^2 T_\mathrm{e}^{-0.6} \tag{2.4}$$

and thus has an opposite temperature dependence than in Eq. 2.3. For typical cluster gas temperatures of $\gtrsim 2$ keV, the cooling function and hence the emissivity in a soft energy band depends only weakly on the gas temperature as shown in Fig. 2.2 for the $0.5 - 2$ keV band.

Another important quantity is the *Emission Integral* (also called *Emission Measure*) defined as

$$EI = \int_V n_\mathrm{e} n_\mathrm{H} \mathrm{d}V. \tag{2.5}$$

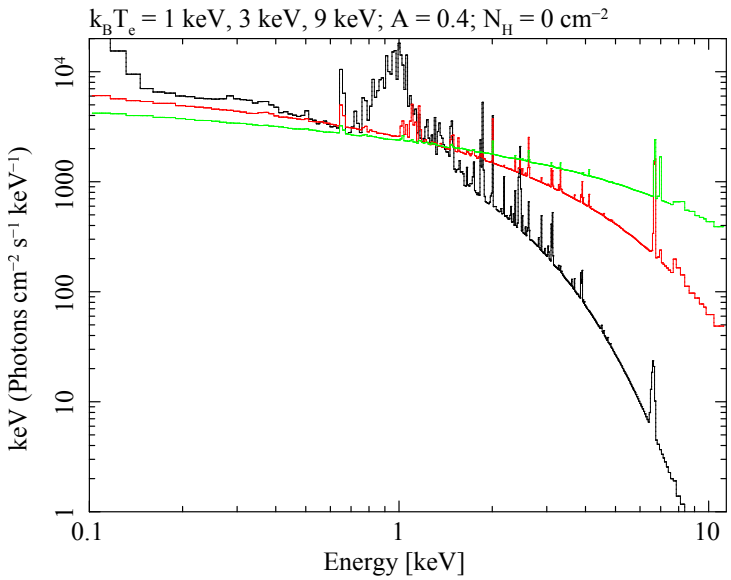

Figure 2.1: Simulated X-ray spectra of the ICM for three temperatures (black 1 keV, red 3 keV, green 9 keV), a metallicity of $A = 0.4\,\mathrm{A}_\odot$ and no absorption. The higher the temperature, the more the exponential cut-off position shifts towards higher energies and the line complexes become less pronounced. Credit: Reiprich et al. (2013).

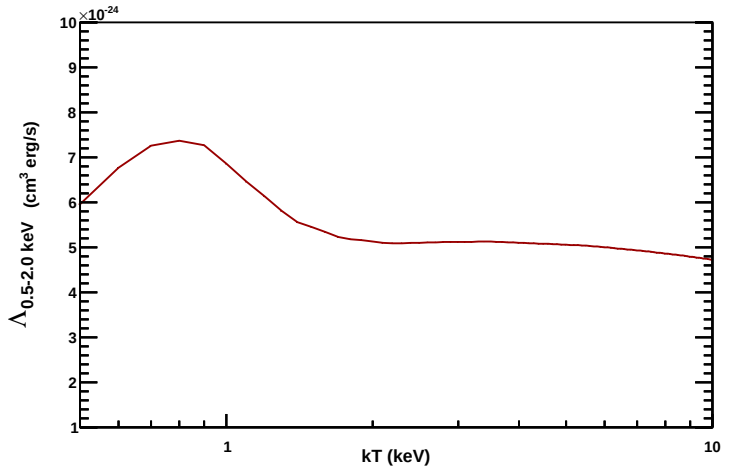

Figure 2.2: Cooling function in the energy band $0.5 - 2.0$ keV as a function of ICM temperature and for a metallicity of $0.3\,\mathrm{Z}_\odot$ and a redshift of $z = 0.05$. The cooling function above 2 keV stays approximately constant.

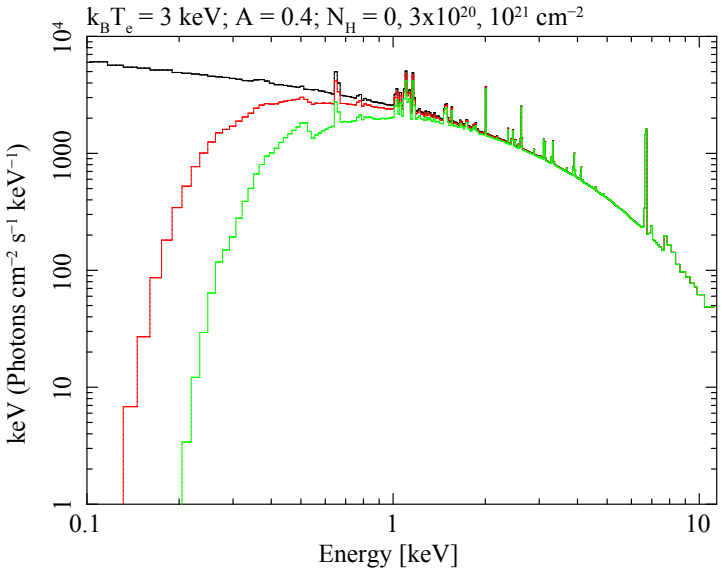

Figure 2.3: Simulated X-ray spectra of the ICM for different values of the hydrogen column density N_{H} (black $N_{\mathrm{H}} = 0\,\mathrm{cm}^{-2}$, red $N_{\mathrm{H}} = 3 \times 10^{20}\,\mathrm{cm}^{-2}$, green $N_{\mathrm{H}} = 10^{21}\,\mathrm{cm}^{-2}$) and a source metallicity of $A = 0.4\,\mathrm{A}_{\odot}$. The higher the column density, the stronger the absorption at the low spectral end. Credit: Reiprich & Zhang (2012).

Two other X-ray producing processes are synchrotron radiation and inverse Compton scattering. Although they are not important in the ICM, synchrotron emission plays a role in active galactic nuclei (AGN) which contribute to the X-ray background (see below) and inverse Compton is essential for observations of the Sunyaev-Zeldovich effect (see Sec. 2.2.3).

Inverse Compton scattering occurs when a highly energetic electron interacts with a photon. The latter gains energy through this interaction which can lead to upscattering of photons into the X-ray regime. Synchrotron radiation is emitted when relativistic electrons travel in a magnetic field and gyrate around the magnetic field lines. Their spectrum has a broad range from radio to X-rays. The energy distribution of these electrons is given by

$$N(E) \propto E^{-\alpha} \tag{2.6}$$

where N is the number of electrons at a given energy E. The total emitted power P is again a power law but with different spectral index

$$P \propto \nu^{\frac{\alpha-1}{2}}. \tag{2.7}$$

When observing clusters in X-rays, absorption of the photons along the line of sight affects the spectra, especially at lower energies, as shown in Fig. 2.3. Although hydrogen is the most frequent element in the universe, the absorption mainly arises due to elements heavier than hydrogen as depicted in Fig. 2.4. The hydrogen abundance can be measured via the 21 cm emission and acts as a tracer for the heavier elements. The amount of absorbing material in the line of sight is given by the column density N_{H} in units of cm^{-2}. Relative abundances of the heavier elements are estimated using abundance tables based on measurements of the solar abundances or the abundance in meteorites, e.g. Asplund et al. (2009), Anders & Grevesse (1989) and Lodders (2003).

Another aspect of absorption are molecules and dust which are not included in measurements of the 21 cm line. To infer this contribution, the total hydrogen column density, including both, atomic and molecular hydrogen, can be used as a tracer. Willingale et al. (2013) measured the abundance of the total absorption by studying the X-ray afterglows of 493 Gamma-Ray-Bursts with the Swift telescope which occur randomly distributed over the sky and can be used to estimate the total column density.

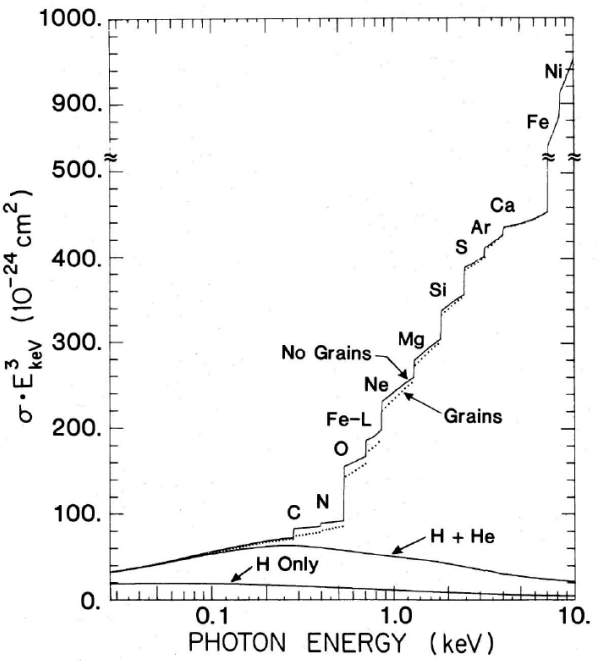

Figure 2.4: The photoelectric absorption cross section per hydrogen atom as a function of energy. The dotted line shows the effect when the elements are condensed into dust grains. Credit: Morrison & McCammon (1983).

The Astrophysical Plasma Emission Code (APEC) The APEC model is a spectral model to describe the spectra of a collisionally ionized and optically thin plasma as the ICM. It is based on the models of Raymond & Smith (1977) but has continuously been improved since then, predicated on current *Atomic Data for Astrophysics* (ATOMDB)[1]. It models all the above described processes of the ICM and is often combined with a photoelectric absorption (*phabs*) model to include absorption. The parameters of the APEC model are in general the temperature of the ICM, the metal abundance, redshift and a normalization which is proportional to the emission measure. The model can be extended using a VAPEC model which allows for constraining individual elemental abundances (He, C, N, O, Ne, Mg, Al, Si, S, Ar, Ca, Fe and Ni). The normalization of the model is related to the density

$$\text{norm} = \frac{10^{-14}}{4\pi[D_\text{A}(1+z)]^2} \int n_\text{e} n_\text{H} \text{d}V \tag{2.8}$$

where D_A is the angular diameter distance to the source in cm.

[1] see `www.atomdb.org`

Amongst others, the APEC model is implemented in the XSPEC fitting package[2], which is used in this work. XSPEC provides fitting and plotting routines and numerous statistical tools to analyze X-ray spectra independent of the instrument used to obtain the spectra.

X-ray background All observations have to deal with different back- and foreground components. In X-ray observations, this background is mainly composed of four different types: 1. An instrumental background which depends on the properties of the instrument and is described in detail in chapter 3 for the two satellites used in this work; 2. a cosmic X-ray background, 3. a Milky Way halo component and 4. a local component.

The cosmic X-ray background (CXB) is caused by the superposition of the emission of distant AGNs. De Luca & Molendi (2004) found that this component can be described by a power law with spectral index 1.41. However, the origin of these X-rays is not fully understood. They can be due to emission from the jets or from the corona of the accretion disc of AGNs and the involved emission processes might be synchrotron radiation, inverse Compton and/or bremsstrahlung.

Also the origin and composition of the local component is not fully clear. One idea is that early supernovae explosions generated a cavity around the sun which is filled with a thin gas of $T \sim 0.1\,\mathrm{keV}$ that emits X-rays, as formulated by Cox & Reynolds (1987). This cavity is called *local hot bubble* (LHB). Later, observations from Schmitt et al. (1991) of the dark side of the moon yielded the surprising result that X-rays were detected from this region. Five years later, Lisse et al. (1996) detected unexpected X-rays from the comet Hyakutake. These two observations led to a new model for the local X-ray component, the *solar wind charge exchange* (SWCX). In this process, solar wind ions interact with neutral atoms or molecules as e.g. present in the corona of a comet and the earths exosphere. The ions gain one or several electrons that subsequently cascade and emit X-ray photons. SWCX thus adds as a foreground to X-ray observations and might (partially) replace or add to the concept of a LHB.

The last background component arises from a hot plasma in the halo of the Milky Way as it was first seen in observations of the ROSAT satellite. These observations revealed X-ray shadows of gas clouds in the Milky Way which immediately gives rise to an X-ray emitting diffuse component behind those clouds, nowadays identified as coronal gas ($\sim 0.2 - 0.3\,\mathrm{keV}$) in the galactic halo (e.g. Burrows & Mendenhall, 1991 and Snowden et al., 1991). As the CXB, this component gets absorbed by material along the line of sight, mainly by dust and gas inside the Milky Way.

2.2.2 Optical observations

Optical observations of galaxy clusters, on the one hand, allow to study the properties of the member galaxies as e.g. color, morphology and the distribution and, on the other hand, provide the opportunity to investigate the cluster mass distribution. Additionally, optical surveys are performed to identify clusters by, qualitatively speaking, looking for overdens regions, i.e. more galaxies in a certain area than on average in the sky. In 1958, George Ogden Abell released the first large catalog of optically detected galaxy clusters based on their richness, compactness and magnitude (Abell, 1958) and still today many clusters are named after this catalog. However, the simple detection of overdens regions suffers from projection effects. To avoid these, redshift information is needed and can be obtained from photometric and spectroscopic measurements of the galaxies, the latter yielding very accurate distance estimates.

[2] `heasarc.gsfc.nasa.gov/xanadu/xspec`

To determine the mass distribution of clusters, the *gravitational lensing* effect is one of the most important tools and a brief description of this effect is given in the following paragraph; a detailed discussion is e.g. presented in Schneider (2005) and Schneider (2015).

Gravitational lensing The basic idea of gravitational lensing is that, as described in Sec. 1.1, matter distorts space-time and thus light gets deflected by mass concentrations such as galaxy clusters, which act as a *lens* to background sources. This, in general, can result in multiple images, distortions and magnification of the lensed objects. A schematic view of the geometry in a lens system is illustrated in Fig. 2.5. Prominent observational evidences for gravitational lensing are luminous, elongated arcs around the mass concentration, e.g. a galaxy cluster. A special case occurs when the source and the lens are perfectly aligned and the image of the source appears as a so-called *Einstein ring* (Fig. 2.6).

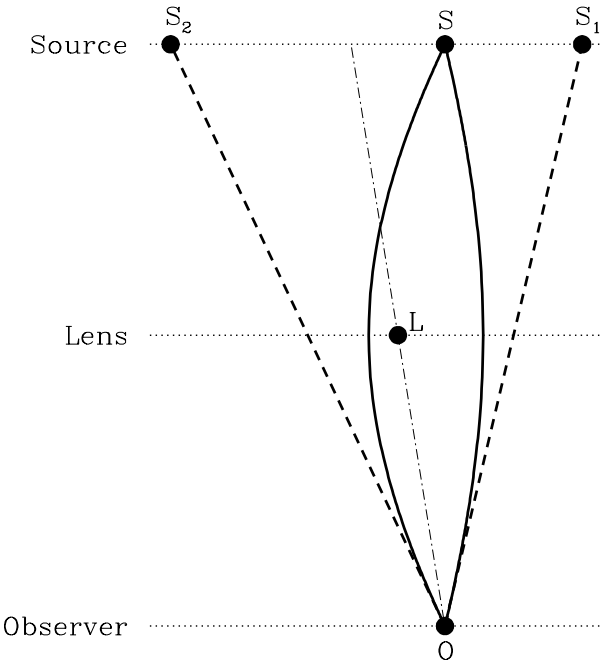

Figure 2.5: Scheme of a lens system. Light rays from the source S get deflected by the lens L on their way to the observer O which produces multiple images S_1 and S_2 of the source. Credit: Wambsganss (1998).

Such rings or arcs only occur in the *strong lensing regime*, e.g. for the central regions of massive galaxy clusters. However, *weak gravitational lensing* can be used to also trace the projected mass profile in lower mass clusters and groups and at larger angular separations from the center of the mass concentration. It causes small distortions of the images of the lensed objects which appear tangentially aligned to the cluster center and can only be measured statistically over a large sample of background sources (which is also called *shear*). This allows to infer the local tidal gravitational field. The basic principle is illustrated in Fig. 2.7. When performing weak gravitational lensing studies, the intrinsic shapes of the background galaxies add as a noise to the lensing signal.

Masses determined through gravitational lensing are important independent cross-checks to other mass estimators as e.g. the X-ray hydrostatic mass, which is introduced in Sec. 2.3.8. The advantage of lensing mass estimates is that – in contrast to the X-ray hydrostatic mass – it does not rely on the assumption of hydrostatic equilibrium and spherical symmetry. Weak

Figure 2.6: Einstein ring around a luminous red galaxy caused by gravitational lensing. Credit: ESA/Hubble & NASA (2011).

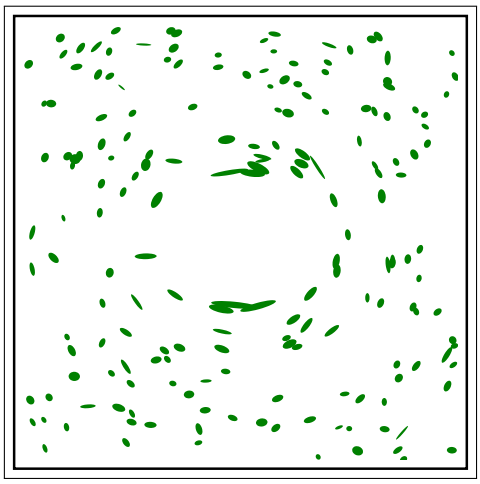

Figure 2.7: Schematic illustration of weak gravitational lensing. The shapes of background galaxies get distorted and, on average, their images appear elongated around the mass concentration (here highly exaggerated) which is measurable as a statistical effect over a large sample of background sources and can be used to infer the projected mass of the lens, e.g. a galaxy cluster. Credit: Adapted from Wikimedia Commons (2008).

gravitational lensing also plays a role in this work in chapter 5 to estimate the mass of the high redshift cluster Cl $J120958.9{+}495352$.

2.2.3 Observations in other wavelengths

Clusters exhibit prominent features also in other wavelengths, e.g. in the radio regime. Extended synchrotron emission from clusters, called radio halos, has been detected by many authors since the 1970s, e.g. Jaffe (1977), Giacintucci et al. (2011), Giacintucci et al. (2013), Cuciti et al. (2015) and Knowles et al. (2016). Radio halos are not assigned to a particular object (galaxy) in the cluster and can have sizes of several hundred kpc up to $\sim$3 Mpc. An extremely large radio halo was observed by Feretti et al. (2001) for the cluster A2163 which is the object studied in the third project of this work (chapter 6). Typically, radio halos follow the distribution of the ICM. Their origin is still not fully understood but is likely related to merging events in which the electrons are accelerated (e.g. Brunetti & Blasi, 2005).

Other prominent structures observed in several clusters are *radio relics*. A relics is a diffuse, extended and elongated emission in the outer regions of clusters (e.g. van Weeren et al., 2010, van Weeren et al., 2016). Their emission is strongly polarized (in contrast to radio halos) and, in some cases, relics are associated with merger shocks where the electrons get accelerated and the magnetic field lines are aligned parallel to the shock front.

Other sources of radio emission in clusters are tailed radio galaxies, i.e. galaxies with a "comet-like" structure which only occur inside clusters and therefore also offer a way to find clusters (e.g. Banfield et al., 2016). The tail is likely to be explained by their motion relative to the ICM which causes a stripping of the gas. In some cases, a small region around an AGN is also found to be a source of radio emission. These regions are called radio mini halo and one explanation for their occurrence is the re-acceleration of former relativistic electrons from the AGN through cooling flows (Sec. 2.3.4).

Another important effect which can be used to study and detect galaxy clusters is the *Sunyaev-Zeldovich effect*. It arises due to inverse Compton scattering of CMB photons with the energetic electrons of the ICM. Although the probability for this interaction is very low, the cumulated effect in the gas of clusters can be detected in the microwave regime as a distortion of the CMB spectrum. The strength of the effect depends on the gas density and temperature. The Compton y-parameter is given by

$$y = \int n_\mathrm{e} \frac{kT_\mathrm{e}}{m_e c^2} \sigma_\mathrm{T} \, \mathrm{d}l \tag{2.9}$$

as the integration along the line of sight with the Thomson cross section σ_T and the electron mass m_e. A schematic view of this effect on the spectrum of the CMB photons is depicted in Fig. 2.8. At frequencies below (above) $\sim$218 GHz it can be observed as a decrement (excess) in the CMB signal. The Sunyaev-Zeldovich effect is independent of redshift and thus very well suited to detect very distant clusters (e.g. Bleem et al., 2015a, Planck Collaboration et al., 2015) and, additionally, provides another method to estimate the mass of clusters.

In principle, yet another conceivable wavelength regime to study galaxy clusters are γ-rays. However, until recently, no γ-ray emission from galaxy clusters has been detected but it is expected due to the presence of relativistic electrons. A very recent study by Branchini et al. (2017) cross correlated the results of the Fermi Large Area Telescope with known catalogs of galaxy clusters and confirmed the detection of a signal at the position of the clusters. The origin of this emission is not fully clear at the moment. Likely it is related to the accumulated signal of AGNs but also a contribution from the ICM might be possible at energies $<$10 GeV.

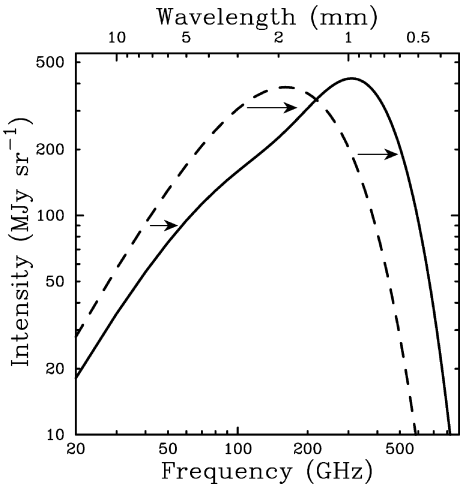

Figure 2.8: Distortion of the CMB spectrum caused by the Sunyaev-Zeldovich effect. The dashed curve is the Planck spectrum of the unperturbed CMB while the solid curve shows the distorted spectrum (exaggerated). At frequencies lower than ∼218 GHz, the intensity decreases and increases at higher frequencies due to inverse Compton scattering of the CMB photons with the electrons of the ICM. Credit: Carlstrom et al. (2002).

2.3 The intracluster medium

The ICM is subject to all projects in this work and thus is described in detail in this section. The method to study radial dependencies of the ICM characteristics is introduced in the next section, followed by the description of the physical properties and an overview of galaxy clusters as cosmological probes.

2.3.1 Studying radial profiles

Before describing the ICM in detail, the general approach to study its X-ray properties as a function of the cluster radius is introduced. This is usually done via spectral fits in several annuli around the cluster center (e.g. the X-ray emission peak or centroid) and is schematically illustrated in Fig. 2.9. In each annulus, spectra are extracted and simultaneously fitted. The choice of the sizes, shapes and the number of annuli depends on the spatial resolution of the instrument as well as the signal-to-noise ratio in each annulus and thus has to be chosen individually for each observation. For sources with a small extent on the sky or instruments with poor spatial resolution, this can result in low radial resolution which affects e.g. the determination of the gas mass and total mass. If the sizes of the annuli are of the order of the resolving capability of the instrument (given by the size of the *point spread function*, short PSF), the mixing of photons from one annulus to another due to the PSF size has to be taken into account and corrected for in the spectral fit.

In the simultaneous spectral fit, every annulus is assigned its own spectral model such that radial profiles (e.g. the temperature profile) can be obtained. Backgrounds (e.g. the instrumental background) might vary with the position on the detector and thus additional individual background models and/or spectra might be used in each annulus.

Often, radial quantities are given at specific overdensities (cf. Sec. 1.2) denoted by the corresponding subscript in the following, e.g. M_{500} is the mass at R_{500}. Until several years ago, X-ray studies mostly incorporated the gas inside R_{500} because satellites as Chandra and

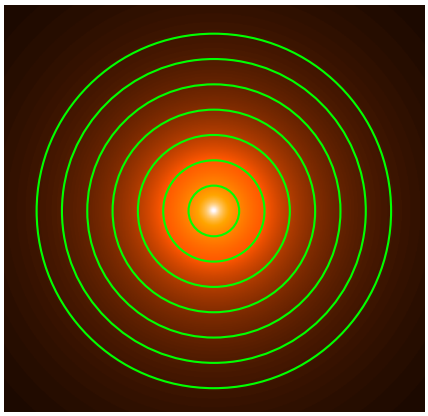

Figure 2.9: Schematic principle of radial analyses of the ICM. Spectra are extracted for every annulus and fitted simultaneously to obtain radial profiles. The sizes of the annuli and the number is individual for each observation. Also, the annuli do not have to be equally spaced and circular as depicted here for illustration.

XMM-Newton are not able to well trace the low surface brightness outer parts of clusters and groups due to instrumental limitations. Until last year, Suzaku provided the opportunity to study radial profiles out to $\sim R_{200}$. As it can be seen in Fig. 2.10, these so-called outskirts – usually defined as $R_{500} <$ cluster outskirts $< 3R_{200}$ (Reiprich et al., 2013) – contain ~90% of the cluster volume and can exhibit interesting features and astrophysical information on e.g. turbulences, clumping and non-equilibrium states.

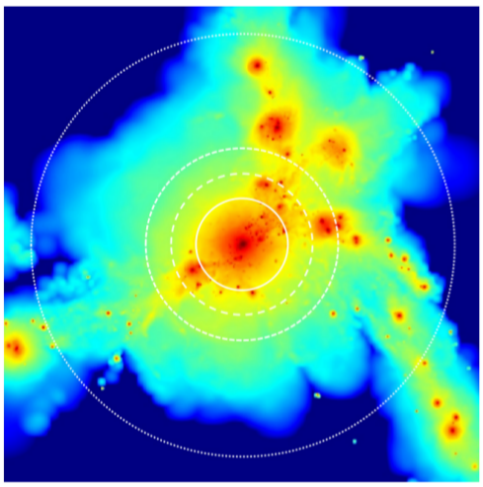

Figure 2.10: Surface brightness map of a simulated galaxy cluster. The colors span 16 orders of magnitude and were chosen to highlight the cluster outskirts. The white circles correspond to R_{500}, R_{200}, $R_{\rm vir}$, $3R_{200}$. Credit: Reiprich et al. (2013).

Projection effects The above described method to determine radial profiles suffers from projection effects, e.g. multiple temperatures along the line of sight, because only the projected 2-dimensional emission of the optically thin ICM is detected. Several attempts exist to deal with this problem and to deproject the results. Some of them include direct modeling of this effect in the spectral fitting while other methods aim for a correction of the projected quantities

afterwards. One common approach is the *onion-peeling* method, i.e. the successive subtraction of onion like shells to deduce the deprojected quantities. This principle is illustrated in Fig. 2.11. Ettori et al. (2002) developed a matrix deprojection method following this concept for which the projected quantities in radial bin i are given by the sum over all overlying shells j

$$T_i = \frac{\sum_{j=i}^{N} \epsilon_j V_{i,j} T_j}{\sum_{j=i}^{N} \epsilon_j V_{i,j}} \qquad \text{Temperature} \tag{2.10}$$

$$EI_i = \sum_{j=i}^{N} n_{\mathrm{e}}^j n_{\mathrm{H}}^j V_{i,j} \qquad \text{Emission Integral} \tag{2.11}$$

where $V_{i,j}$ is the volume along the line of sight of shell j for radial bin i (see also reddish area in Fig. 2.11) and ϵ is the emissivity. In general, it is also possible to assume a continuous model for the temperature and density profiles in which case the sum translates into an integral over the volume. The deprojection is then performed through a minimization of the model parameters to match the observed values (cf. Sec. 4.4.6).

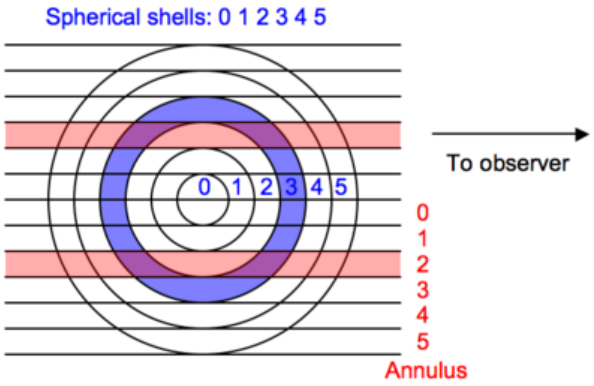

Figure 2.11: Schematic principle of the onion shell deprojection method. The projected quantities in each annulus $0-5$ are given by the sum of the contributions from all shells in the line of sight to the observer. Hence, the deprojected quantities are obtained by successive subtraction of these contributions. Credit: CXC/SAO (2009).

2.3.2 Surface brightness

An image of a typical relaxed and spherically symmetric galaxy cluster is shown in Fig. 2.12. Already by eye it is clear that the surface brightness decreases fast with the distance from the cluster center. In general, the X-ray surface brightness S_{X} along the line of sight l is

$$S_{\mathrm{X}} = \frac{1}{4\pi(1+z)^4} \int \epsilon \, \mathrm{d}l. \tag{2.12}$$

The emissivity ϵ is proportional to n_{e}^2 (cf. Eq. 2.1). Based on this, a typical profile for modeling the surface brightness was motivated by King (1962) that originally described the density profile in globular clusters; but it was found that to also match the profiles of galaxy clusters. This so-called beta-model generally well describes densities and surface brightness profiles of clusters

Figure 2.12: Composite image of the cluster A383 in X-rays (purple) overlaid over an optical image. The smooth spherical distribution of the X-ray emission indicates that this cluster is relaxed. Credit: X-ray: NASA/CXC/Caltech/A.Newman et al./Tel Aviv/A.Morandi & M.Limousin; Optical: NASA/STScI, ESO/VLT, SDSS.

and groups. It assumes spherical symmetry and an isothermal ICM and is given by

$$S_{\mathrm{X}} = S_0 \left(1 + \frac{r^2}{R_{\mathrm{c}}^2}\right)^{(-3\beta+0.5)} \tag{2.13}$$

with the normalization S_0, the core radius of the cluster R_{c}, the index β and the *projected* radius r.

Note that in the integration from Eq. 2.12 to Eq. 2.13, the cooling function is assumed to be constant along the line of sight which is a reasonable assumption for most clusters with temperatures >2 keV in the soft energy regime (cf. Fig. 2.2).

E.g. Vikhlinin et al. (1999) and Neumann (2005) measured typical values of β for clusters between $0.65-0.85$ while for galaxy groups lower values between $0.4-0.5$ are found (e.g. Komossa & Böhringer, 1999 and Hwang et al., 1999). Often, a second beta-model is needed to properly describe the profile in the core region, i.e. a double beta-model of the form $S_{\mathrm{X}} = S_{\mathrm{X},1} + S_{\mathrm{X},2}$. This is illustrated in Fig. 2.13 which shows the surface brightness profile together with the double beta-model for the cluster A2390.

The *peakyness* of the surface brightness profile is one indicator for the morphology of the cluster (e.g. Santos et al., 2008, Mantz et al., 2015). Relaxed clusters typically show more concentrated surface brightness distributions and higher central surface brightnesses than disturbed clusters (e.g. Zhang et al., 2008) and correspondingly higher central densities (e.g. Hudson et al., 2010).

Towards the outskirts, the surface brightness drops fast which makes analyses of those regions challenging and background dominated over a wide range of the spectrum. Suitable instruments, such as the Suzaku satellite described in Sec. 3.1, are needed for these kinds of studies.

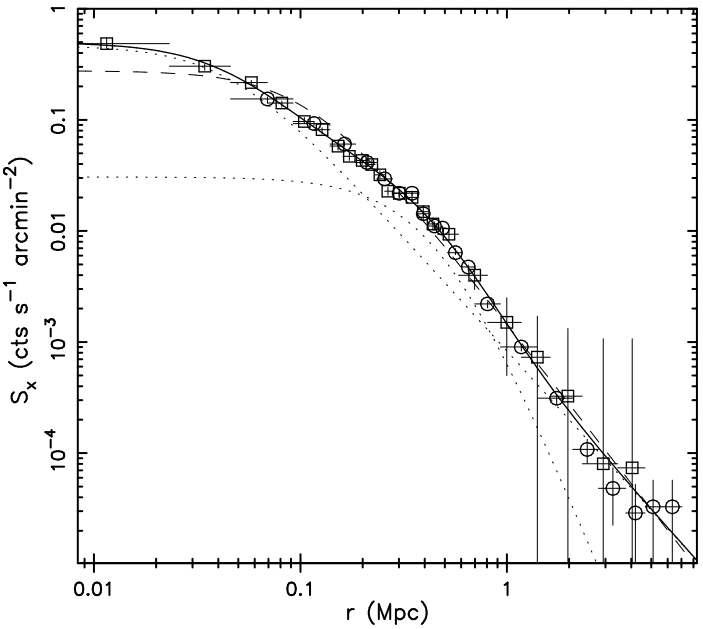

Figure 2.13: Surface brightness profile of Abell 2390. The solid line shows the double beta-model which fits the surface brightness well also in the core region while the single beta-model (dashed line) lacks the central peak. The dotted lines show the two components of the double beta-model. Credit: Xue & Wu (2000).

2.3.3 Density

As mentioned above, the typical ICM density profile is described by a beta-model of the form

$$n_{\rm gas} = n_0 \left(1 + \frac{R^2}{R_{\rm c}^2}\right)^{(-\frac{3}{2}\beta)}, \tag{2.14}$$

where R is now the spherical cluster radius (not a projected quantity). The gas density is not a direct observable, however, if a good fit to the surface brightness profile can be performed, the density profile should be described similarly well by the fitted parameters β and $R_{\rm c}$. Also for the density, often a double beta-model is needed to well describe the central regions. Fig. 2.14 shows that density profiles can exhibit large scatter, especially in the inner regions of clusters and groups (which are often affected by cooling flows, cf. Sec. 2.3.4), while the scatter around R_{500} is much smaller and the profiles follow the typical beta-model shape with $\beta \approx 2/3$, as expected from the above mentioned beta-value for the surface brightness profiles.

The ICM density can be affected by *clumping* of the gas which occurs randomly over the cluster volume and leads to an overestimation of the gas mass by up to 12% as shown by Roncarelli et al. (2013) in hydrodynamical simulations. Eckert et al. (2015) showed that clumping is a small effect inside R_{500} when including cooling, star formation, and AGN feedback while non-radiative simulations overpredict the level of inhomogeneities. Nevertheless, e.g. Nagai & Lau (2011) found that clumping might be a significant effect in the outskirts of groups and clusters. Observational evidence for clumping was e.g. found by Simionescu et al. (2011) for the outskirts of the Perseus cluster, however, to explain their results, much higher clumping factors are needed than found in the simulations. Clumping might significantly contribute to a flattening of the density profile at large radii, which results in an underestimation of the total

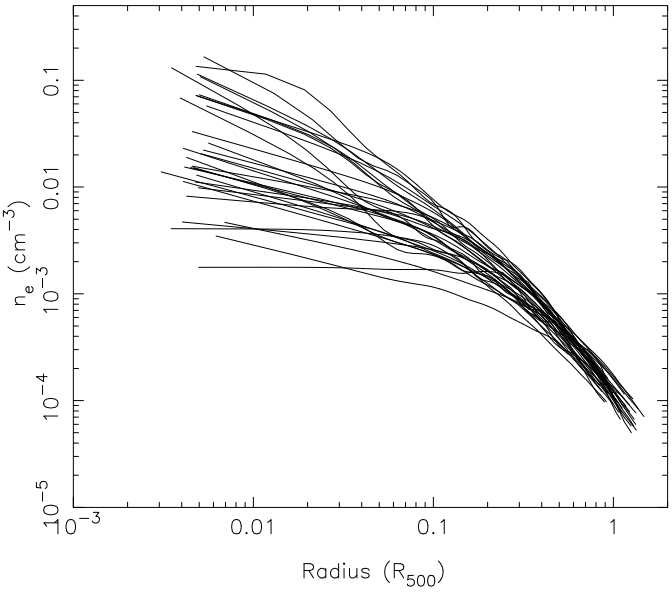

Figure 2.14: Density profiles of the REXCESS cluster sample. A wide spread can be seen in the inner parts of the profiles while towards R_{500} the scatter clearly reduces and the profiles follow the typical slope of ∼2/3. Credit: Croston et al. (2008).

mass and a flattening of the entropy profile. The latter was observed for several clusters and will be discussed in Sec. 2.3.5.

2.3.4 Temperature

The temperature is one of the most important properties of the ICM and, beside the density, it is the second quantity that goes into the X-ray hydrostatic mass equation which will introduced in Sec. 2.3.8. The ICM temperature is a direct parameter of the spectral model and is thus constrained in the spectral fit. For spectral temperature estimates, the question arises if the measured temperature actually represents the global electron temperature, i.e. if the electrons are in collisional ionization equilibrium (CIE). According to Smith & Hughes (2010), a typical time scale to reach CIE is

$$t_{\mathrm{CIE}} \approx 3 \times 10^7 \text{ yr } \left(\frac{n_{\mathrm{e}}}{10^{-3}\mathrm{cm}^{-3}}\right)^{-1}. \tag{2.15}$$

For typical densities of $\sim 0.01\,\mathrm{cm}^{-3}$ this yields $t_{\mathrm{CIE}} \approx 3 \times 10^6\,\mathrm{yr}$ and hence CIE is generally a good assumption. In the outskirts, densities can drop to $\sim 10^{-5}\,\mathrm{cm}^{-3}$ making the CIE timescale considerably large. Reiprich et al. (2013) showed that wrongly assumed CIE might result in underestimated temperatures in the outskirts and thus steeper profiles resulting in lower total mass estimates.

Another question is whether the ion temperature is equal to the measured electron temperature. As protons have a much larger mass, they will carry most of the kinetic energy gained in accretion or merger shocks. Hence, electrons and protons will reach thermal equilibrium at different timescales and different temperatures. As pointed out in Reiprich & Zhang (2012), these timescales are generally short and each of the species will settle in thermal equilibrium quickly, however, the time needed to redistribute the energy between electrons and protons through collisions (and to settle them at the same temperature) can take up to one Gyr in the outskirts

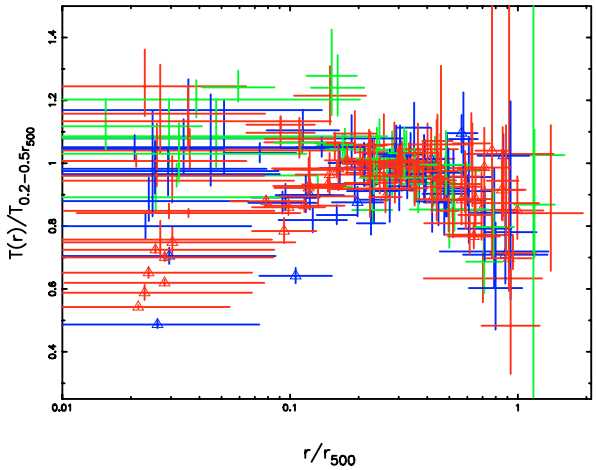

Figure 2.15: Temperature profiles of the LoCuSS sample. Clusters that appear to have an "off-center" morphology are shown in green, elliptical or complex structure is shown in blue and undisturbed morphology in red. Cool core clusters are marked by triangles. Credit: Zhang et al. (2008).

where e.g. accretion shocks might have occurred recently. Observational indications for such a non-equilibrium state with $T_\mathrm{e} < T_\mathrm{gas}$ at large cluster radii has e.g. been found by Akamatsu et al. (2011) and might result in an underestimation of the total mass.

Galaxy clusters can exhibit a *cool core*, i.e. a decline of the temperature due to radiative cooling in the center where the gas is densest. As the gas cools, it flows inwards caused by the weight and pressure of the overlaying gas. This slow hydrostatic flow is called a *cooling flow* (e.g. Fabian, 1994) and is an idealized picture to explain the observations of cold centers in clusters and groups. In this picture, gas cools down to very low temperatures and should be detectable through strong emission lines. However, as revealed by the XMM-Newton satellite, these emission lines are not detected in the ICM and thus the simplified picture needed to be revised. The currently most common idea is that of additional heating sources which prevent the gas from reaching the very low temperatures (e.g. Gaspari et al., 2013). Such a heating source is probably the central AGN which is present in almost all cool core clusters as found by Mittal et al. (2009) while only half of the non-cool core clusters exhibit a central AGN. Interaction of the ICM with the central AGN might be even self-regulating in a feedback process. When cool gas flows towards the center, more gas is accreted by the AGN and thus more energy is dissipated which again heats the gas. The details of this process, whether it is due to interactions with the accretion disc, heat redistribution through mixing or other precesses is not fully clear. The described effects result in a variety of temperature characteristics in the central regions of clusters as shown in Fig. 2.15. This wide spread makes it difficult to constrain a universal temperature profile for clusters as it e.g. exists for the surface brightness, however, attempts for such a generalized profile exist (e.g. Loken et al., 2002 and Baldi et al., 2012).

It is found (e.g. Hudson et al., 2010, Zhang et al., 2008) that the presence and strength of a cool core is strongly correlated with the dynamical status, i.e. relaxed clusters often exhibit a cool core while in disturbed clusters the core is more likely to be destroyed in the merging process. A cool core cluster is usually characterized by its cooling time, which is given by the ratio of the internal energy U to the emissivity (Reiprich & Zhang, 2012)

$$t_\mathrm{cool} = \frac{U}{\epsilon_\mathrm{ff}} \propto \frac{n_\mathrm{e} T_\mathrm{e}}{\epsilon_\mathrm{ff}} \propto n_\mathrm{e}^{-1} T_\mathrm{e}^{\frac{1}{2}}. \tag{2.16}$$

As this is inverse proportional to the density, the cooling time can become shorter than the Hubble time for dens cluster centers. E.g. Hudson et al. (2010) define a cool core cluster by the central (within 0.4% R_{500}) cooling time whereas strong cool cores correspond to $t_{\rm cool}^{\rm CC} \leq 1\,{\rm h}_{71}^{-0.5}$ Gyr, weak cool cores (CC) to $t_{\rm cool}^{\rm CC} \leq 7.7\,{\rm h}_{71}^{-0.5}$ Gyr and a non-cool core clusters (NCC) to $t_{\rm cool}^{\rm NCC} > 7.7\,{\rm h}_{71}^{-0.5}$ Gyr.

Due to the above mentioned processes and gas inhomogeneities, a multi-temperature structure can be present in the ICM and thus multi-temperature models are sometimes needed to properly describe the core region. But also the outskirts can exhibit a multi-temperature structure through clumping, accretion shocks or turbulences. In this low density and low surface brightness regions it becomes more difficult to constrain multi-temperature models. Hence, the actual determined temperature from a single-temperature model depends on the response of the detector, as shown in Reiprich et al. (2013). Despite some simplifications in their simulation (e.g. no background emission), the findings suggest that, for instance, the upcoming eROSITA satellite will measure steeper temperature profiles than e.g. Suzaku, when a single temperature model is used due to different instrumental responses. This would result in lower total mass estimates obtained by eROSITA. However, the authors also note that in cases where the difference between the temperature phases is large and one component is $T \lesssim 1\,{\rm keV}$, the single temperature spectral fit does not perform well (regarding the reduced χ^2) and therefore the necessity of a second temperature component is obvious. The same is true for the inner cluster regions where the statistics are usually sufficient to disentangle multiple temperatures.

Reiprich et al. (2013) also investigated the general shape of temperature profiles up to $1.15R_{200}$ measured with Suzaku as shown in Fig. 2.16. The averaged profile over these spectra shows a typical decline of a factor of ∼3 from the central region to the outskirts in overall agreement with numerical simulations.

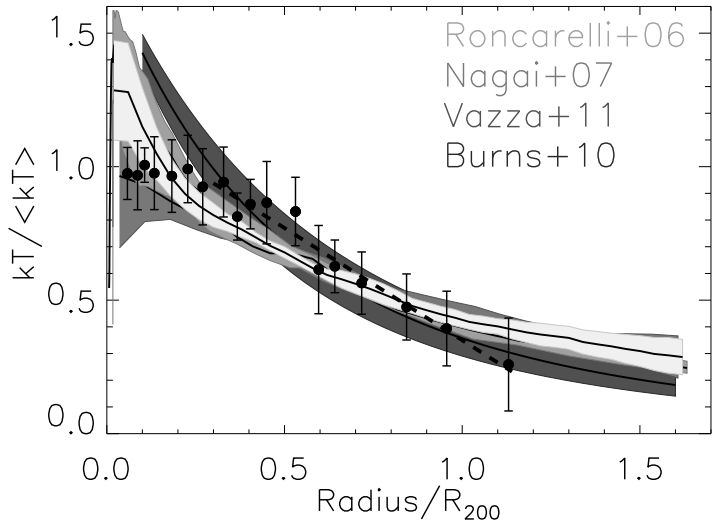

Figure 2.16: Averaged and normalized temperature profiles measured with Suzaku and shown together with several numerical simulations. The dashed line represents the best linear fit to the data in the range $0.3R_{200} < R < 1.15R_{200}$. Credit: Reiprich et al. (2013).

2.3.5 Entropy

The entropy of the ICM is defined as (e.g. Boehringer & Werner, 2009)

$$K(R) = kT(R) n_{\rm e}^{-\frac{2}{3}}(R). \tag{2.17}$$

Hence, all effects described above concerning the density and temperature profiles also apply for the entropy. Especially, the flattening of the density profile due to e.g. clumping and the steepening of the temperature profile caused by deviations from CIE or thermal equilibrium as well as deviations from hydrostatic equilibrium, can lead to a flattening or even a drop of the entropy profiles at large radii (e.g. Su et al., 2013, Hoshino et al., 2010, Akamatsu et al., 2011). Additionally, influences from the central AGN (heating mechanisms) are believed to be responsible for the often observed entropy excess in the central regions of clusters (e.g. Eckert et al., 2013b).

The shape of the entropy profiles was intensively studied by Walker et al. (2013) who found an excess in the inner cluster regions compared to the typical slope of $K(R) \propto R^{1.1}$ and the predictions from non-radiative gravitational structure formation simulations performed by Voit (2005). Conversely, their measured profiles deviate towards lower entropy in the outskirts as shown in Fig. 2.17 (left). In contrast to that, results from Eckert et al. (2013a) indicate an agreement of the entropy profiles with the simulations in the outer regions of the clusters as depicted in Fig. 2.17 (right). These contradicting results were also seen for galaxy groups e.g. by Su et al. (2013) who found an entropy drop for the fossil groups ESO 3060170 around R_{200} and Humphrey et al. (2012) who obtained a profile in agreement with the simulation by Voit (2005) at large radii. Thus, no definite conclusion can be drawn about the entropy profile in the outskirts of galaxy clusters and groups and large samples and detailed analyses (especially of the less intensively studied galaxy groups) are needed. This is also important to investigate the self-similar behavior between clusters and groups regarding the entropy. Therefore, the first project of this work (cf. chapter 4), in which the local group UGC 03957 is analyzed in great detail, adds a valuable contribution to approach this issue.

In some cases, a correction of the entropy profile depending on the gas mass fraction (see Sec. 2.3.9) needs to be applied to find an agreement with the numerical simulations and to e.g. correct for gas depletion effects. This correction was suggested by Pratt et al. (2010) and is also used in Walker et al. (2013) and Eckert et al. (2013b) and in this work as described in Sec. 4.6.6.

2.3.6 Metallicity profiles

The metallicity of the ICM can be directly constrained from the spectral data. Often, the average elemental abundance (e.g. using the APEC model, cf. Sec. 2.2.1), assuming a certain abundance table, is estimated but generally also individual elemental abundances can be constrained. Metals are produced inside of stars and are distributed to their surrounding by supernovae (SN) explosions and stellar winds. From their host galaxy, the metals can be distributed to the ICM by galactic winds, galaxy interactions, AGN outflows and ram pressure stripping. The latter is the stripping of galactic gas due to the relative motion of the galaxies in the ICM of the cluster. Simulations by e.g. Kapferer et al. (2007) showed that clusters enriched by ram pressure stripping show a steeper abundance profile than clusters enriched by galactic winds, which is intuitive because of the higher density towards cluster centers. Werner et al. (2013) measured the metal distribution in the Perseus cluster and found a remarkably flat distribution of the iron abundance, which they interpret as an early enrichment due to galactic winds and AGN feedback between $z \approx 2 - 3$. A similar result was obtained by Simionescu et al. (2015) for the Virgo cluster for the elements Si, S and Mg which show flat abundances out to beyond the virial radius. From the ratios of these α-elements relative to the iron abundance, the amount of SN that enriched the ICM can be inferred because different SN Types produce different elemental abundance patterns. They found that an enrichment solely due to core-collapse SN is ruled out with very high significance and obtained a ratio of SN Type Ia to the total amount of SN

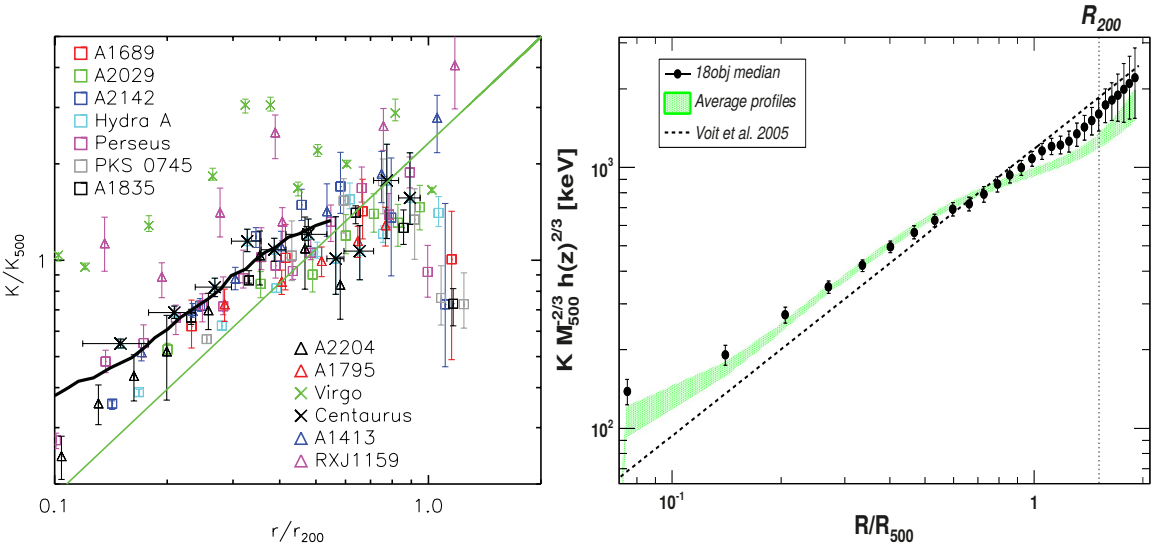

Figure 2.17: *Left*: Scaled entropy profiles for clusters studied with Suzaku, XMM-Newton and Chandra, compared to the prediction from Voit (2005) (green solid line) and the median entropy from the REXCESS sample (black line). The flattening/drop of the entropy at large radii is clearly visible. Credit: Walker et al. (2013). *Right*: Median of 18 cluster entropy profiles and the same baseline prediction from numerical simulations as in the left figure (dashed line). The profiles also show an excess in the central region but a better agreement with the simulations in the outskirts. Credit: Eckert et al. (2013b).

between 12% and 37% which is in agreement with estimates for cluster cores from e.g de Grandi & Molendi (2009).

2.3.7 Shocks in the ICM

Shocks affect almost all quantities of the ICM described above and a detailed review about their properties can be found in Markevitch & Vikhlinin (2007), however, the most important aspects are summarized here. The most prominent example for a distinct shock is the previously mentioned Bullet cluster shown in Fig. 2.18. This cluster exhibits a clear shock front arising from the crossing of the merging constituents. Although the bow shock seems clearly visible in the figure, the actual shock front lies close in front of this prominent feature which is actually a *cold front*. Fig. 2.18 (right) shows the temperatures map of the Bullet cluster and reveals the "true" shock front. Similar features have e.g. been seen by Markevitch et al. (2000) for the merging cluster A2142 and Vikhlinin et al. (2001) in the central region of A3667. The proposed explanation is that these cold fronts are relics from dens and cold cluster cores which were not destroyed in the merging process.

From the distinct jumps in the temperature and density profiles at the position of the shock, the Mach number can be inferred and thus the shock velocity. The *Rankine-Hugoniot jump conditions* (e.g. Wesseling, 2009) describe the discontinuities in a shock front by the ratio of the properties behind the shock (post-shock) denoted by index 2 and in front of the shock (pre-shock) denoted by index 1

$$\frac{\rho_2}{\rho_1} = \frac{(\gamma+1)M^2}{(\gamma-1)M^2+2} \tag{2.18}$$

$$\frac{T_2}{T_1} = \frac{[2\gamma M^2-(\gamma-1)][(\gamma-1)M^2+2]}{(\gamma+1)^2 M^2}. \tag{2.19}$$

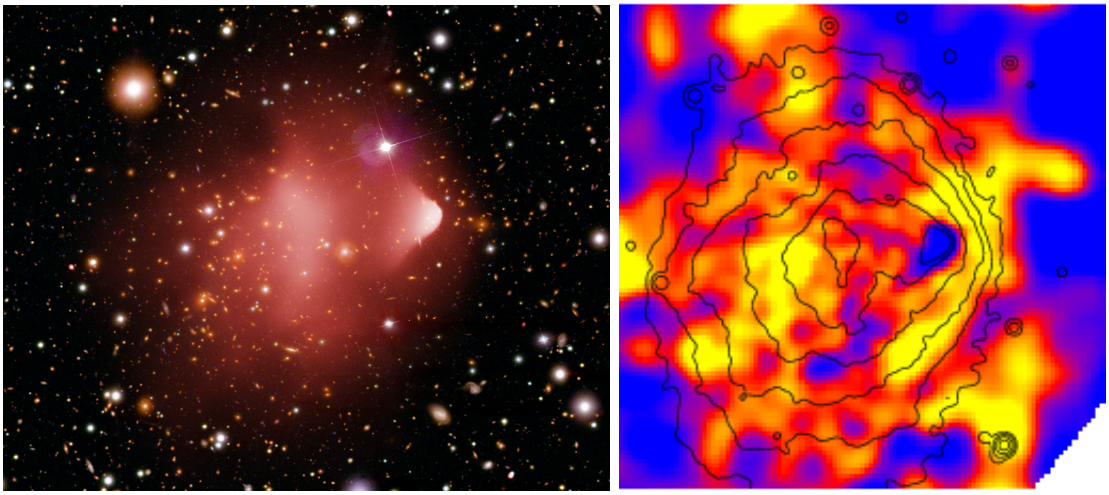

Figure 2.18: Observations of the Bullet cluster. *Left:* Composite image of Chandra X-ray observations (shown in red) and optical observations. The prominent "bullet"-like feature originates from the crossing of one merging constituent through the ICM of the other constituent and is actually a cold front. Credit: X-ray: NASA/CXC/CfA/M.Markevitch et al.; Optical: NASA/STScI; Magellan/U.Arizona/D.Clowe et al. *Right:* Temperature map and overlaid X-ray surface brightness contours. The shock front with a clear temperature increase is located right in front of the cold front. Credit: Markevitch (2010).

γ is the adiabatic index, whereas $\gamma = \frac{5}{3}$ for a monoatomic gas, and M is the Mach number. The latter is related to the velocity by

$$M = \frac{v}{c_\mathrm{s}}, \tag{2.20}$$

with the speed of sound c_s and typical values in shocks are $M \lesssim 3$ (e.g. Simionescu et al., 2009a, Bourdin et al., 2013). The speed of sound is given by

$$c_\mathrm{s} = \left(\frac{\partial P}{\partial \rho_\mathrm{gas}}\right)^{\frac{1}{2}} = \left(\frac{\gamma k T_\mathrm{gas}}{\mu m_\mathrm{p}}\right)^{\frac{1}{2}} \tag{2.21}$$

with the mean molecular weight μ and the proton mass m_p. Typical values are about 1000 km/s.

The Bullet cluster's infall velocity determined by Markevitch et al. (2002) is $3000 - 4000$ km/s relative to the main cluster, which appears unlikely high in the standard ΛCDM cosmology and is not fully understood yet (Lee & Komatsu, 2010). Although shocks should be a common feature in regions where structure formation and merging takes place (e.g. intersections of filaments), only relatively few distinct shocks in X-rays have been detected so far. An example is the irregular cluster Hydra A studied by Simionescu et al. (2009a) who found a large scale shock using data from the Chandra satellite with a Mach number of $M \sim 1.3$. Also the merging cluster A521 studied by Bourdin et al. (2013) exhibits a shock front with $M \sim 2.4$ coinciding with a radio relic. The study of shock fronts is also one project of this work and presented in chapter 6 for the merging cluster A2163.

2.3.8 Total mass

As mentioned before, measuring the properties of the ICM provides an independent method to constrain the total mass of the cluster (including dark matter) because, qualitatively speaking, the ICM traces the dark matter potential. The *X-ray hydrostatic mass* can be inferred by solving

the hydrostatic equilibrium equation

$$\frac{1}{\rho_{\rm gas}}\frac{{\rm d}P_{\rm gas}}{{\rm d}R} = -\frac{{\rm d}\Phi}{{\rm d}R} = -\frac{GM_{\rm tot}}{R^2}. \tag{2.22}$$

with $P_{\rm gas}$ being the pressure and Φ the gravitational potential. The mass inside radius R is then given by

$$M_{\rm tot}(<R) = -\frac{kT_{\rm gas}R}{G\mu m_{\rm p}}\left(\frac{{\rm d}\ln\rho_{\rm gas}}{{\rm d}\ln R} + \frac{{\rm d}\ln T_{\rm gas}}{{\rm d}\ln R}\right). \tag{2.23}$$

This estimate relies on accurate measurements of the density and temperature profiles and follows several assumptions as pointed out in Reiprich & Zhang (2012) and Reiprich et al. (2013). Those are (approximately sorted by importance):

- The gas is in hydrostatic equilibrium
- The only external field is the gravitational field
- The cluster is spherically symmetric
- No pressure is added by relativistic particles
- The gas is thermodynamically ideal
- The mean molecular weight μ is constant with radius
- No relativistic corrections are needed, i.e. Newtonian description is adequate
- The effect of dark energy is negligible

The most important assumption, hydrostatic equilibrium, is justifiable in most cases for relaxed clusters because a sound wave traveling through the cluster needs much less time to cross it than the age of the cluster. This assumption might not be valid in the outer and very inner parts of clusters and in mergers as discussed in the previous sections. The results of N-body simulations of about 100 clusters by Piffaretti & Valdarnini (2008) showed that masses can be underestimated by $\sim$15% at R_{200} due to wrongly assumed hydrostatic equilibrium.

Clusters only have small magnetic fields and Dolag & Schindler (2000) showed in *smoothed particle hydrodynamic* (SPH) simulations that, for relaxed clusters, the effect of magnetic fields on the total mass is at most 15%. Thus, also the second assumption is reasonably valid. Spherical symmetry is a good assumption for most relaxed clusters. For irregular clusters the morphology might be complicated, however, in this case already the assumption of hydrostatic equilibrium is problematic and one better falls back to different mass estimates as e.g. gravitational lensing. Piffaretti et al. (2003) modeled the effect of asphericity and found that it is small for slight deviations from spherical symmetry but can increase to a difference of 30% between weak lensing and X-ray hydrostatic masses for clusters elongated along the line of sight. Relativistic particles can be neglected and hence also their pressure support but e.g. Nagai et al. (2007) showed in their N-body simulations that sub-sonic bulk motions and/or turbulences can add pressure support, especially in the outskirts of clusters which might bias low the total mass estimated at this radii by $5\% - 20\%$.

If no significant helium sedimentation is present, i.e. a higher He/H ratio towards the center, the assumption of a constant μ is justified. If Helium sedimentation plays a significant role, e.g. a factor of two difference from the primordial He/H ratio, μ would be underestimated by 12% and thus the total mass overestimated by this factor as shown by Peng & Nagai (2009).

The Schwarzschildradius given by $R_{\rm SR} = 2GM/c^2$ is typically about $\sim$10 pc for galaxy clusters and thus much smaller than the cluster radius, implying that no relativistic corrections are needed. Also, dark energy does not cluster strongly and thus should be negligible.

In general, mass estimates from weak lensing and X-ray studies agree well, especially for relaxed clusters, as e.g. shown by Zhang et al. (2008) and Zhang et al. (2010) who measured a ratio of $M_{\rm X}/M_{\rm WL}$ between $0.9 - 1.0$. However, e.g. Mahdavi et al. (2008) showed that the ratio can decrease to about $\sim$80% around R_{500}, possibly due to non-thermal pressure support. This trend was later confirmed again by Mahdavi et al. (2013) who state that X-ray hydrostatic masses on average are biased low by 10% while non-cool core clusters account for the bulk of the bias. The ratio $M_{\rm X}/M_{\rm WL}$ for cool core clusters in their sample is compatible with one.

The mass profiles or respectively the corresponding density profiles in clusters (e.g. estimated from X-ray or weak lensing studies) often follow a universal form. Such a universal profile is the *Navarro–Frenk–White* (NFW) profile found by Navarro et al. (1996) from their N-body simulations of dark matter halos. It holds for virialized halos and is given by

$$\rho(R) = \frac{\rho_0}{\frac{R}{R_{\rm s}}\left(1 + \frac{R}{R_{\rm s}}\right)^2}, \tag{2.24}$$

with normalization ρ_0 and a scale radius $R_{\rm s}$, both varying from halo to halo. Integrating this equation up to the virial radius and introducing the so-called *concentration parameter* c via $R_{\rm vir} = cR_{\rm s}$ yields an expression for the total mass $M_{\rm tot}$ within $R_{200}{\sim}R_{\rm vir}$

$$M_{\rm tot} = 4\pi\rho_0 R_{\rm s}^3 \left[\ln(1+c) - \frac{c}{1+c}\right]. \tag{2.25}$$

The NFW profile well describes the dark matter density profiles for many clusters (e.g. Okabe et al., 2013 and Viola et al., 2015) and is now a commonly used model.

2.3.9 Gas mass fraction

The gas mass fraction as a function of the cluster radius R is defined as

$$f_{\rm gas}(R) = \frac{M_{\rm gas}(R)}{M_{\rm tot}(R)}. \tag{2.26}$$

The gas mass is simply obtained by integrating the gas density profile inside a certain radius while the total mass is given by Eq. 2.23 or an independent mass estimate (e.g. weak lensing). $f_{\rm gas}$ generally is an increasing function with radius and at large radii should approach the cosmic mean value of 0.15 (Planck Collaboration et al., 2014b). Often it is found that gas depletion through gas motions and AGN and SN feedback affects $f_{\rm gas}$, especially in the central regions. This was e.g. observed by Pratt et al. (2016) for four fossil systems and simulated in hydrodynamical simulations of galaxy clusters and groups by Planelles et al. (2013). The effect might be stronger for galaxy groups than for clusters because of the shallower potential well. Additionally, due to violations of e.g. hydrostatic equilibrium or other effects affecting the gas density profile (see previous sections), the cosmic mean value might be even exceeded in the outskirts as e.g. found for the Perseus cluster by Simionescu et al. (2011). Also Eckert et al. (2013a) studied the gas mass fractions of 18 clusters for which the averaged profile is shown in Fig. 2.19. The profile for the cool core clusters, for which hydrostatic equilibrium is generally a good assumption, stays below the cosmic mean value while, in contrast, the profile for the

non-cool core clusters exceeds the universal value around R_{200}.

The gas mass fraction can be used as a cosmological probe and is described in this context in the following section.

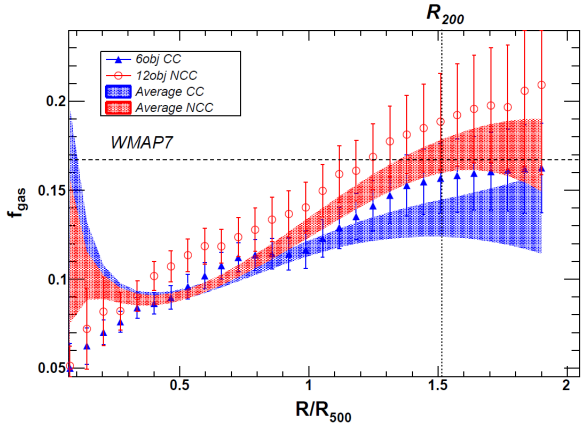

Figure 2.19: Averaged gas mass fraction profiles for a sample of cool core (CC) and non-cool core (NCC) clusters. The CC profile approaches the cosmic mean value at large radii while the NCC profile exceeds it, likely due to violations of hydrostatic equilibrium. Credit: Eckert et al. (2013a).

2.4 Cosmology with galaxy clusters

The abundance of a (large) sample of clusters as a function of their total mass and redshift is of special interest to cosmology. This distribution contains informations about the cosmological parameters and Press & Schechter (1974) were the first who suggested an analytical function. Beside this Press-Schechter formulation, e.g. Tinker et al. (2008) estimated the mass function from numerical N-body simulations and Vikhlinin et al. (2009) measured it for a sample of clusters observed with the Chandra satellite as shown in Fig. 2.20. The data from the latter are clearly incompatible with a universe without dark energy at high redshifts, which illustrates the high sensitivity of this cosmological probe.

The above example shows that an accurate measurement of the total cluster mass is essential for cosmology and therefore also the understanding of the various physical effects inside galaxy clusters is crucial as the latter can affect the total mass estimates. However, obtaining the X-ray hydrostatic mass from spectral analyses requires some effort and sufficient exposure time for each object. Hence, this is not feasible for extensive X-ray surveys which yield large samples of clusters with only short exposures for each object. The analysis of these data relies on *scaling relations* which relate easy-detectable quantities as e.g. the luminosity to the total cluster mass. The calibration of these scaling laws is vital and it is found in many studies that they differ, depending on the dynamical status (e.g. Zhang et al., 2007, Pratt et al., 2009), the redshift (Reichert et al., 2011) and the cluster mass (Lovisari et al., 2015). For a detailed review on scaling relations see Giodini et al. (2013). In particular, the conditions in galaxy groups can be different from those in clusters leading to deviations in the scaling relations from the self-similar predictions. The analysis of the physical properties of a galaxy group are subject to the project discussed in chapter 4.

Objects at high redshifts and/or with high mass (as the one studied in chapter 5) can be used to test the scaling laws for extreme cases. Additionally, the baryonic content of such distant clusters contains valuable information for cosmology. The gas mass fraction is expected to

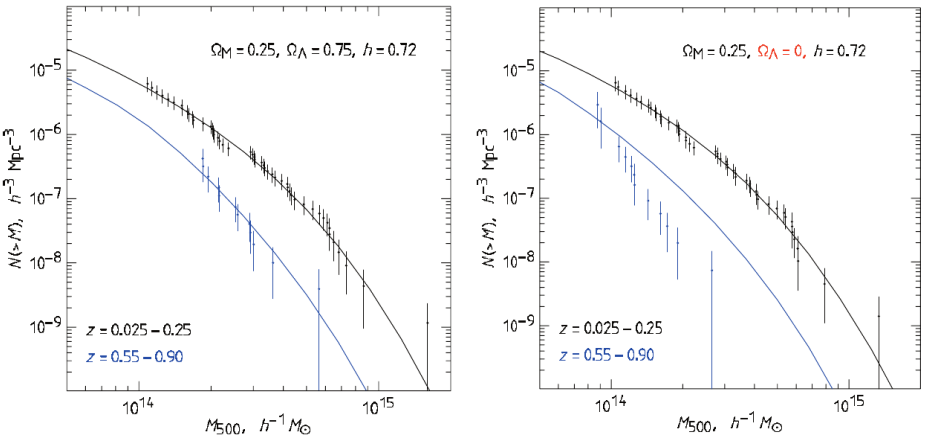

Figure 2.20: Measured cluster mass function for sample of clusters observed with the Chandra satellite compared to predicted models for different assumed cosmologies and different redshifts. A $\Lambda = 0$ universe (right) is disfavored by the data while $\Omega_\mathrm{m} = 0.25$, $\Omega_\Lambda = 0.75$ (left) yields a good description. Credit: Vikhlinin et al. (2009).

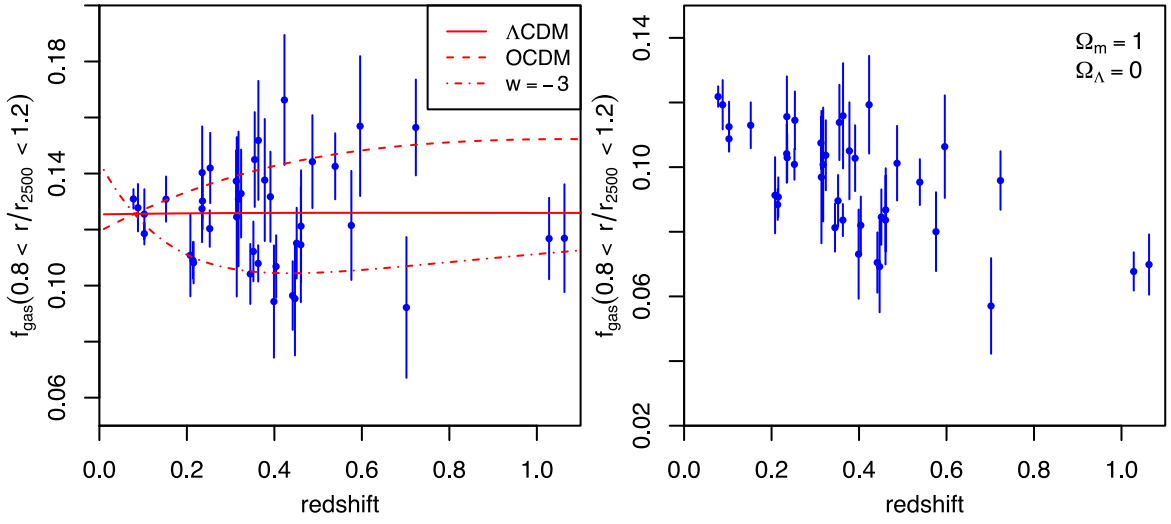

Figure 2.21: *Left:* Gas mass fraction as function of redshift for different cosmologies compared to measurements. The leverage on cosmology is larger, the larger the redshifts of the clusters. The dashed line shows an open model with $\Omega_\mathrm{m} = 0.3$, $\Omega_\Lambda = 0$, the dashed-dot line a flat model with $\Omega_\mathrm{m} = 0.3$ and an equation of state parameter $w = -3$ and the solid line the common ΛCDM model with $\Omega_\mathrm{m} = 0.3$, $\Omega_\Lambda = 0.7$. The latter best matches to data which are consistent with being constant with redshift. *Right:* Gas mass fractions estimated using an EdS cosmology which show a clear trend with redshift and this model is thus disfavored. Credit: Mantz et al. (2014).

approximately represent the average baryon fraction in the universe $\Omega_{\rm baryon}/\Omega_{\rm m}$ and should be constant with time (e.g. White et al., 1993, Allen et al., 2011). Measurements of $f_{\rm gas}$ depend on the cluster distance and hence on the assumed cosmology. They are therefore important cosmological probes, especially at high redshifts as shown in Fig. 2.21 (left) for different cosmological models that result in an apparent $f_{\rm gas}$ evolution.

Perturbations of the baryonic content, e.g. due to merging, can affect the gas mass estimate and thus bias the $f_{\rm gas}$ measurement. For this reason, the dynamical status of these distant clusters is important and can be inferred from X-ray observations (as it is done in this work in chapter 5). As mentioned before, a cool core is one possible indicator for the dynamical status but also other indications exist as e.g. the offset between the X-ray emission centroid and the BCG (Rossetti et al., 2016, Hudson et al., 2010). Mantz et al. (2015) developed a method to test clusters for being relaxed (and thus suited for the $f_{\rm gas}$ test) by investigating their symmetry, the "peakyness" of the surface brightness profile and the alignment of the isophotes. Based in these criteria, Mantz et al. (2014) studied the gas mass fraction for a sample of relaxed clusters and found that their results are in agreement with the standard cosmology of $\Omega_{\rm m} = 0.3$, $\Omega_\Lambda = 0.7$ as also shown in Fig. 2.21 (left) and disfavor models without dark energy. However, the constraints will clearly benefit from larger samples of (relaxed) high redshift clusters. A recent search for such clusters has been performed by Buddendiek et al. (2015) resulting in 83 high-grade cluster candidates between $0.6 < z < 1$ out of which Cl $J120958.9{+}495352$ – the cluster studied in chapter 5 – is the one with the second highest redshift and a promising candidate for a relaxed cool core cluster.

CHAPTER 3

Instruments

The two important X-ray instruments for this work are the Suzaku satellite and the XMM-Newton satellite. Both instruments have their own (dis)advantages which make them suited for different kinds of studies and different aspects are important for the data analysis as described in this chapter. Suzaku is introduced in Sec. 3.1 based on the *Suzaku Technical Description* by Arida (2012) and XMM-Newton is described in Sec. 3.2 following the *XMM-Newton technical description* from ESA (2017).

3.1 The Suzaku satellite

3.1.1 Instrumentation

The Suzaku satellite was launched on the 10^{th} of July 2005 and completed its mission in August 2015 after 10 years of operation. It was the fifth Japanese X-ray mission and developed in a collaboration between the Japanese Institute of Space and Aeronautical Science and the NASA Goddard Space Flight Center. The precursor of Suzaku was the ASTRO-H satellite which was lost during launch due to a malfunction of the carrier rocket in the year 2000. One year after this loss, the building of the ASTRO-H2 satellite started and after the launch it was renamed *Suzaku* after a mythological bird.

Suzaku's science objective was the study of many different X-ray sources in a wide range of energies between $0.2 - 600\,\text{keV}$. This includes investigations of hot plasma properties as well as measurements of the structure and evolution of galaxies and spectroscopic analyses of AGNs. Suzaku is orbiting in a circular orbit 551 km above ground. In this *low earth orbit* it benefits from the shielding of the earth's magnetosphere against solar wind particles that cause unwanted signals in the CCD chips. This is one big advantage of Suzaku because the particle background, which affects the science observations, is significantly reduced compared to other X-ray missions. The low and stable instrumental background makes Suzaku well suited for observations of low surface brightness sources. The following technical description is a summary of the *Suzaku Technical Description* by Arida (2012).

Suzaku is equipped with several telescopes using a conical approximation of the Wolter-I type. It has five telescopes for the soft X-ray regime between $0.4 - 10\,\text{keV}$ and one for the hard X-ray regime between $10 - 600\,\text{keV}$. The *X-ray telescopes* (XRT, Fig. 3.1) consist of five mirrors and focal plane detectors. The important instruments aboard Suzaku are the *X-ray imaging spectrometers* (XIS), the *X-ray spectrometer* (XRS) and the *hard X-ray detector* (HXD). In this work, data from the XIS instrument is analyzed.

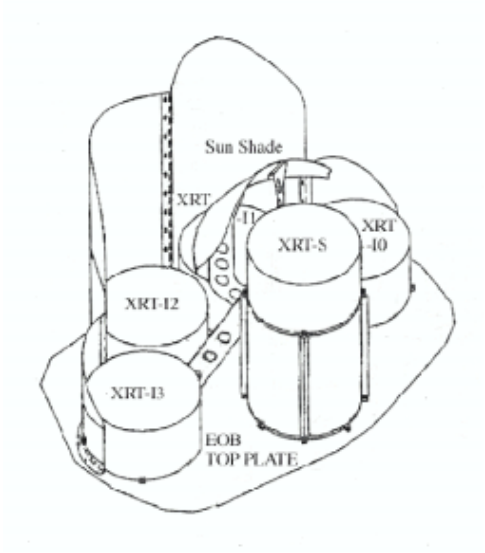

Figure 3.1: The Suzaku soft X-ray telescopes (XRT). Credit: Arida (2012).

XRS The XRS was designed to be the prime instrument of Suzaku obtaining high-resolution spectra with a resolution of $6 - 7\,\mathrm{eV}$ (FWHM) in the energy range $0.3 - 12\,\mathrm{keV}$. However, this instrument was lost shortly after launch due to a malfunction which caused the evaporation of the liquid helium which is needed for cooling.

XIS The XIS uses four independent and co-aligned soft XRTs with each having 4.75 m focal length and a spacial resolution of $2'$(HPD). XIS has an energy resolution of $\sim$130 eV at 6 keV and is sensitive in the energy range $0.2 - 12\,\mathrm{keV}$. It detects photons on four CCDs labeled XIS0–XIS3 each with a $18' \times 18'$ field of view (FOV). A schematic view of the four detectors is shown in Fig. 3.2. XIS0, 2 and 3 are front-side illuminated detectors whereas XIS1 is back-illuminated. The different building techniques give rise to different responses in the soft- and hard regime of the X-ray spectra. The CCDs consists of four segments named A–D with 1024px $\times$ 1024px each. Each chip has two ^{55}Fe calibration sources at the edges. These parts of the chips can not be used for the scientific analysis. This is also the case for XIS2 and parts of XIS0 which were damaged in November 2006 after being hit by a micrometeorite.

All detectors are also sensitive in the optical and UV regime. For this reason, an optical blocking filter is shielding the detectors from these photons. This filter is subject to calibration issues because material is accumulating on its surface which affects the low-energy regime. Additionally, over time several holes showed up in the blocking filter, however, no significant impact on the scientific operation is expected[1]. Due to constant degrading of the chips and radiation damages, the charge transfer inefficiency increases. This effect is measured and monitored using the calibration sources and is partially compensated by charge injection into several rows of the CCDs to fill up charge traps.

XIS has several operational modes to be chosen by the user for the specific scientific purpose. The *clocking modes* affect the timely read out of the CCDs. This allows for e.g. short read-out intervals to avoid photon pile-up (i.e. the arrival of two or more photons in the same pixel within one read-out time) for the observation of bright sources.

The *editing modes* affect the telemetry of an event on the detector. XIS has four editing

[1] see `www.astro.isas.ac.jp/suzaku/doc/suzakumemo/suzakumemo-2013-01.pdf`

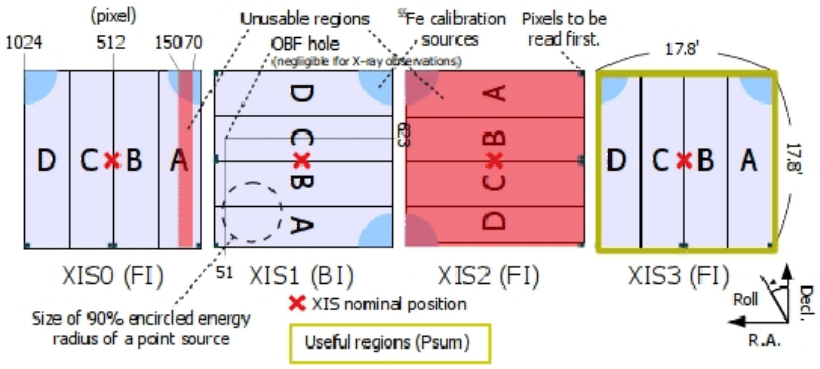

Figure 3.2: The four XIS detectors. See text for a detailed description. Credit: Arida (2012).

modes which define how many pixels are considered in the event reconstruction as illustrated in Fig. 3.3. The 3×3 and 5×5 modes are the most common ones (with basically no practical difference) and were also chosen for the Suzaku data analyzed in this work. Events which are detected during the read out (which in total takes 25 ms) are called out-of-time events and show up as stripes on the detectors. Since the frame time is about 8 seconds, roughly 0.3% of all events are out-of-time events.

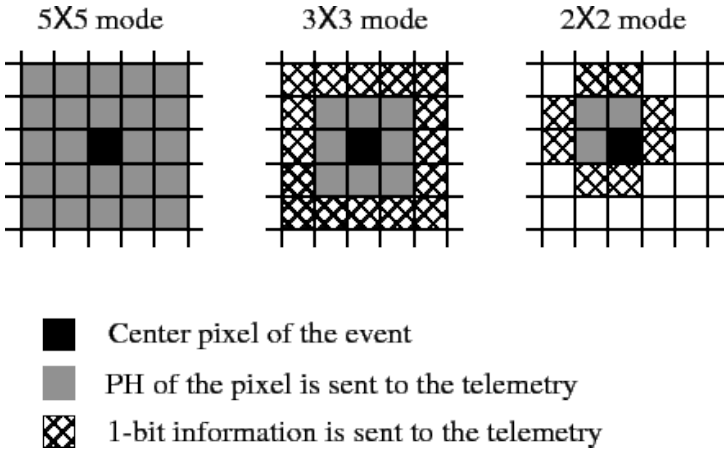

Figure 3.3: Editing modes of the Suzaku XIS-detectors. In the first (left) mode 5×5 pixels around the event center are sent to the telemetry; similar in the 3×3 and 2×2 mode whereas here additionally a 1-bit information whether the surrounding pixels (hatched pixels) are above the split-threshold, is sent. The latter defines when a charge is split into two pixels. Credit: Arida (2012).

HXD In this work data from the XIS instrument is analyzed, however, Suzaku is also equipped with a hard X-ray detector which was build to extend the energy range of Suzaku and allow for broad band studies of X-ray emitting objects. It is a non-imaging detector and is sensitive in an energy range between $10 - 600$ keV. It consists of 4×4 main detectors surrounded by 20 Bismuth Germanate crystals which are read out by photomultiplier tubes. HXD has two different types of detectors for different energy ranges. The *PIN diode* is sensitive below ~60 keV while the *Gadolinium Silicate crystals (GSO)* are sensitive above ~40 keV. The detectors are shielded by the 20 Bismuth Germanate crystals which also act as a collimator. The PIN diode

has an energy resolution of 4.5 keV (FWHM) while the scintillators lie between 35-10% in the $40 - 600$ keV range, respectively. The HXD in general has a time resolution of 61 μs.

3.1.2 The XIS instrumental background

For all X-ray observations and the analyses in this work, several background components have to be taken into account. Especially for observations of faint sources, the instrumental background can become important and even dominate the spectrum over a large range. It depends on the instrumentation as well as the materials of which the satellite is build.

The Suzaku instrumental background is mainly caused by cosmic rays hitting the detector and fluorescent lines from materials of the spacecraft itself (cf. Fig. 3.4). Also the ^{55}Fe calibration edges add to this background. Through the grading of the events by their pattern on the CCD, most of the background events are immediately filtered out aboard but a fraction still remains in the science observations. Due to the advantage of an low earth orbit, the instrumental background is very stable over the period of months. The level of the background depends on the earth's geomagnetic cut-off rigidity which is used to characterize the background. The spectrum of the background is obtained by observations of the earth at night and can be subtracted from the data for the spectral analyses. This is done by matching the geomagnetic cut-off rigidity conditions of the background observations to the conditions at the time of the scientific observation and selecting the appropriate time intervals.

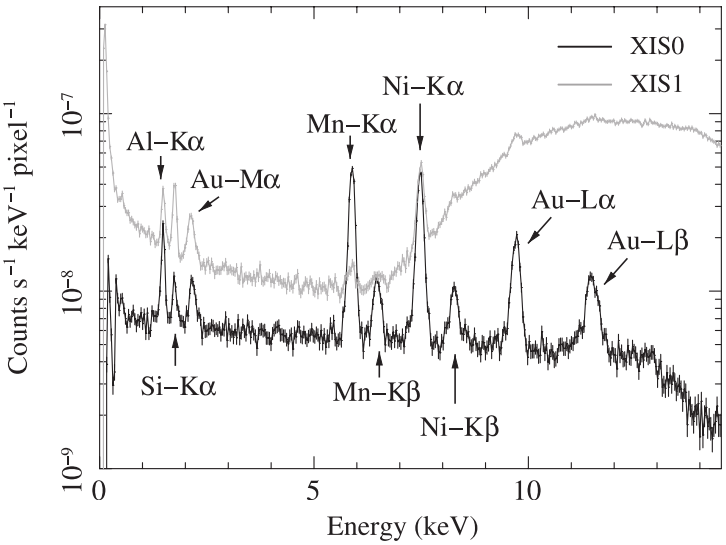

Figure 3.4: The XIS instrumental background spectrum for XIS0 (front-illuminated) and XIS1 (back-illuminated) with several fluorescent lines. The back-illuminated detector shows an overall higher background level. Credit: Tawa et al. (2008).

3.2 The XMM-Newton satellite

3.2.1 Instrumentation

XMM-Newton is a science mission carried out by the European Space Agency (ESA) and is part of the "Horizon 2000" plan which was already set up in the year 1984. The goal of this plan

was to develop new missions and also secure their future funding. The name XMM-Newton stands for *X-ray Multi-Mirror Mission* and a tribute to Sir Isaac Newton.

XMM-Newton was launched in December 1999 and was originally planned as a two year mission but was extended several times; the last extension was approved in November 2015 securing operation until 2018. It is orbiting in a highly elliptical orbit with a perigee about 5700 km and a apogee of ∼118000 km and an orbital period of about 47 h.

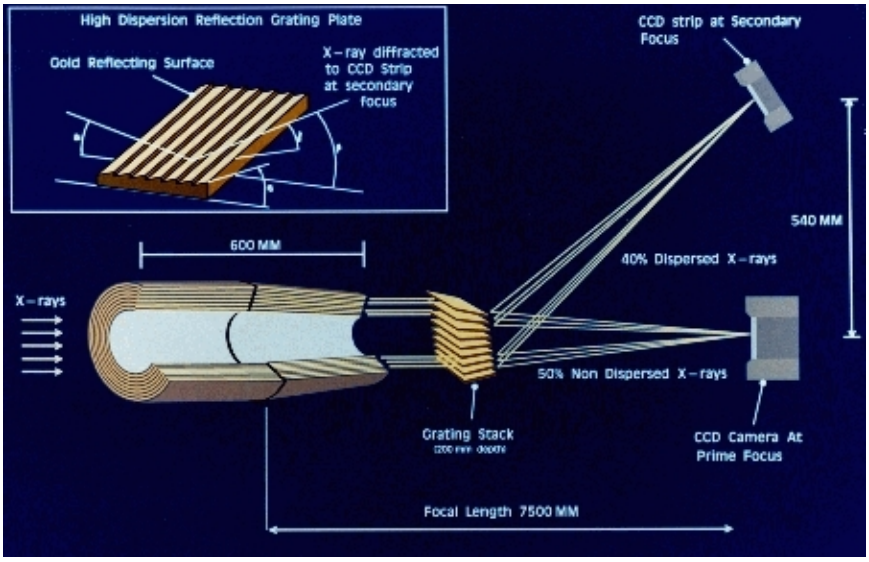

Figure 3.5: The XMM-Newton telescopes and the light path for the two telescopes carrying the RGS devices. For the one without RGS, no grating stack is placed in the light path. See text for a description. Credit: ESA (2017).

The science objectives for the XMM-Newton mission are to study the distribution and spectra of celestial X-ray sources in the energy range between $0.1 - 15$ keV of e.g. galaxies, AGNs, neutron stars and pulsars, SN remnants and plasmas. Additionally, it is able to simultaneously detect the optical/UV properties of the objects via its *optical monitor*. The following technical description of the satellite is based on the *XMM-Newton technical description* by ESA (2017).

XMM-Newton has three Wolter-I X-ray telescopes with each 7.5 m focal length and a spacial resolution of $6''$ (FWHM). Two of the telescopes also carry a *Reflection Grating Spectrometer* (RGS, description see below) which utilizes 56% of the X-ray light. A schematic view of the telescopes is shown in Fig. 3.5. The XMM-Newton field of view is about 30 arcmin^2 and it is designed to observe sources down to a limiting flux of the order of 10^{-16} erg/s/cm^2. The different instruments, in particular the *European Photon Imaging Camera* (EPIC) which is important for this work, is described below.

European Photon Imaging Camera (EPIC) Two of the three X-ray telescopes are connected to Metal Oxide Semi-conductor CCDs, called MOS1 and MOS2. The third one is linked with another type of CCD, the PN detector. Each MOS detector consists of seven chips as illustrated in Fig. 3.6 (left). The MOS2 camera is rotate by 90° compared to MOS1 and both detectors are front-illuminated. Due to the RGS, only 44% of the light is reflected onto the MOS detectors. They are most sensitive in the energy range between $0.2 - 10$ keV and have an energy resolution of $\sim 50 - 150$ eV (depending on energy). In the years 2005 and 2012, CCD6 and CCD4 of MOS1 were damaged, respectively, likely by micrometeorite events and are no longer available for

science. Due to the last event, also CCD4 suffers from a higher noise level.

PN is a back-illuminated silicon detector with 12 chips as illustrated in Fig. 3.6 (right). The detector is slightly offset from the optical axis of the telescope due to the chip boundary in the center. Compared to the MOS detectors it has a much faster read out of about 0.03 ms in the timing mode (for a descriptions of the modes see below) as every row is quipped with its own readout node.

All EPIC detectors are equipped with optical blocking filters as they are also sensitive to infrared, optical and UV photons which can contaminate the X-ray signal. Depending on the optical flux of the source, the observer can chose between a *thin*, *medium* and *thick* filter. The thicker the filter, the lower the effective area, especially at low energies. The filters are also useful for another purpose, namely to estimate the instrumental background as described in Sec. 3.2.2. The effective area of EPIC is about 4650 cm^2 and is limited at high energies by the quantum efficiency of the chips.

The event selection for the MOS detectors is performed aboard XMM-Newton. The characterization of the patterns of the events is based on the ASCA event grades[2]. For PN, the information of all activated pixels is transmitted and the event selection is performed during the data analysis.

EPIC has several operational modes which can be chosen by the observer. For this work, the *Full frame* (MOS + PN) and *Extended full frame* (only PN) mode are relevant for which the whole CCDs are read out. For a description of the other modes see ESA (2017). Out-of-time (OoT) events can occur in these modes, i.e. photons are detected during the read-out process. For the MOS detectors, the fraction of OoT events is below 0.5% but for PN can range up to roughly 6%. Thus, during the analysis, PN OoT events have to be simulated and subtracted from the data.

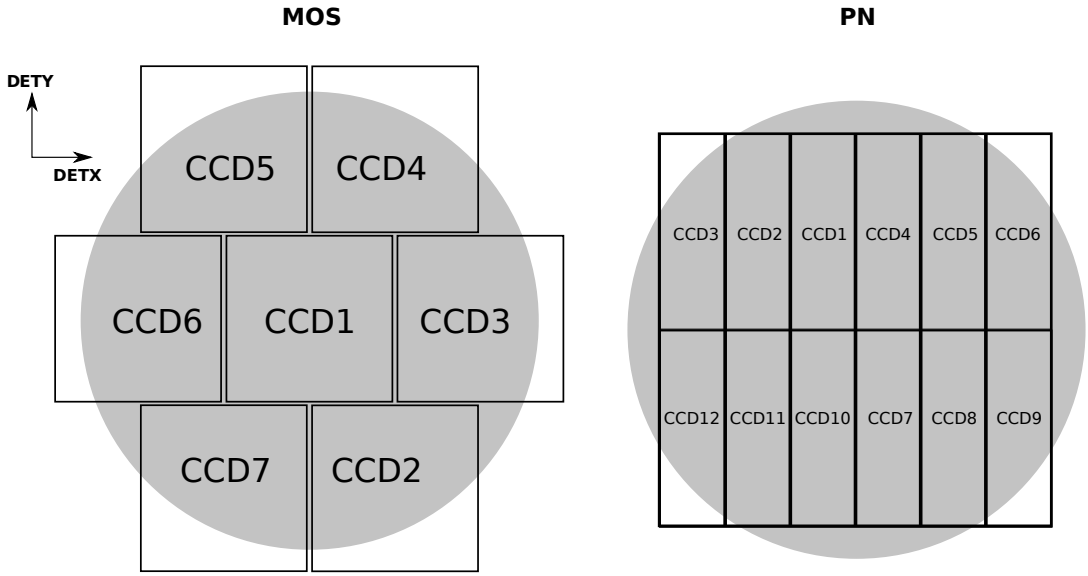

Figure 3.6: The XMM-Newton MOS (left) and PN (right) detectors. The stripes in the detectors mark the chip boundaries where no emission is detected. The gray shaded circle approximately indicates the FOV. Adapted from ESA (2017).

[2] `http://heasarc.gsfc.nasa.gov/docs/asca/abc/node5.html`

Reflection Grating Spectrometer (RGS) The RGS is designed to allow high resolution X-ray spectroscopy in the energy range $0.33 - 2.5\,\mathrm{keV}$ with $\frac{E}{\Delta E}$ between 200 and 800. This range is well suited to study X-ray emission lines and thus the chemical composition of celestial objects. Each telescope associated with a MOS detector also carries a RGS device. A *Reflection Grating Array* (RGA), directly assembled in front of the telescope as illustrated in Fig. 3.5, deflects parts of the light into a secondary focus where it is detected by a *Focal Plane Camera (RFC)*. The RFC consists of nine back-illuminated CCDs in a row which are cooled and heat-shielded in several shells with operation temperatures down to $-120°\mathrm{C}$. It also contains four calibration sources for constant monitoring of the efficiency and energy gain and an optical filter for shielding. The *Analogue Electronic (RAE)* and the *Digital Electronic (RDE)* are responsible for the read out, controlling and timing of the detector. Each RGS unit has two RDEs for a redundant read out in the case of a failure.

Optical Monitor (OM) The OM is suited to perform simultaneous observations in the optical and UV band in addition to the X-ray observations. It is located at the mirror platform of XMM and consists of an optical Ritchey-Chretien telescope with a focal length of 3.8 m with a primary mirror of 30 cm. The OM has two redundant detectors, digital electronics modules and filter wheels; the latter have 11 apertures for different wavelengths. The OM covers a spectral range between $170 - 650\,\mathrm{nm}$ and the central $17\,\mathrm{arcmin}^2$ of the X-ray FOV.

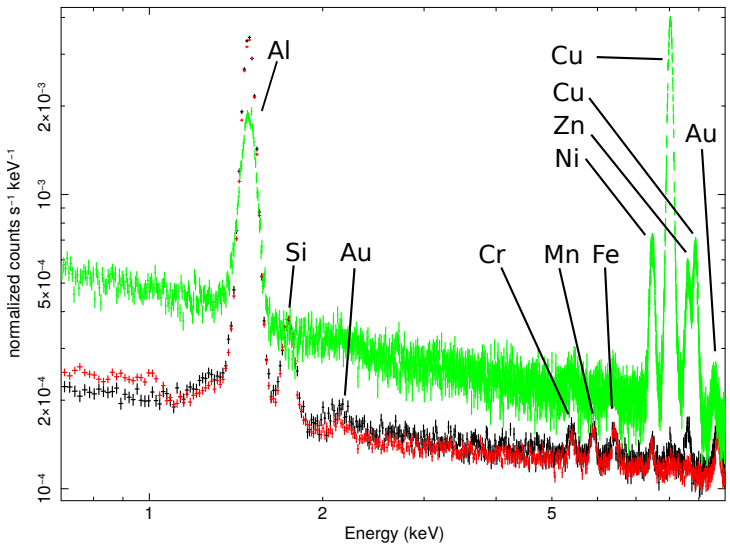

Figure 3.7: The EPIC instrumental background spectra obtained from the filter-wheel-closed observations for MOS1 (black), MOS2 (red) and PN (green) consisting of a continuum part and several fluorescent lines caused by the materials in the detector and the assembly.

3.2.2 The EPIC instrumental background

In this work, data from the EPIC instrument is analyzed. The EPIC instrumental background is composed of an internal and an external component. The external component is caused by flares consisting of soft protons with energies below $\sim$1 keV. These protons are funneled towards the detector by the mirrors. The flare-component is changing strongly and irregular with time and heavily flared time intervals have to be filtered out, reducing the effective observation time.

However, even after the filtering a residual soft proton component might be left and has to be taken into account.

The quiescent internal background, shown in Fig. 3.7, is caused by detector noise and highly energetic particles (cosmic rays) hitting the detector and the assembly, producing particle-induced X-rays. Also this component is time-varying, however, on much larger timescales and smaller intensity variations than the external component. In addition to a continuum part in the spectrum, these particles also cause several fluorescent lines.The instrumental background is monitored through filter-wheel-closed observations, i.e. when the filter blocks everything but the particle background emission. These observations can be used to either model or subtract the background from the science data.

The overall EPIC instrumental background is found to vary as a function of distance to the earth, satellite attitude, solar activity and time. This can cause an order of magnitude difference in intensity between the beginning and the end of a revolution. The intensity also depends on the chosen optical filter and is different for the MOS and PN detectors (cf. Fig. 3.7). In addition, the instrumental background shows significant differences depending on the position on the detector as depicted in Fig. 3.8. This has to be taken into account when modeling or subtracting the background for scientific purposes, especially for different regions of extended sources.

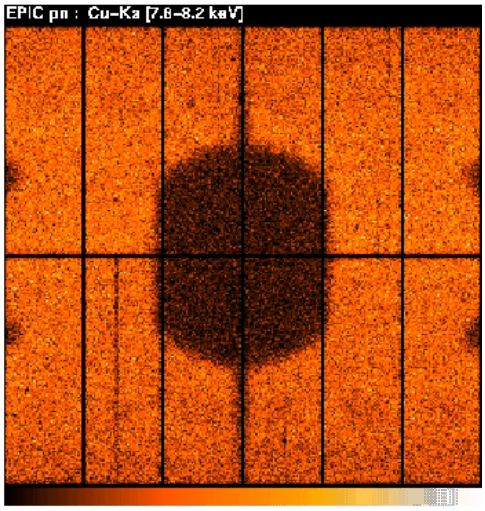

Figure 3.8: Image of the PN instrumental background in the energy range $7.8 - 8.2\,\mathrm{keV}$ (Cu and Ka lines). The prominent inhomogeneity is due to electronics installed below the PN CCDs and the variations depending on the position on the detector have to be taken into account in scientific analyses. Credit: ESA (2017).

CHAPTER 4

X-ray analysis of the galaxy group UGC 03957 beyond R_{200} with Suzaku

This project focuses on the physical properties of a galaxy group using X-ray observations performed with the Suzaku satellite and aims to investigate the gas properties up to large radii. These regions are potentially influenced by structure formation effects and analyses of galaxy group outskirts have only been performed for a few objects in such detail as presented here. Additionally, possible differences to the more widely studied galaxy clusters are examined. The content of this chapter has been published in *Astronomy & Astrophysics* in July 2016 as Thölken et al. (2016) (DOI: 10.1051/0004-6361/201527608)[1]. Dr. Lorenzo Lovisari provided the point source fluxes obtained from the analysis of the Chandra snapshot observations (Sec. 4.3.2 and Sec. 4.4.1). Parts of Sec. 4.2 and 4.6 are a summary of the discussions in previous sections, in particular Sec. 2.3.

4.1 Abstract

In the last few years, the outskirts of galaxy clusters have been studied in detail and the analyses have brought up interesting results such as indications of possible gas clumping and the breakdown of hydrostatic, thermal, and ionization equilibrium. These phenomena affect the entropy profiles of clusters, which often show deviations from the self-similar prediction around R_{200}. However, significant uncertainties remain for groups of galaxies. In particular the question, of whether entropy profiles are similar to those of galaxy clusters. We investigated the gas properties of the galaxy group UGC 03957 up to $1.4\,R_{200} \approx 1.4\,\mathrm{Mpc}$ in four azimuthal directions with the Suzaku satellite. We checked for azimuthal symmetry and obtained temperature, entropy, density, and gas mass profiles. Previous studies point to deviations from equilibrium states at the outskirts of groups and clusters and so we studied the hydrodynamical status of the gas at these large radii. We performed a spectral analysis of five Suzaku observations of UGC 03957 with ∼138 ks good exposure time in total and five Chandra snapshot observations for point source detection. We investigated systematic effects such as point spread function and uncertainties in the different background components, and performed a deprojection of the density and temperature profile. We found a temperature drop of a factor of ∼3 from the center to the outskirts that is consistent with previous results for galaxy clusters. The metal abundance profile shows a flat behavior towards large radii, which is a hint for galactic winds as the primary ICM enrichment process. The entropy profile is consistent with numerical

[1] Reproduced with permission from *Astronomy & Astrophysics*, © ESO

simulations after applying a gas mass fraction correction. Feedback processes and AGN activity might be one explanation for entropy modification, imprinting out to larger radii in galaxy groups than in galaxy clusters. Previous analyses for clusters and groups often showed an entropy flattening or even a drop around $\sim R_{200}$, which can be an indication of clumping or non-equilibrium states in the outskirts. Such entropy behavior is absent in UGC 03957. The gas mass fraction is well below the cosmic mean but rises above this value beyond R_{200}, which could be a hint for deviations from hydrostatic equilibrium at these large radii. By measuring the abundance of the α-elements Si and S at intermediate radii we determined the relative number of different supernovae types and found that the abundance pattern can be described by a relative contribution of 80% – 100% of core-collapse supernovae. This result is in agreement with previous measurements for galaxy groups.

4.2 Introduction

The outskirts of galaxy clusters, and in particular galaxy groups, still remain unexplored to a large extent. X-ray studies are the best tool for investigating temperature and metallicity of the hot gas component in these objects, which accounts for ∼90% of the total baryon content. In the recent years, several analyses investigating the outskirts have been performed (e.g., Sato et al., 2014, for a review see Reiprich et al., 2013). However, most of them deal with properties of galaxy clusters and there is a clear lack of detailed analyses at the low mass end. These analyses have brought up interesting results such as possible non-equilibrium states (e.g., Hoshino et al., 2010, Akamatsu et al., 2011, Akamatsu et al., 2012a) or gas clumping (Simionescu et al., 2011) due to the infalling material from the large-scale structure around the virial radius. For understanding these effects and their interplay in detail, galaxy groups can give important insights. In these objects the non-gravitational processes are expected to be more important owing to the shallower gravitational potential well. In a self-similar picture of the cluster formation process, galaxy groups should behave as scaled down versions of galaxy clusters regarding, e.g., temperature, density, and entropy profile. In particular the entropy profile is an important indicator of the hydrodynamical status of the gas. However, for galaxy clusters several previous studies (e.g., Ichikawa et al. (2013), Walker et al. (2012a) and Walker et al. (2012b)) have found a flattening or even a drop of the entropy profile at large radii compared to the expectation from numerical simulations of the gravitational collapse formation model performed by Voit (2005). This behavior may indicate a breakdown of thermal equilibrium between electrons and protons (e.g., Akamatsu et al., 2011) or inhomogeneous gas distributions in the outskirts; the latter possibility is also supported by simulations performed by Nagai & Lau (2011). A study of a galaxy group by Su et al. (2013) have also found an entropy drop, whereas Humphrey et al. (2012) have obtained an entropy profile for a fossil group in agreement with the simulations by Voit (2005). Other studies of entropy profiles for clusters and groups have been performed by, e.g., Chaudhuri et al. (2012) and Su et al. (2015) yielding different behaviors of the entropy profiles at large radii. Therefore, the question remains whether galaxy groups behave in a self-similar way compared to galaxy clusters regarding, e.g., the entropy profile.

Self-similarity is an important assumption when dealing with scaling relations, in particular at the low mass end of galaxy groups. As measured by, e.g., Eckmiller et al. (2011) and Lovisari et al. (2015) scaling relations often show deviations from the self-similar prediction in this regime. However, the scatter is still large and more detailed studies are required out to the virial radius to avoid biases due to the extrapolation of the measured profiles. Maughan et al. (2012)

among others have studied the L_X - T relation for 114 clusters. They combined their cluster sample with the cool core cluster sample of Pratt et al. (2009) to reach the low mass regime and temperatures <3.5 keV. In this regime they found a strong deviation from the self-similar prediction. One possibility for a deviating process in clusters and groups is AGN feedback (e.g., Bharadwaj et al., 2014). AGN heating might have a significant impact at larger radii in galaxy groups than in galaxy clusters because of their lower mass, which leads to further expansion of the heated gas. Other non-gravitational processes such as galactic winds or star formation can also play a significant role in low mass systems, while they should be less important in galaxy clusters. Eckert et al. (2013b) investigated the average entropy profile of 18 galaxy clusters confirming an entropy excess at smaller radii and a better agreement with the numerical simulations farther out. This entropy excess suggests that non-gravitational effects such as feedback from the central AGN or preheating processes are present in the intracluster medium (ICM).

Another aspect of the evolution of galaxy clusters and groups is the chemical enrichment history. Measuring the abundance and especially individual abundances of α-elements can give important insights into the chemical evolution of the ICM. This has been done previously by, e.g., Tamura et al. (2004), de Plaa et al. (2007), Sato et al. (2007b), Matsushita et al. (2007), Tokoi et al. (2008), Komiyama et al. (2009), and Simionescu et al. (2009b). The heavy elements that can be found in the ICM are thrown out by supernova explosions into the surrounding medium. This material is then distributed to the ICM, mainly by galactic winds and ram pressure stripping. As was simulated by Kapferer et al. (2007), clusters primarily enriched by ram pressure stripping show a steeper abundance profile than clusters where the enrichment is dominated by galactic winds, i.e., ram pressure stripping acts more efficiently in the dense cluster centers whereas galactic winds are present at all radii. The radial profile is not the only important aspect, however; the ratio between different elements also contains information about the past. The ratio of alpha-elements to iron abundances gives information about the amount of Supernovae Type Ia (SNIa) compared to core-collapse supernovae (SNCC) events in the past (e.g., Mernier et al., 2015, Simionescu et al., 2015, Lovisari et al., 2011). This ratio can be computed for different supernovae yield models and in principle allows to distinguish between the models (e.g., Sato et al., 2007a).

Measuring all the mentioned profiles and properties of clusters and in particular of galaxy groups is challenging as the surface brightness (SB) drops quickly towards the outskirts and therefore the treatment of the background emission is crucial. The Suzaku satellite is of special importance for these kinds of analyses because of its low and stable instrumental background due to its low Earth orbit and short focal length. Here we present an X-ray analysis of the galaxy group UGC 03957 with Suzaku reaching $1.4R_{200}$, where $R_{200} = 23.7'$ is obtained from the Suzaku data in this work (see Sec. 4.6.5). We measure temperature, metallicity, density, entropy, surface brightness, and gas mass fraction profiles up to and beyond R_{200} and the entropy profile. In addition we investigate the ratio of SNIa to SNCC from the abundance pattern of α-elements in the center and compare different SNIa yield models. Throughout the analyses we assume a flat universe with $H_0 = 70\,\mathrm{km\,s^{-1}\,Mpc^{-1}}$ and $\Omega_\Lambda = 0.73$. All errors are given at a 68% confidence level.

4.3 Observations and data reduction

4.3.1 Suzaku

The galaxy group UGC 03957 is one of the most luminous local groups with a redshift of $z = 0.034$. We analyze five Suzaku observations performed with the XIS instrument aboard of Suzaku with 138 ks total cleaned exposure time (see Tab. 4.1). One short archival observation (analyzed as part of a sample in Shang & Scharf, 2009) points towards the center of the group, while we placed four additional deeper observations in each azimuthal direction around the center (called north, east, south, and west observations in the following) as shown in Fig. 4.1. These observations are very well suited to study possible azimuthal deviations in the outskirts, each of the four reaching beyond R_{200}. The central Suzaku observation was taken in 2006, while the other four were performed in March 2012. XIS2 was damaged by a micrometeorite hit in November 2006; therefore, only XIS0, XIS1, and XIS3 data can be used for the analyses of the outer observations, while data of all four XIS chips is available for the central observation. Further details are listed in Tab. 4.1. A first estimate for the radius R_{200} where the gas density is 200 times the critical density of the universe was determined using Rosat All-Sky Survey (RASS) data (Reiprich & Böhringer, 2002). This yields a value of $R_{200} = 34.06'$, which is also the maximum radius we reach with our observations. We determine R_{200} using Suzaku data in Sec. 4.6.5.

The data reduction was performed using CALDB version 20150105 and followed the standard

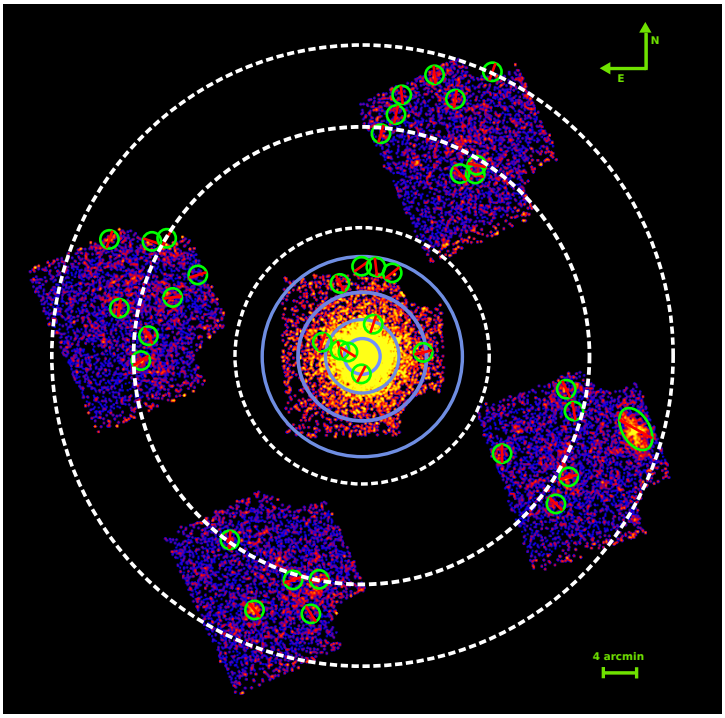

Figure 4.1: Exposure corrected mosaic image of UGC 03957. The central observation was performed in 2006; the outer observations (north, east, south and west) are from 2012. For observation details see Tab. 4.1. Light blue solid regions correspond to $0' - 2'$,$2' - 4'$,$4' - 7'$, and $7' - 11'$ (labeled from one to four outwards in the following), white dashed regions to $14' - 25'$ and $25' - 34'$ (labeled five and six in the following). All removed point sources detected with Chandra are indicated by green circles. The image is not corrected for vignetting and only used for demonstration purposes.

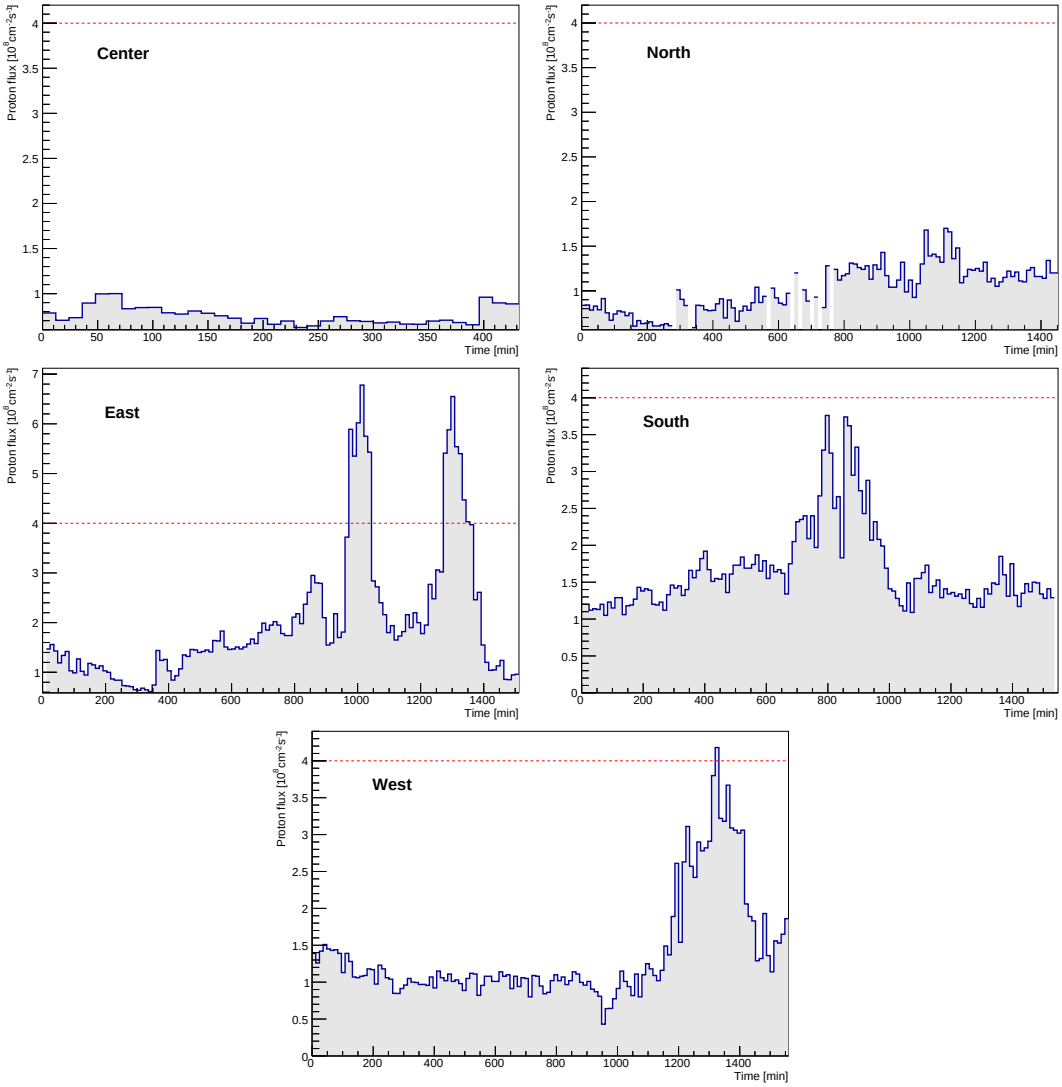

Figure 4.2: Proton flux during the five Suzaku observation time periods measured with SWEPAM/SWICS and corrected for the travel time of the solar protons to Earth. If no data is available, the bin is left empty. The red dashed line shows the limit for flaring determined by Fujimoto et al. (2007).

Table 4.1: Details of all analyzed observations of UGC 03957. The exposure time is given after data reduction.

	Date	(R.A., Dec.)	Exp. Time	Obs-ID
center	2006 Apr	(115.238, 55.407)	9.5 ks	801072010
north	2012 Mar	(114.899, 55.790)	28.2 ks	806091010
east	2012 Mar	(115.959, 55.476)	32.7 ks	806094010
south	2012 Mar	(115.511, 55.004)	34.0 ks	806092010
west	2012 Mar	(114.537, 55.221)	33.9 ks	806093010

reduction procedure as described in the Suzaku data reduction guide. This includes the tasks *xiscoord* to calculate event coordinates, *xisputpixelquality* to assign the quality code to each event (e.g., falls in bad pixel), *xispi* to calculate pulse invariant values using gain- and charge-transfer-inefficiency correction, *xistime* to assign correct arrival times, and *cleansis* to identify anomalous pixels. The requirement on the geomagnetic cutoff rigidity is COR2>6 and we removed events falling in the second trailing rows of the charge injection rows. We selected six annular regions around the center as shown in Fig. 4.1: the four inner regions ($0' - 2'$, $2' - 4'$, $4' - 7'$, and $7' - 11'$) covering the central Suzaku observation and the two outer regions ($14' - 25'$ and $25' - 34'$) covering the four observations of the outskirts. Owing to the long time period between the central and the outskirts observations of almost six years, the central observation was analyzed separately from the four outer observations.

To investigate the impact of flares during the observations that may be caused by high solar-wind-charge-exchange emission, we checked the solar proton flux using SWEPAM/SWICS Level 3 data[2]. This data includes measurements of the proton speed and proton density from both instruments, but SWEPAM data is preferentially used owing to the higher quality, and only gaps in this data set are filled with SWICS data. For slow solar winds SWEPAM may underestimate the proton flux, and SWICS data is used instead. The measured fluxes for all pointings are shown in Fig. 4.2. The travel time of the solar protons to Earth was considered. We found a very low proton flux during the time period of the central observation so that the impact of flares for this observation is negligible. During the observation time period of the outskirts, the proton flux is higher and in the case of the east, south, and west observations reaches the limit of $\sim 4 \times 10^8\,\mathrm{cm^{-2}\,s^{-1}}$ (as was determined by Fujimoto et al., 2007), which can lead to flare contamination of the lightcurves. Therefore, we applied a three-sigma clipping to the lightcurves for all outer observations and filtered the corresponding time intervals.

4.3.2 Chandra

In 2013 and 2014, we obtained four supporting Chandra snapshot observations of ∼10 ks exposure each to detect point sources in the north, east, south, and west Suzaku pointings. For point source detection in the central observation we used archival Chandra data from 2006 of ∼8 ks exposure. The Chandra data reduction was performed using the CIAO software (CIAO 4.5, CALDB 4.6.7). The data was reprocessed from the "level 1" events files using the contributed script *chandra_repro*. Periods of high background were cleaned by creating a lightcurve with the suggested values from Markevitch's Cookbook[3] and the *lc_clean* algorithm. Point sources were identified using the *wavdetect* algorithm using a range of wavelet radii between 1 and 16 pixels to ensure that all point sources were detected.

4.4 Analysis

4.4.1 Point sources

To identify point sources in the field of view (FOV) we analyzed five Chandra snapshot observations matching the five Suzaku pointings. The chosen flux limit to remove point sources should be 1.) independent of statistical fluctuations in the source counts and 2.) a compromise between the removed area and accurate treatment of the point sources. Therefore, we made a cumulative $\log N$-$\log F$ plot with N being the number of sources above or equal to a given

[2] http://www.srl.caltech.edu/ACE/ASC/
[3] http://cxc.harvard.edu/contrib/maxim/acisbg/COOKBOOK

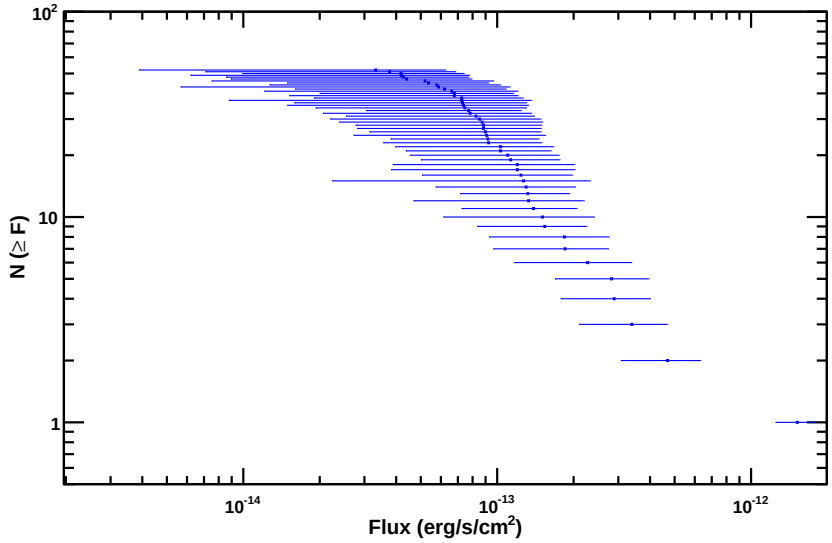

Figure 4.3: Cumulative $\log N - \log F$ plot for all five Chandra observations with N being the number of point sources brighter than or equal to flux F. All point sources brighter than $7 \times 10^{14}\,\mathrm{erg\,s^{-1}\,cm^{-2}}$ in the $0.5 - 2\,\mathrm{keV}$ band, assuming a power law with spectral index 2, were removed.

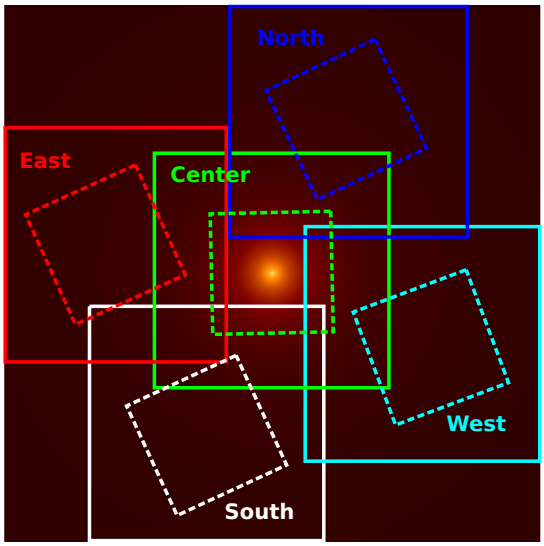

Figure 4.4: Five Suzaku pointings (dashed) shown together with the underlying double-beta-model surface brightness image obtained with Suzaku and XMM-Newton and the cut-out regions (solid squares) for ARF generation.

flux F as shown in Fig. 4.3. When the detection limit of the instrument is reached no more sources are expected to be detected, which results in a flattening of the distribution towards lower fluxes as is the case for $7 \times 10^{-14}\,\mathrm{erg\,s^{-1}\,cm^{-2}}$. All sources brighter than this limit in the $0.5 - 2\,\mathrm{keV}$ band, assuming a power-law model with spectral index 2, were removed using a circular region of radius $1'$ around the point source. In Fig. 4.1 all removed point sources are shown.

4.4.2 Response files

In a first step, the ancillary response files (ARF) were created using a double-beta model surface brightness image of the galaxy group as was determined using XMM-Newton data (Lovisari et al., 2015) and later iterated using the Suzaku results together with the XMM-Newton data. The profile obtained with XMM-Newton was extrapolated to reach the outskirts of the group. The impact of the input image for the ARF generation on the fit results was investigated and is discussed in Sec. 4.5. To ensure sufficient statistics and to save computation time, each observation has its own input image, which is simply a region cut out of the large modeled SB image. This is illustrated in Fig. 4.4 where the five cut-out regions around the central position of each pointing are shown. The regions are larger than the FOV to account for stray light reaching the detector from outside the FOV. The effect of stray light from the galaxy group center can be neglected as is described in Sec. 4.4.3.

It has to be taken into account that the normalizations and fluxes obtained in the fitting process assume emission from the whole input image (cf. Ishisaki et al., 2007). Therefore, when comparing or linking normalizations of different observations during the fitting process, these parameters have to be rescaled according to the ratio of counts in the corresponding input images used for ARF generation. Also, if it is assumed that the emission spectrum is identical over the whole sky and only the normalization decreases as a function of increasing radius, the XSPEC normalization and flux for each fitted annulus should give the same value as they are rescaled to refer to the whole input image (cf. Ishisaki et al., 2007). However, this assumption does not hold in reality. The flux is a function of temperature and metallicity and, especially for low temperatures, this aspect is not negligible and leads to different normalizations.

For the X-ray background (XRBG), uniform sky ancillary response files, each with a circle of $20'$ radius, were used. For all ARFs 10^7 photons were simulated in 157 energy steps using *xissimarfgen* and the contamination of the XIS optical blocking filter was taken into account.

4.4.3 PSF correction

Suzaku has a PSF of $2'$ half power diameter which is large enough for photons to be detected in another annulus than the one they truly originate from on the sky. This has influence on the fit results and thus a PSF correction may need to be applied during the fitting process to take the photons actually coming from another annulus into account, as well as stray light. We performed a simulation using the *xissim* simulator which is also used for the ARF generation. We generated a photon list of 10^7 monochromatic X-ray photons of 2 keV using *mkphlist* and determined the photon mixing factors. As input for the simulation we used the same input images as for the ARF generation described earlier. We also performed the simulation for five different energies, but found no significant energy dependence. For the central observation the correction factors are listed in Tab. 4.2. For the outskirts we found that introducing the PSF correction in the fit did not change the fit results significantly – as is expected owing to the large bin size – but has influence on the fit stability. Therefore, we neglected the PSF effect in the outskirts. From Tab. 4.2 it can be seen that the mixing of photons from the center to the outer annulus is minimal. Therefore we do not expect strong contamination in the outskirts from stray light and PSF effects from the bright galaxy group center.

4.4.4 Background

The non-X-ray background (NXB) was determined with *xisnxbgen* using Suzaku night Earth data within a time interval of ± 150 days around the observation date. A careful treatment of the

Table 4.2: PSF correction factors for the inner four regions of the central observation (numbered from 1 to 4 outwards) for the final ARF input image (see Sec. 4.5). The average of the simulation results for all four detectors is given. The entries should be read as "Photons coming from annulus 1 on the sky and being detected in annulus 2 on the detector" indicated as $1 \longmapsto 2$ for example.

To annulus 1		To annulus 2		To annulus 3		To annulus 4	
$1 \longmapsto 1$	0.915	$1 \longmapsto 2$	0.409	$1 \longmapsto 3$	0.110	$1 \longmapsto 4$	0.081
$2 \longmapsto 1$	0.082	$2 \longmapsto 2$	0.521	$2 \longmapsto 3$	0.225	$2 \longmapsto 4$	0.046
$3 \longmapsto 1$	0.003	$3 \longmapsto 2$	0.069	$3 \longmapsto 3$	0.618	$3 \longmapsto 4$	0.215
$4 \longmapsto 1$	0.000	$4 \longmapsto 2$	0.001	$4 \longmapsto 3$	0.047	$4 \longmapsto 4$	0.658

background is important, especially in the outskirts where the group emission is low. The local component of the X-ray background (LHB) is modeled by an unabsorbed apec (astrophysical plasma emission code[4]) model with solar metallicity; the temperature is left as a free parameter. The halo component of the background is modeled by an absorbed apec model, also with solar metallicity and a temperature of 0.28 keV (e.g., Hoshino et al., 2010, Akamatsu et al., 2011). The superposition of extragalactic sources is modeled by an absorbed power law with a spectral index of 1.41 (De Luca & Molendi, 2004). The full XRBG model is then phabs × (pow + apec) + apec. All normalizations are floating in the fit.

The estimation of the background parameters is supported by ROSAT all-sky survey data in the energy range from $0.1 - 2$ keV. Therefore, the ROSAT spectrum[5], obtained in an annulus of $0.7 - 1$ deg from the center where no group emission is expected, is fitted simultaneously with the Suzaku data, taking into account the different normalizations of the spectra. The background is assumed to be constant across the full analyzed area.

As discussed by Yoshino et al. (2009), in some cases a galactic component with higher temperature ($0.4 - 0.9$ keV) is needed to describe the X-ray background. We tested for the presence of a higher temperature gas by fitting the ROSAT data with an additional apec component. We found that this model is clearly disfavored by the data comparing the reduced χ^2 values. This is not unexpected as such a model is more often needed at low galactic latitudes, which is not the case for our object. Thus, we performed the analysis with the previously described model without an additional component.

4.4.5 Fitting Strategy

For the central observation the quality of the data allowed us to constrain some individual abundances or determine upper limits, especially in the inner annuli. Thus, for the group emission we used a phabs × vapec[6] model with the solar abundance table of Asplund et al. (2009). A vapec model allows individual abundances to be constrained, in contrast to the widely used apec model, which only allows an overall abundance for all elements to be determined. The effect of the chosen abundance table on the fit results is described in Sec. 4.4.7. The farther out the annuli lie, the fewer abundance parameters can be constrained by the fit. For this reason, a first fit is performed using an apec model instead of a vapec model in order to determine the

[4] for details about this model see `www.atomdb.org`

[5] obtained with the HEASARC X-ray background tool `heasarc.gsfc.nasa.gov/cgi-bin/Tools/xraybg/xraybg.pl`

[6] Because of the PSF correction this model has to be extended to phabs × (vapec + vapec + vapec + vapec) to account for the contaminating photons that originate from a different annulus on the sky than they are detected in.

average metallicity in each annulus. Then, in a second fit, the abundance parameters of the vapec model, which cannot be constrained by the fit, are fixed to the average value of the first apec fit. The hydrogen column density is fixed to $4.27 \times 10^{20}\,\mathrm{cm}^{-2}$ (Kalberla et al., 2005) and the spectral fitting is performed in the energy range 0.5 – 8.0 keV.

In the outskirts there is much less group emission than in the center and thus the statistics to constrain parameters is limited. For this reason, the analysis in the outskirts follows two major points: 1.) In a first step one large annulus from $14' - 34'$ covering almost the full FOV is analyzed in each of the four observations to check if the group is azimuthally symmetric, and 2.) If the group turns out to be symmetric, a simultaneous fit including all four observations is performed to reduce the statistical error and the number of annuli can be increased to two.

For the north, east, south, and west observations the group emission is modeled by an absorbed apec model. The temperature, abundance, and normalization of the apec model and also the normalizations of the three background components and the LHB temperature were left as free parameters in the fit. The background temperature for the halo was set to 0.28 keV (see Sec. 4.4.4). For the simultaneous analyses the same models and parameters were used, but increasing the number of annuli to two in the outskirts (from $14' - 25'$ and $25' - 34'$) resulting in two apec models, one for each annulus.

The fitting range was reduced compared to the central observation to 0.8 – 5.0 keV because no strong emission from the group is expected at high energies in the outskirts and the impact of the contamination of the XIS optical blocking filter is strongest in the low energy regime. Owing to imperfect calibration between front- and back-illuminated chips, the normalizations for XIS1 were allowed to vary with respect to XIS0 and XIS3 for all models by introducing a multiplicative constant to the model. The value of this constant is on the order of 75%.

4.4.6 Deprojection method

The electron density n_e as a function of radius R is related to the XSPEC normalization N_i in annulus i for an (v)apec model as

$$N_i = \frac{10^{-14}}{4\pi D_\mathrm{A}^2 (1+z)^2} \int_{V_i} n_\mathrm{e}(R) n_\mathrm{H}(R)\,\mathrm{d}V \tag{4.1}$$

with n_H being the hydrogen density and D_A the angular diameter distance. The emission weighted projected temperature T_i^p (following Ettori et al., 2002) in annulus i is given by

$$T_i^p = \frac{\int_{V_i} \epsilon(R) T(R)\,\mathrm{d}V}{\int_{V_i} \epsilon(R)\,\mathrm{d}V} \tag{4.2}$$

with emissivity ϵ and the volume along the line of sight V_i. The deprojection of density and temperature was done simultaneously by performing a χ^2 minimization. For the density profile we assumed a single-beta model,

$$n_\mathrm{e}(R) = n_0 \left(1 + \frac{R^2}{R_\mathrm{c}^2}\right)^{-\frac{3}{2}\beta}, \tag{4.3}$$

where R_c is the core radius.

The temperature is described by a simple power law,

$$T(R) = AR^b, \tag{4.4}$$

whereas the cool core (the innermost bin) was excluded as it cannot be described by this simplified model. The emissivity is given by $\epsilon = n_e n_H \Lambda$ with Λ being the cooling function which we assume to be constant along the line of sight. More complicated models, which also include the cool core, cannot be used in this case owing to the limited amount of data. However, we find that the temperature profile outside $R > 2'$ is well described by a power law (see Sec. 4.6.3) and therefore this model is suited for deprojection. In the minimization we computed the XSPEC normalization in each annulus using the single-beta model for the electron density, executing the integral in Eq. 4.1, and compared it to the measured normalization in the considered annulus. The same was done simultaneously with the temperature following Eq. 4.2. The parameters of the single-beta and the power law model were free to vary in the minimization.

We also tested a double-beta model with fixed core radii (taken from the SB fit of the Suzaku and XMM-Newton data), but we found no improvement in the minimization and the β-values of the two components were approximately the same indicating that a single-beta model is sufficient to reproduce the measured normalizations and temperatures.

The integrated volume V_i corresponding to each annulus i (i.e, the volume along the line of sight) is the cylindrical cut through a sphere with a radius of three times the maximum radius we reach with our observation ($= 102'$). Increasing this radius even further did not change the values of the obtained parameters significantly. The errors were determined using 1000 Monte Carlo (MC) realizations of the measured normalizations and temperatures assuming Gaussian errors and repeating the minimization. For the minimization and the variation in each MC step we take the correlation between all data points into account using the appropriate covariance matrix.

4.4.7 Systematics

Several sources of systematic uncertainties have been investigated: the chosen abundance table, the uncertainties on the NXB level, and the fluctuation of the CXB due to unresolved point sources. The results of all of these checks are given in Tab. 4.9.

Selecting the abundance table of Anders & Grevesse (1989) instead of Asplund et al. (2009) has a minor influence on the fit results. The values for the iron abundances in the central observation are slightly lower, as are the other abundance values. However, most of them are consistent within the 68% confidence interval. The lower iron abundances are expected due to the different solar Fe abundances in the two tables. The temperatures are consistent within the uncertainties.

The NXB background was scaled by $\pm 3\%$ (according to Tawa et al., 2008) and the fits were repeated. No strong deviations were observed in the fit results compared to the nominal values (cf. Tab. 4.9 and 4.10).

Lumb et al. (2002) among others measured a lower value for the MWH gas temperature of 0.2 keV. Therefore, we tested the influence of fixing this parameter to 0.2 keV, but found no notable impact on the fit results.

The fluctuations of the CXB due to the statistical fluctuation of the number of point sources in the FOV was measured by Hayashida et al. (1989) with the Ginga satellite. Following the procedure described in Ichikawa et al. (2013), the fluctuations were rescaled to the flux limit for point sources used in this analysis and to the analyzed FOV area. The fluctuation width is then given by

$$\frac{\sigma_{\mathrm{Suzaku}}}{I_{\mathrm{CXB}}} = \frac{\sigma_{\mathrm{Ginga}}}{I_{\mathrm{CXB}}} \left(\frac{\Omega_{\mathrm{e,Suzaku}}}{\Omega_{\mathrm{e,Ginga}}} \right)^{-0.5} \left(\frac{S_{\mathrm{c,Suzaku}}}{S_{\mathrm{c,Ginga}}} \right)^{0.25} \tag{4.5}$$

Table 4.3: Fluctuations in the CXB due to statistical fluctuation of the number of point sources in the FOV.

Annulus	1	2	3	4	5	6
CXB fluctuations (%)	21.0	11.4	6.4	5.1	2.9	2.6

with S_c being the flux limit and Ω_e the effective solid angle of the analyzed region ($\Omega_{e,Ginga} = 1.2\,deg^2$). The flux limit for Ginga is $S_{c,Ginga} = 6 \times 10^{-12}\,erg\,s^{-1}\,cm^{-2}$ in the $2 - 10\,keV$ band and has been rescaled to the energy band 0.5 – 2.0 keV (assuming a power law with spectral index 2.0). The value of $\frac{\sigma_{Ginga}}{I_{CXB}} = 5$ is adopted. The flux limit for our observations determined with Chandra (see Sec. 4.4.1) is $S_{c,Suzaku} = 7 \times 10^{-14}\,erg\,s^{-1}\,cm^{-2}$ in the 0.5 – 2.0 keV band.

The resulting values can be found in Tab. 4.3. The CXB of each region was scaled according to these values and the fits were repeated. Tables 4.9 and 4.10 show the results. No significant influence on the fit results is observed.

4.5 Results

In a first step, the impact of the input image used for the ARF generation on the fit results was investigated using an iterative approach. The Suzaku spectral data was fitted using an ARF input image which was created based on the best fit double-beta model for the SB from Lovisari et al. (2015). From the results of this spectral fit the SB was recomputed. The next iteration step is to create a new input image based on these fit results. Owing to the limited spatial resolution of Suzaku we additionally use the SB profile from Lovisari et al. (2015). From their best fit SB model to XMM-Newton we created pseudo-data that was then fitted simultaneously with the Suzaku results. We use this pseudo-data because the XMM-Newton best fit beta-model profile is corrected for PSF effects (which is not the case for the original data) that is needed in order to fit simultaneously with the PSF corrected Suzaku data. We created pseudo-data up to $\sim 10'$ where the signal-to-noise ratio for XMM-Newton approaches one. The simultaneous fit allows us to optimally constrain the surface brightness in the center with XMM-Newton and in the outskirts with Suzaku. With this new SB profile we created a new input image and recreated the ARF files. Using these ARFs we again performed the spectral fits and determined the SB profile with Suzaku. We take into account that the PSF correction changes using the new input image, thus, we repeated the PSF simulation for each new SB profile and used the updated factors in the fit. The profiles after one iteration are shown in Fig. 4.7 together with the XMM-Newton pseudo-data. The two profiles mostly overlap, especially in the central parts and are in good agreement within the uncertainties. Thus, we conclude that one iteration is sufficient to get a good representation of the actual SB profile of the group in the ARF generation. For further discussion of the SB profile see Sec. 4.6.

As described in Sec. 4.4.5, the first fit to the data of the central observation was performed using an apec model. The results for this fit are given in Tab. 4.4. The abundance values determined in this fit were then used to fix the indeterminable abundance parameters of the vapec model in the second fit. The results for the second fit are given in Tab. 4.9. We measured individual abundances for Mg, Si, S, Ar, and Ca whereas some of these can only be constrained in the inner annuli or only upper limits are given (cf. Tab. 4.9). The temperature for the local background component agrees well with Hoshino et al. (2010) and Akamatsu et al. (2011). The CXB intensity in the $2 - 10\,keV$ band is $2.30^{+0.18}_{-0.17} \times 10^{-11} erg\,s^{-1}\,cm^{-2}\,deg^{-2}$ and in good

Table 4.4: Fit results for the central observation using an apec emission model.

Annulus	T [keV]	Z [$Z_\odot$]	norm*
1	$2.64^{+0.04}_{-0.04}$	$0.94^{+0.06}_{-0.06}$	$2.31^{+0.04}_{-0.04}$
2	$3.23^{+0.15}_{-0.15}$	$0.47^{+0.14}_{-0.14}$	$2.17^{+0.04}_{-0.04}$
3	$2.45^{+0.16}_{-0.17}$	$0.35^{+0.12}_{-0.10}$	$2.02^{+0.07}_{-0.07}$
4	$2.07^{+0.26}_{-0.25}$	$0.41^{+0.22}_{-0.18}$	$1.68^{+0.14}_{-0.12}$
XRBG			
	$\text{norm}^{\dagger}_{\text{CXB}}$	$1.21^{+0.10}_{-0.10}$	
	$\text{norm}^{\circ}_{\text{MWH}}$	$0.43^{+0.15}_{-0.15}$	
	$T_{\text{LHB}}(10^{-2}\,\text{keV})$	$9.87^{+0.44}_{-0.47}$	
	$\text{norm}^{\circ}_{\text{LHB}}$	$0.98^{+0.04}_{-0.04}$	

* norm $= \frac{1}{4\pi[D_A(1+z)]^2}\int n_e n_H dV\, 10^{-16}\,\text{cm}^{-5}$ with D_A being the angular diameter distance to the source.
° Normalization of the apec component scaled to area 400π assumed in the uniform-sky ARF calculation. norm $= \frac{1}{4\pi[D_A(1+z)]^2}\int n_e n_H dV\, 10^{-20}\,\text{cm}^{-5}$.
† in units of 10^{-3} photons/s/cm^2 at 1 keV scaled to the area 400π.

Table 4.5: Fit results for the north, east, south, and west observations in the region $14' - 34'$.

	north	east	south	west
T (keV)	$1.14^{+0.12}_{-0.10}$	$1.08^{+0.11}_{-0.05}$	$1.16^{+0.12}_{-0.16}$	$1.33^{+0.20}_{-0.08}$
Z ($Z_\odot$)	$0.38^{+0.80}_{-0.61}$	$0.37^{+0.06}_{-0.52}$	$0.29^{+0.13}_{-0.44}$	$0.23^{+-0.11}_{-0.31}$
norm*	$1.45^{+1.08}_{-1.01}$	$1.91^{+0.89}_{-0.91}$	$1.90^{+1.00}_{-0.95}$	$3.60^{+0.82}_{-0.82}$
XRBG				
$\text{norm}^{\dagger}_{\text{CXB}}$	$1.26^{+0.05}_{-0.05}$	$1.25^{+0.05}_{-0.05}$	$1.28^{+0.05}_{-0.05}$	$1.14^{+0.05}_{-0.06}$
$\text{norm}^{\circ}_{\text{MWH}}$	$4.41^{+1.24}_{-1.23}$	$4.62^{+1.31}_{-1.33}$	$5.17^{+1.21}_{-1.54}$	$7.03^{+1.34}_{-1.22}$
$T_{\text{LHB}}(10^{-2}\,\text{keV})$	$9.87^{+0.44}_{-0.47}$	$9.84^{+0.45}_{-0.47}$	$9.74^{+0.45}_{-0.48}$	$9.78^{+0.45}_{-0.47}$
$\text{norm}^{\circ}_{\text{LHB}}$	$9.81^{+0.43}_{-0.43}$	$9.76^{+0.43}_{-0.43}$	$9.63^{+0.43}_{-0.43}$	$9.76^{+0.43}_{-0.43}$

* norm $= \frac{1}{4\pi[D_A(1+z)]^2}\int n_e n_H dV\, 10^{-16}\,\text{cm}^{-5}$ with D_A being the angular diameter distance to the source and rescaled to the central observation for better comparability.
° Normalization of the apec component scaled to area 400π assumed in the uniform-sky ARF calculation. norm $= \frac{1}{4\pi[D_A(1+z)]^2}\int n_e n_H dV\, 10^{-20}\,\text{cm}^{-5}$.
† in units of 10^{-3} photons/s/cm^2 at 1 keV scaled to the area 400π.

agreement with measurements by, e.g., Lumb et al. (2002) and De Luca & Molendi (2004). The spectra together with the best fit vapec models are shown in Fig. 4.5. No strong residuals can be seen and the reduced χ^2 is 1.2.

The fit results for individual fits of the north, east, south, and west observations are given in Tab. 4.5. For better comparability the normalizations have been rescaled to match the central input image which is necessary owing to the different input images during ARF generation. The values for temperatures, abundances, and normalizations are mostly consistent within

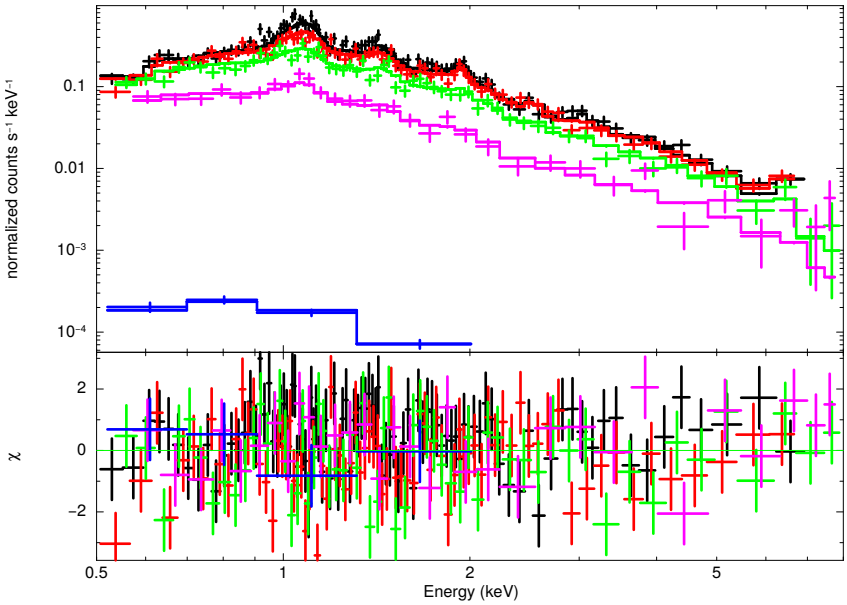

Figure 4.5: Suzaku spectra for XIS1 and best fit models (solid lines) and residuals of all four regions in the central observation. The lowermost blue data points correspond to the ROSAT spectrum of the XRBG, which also extends to lower energies (not shown).

one standard deviation. Only the western observation shows slightly higher temperature and normalization but this deviation is not significant (less than 2σ). Of course, the uncertainties are quite large due to the limited statistics in the outskirts which we improved in a simultaneous fit of all outer observations. The values for the background parameters agree within the uncertainties and gives us confidence in our treatment of the background. For these reasons we conclude that the galaxy group is sufficiently symmetric in the azimuthal directions so that a simultaneous fit of all outskirts observations is justified. The increased statistics in the fit allows for splitting the outer region from $14' - 34'$ into two annuli from $14' - 25'$ and $25' - 34'$. The results for this fit are given in Tab. 4.6. The corresponding spectra are shown in Fig. 4.6 where no strong residuals are visible.

As expected from the individual fits, the temperature in the outskirts is slightly higher than $\sim$1 keV. The abundance in both regions is consistent within the uncertainties. The background parameters are all consistent with the ones from the individual analyses and the reduced χ^2 is 1.1 which gives us confidence that azimuthal symmetry is a good assumption.

4.6 Discussion

4.6.1 Surface brightness profile

Vikhlinin et al. (1999) found that a single-beta model profile with $\beta = 0.65 - 0.85$ accurately describes the surface brightness profiles for 39 local clusters in the range $(0.3 - 1)\, R_{180}$ measured with ROSAT PSPC. However, e.g. Komossa & Böhringer (1999) and Hwang et al. (1999) measured flatter profiles for galaxy groups with $\beta \sim 0.4 - 0.5$. When we perform a single-beta model fit to the Suzaku SB data (dot-dashed line and red data points in Fig. 4.7) we obtain $\beta = 0.55 \pm 0.01$, which is in agreement with the results for galaxy groups. Khosroshahi et al. (2007) among others measured the SB profiles of a sample of fossil groups and found values of

Table 4.6: Results for the simultaneous fit to the outskirts observations.

Annulus	T [keV]	Z $[Z_\odot]$	norm*
5	$1.20^{+0.07}_{-0.10}$	$0.28^{+0.17}_{-0.11}$	$1.48^{+0.43}_{-0.39}$
6	$1.18^{+0.07}_{-0.09}$	$0.39^{+0.29}_{-0.15}$	$1.84^{+0.67}_{-0.64}$
XRBG			
	$\mathrm{norm}^{\dagger}_{\mathrm{CXB}}$	$1.24^{+0.03}_{-0.03}$	
	$\mathrm{norm}^{\circ}_{\mathrm{MWH}}$	$6.32^{+1.91}_{-0.96}$	
	$T_{\mathrm{LHB}}(10^{-2}\,\mathrm{keV})$	$9.71^{+0.93}_{-0.48}$	
	$\mathrm{norm}^{\circ}_{\mathrm{LHB}}$	$9.65^{+0.85}_{-0.43}$	

* norm $= \frac{1}{4\pi[D_A(1+z)]^2}\int n_{\mathrm{e}} n_{\mathrm{H}} \mathrm{d}V\, 10^{-16}\,\mathrm{cm}^{-5}$ with D_A being the angular diameter distance to the source and rescaled to the central observation for better comparability.
° Normalization of the apec component scaled to area 400π assumed in the uniform-sky ARF calculation.
norm $= \frac{1}{4\pi[D_A(1+z)]^2}\int n_{\mathrm{e}} n_{\mathrm{H}} \mathrm{d}V\, 10^{-20}\,\mathrm{cm}^{-5}$.
† in units of 10^{-3} photons/s/cm^2 at 1 keV scaled to the area 400π.

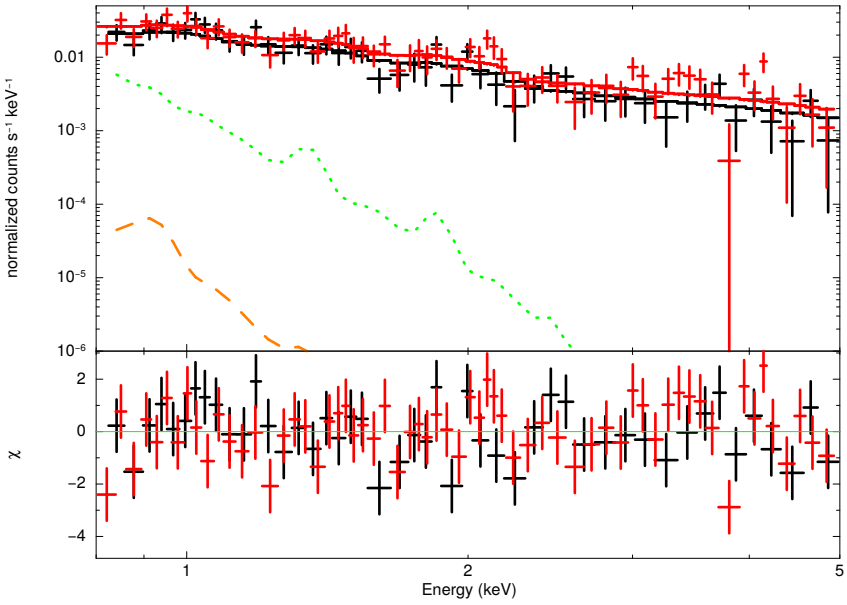

Figure 4.6: Suzaku spectra and residuals of the two outskirts regions for the north observation and XIS1. The solid lines show the best fit model, the orange dashed line shows the model component for the local background, and the green dotted line corresponds to the halo background model component.

$\beta = 0.43 - 0.60$, which is similar to our findings. These smaller β-values compared to galaxy clusters have already been seen in early ROSAT results from, e.g., David et al. (1995) and Henry et al. (1995). The former studied three groups as part of a larger cluster sample and found $\beta = 0.38 - 0.53$, whereas the clusters gave higher values between $\beta = 0.53 - 0.74$. Henry et al. (1995) found comparable results for their study of four galaxy groups. Doe et al. (1995) measured the SB profile for five poor clusters with ROSAT PSPC and also found values between $\beta = 0.47 - 0.60$. These results all clearly show that there is a deviating behavior of galaxy groups compared to galaxy clusters concerning the surface brightness. For our measurement (cf. Fig. 4.7) we note that the last data point shows a weak indication of a flattening of the profile towards larger radii. This flattening could be reflected in the density profile (cf. Sec. 4.6.2) and has been observed previously with Suzaku by, e.g., Kawaharada et al. (2010). They found a flattening in the density profile for a Suzaku observation of the cluster A1689. A flatter profile affects the hydrostatic mass estimate and can result in lower total cluster masses. We note that a flattening has also been observed by other Suzaku studies. Su et al. (2013) measured a clearly higher density in the outskirts compared to their best fit single-beta model for a fossil group. Simionescu et al. (2011) also measured a flattening of the density profile for the north-east direction of the Perseus cluster. One explanation for the flattening is gas clumping in the outskirts of clusters and groups which can lead to an overestimate in the gas density. Nagai & Lau (2011) performed hydrodynamical simulations of 16 galaxy clusters and studied the effect of gas clumping in the outer parts. Their results suggest that this effect is not negligible when dealing with cluster outskirts. Therefore, it is very important to have accurate calibration of the instruments and more studies reaching large radii to deduce whether the flattening is an instrumental effect or a real property of the gas in the outskirts of groups and clusters.

However, for our measured SB profile, the simultaneous double-beta model fit to XMM-Newton pseudo-data and Suzaku prefers a slightly flatter profile in the outskirts, indicating that XMM-Newton tends to larger SB values compared to Suzaku when going to larger radii. This is also represented by the green dashed line, which shows the extrapolated XMM-Newton profile obtained by Lovisari et al. (2015). The extrapolated profile clearly differs from the Suzaku measurement in the outer parts of the group and emphasizes the importance of having accurate measurements out to large radii to avoid biases in the calculations due to extrapolation.

4.6.2 Density profile

The deprojected density profile is shown in Fig. 4.8. The best fit parameters for the single-beta model can be found in Tab. 4.7. For the deprojection we reconstructed the XSPEC normalizations using Eq. 4.1. The statistical uncertainties are small owing to the small statistical errors of the XSPEC normalization (see Tab. 4.9) which dominate the shape of the beta model. We note that especially for a low temperature plasma the normalization and abundance parameter of the apec model are correlated. Therefore, we checked whether fixing the abundance leads to significantly different normalizations. We tested for two cases: 1.) fixing the abundance to $0.3\,Z_{\odot}$ for both regions and 2.) a more extreme case, fixing the parameters to $0.4\,Z_{\odot}$ and $0.2\,Z_{\odot}$ for regions 5 and 6, respectively. The first case yields similar results to the nominal fit for temperature and normalization. For the second case we find a $\sim$35 % higher normalization in the outermost region however, all the values are consistent within the uncertainties with the results when the abundance parameters are left as free parameters in the fit. Thus, we proceed using the results from the latter fit as in this case the statistical uncertainties on the abundance can be taken into account for the further analysis.

The measured normalizations from each annulus and the normalizations determined from

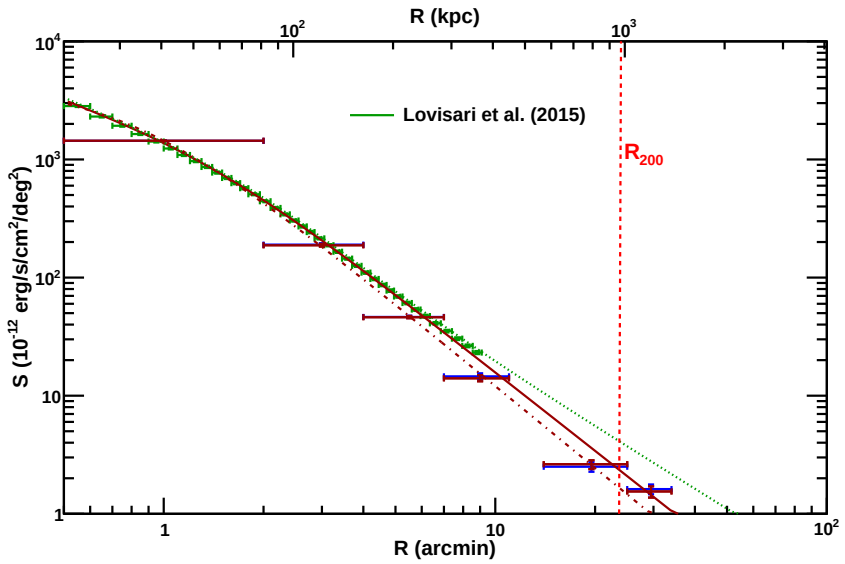

Figure 4.7: Surface brightness profile of UGC 03957 in the 0.7 – 2 keV band for different input images used for the ARF creation. Green data points correspond to XMM-Newton pseudo-data and the green dotted line shows the extrapolated SB profile from Lovisari et al. (2015). Blue data points correspond to the measured SB when an input image following the extrapolated XMM-Newton results is used. Red data points correspond to the SB using an ARF input image created from the best fit to the measured Suzaku SB from the first iteration step and the XMM-Newton pseudo-data simultaneously. The red dot-dashed line shows the best fit single-beta model to the red data points; the red solid line represents the best fit double-beta model to the red data points and XMM-Newton pseudo-data simultaneously.

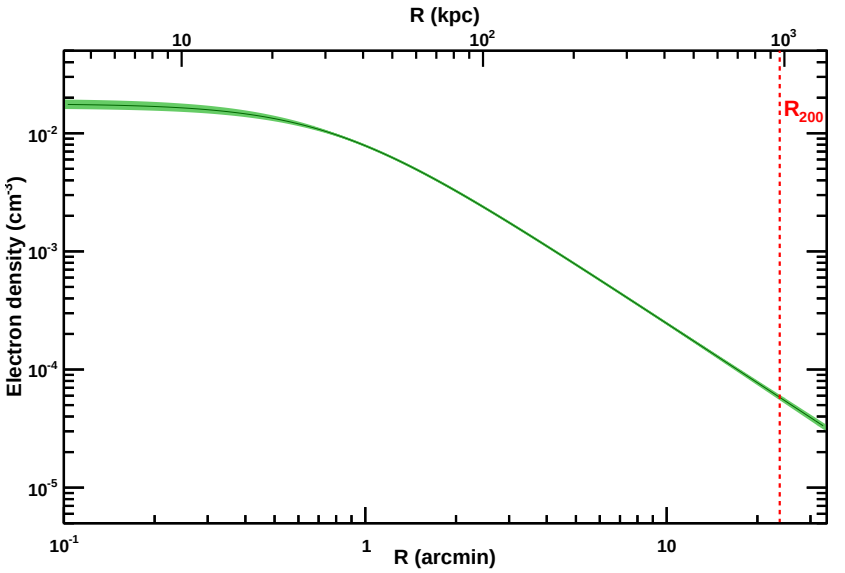

Figure 4.8: Deprojected density profile of UGC 03957. Shaded area corresponds to the formal 90% confidence region. For a description of the deprojection method see Sec. 4.4.6.

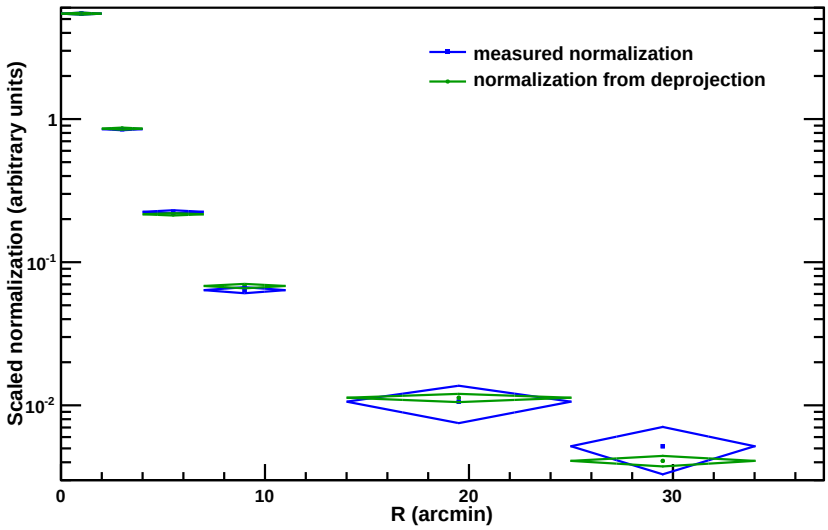

Figure 4.9: Normalizations of the vapec model scaled by the integrated volume V_i (c.f. Eq. 4.1) along the line of sight in arbitrary units. Blue diamonds correspond to the measured normalizations, while green diamonds show the normalizations obtained from the deprojected density profile.

Table 4.7: Single-beta model parameters for the deprojected density profile.

n_0 (cm^{-3})	$(1.77^{-0.09}_{+0.10}) \times 10^{-2}$
R_c (arcmin)	$0.78^{+0.04}_{-0.05}$
β	$0.56^{+0.01}_{-0.01}$

the minimization are shown in Fig. 4.9 normalized to the integrated volume V_i (cf. Eq. 4.1) in arbitrary units. The comparison shows that our measurement can be reproduced well by a single-beta model profile. The last data point is slightly lower than the measured XSPEC normalization however, the indication of a flattening is weak (see also the SB profile in Fig. 4.7). If the determined deprojected density profile in the outskirts is slightly steeper than the actual profile, the normalizations determined in the minimization will lead to a lower value than the observed one. The indication for a flattening is not significant and in our case, the overall profile is reproduced well by our method using a single-beta model. As mentioned above, a systematic flattening would have significant impact on the mass estimates. As it is difficult to get robust constraints in the outskirts and many analyses are limited to R_{500}, density profiles are often extrapolated to larger radii. If the actual density profile is flatter in the outer parts, this extrapolation results in an overestimation of the total mass or, on the other hand, if non-gravitational effects such as clumping bias gas density measurements in the outskirts towards higher values this would cause an underestimation of the cluster mass. These effects have a direct influence on the determination of cosmological parameters and could cause biases. Additionally, we need to know which other non-gravitational effects might affect the measurements. In addition to clumping, non-equilibrium states such as deviations from thermal equilibrium between protons and electrons might also be present as suggested by measurements from, e.g., Akamatsu et al. (2011). See Reiprich et al. (2013) for a review of these effects. This can be best tested using the entropy profile and the gas mass fraction, which we investigate in Sec. 4.6.5.

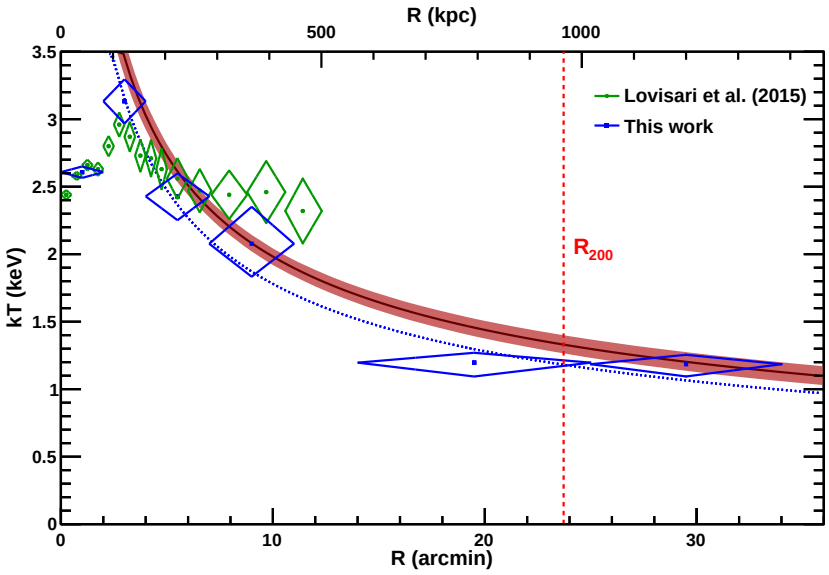

Figure 4.10: Temperature profile of UGC 03957 measured with Suzaku (blue) and XMM-Newton (green). The blue dotted line shows the best fit power law to the Suzaku data excluding the cool core. The red solid line corresponds to the deprojected temperature profile, and the shaded area shows the 68% uncertainties. Uncertainties on the measurements in the inner four annuli are larger due to the shorter exposure time (cf. Tab. 4.1).

4.6.3 Temperature profile

The temperature profiles for UGC 03957 measured with Suzaku and by Lovisari et al. (2015) with XMM-Newton are shown in Fig. 4.10. Both profiles clearly show the cool core of the group and are in very good agreement within the uncertainties. Nevertheless, we note that XMM-Newton tends to higher values around $R{\sim}10'$ which would lead to a bias if the profile is extrapolated to larger radii.

A temperature drop of a factor of $\sim$3 from the center to the outskirts of the group is consistent with previous Suzaku measurements of galaxy clusters (cf. Fig. 9 of Reiprich et al., 2013). The solid lines in Fig. 4.10 correspond to the best fit power-law model to the projected Suzaku data points (blue line) and the deprojected profile (red line). The innermost bin was excluded. As expected from the negative temperature gradient, we see that the deprojected temperature profile is slightly higher than the projected one. In the following the deprojected temperature profile is used to compute mass and entropy.

4.6.4 Abundance and supernova ratio

Figure 4.11 shows the abundance profile using the average abundances determined in the apec fit for the central observation and the abundance measured in the outer observations reaching beyond R_{200}. The abundance drops from the innermost to the second bin and then shows a rather flat behavior out to the outskirts. The profile is in good agreement with the XMM-Newton measurements where they overlap in the inner parts.

Kapferer et al. (2007) simulated two possible mechanisms for the enrichment of the ICM: ram pressure stripping and galactic winds. Ram pressure stripping is most effective at high densities, thus in the center of galaxy groups and clusters, whereas it is expected to have less influence

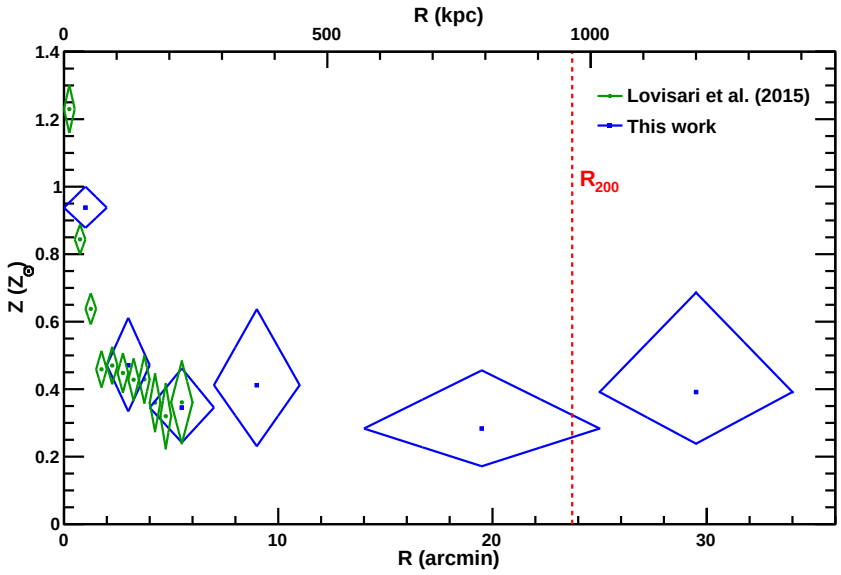

Figure 4.11: Abundance profile of UGC 03957 measured with Suzaku (for values see Tab. 4.4) in blue and XMM-Newton (Lovisari et al., 2015) in green.

at the outer parts. Galactic winds are more effective in lower density regions because of the lower pressure of the surrounding material. In their simulation Kapferer et al. (2007) showed that when ram pressure stripping is the primary process a steeper abundance profile is expected than for galactic winds. Therefore, the flat profile in our measurement is a hint that galactic winds are the dominant enrichment process outside the group center. This is consistent with the first abundance measurements out to the virial radius of two galaxy clusters (Fujita et al., 2008). From the central to the second bin a steep gradient is observed. Here the impact of the brightest central galaxy, which probably contributes significantly to the enrichment, is an important factor.

We also studied individual abundances in the inner annuli of the central observation. We note a high Ar and Ca abundance in the innermost annulus (albeit with high uncertainties), yielding Ar/Fe $= 2.6 \pm 0.7$ and Ca/Fe $= 1.3^{+0.6}_{-0.5}$, respectively. Simionescu et al. (2009b) found comparable high values for Ca/Fe in the central region of the Hydra A cluster. Also de Plaa et al. (2007) measured individual abundances for a sample of 22 galaxy clusters observed with XMM-Newton and found high Ca/Fe values of $\sim$1.5 $Z_\odot$ for several clusters. However, they found lower Ar/Fe values in the central parts, whereas a stacked analyses of all archival X-ray ASCA data performed by Baumgartner et al. (2005) yield comparable high Ar abundance for the low temperature systems. Our measured abundance values for Mg, Si, and S in the central parts are in good agreement with Suzaku measurements by, e.g., Sato et al. (2007b) and Tokoi et al. (2008), and by Komiyama et al. (2009) who also studied a galaxy group.

The ratio of SNIa and SNCC that exploded in the past can be determined using the abundances of α-elements such as Si and S compared to Fe. We measured the abundance of these elements at intermediate radii between $2' - 11'$ to minimize a possible influence of the central galaxy (indicated by the steep gradient in Fig. 4.11) yielding $Z_{\rm Fe} = 0.39^{+0.06}_{-0.06}\, Z_\odot$, $Z_{\rm Si} = 0.46^{+0.16}_{-0.15}\, Z_\odot$, and $Z_{\rm S} = 0.70^{+0.25}_{-0.24} Z_\odot$. Then we followed the procedure described by Lovisari et al. (2009) and determined the SN ratio for each of the two elements. Two models for the yields of SNIa were tested: a deflagration model (W7-model) and a delayed detonation model (WDD2), as described

Table 4.8: Ratio of the relative number of Supernovae Type II for the elements Si and S and two different SNIa yield models.

	R_{Si}	R_{S}
W7	$0.81^{+0.14}_{-0.15}$	> 0.91
WDD2	$0.80^{+0.15}_{-0.18}$	> 0.90

in Iwamoto et al. (1999). Average SNCC yields in the mass range of $10M_{\odot}$ to $50M_{\odot}$, calculated by Tsujimoto et al. (1995) assuming a Salpeter initial mass function, were used. The SN ratio is defined as $R = N_{\mathrm{SNCC}}/(N_{\mathrm{SNCC}} + N_{\mathrm{SNIa}})$, where N is the number of SN for a given type.

The results are given in Tab. 4.8. Both models yield similar results and are consistent within the uncertainties. The SN ratios for Si and S also match within the uncertainties; thus, the observed abundances for UGC 03957 can be explained by a relative contribution to the ICM enrichment of 80% – 100% for SNCC. Similar results have been reported by Sato et al. (2010) for the fossil group NGC 1550. Also Rasmussen & Ponman (2007) found that for their galaxy group sample outside the cool core SNCC dominate the enrichment over SNIa. Recent results from Simionescu et al. (2015) from Suzaku observations of the Virgo Cluster gave comparable results with a relative contribution of $79\% - 85\%$ for SNCC indicating a similar enrichment history for galaxy groups and clusters. They measured abundance ratios beyond the virial radius for the first time and ruled out an enrichment of solely SNCC at large radii at 9σ level. However, the authors note that owing to the limited accuracy of the SN yield models uncertainties in the measurements still remain.

4.6.5 Gas mass and total mass

With the deprojected gas density and the temperature profiles we computed the X-ray hydrostatic mass of the galaxy group using the hydrostatic equation

$$M_{\mathrm{tot}}(< R) = -\frac{kT_{\mathrm{gas}}R}{G\mu m_{\mathrm{p}}}\left(\frac{\mathrm{d}\ln\rho_{\mathrm{gas}}}{\mathrm{d}\ln R} + \frac{\mathrm{d}\ln T_{\mathrm{gas}}}{\mathrm{d}\ln R}\right) \tag{4.6}$$

with m_{p} being the proton mass, μ the mean molecular weight, and G the gravitational constant. We find a value of $M(< R_{200}) = (1.02^{+0.04}_{-0.04}) \times 10^{14}\,\mathrm{M}_{\odot}$. Using the density profile we obtain an estimate for R_{200} yielding $R_{200} = 23.7'$. This value is considerably lower than the first estimate from the RASS data.

We obtain the gas mass fraction profile as shown in Fig. 4.12 (the innermost part is not shown owing to our simplified temperature model that does not describe the cool core). Up to R_{500} the gas mass fraction is below 10%, which is a typical value found for galaxy groups as in, e.g., Lovisari et al. (2015), Sun et al. (2009) and Humphrey et al. (2012). Galaxy clusters typically show somewhat higher gas mass fraction above 0.1 as found by, e.g., Vikhlinin et al. (2006). In galaxy groups feedback processes have more effect than in clusters and lead to further expulsion of the gas. Beyond R_{500} the fraction of UGC 03957 rises up to $\sim$13% at R_{200} and $\sim$18% at the maximum radius we reach with our observation, which is slightly above the cosmic mean value. This behavior is in contrast to measurements by, e.g., Simionescu et al. (2011) for the Perseus cluster and Walker et al. (2012a) for the cluster PKS 0745–191. They measured gas mass fractions of $\sim$0.23 and $\sim$0.19 already around R_{200}, respectively, while UGC 03957 only rises above this value far beyond R_{200}. Eckert et al. (2013a) investigated the gas properties for a sample of 18 galaxy clusters with combined ROSAT and Planck data. They found f_{gas}

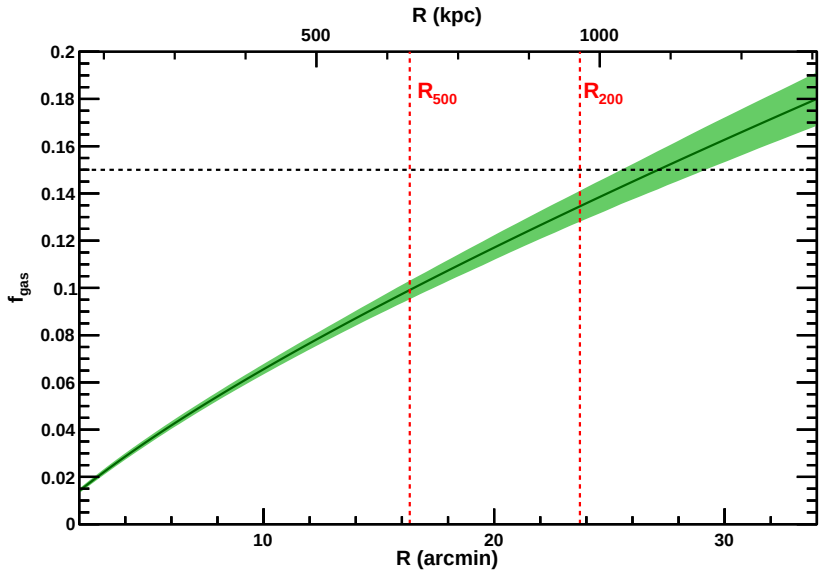

Figure 4.12: Gas mass fraction profile of UGC 03957. The horizontal dashed line shows the cosmic mean value of 0.15 (Planck Collaboration et al., 2014b). The shaded area corresponds to the 68% confidence region.

around 18% beyond R_{200} in agreement with our findings. A likely explanation for this excess is a deviation from hydrostatic equilibrium. If the assumption of hydrostatic equilibrium is violated this can result in a lower total mass estimate and therefore a higher gas mass fraction. Piffaretti & Valdarnini (2008) showed – by performing N-body/SPH simulations of about 100 galaxy clusters – that masses can be underestimated by up to 15% at R_{200}.

4.6.6 Entropy profile

A good indicator for the hydrodynamical status of the ICM is the entropy, which we obtained by combining the deprojected density and temperature profiles using the entropy definition $K = \mathrm{k}T n_\mathrm{e}^{-\frac{2}{3}}$ with Boltzmann constant k. The derived profile is shown in Fig. 4.13 in green. Voit (2005) performed non-radiative simulations from gravitational structure formation and found that their simulated cluster sample follows the relation

$$\frac{K_\mathrm{sim}}{K_{200}} = 1.32 \left(\frac{R}{R_{200}}\right)^{1.1} \tag{4.7}$$

with the normalization

$$K_{200} = 362 \frac{G M_{200} \mu m_\mathrm{p}}{2 R_{200}} \left(\frac{1}{\mathrm{keV}}\right) \times \left(\frac{H(z)}{H_0}\right)^{-\frac{4}{3}} \left(\frac{\Omega_m}{0.3}\right)^{-\frac{4}{3}} \mathrm{keV\,cm^{-2}}. \tag{4.8}$$

However, in this fit to the simulated data the slope was fixed to the common literature value of 1.1, but the authors note that outside $0.2R_{200}$ their sample seems to indicate a slightly steeper slope. For this reason they performed another fit with free slope and normalization and found

$$\frac{K_\mathrm{sim}}{K_{200}} = 1.45 \left(\frac{R}{R_{200}}\right)^{1.24}. \tag{4.9}$$

Fig. 4.13 shows both fits together with our measurement (green line and shaded area corresponding to the 68% confidence region). At $\sim R_{200}$ our measurements agree with the expectation, but at smaller radii we find a clear entropy excess compared to the numerical prediction. Pratt et al. (2010) analyzed 31 nearby clusters and found a similar behavior for their sample, i.e., many entropy profiles showing larger deviation towards the central regions. They reported that the profiles match well with the numerical simulations by Voit (2005) when a gas mass fraction correction is applied, which also reduces the scatter in the entropy profiles significantly. The correction is as follows,

$$K_{\rm corr} = K_{\rm measure} \times f_{\rm gas}(< R)^{2/3} f_{\rm b}^{-2/3}, \tag{4.10}$$

with the cosmic baryon fraction $f_b = 0.15$ (Planck Collaboration et al., 2013b). We applied the correction to our entropy profile (in red in Fig. 4.13). The resulting profile is in much better agreement with Eq. 4.7 with a fixed slope of 1.1. Compared to Eq. 4.9 (the fit to the simulated cluster sample of Voit (2005) with free slope) we even find a perfect agreement. As in their sample, our measurement for UGC 03957 suggests a slightly steeper slope than the literature value of 1.1. Pratt et al. (2010) discussed several possible explanations for entropy modification. Pre-heating processes or AGN feedback can lift the entropy in the central region as discussed by, e.g., Wang et al. (2010). Feedback from the central AGN or convection and bulk motion can push the central gas farther outwards or even eject gas from the object, especially in low mass systems with a shallower gravitational potential well, leading to higher entropy. Wang et al. (2010) measured entropy profiles for 31 galaxy groups and clusters and found a clear central entropy excess for all objects. They compared their observation with observationally constrained supernovae explosion rates and also the contribution of AGN feedback and concluded that AGNs can be responsible for the excess entropy. However, the observations were performed with the Chandra satellite and in most cases only reach R_{500}. To explain the excess in our analysis, the described effects must have an impact on the gas out to large radii, which is more probable for the low mass systems. McCarthy et al. (2010) explicitly focused on simulations of AGN feedback in galaxy groups. Their simulations reproduce the observations up to R_{500} and the central entropy excess very well.

Humphrey et al. (2012) and Su et al. (2013) studied the galaxy groups RXJ1159+5531 and ESO 3060170, respectively, and obtained similar results to our study. Both found an entropy excess out to large radii for their objects and good overall agreement with the simulations by Voit (2005) after applying the $f_{\rm gas}$ correction. Recently Su et al. (2015) extended the study of RXJ1159+5531 to full azimuthal completeness and confirmed this entropy behavior. Nevertheless, Su et al. (2013) reported an entropy drop at $\sim R_{200}$, which is consistent with observations for several galaxy clusters. Walker et al. (2013) compared the entropy profile for seven clusters obtained in previous analyses to the baseline prediction of Voit (2005) and found a significant entropy flattening (or even a drop for some clusters) at large radii. They suggest clumping as one possible explanation, but deviations from thermal equilibrium between electrons and protons can also lower the entropy. However, the results of Humphrey et al. (2012), Su et al. (2015), and also our results closely match the simulation in the outskirts. This seems to indicate a difference between galaxy groups and clusters regarding the impact of non-gravitational effects on the entropy profile in the outskirts. We note that using simple models for temperature and density profiles (i.e., power law and single-beta model, respectively) results in a power-law description of the entropy profile that in principle cannot reflect more complicated behavior. However, these models describe our data very well and an entropy flattening is absent for our object. Additionally, we tested a double-beta model for the deprojection and find a consistent

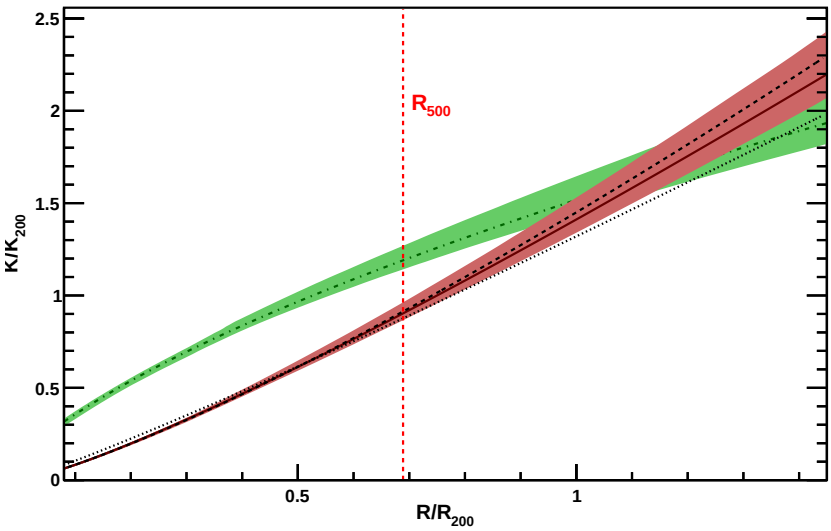

Figure 4.13: Scaled entropy profile of UGC 03957. The green dot-dashed line shows the entropy profile estimated from the deprojected temperature and density profiles. The red solid line represents the profile corrected for the gas mass fraction as suggested by Pratt et al. (2010) (Eq. 4.10). Dotted and dashed lines represent the predictions from gravitational structure formation simulations by Voit (2005) and correspond to Eq. 4.7 and Eq. 4.9, respectively.

profile compared to the single-beta case in the outskirts (cf. Sec. 4.4.6). Hence, we are confident that our models yield a reliable entropy profile.

However, even for galaxy clusters the entropy measurements are contradictory as shown by Eckert et al. (2013b) who analyzed 18 clusters and found a better agreement of the average entropy profile with numerical simulations at $R > R_{500}$ in contrast to Walker et al. (2013). One point discussed in Eckert et al. (2013b) is the missing azimuthal completeness in most Suzaku studies, which might explain the different findings. Our study and that of Su et al. (2015) have good azimuthal coverage, while Su et al. (2013) only studied one azimuthal direction. Thus, good azimuthal coverage may be important in order to obtain overall cluster and group entropy profiles. Nevertheless, to constrain a "universal entropy profile" for galaxy clusters and in particular for galaxy groups, larger samples are needed, which then also allow the impact of non-gravitational effects to be studied in greater detail.

4.7 Conclusion

We analyzed five Suzaku observations of a galaxy group, reaching $\sim 1.4 R_{200}$. We found that the group is azimuthally symmetric and performed a simultaneous fit of all outskirts observations and determined the temperature, abundance, surface brightness, density, entropy, and $f_{\rm gas}$ profiles. Our main findings are the following:

- The surface brightness profile is consistent with previous measurements of galaxy groups with a single-beta model fit to the Suzaku data yielding $\beta = 0.55 \pm 0.01$. Extrapolation of the XMM-Newton best fit double-beta model leads to large deviation from our Suzaku measurements and emphasizes the importance of accurate measurements out to large radii to avoid biases.

- The temperature profile drops by almost a factor of three from the center to the outskirts. This is consistent with previous Suzaku analyses for galaxy clusters as shown in Reiprich et al. (2013) and supports a self-similar picture.
- The abundance profile shows a flat behavior outside the center which points to galactic winds as the primary enrichment process, as found in simulations by Kapferer et al. (2007).
- The abundance pattern of the group can be explained by a relative contribution of $\sim 80\% - 100\%$ for SNCC to the ICM enrichment. This is comparable with the results from previous measurements for galaxy groups (e.g., Sato et al., 2010 and Sato et al., 2007a) and also with recent results for the Virgo cluster (Simionescu et al., 2015).
- The gas mass fraction increases with radius and is <0.1 inside R_{500} which is comparable to previous results for galaxy groups (e.g., Lovisari et al., 2015, Sun et al., 2009, Humphrey et al., 2012), but is in contrast to galaxy clusters which show higher gas mass fractions. One explanation are feedback processes that act more efficient in galaxy groups. Outside R_{200} the gas mass fraction exceeds the cosmic mean value while inside this radius it stays below $\sim 13\%$ in contrast to what was previously observed for the Perseus cluster (Simionescu et al., 2011) which showed high gas mass fractions already around R_{200}. A likely explanation is the breakdown of hydrostatic equilibrium in the outer parts of the group where the gas has not yet virialized.
- The measured entropy profile shows an excess compared to numerical simulations performed by Voit (2005). Correcting the entropy profile as suggested by Pratt et al. (2010) leads to good agreement with the simulations and indicates a slightly steeper slope than the expected value of 1.1. We conclude that feedback processes and the redistribution of material, for example due to AGN activity – especially imprinting in galaxy groups with a lower potential well –, play a major role out to larger radii than in galaxy clusters. Pre-heating processes might also be responsible for the observed excess. Our findings are in agreement with Eckert et al. (2013b) and the study of a fossil group performed by Humphrey et al. (2012), but are in contrast to results for galaxy clusters measured by Walker et al. (2013), which showed an entropy drop around R_{200} pointing to non-gravitational effects such as gas clumping or non-equilibrium states in the outskirts of the clusters. This hints at a possible difference between groups and clusters however, azimuthal completeness of the studies is an important factor and might at least partially explain the different findings.

4.8 Appendix - Fit results and systematic uncertainties

Table 4.9: Fit results and systematics for the central observation. The CXB in Cols. 3 and 4 was scaled according to Tab. 4.3. The NXB was scaled by ±3%. Upper limits are given at 90% confidence level.

Annulus	Nominal	CXB ↓	CXB ↑	NXB ↓	NXB ↑	Abundance table Anders & Grevesse (1989)
			T (keV)			
1	$2.61^{+0.04}_{-0.04}$	$2.61^{+0.04}_{-0.04}$	$2.61^{+0.04}_{-0.04}$	$2.61^{+0.04}_{-0.04}$	$2.61^{+0.04}_{-0.04}$	$2.58^{+0.04}_{-0.04}$
2	$3.13^{+0.16}_{-0.17}$	$3.15^{+0.16}_{-0.16}$	$3.11^{+0.16}_{-0.17}$	$3.14^{+0.16}_{-0.17}$	$3.13^{+0.16}_{-0.17}$	$3.03^{+0.17}_{-0.17}$
3	$2.43^{+0.17}_{-0.18}$	$2.47^{+0.15}_{-0.16}$	$2.35^{+0.16}_{-0.17}$	$2.45^{+0.17}_{-0.18}$	$2.40^{+0.17}_{-0.18}$	$2.36^{+0.17}_{-0.18}$
4	$2.08^{+0.27}_{-0.24}$	$2.12^{+0.29}_{-0.19}$	$1.95^{+0.20}_{-0.25}$	$2.11^{+0.33}_{-0.23}$	$2.04^{+0.24}_{-0.27}$	$2.05^{+0.24}_{-0.25}$
			Mg			
1	$1.02^{+0.22}_{-0.22}$	$1.02^{+0.22}_{-0.22}$	$1.02^{+0.21}_{-0.22}$	$1.02^{+0.22}_{-0.22}$	$1.02^{+0.22}_{-0.22}$	$1.07^{+0.23}_{-0.24}$
2	< 0.80	< 0.82	< 0.73	< 0.80	< 0.80	< 0.76
			Si			
1	$1.08^{+0.16}_{-0.15}$	$1.08^{+0.16}_{-0.15}$	$1.07^{+0.16}_{-0.15}$	$1.08^{+0.16}_{-0.15}$	$1.08^{+0.16}_{-0.15}$	$0.98^{+0.15}_{-0.15}$
2	$1.05^{+0.43}_{-0.42}$	$1.05^{+0.43}_{-0.43}$	$1.05^{+0.42}_{-0.42}$	$1.06^{+0.43}_{-0.42}$	$1.05^{+0.43}_{-0.42}$	$0.94^{+0.39}_{-0.39}$
3	< 0.44	< 0.46	< 0.38	< 0.44	< 0.44	< 0.36
			S			
1	$0.83^{+0.21}_{-0.21}$	$0.84^{+0.21}_{-0.21}$	$0.83^{+0.21}_{-0.21}$	$0.84^{+0.21}_{-0.21}$	$0.83^{+0.21}_{-0.21}$	$0.66^{+0.18}_{-0.18}$
2	$1.13^{+0.61}_{-0.61}$	$1.12^{+0.62}_{-0.62}$	$1.14^{+0.61}_{-0.61}$	$1.13^{+0.61}_{-0.62}$	$1.14^{+0.61}_{-0.61}$	$0.92^{+0.50}_{-0.50}$
3	$0.57^{+0.45}_{-0.45}$	$0.59^{+0.46}_{-0.46}$	$0.51^{+0.43}_{-0.43}$	$0.57^{+0.46}_{-0.46}$	$0.57^{+0.45}_{-0.45}$	$0.40^{+0.37}_{-0.37}$
			Ar			
1	$2.40^{+0.59}_{-0.59}$	$2.40^{+0.59}_{-0.59}$	$2.40^{+0.59}_{-0.59}$	$2.40^{+0.59}_{-0.59}$	$2.41^{+0.59}_{-0.59}$	$1.60^{+0.43}_{-0.43}$
			Ca			
1	$1.21^{+0.50}_{-0.49}$	$1.21^{+0.50}_{-0.49}$	$1.21^{+0.50}_{-0.49}$	$1.20^{+0.50}_{-0.49}$	$1.21^{+0.50}_{-0.49}$	$1.14^{+0.50}_{-0.50}$
			Fe			
1	$0.92^{+0.06}_{-0.06}$	$0.92^{+0.06}_{-0.06}$	$0.91^{+0.06}_{-0.06}$	$0.92^{+0.06}_{-0.06}$	$0.92^{+0.06}_{-0.06}$	$0.66^{+0.04}_{-0.04}$
2	$0.44^{+0.13}_{-0.13}$	$0.44^{+0.13}_{-0.13}$	$0.43^{+0.13}_{-0.13}$	$0.44^{+0.13}_{-0.13}$	$0.43^{+0.13}_{-0.13}$	$0.30^{+0.10}_{-0.09}$
3	$0.34^{+0.11}_{-0.10}$	$0.35^{+0.11}_{-0.10}$	$0.31^{+0.11}_{-0.09}$	$0.35^{+0.11}_{-0.10}$	$0.33^{+0.11}_{-0.10}$	$0.23^{+0.08}_{-0.07}$
4	$0.43^{+0.20}_{-0.17}$	$0.45^{+0.21}_{-0.17}$	$0.35^{+0.19}_{-0.15}$	$0.44^{+0.22}_{-0.17}$	$0.42^{+0.20}_{-0.17}$	$0.31^{+0.14}_{-0.12}$
			Norm*			
1	$2.30^{+0.04}_{-0.04}$	$2.30^{+0.04}_{-0.04}$	$2.30^{+0.04}_{-0.04}$	$2.30^{+0.04}_{-0.04}$	$2.30^{+0.04}_{-0.04}$	$2.18^{+0.03}_{-0.03}$
2	$2.14^{+0.04}_{-0.04}$	$2.15^{+0.04}_{-0.04}$	$2.14^{+0.04}_{-0.04}$	$2.14^{+0.04}_{-0.04}$	$2.14^{+0.04}_{-0.04}$	$2.06^{+0.04}_{-0.04}$
3	$2.02^{+0.05}_{-0.05}$	$2.02^{+0.05}_{-0.05}$	$2.04^{+0.05}_{-0.05}$	$2.02^{+0.05}_{-0.05}$	$2.02^{+0.05}_{-0.05}$	$1.96^{+0.05}_{-0.05}$
4	$1.67^{+0.08}_{-0.08}$	$1.69^{+0.07}_{-0.08}$	$1.70^{+0.09}_{-0.08}$	$1.68^{+0.08}_{-0.08}$	$1.67^{+0.08}_{-0.08}$	$1.61^{+0.08}_{-0.08}$
			XRBG			
$\mathrm{norm}^{\dagger}_{\mathrm{CXB}}$	$1.22^{+0.10}_{-0.10}$	fix	fix	$1.23^{+0.10}_{-0.10}$	$1.21^{+0.10}_{-0.10}$	$1.21^{+0.10}_{-0.10}$
$\mathrm{norm}^{\circ}_{\mathrm{MWH}}$	$4.30^{+2.82}_{-1.42}$	$4.89^{+2.16}_{-1.08}$	$1.88^{+2.18}_{-1.09}$	$4.23^{+2.86}_{-1.41}$	$4.37^{+2.85}_{-1.44}$	$3.46^{+1.94}_{-0.98}$
T_{LHB} (10^{-2} keV)	$9.87^{+0.91}_{-0.47}$	$9.87^{+0.91}_{-0.47}$	$9.87^{+0.91}_{-0.47}$	$9.87^{+0.91}_{-0.47}$	$9.87^{+0.91}_{-0.47}$	$10.06^{+0.90}_{-0.46}$
$\mathrm{norm}^{\circ}_{\mathrm{LHB}}$	$9.80^{+0.86}_{-0.43}$	$9.81^{+0.86}_{-0.43}$	$9.78^{+0.86}_{-0.43}$	$9.80^{+0.86}_{-0.43}$	$9.81^{+0.86}_{-0.43}$	$8.70^{+0.72}_{-0.36}$

* norm $= \frac{1}{4\pi[D_A(1+z)]^2} \int n_e n_H \mathrm{d}V \, 10^{-16} \, \mathrm{cm}^{-5}$ with D_A being the angular diameter distance to the source.

° Normalization of the apec component scaled to area 400π assumed in the uniform-sky ARF calculation. norm $= \frac{1}{4\pi[D_A(1+z)]^2} \int n_e n_H \mathrm{d}V \, 10^{-20} \, \mathrm{cm}^{-5}$.

† in units of 10^{-3} photons/s/cm^2 at 1 keV scaled to the area 400π.

Table 4.10: Fit results and systematics for the simultaneous fit of the north, east, south, and west observations. The CXB in Cols. 3 and 4 was scaled according to Tab. 3. The NXB was scaled by ±3%.

Annulus	Nominal	CXB ↓	CXB ↑	NXB ↓	NXB ↑	Abundance table Anders & Grevesse (1989)
			T (keV)			
5	$1.20^{+0.07}_{-0.10}$	$1.22^{+0.07}_{-0.09}$	$1.18^{+0.08}_{-0.11}$	$1.19^{+0.07}_{-0.10}$	$1.20^{+0.07}_{-0.10}$	$1.20^{+0.07}_{-0.10}$
6	$1.18^{+0.07}_{-0.09}$	$1.21^{+0.07}_{-0.08}$	$1.17^{+0.07}_{-0.10}$	$1.18^{+0.07}_{-0.09}$	$1.19^{+0.07}_{-0.09}$	$1.18^{+0.07}_{-0.09}$
			Z ($Z_\odot$)			
5	$0.28^{+0.17}_{-0.11}$	$0.24^{+0.11}_{-0.08}$	$0.35^{+0.24}_{-0.15}$	$0.31^{+0.20}_{-0.12}$	$0.26^{+0.15}_{-0.10}$	$0.20^{+0.11}_{-0.07}$
6	$0.39^{+0.29}_{-0.15}$	$0.31^{+0.15}_{-0.10}$	$0.54^{+0.47}_{-0.23}$	$0.45^{+0.40}_{-0.18}$	$0.35^{+0.23}_{-0.13}$	$0.25^{+0.15}_{-0.09}$
			Norm*			
5	$1.48^{+0.43}_{-0.39}$	$1.74^{+0.38}_{-0.33}$	$1.20^{+0.42}_{-0.34}$	$1.37^{+0.43}_{-0.39}$	$1.59^{+0.44}_{-0.39}$	$1.58^{+0.41}_{-0.37}$
6	$1.84^{+0.67}_{-0.64}$	$2.30^{+0.55}_{-0.49}$	$1.35^{+0.58}_{-0.51}$	$1.61^{+0.67}_{-0.64}$	$2.06^{+0.67}_{-0.64}$	$2.12^{+0.64}_{-0.61}$
			XRBG			
$\mathrm{norm}^{\dagger}_{\mathrm{CXB}}$	$1.24^{+0.03}_{-0.03}$	fix	fix	$1.27^{+0.03}_{-0.03}$	$1.22^{+0.03}_{-0.03}$	$1.24^{+0.03}_{-0.03}$
$\mathrm{norm}^{\circ}_{\mathrm{MWH}}$	$6.32^{+1.91}_{-0.96}$	$6.52^{+1.88}_{-0.94}$	$6.14^{+1.90}_{-0.95}$	$6.12^{+1.90}_{-0.95}$	$6.51^{+1.92}_{-0.96}$	$4.56^{+1.34}_{-0.67}$
T_{LHB} (10^{-2} keV)	$9.71^{+0.93}_{-0.48}$	$9.73^{+0.93}_{-0.47}$	$9.70^{+0.93}_{-0.48}$	$9.71^{+0.93}_{-0.48}$	$9.72^{+0.93}_{-0.48}$	$9.91^{+0.92}_{-0.47}$
$\mathrm{norm}^{\circ}_{\mathrm{LHB}}$	$9.65^{+0.85}_{-0.43}$	$9.67^{+0.85}_{-0.43}$	$9.63^{+0.85}_{-0.43}$	$9.64^{+0.85}_{-0.43}$	$9.66^{+0.85}_{-0.43}$	$8.60^{+0.71}_{-0.36}$

* norm $= \frac{1}{4\pi[D_A(1+z)]^2} \int n_e n_H \mathrm{d}V \, 10^{-16} \, \mathrm{cm}^{-5}$ with D_A being the angular diameter distance to the source and rescaled to the central observation for better comparability.

° Normalization of the apec component scaled to area 400π assumed in the uniform-sky ARF calculation. norm $= \frac{1}{4\pi[D_A(1+z)]^2} \int n_e n_H \mathrm{d}V \, 10^{-20} \, \mathrm{cm}^{-5}$.

† in units of 10^{-3} photons/s/cm^2 at 1 keV scaled to the area 400π.

4.9 Acknowledgements

We would like to thank Gerrit Schellenberger, Brenda Selene Miranda Ocejo, Bharadwaj Vijaysarathy, Hiroki Akamatsu, Sandra Martin, and Dominik Klaes for fruitful discussions and helpful support. We also thank the anonymous referee for the helpful comments. S.T. acknowledges support from the DFG through grant RE 1462/6 and Transregional Collaborative Research Centre TRR33 "The Dark Universe" and the Bonn-Cologne Graduate School of Physics and Astronomy. L.L. acknowledges support by the DFG through grant LO 2009/1-1 and TRR33. T.H.R. acknowledges support from the DFG through Heisenberg grant RE 1462/5 and grant RE 1462/6, and from TRR 33.

CHAPTER 5

XMM-Newton X-ray and HST weak gravitational lensing study of the extremely X-ray luminous galaxy cluster Cl $J120958.9+495352$ ($z = 0.902$)

In the last chapter, the properties of a local low mass object were studied, while the project presented in this chapter is about the "counterpart" – a very distant, massive cluster with an extremely high luminosity, studied with the XMM-Newton satellite and the Hubble Space Telescope (the data from the latter were analyzed by Dr. Tim Schrabback). XMM-Newton is well suited for this kind of study due to its large effective area and relatively high spatial resolution, that is needed because the extent of this distant object on the sky is small. The cluster analyzed here is particularly interesting with respect to structure formation as such objects are expected to be very rare in a bottom-up scenario. Additionally, they provide important tests of the cosmological model. To perform these tests, the dynamical status needs to be clarified as only relaxed clusters are suited for this purpose. Thus, the aim of this project is the investigation of the ICM properties concerning the presence of a cool core, the cooling time and the gas mass fraction as a cosmological probe.

The content of this chapter was submitted to *Astronomy & Astrophysics* in April 2017[1]. Tim Schrabback performed the analysis of the HST data and provided the corresponding results and content for the publication, precisely Sec. 5.3.2 and 5.4.1. The total mass estimated from his analysis was used to determine the gas mass fraction of Cl $J120958.9+495352$. Parts of Sec. 5.2 and 5.5 are a summary from previous sections, in particular Sec. 2.3 and 2.4.

5.1 Abstract

Observations of relaxed, massive and distant clusters can provide important tests of standard cosmological models e.g. using the gas mass fraction. To perform this test, the dynamical state of the cluster has to be investigated as well as its gas properties. X-ray analyses provide one of the best opportunities to access this information and determine important properties as e.g. temperature profiles, gas mass and the total X-ray hydrostatic mass. For the latter, weak gravitational lensing analyses are complementary, independent probes that are essential to test

[1] The revised final version has been accepted by *Astronomy & Astrophysics* as *Thölken et al. 2018, A&A, DOI: 10.1051/0004-6361/201730913* (in press),

if X-ray masses could be biased. We study the very luminous, high redshift ($z = 0.902$) galaxy cluster Cl $J120958.9+495352$ using XMM-Newton data and measure the temperature profile and cooling time to investigate the dynamical status with respect to the presence of a cool core as well as global cluster properties. We use HST weak lensing data to estimate its total mass and determine the gas mass fraction. We perform a spectral analysis using an XMM-Newton observation of 15 ks cleaned exposure time. As the treatment of the background is crucial, we use two different approaches to account for the background emission to verify our results. We account for point-spread-function effects and deproject our results to estimate the gas mass fraction of the cluster. We measure weak lensing galaxy shapes from mosaic HST/ACS imaging and select background galaxies photometrically in combination with WHT/ACAM imaging. The X-ray luminosity of Cl $J120958.9+495352$ in the $0.1 - 2.4$ keV band estimated from our XMM-Newton data is $L_X = (18.7^{+1.3}_{-1.2}) \times 10^{44}$ erg/s and thus, according to the updated Planck catalog of Sunyaev-Zeldovich sources, it is one of the most X-ray luminous clusters known at similarly high redshift. We find clear indications for the presence of a cool core from the temperature profile and the central cooling time, which is very rare at such high redshifts. Based on the weak lensing analysis we estimate a cluster mass of $M_{500}/10^{14} M_{\odot} = 4.4^{+2.2}_{-2.0}(\text{stat.}) \pm 0.6(\text{sys.})$ and a gas mass fraction of $f_{\text{gas},2500} = 0.11^{+0.06}_{-0.03}$ in good agreement with previous findings for high redshift and local clusters.

5.2 Introduction

In the paradigm of hierarchical structure formation very massive and distant clusters should be extremely rare. These clusters provide the opportunity for many interesting astrophysical and cosmological studies. The gas mass fraction (f_{gas}) of dynamically relaxed clusters is an important probe of cosmological models (Allen et al., 2008, Mantz et al., 2014) as the matter content of these objects should approximately match the matter content of the universe (e.g. White et al., 1993, Allen et al., 2011, and references therein). In particular clusters at high redshifts are of interest where the leverage on the cosmology is largest.

The cooling time for these clusters is very short and the presence of a cool core is believed to be strongly related to the dynamical status of the cluster (e.g. Hudson et al., 2010). McDonald et al. (2017) studied the evolution of the ICM and cool core clusters over the past 10 Gyr. Their results imply that from redshift $z = 0$ to $z = 1.2$ cool-cores basically do not evolve in size, density and mass. Additionally, the level of agreement of the properties of these rare clusters with existing scaling relations (e.g. Reichert et al., 2011, Pratt et al., 2009) has great significance for cosmology as they can provide tests of these scaling laws and assess whether they are in line with standard cosmological predictions.

So far, only a few of these rare, relaxed, massive and high-redshift objects have been found, examples are Cl$J0046.3+8530$ (Maughan et al., 2004b) and Cl$J1226.9+3332$ (Maughan et al., 2004a). Also in the Massive Cluster Survey (MACS) (Ebeling et al., 2007, Ebeling et al., 2010) many interesting objects have been identified, e.g. extreme cooling in cluster cores as MACSJ0947.2+7623, and a number of dynamically relaxed clusters that can be used for cosmological tests. However, almost all of those relaxed clusters are at smaller redshift than the object studied here. Two of the most distant clusters at $z > 1$, Cl$J1415.1+3612$ and 3C 186, were studied in detail by Babyk (2014) and Siemiginowska et al. (2010) using deep Chandra observations. The observations revealed a cool core for both objects with a short cooling time for Cl$J1415.1+3612$ within the core region of < 0.2 Gyr and a gas-mass fraction consistent with local clusters for 3C 186. With respect to the luminosity, another extreme example is the

El-Gordo galaxy cluster at $z = 0.87$ with $L_X = (2.19 \pm 0.11) \times 10^{45}\, h_{70}^{-2}\,\mathrm{erg/s}$ (Menanteau et al., 2012) which is one of the most massive and luminous clusters found so far.

For cosmological tests, the total cluster mass is an important quantity for which weak gravitational lensing provides an independent probe beside the X-ray hydrostatic mass. The gravitational potential imprints coherent distortions onto the observed shapes of background galaxies (e.g. Bartelmann & Schneider, 2001, Schneider, 2006). Measurements of these weak lensing distortions directly constrain the projected mass distributions and cluster masses (Hoekstra et al., 2013). These measurements are sensitive to the total matter distribution, including both dark matter and baryons. Especially at high redshifts, the Hubble Space Telescope (HST) is an essential tools for the analysis of such objects as ground-based telescopes are not able to resolve the shapes of the very distant background galaxies.

Recently, Buddendiek et al. (2015) performed a combined search of distant massive clusters using ROSAT All-Sky-Survey and Sloan Digital Sky Survey data covering an area of 10,000 deg^2. They found 83 high-grade candidates for X-ray luminous clusters between $0.6 < z < 1$ and obtained WHT or LBT imaging to confirm the candidates. One of the clusters they found is special in many respects: Cl $J120958.9{+}495352$ is the most X-ray luminous cluster in their sample. Also, it has the second highest spectroscopically confirmed redshift in their sample and their richness and Sunyaev-Zel'dovich (SZ) measurements independently indicate a high cluster mass. According to the Planck catalog of SZ sources (Planck Collaboration et al., 2015) Cl $J120958.9{+}495352$ is on par with the five most luminous cluster found at $z{\sim}0.9$. It is thus a valuable candidate for a distant cooling-core cluster and provides a great opportunity to study one of these rare systems in detail.

In this work we perform a spectroscopic XMM-Newton and HST weak lensing study of this extraordinary object found by Buddendiek et al. (2015). We investigate the temperature profile with respect to the presence of a cool core and determine the cooling time within $< 100\,\mathrm{kpc}$. In Sec. 5.3 we describe the properties of Cl $J120958.9{+}495352$, the data reduction procedure and the analysis strategy for HST and XMM-Newton as well as the XMM-Newton background. Sec. 5.4 gives the results which are discussed in Sec. 5.5.

Throughout the analysis we use a flat ΛCDM cosmology with $H_0 = 70\,\mathrm{km/s/Mpc}$, $\Omega_m = 0.3$ and $\Omega_\Lambda = 0.7$. All uncertainties are given at the 68% confidence level and overdensities refer to the critical density. All magnitudes are in the AB system.

5.3 Observations and data analysis

5.3.1 XMM-Newton analysis

5.3.1.1 Data reduction

Cl $J120958.9{+}495352$ is the most luminous cluster in the sample of Buddendiek et al. (2015). Already from the ROSAT data, this cluster appears to be one of the most luminous ones known at high redshifts with $L_{0.1-2.4\,\mathrm{keV}} = 20.3 \pm 6.2 \times 10^{44}\,\mathrm{erg/s}$. They measure the spectroscopic redshift to be $z = 0.902$ and their SZ data yields a mass of $M_{500} = (5.3 \pm 1.5) \times 10^{14}\, h_{70}^{-1}\mathrm{M}_\odot$.

We analyze XMM-Newton observations of the cluster with ∼15 ks cleaned exposure time (XMM-Newton observation IDs 0722530101 and 0722530201, PI of the joint XMM-Newton and HST program: T. Schrabback). The observations were performed in Oct. and Nov. 2013, details can be found in Tab. 5.1, and were executed over the course of two revolutions, which we analyze simultaneously.

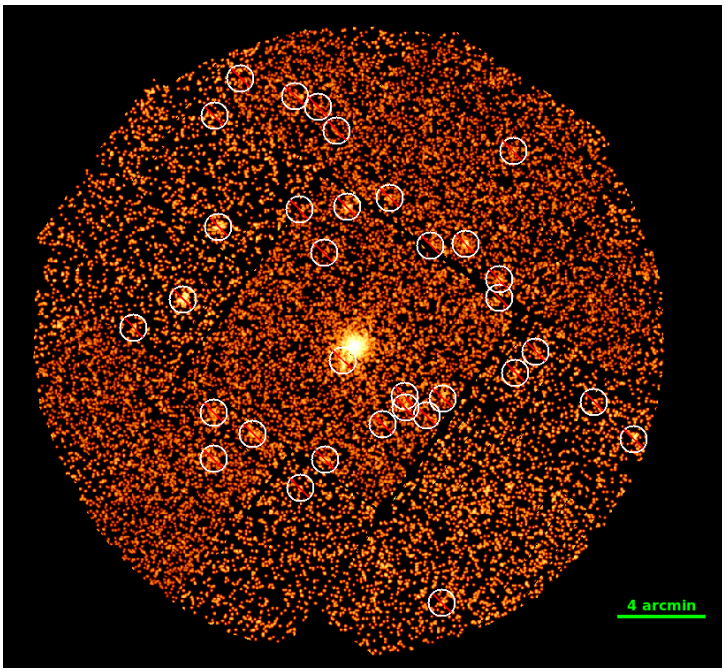

Figure 5.1: Combined, cleaned, exposure corrected and smoothed MOS image of Cl J120958.9+495352. White circles show the excluded point sources.

Following the standard data reduction procedure[2] using SAS version 14.0.0, we use the ODF data and apply *cifbuild* to catch up with the latest calibration and *odfingest* to update the ODF summary file with the necessary instrumental housekeeping information. Then we proceed by applying *emchain* and *epchain* (for MOS and PN detector, respectively) to create calibrated event files.

On these calibrated files we apply the following filters for the event pattern of the triggered CCD pixels (the numbering is based to the ASCA GRADE selection) and the quality flag of the pixels: PATTERN ≤ 12 for the MOS detectors, for PN PATTERN $= 0$; FLAG $= 0$ for both detectors. Because of anomalous features on CCD4 of MOS1, we additionally filter out events falling onto this chip. CCD3 and CCD6 of MOS1 have been damaged by micro meteorite events and the data of these detectors cannot be used.

In a next step we create light curves for both revolutions and all detectors in the energy range $0.3 - 10$ keV. The observation in the second revolution shows strong flaring for a large fraction of the exposure time. We apply a three-sigma-clipping to all the light curves to filter the flared time intervals and inspected the light curves afterwards which then show no further hint of flaring. This removes approximately half of the exposure time for the second observation (revolution 2546).

For detecting point sources in the field of view (FOV) we create images from the event files for all detectors in five energy bands between $0.2 - 12$ keV. These images are provided to the task *edetect_chain*.

[2] see `heasarc.gsfc.nasa.gov/docs/xmm/abc/`

Table 5.1: Details of the XMM-Newton observation of Cl $J120958.9+495352$.

Rev.	date	R.A.	Dec.	Cleaned exp. time	Filter
2545	Okt. 2013	182.512	49.926	9.6 ks	thick
2546	Nov. 2013	182.510	49.924	5.1 ks	thick

5.3.1.2 Spectral fitting

An X-ray image of the cluster is shown in Fig. 5.1. We select three annular regions around the center and choose the region sizes such, that we can achieve a S/Bkg ratio (i.e. $\text{counts}_{source}/\text{counts}_{bkg}$) of $\sim$1 in the outermost annulus and larger for the inner regions to avoid systematic biases. The final regions are $0' - 0\farcm3, 0\farcm3 - 0\farcm8$, and $0\farcm8 - 1\farcm3$. We fit the spectra of all annuli and for all detectors and the two observations simultaneously using the Cash-Statistic (cstat option in XSPEC). For the cluster emission we use an absorbed APEC model with a column density from Willingale et al. (2013), which also includes molecular hydrogen and the solar metal abundance table from Asplund et al. (2009). We assume the same abundance in all annuli and thus link the corresponding model parameters. The XMM-Newton point-spread-function (PSF) is $\sim 17''$ HEW. We correct for the effect of photon-mixing between different annuli because of the PSF as described in Sec. 5.3.1.5.

From our HST data (cf. Sec. 5.4.1) we estimate $R_{500} = 1\farcm8$ and therefore, for the estimation of the global cluster properties, extract spectra in this region. For the analysis of such a high redshift cluster, the background treatment is crucial. The different background components are described in Sec. 5.3.1.3 and 5.3.1.4 and we follow two approaches for the treatment of the background:

1. **Background modeling** One approach is to model all the different background components individually in the fitting procedure. These components are described in the following sections. We determine models for the quiescent particle background and the X-ray background and use them in the fitting of the cluster emission. We additionally introduce a power-law model to account for the residual soft proton emission, which is left over emission after the flare filtering. The index is linked for the two MOS detectors while the normalizations for each detector are a independent. We use an energy range between $0.7 - 10$ keV. The results of this approach can be found in Sec. 5.4.2.

2. **Background subtraction** The cluster has a small extent on the sky, thus we do not expect significant cluster emission beyond $R_{200} = 2.7'$ estimated from our HST data. For this reason we are able to subtract the full background from the spectra. To do so, we extract background spectra in an annulus between $3' - 5'$. This region lies completely on the MOS CCD1 chips which is important because the particle background shows strong variations between the different chips. Also for PN this region is close enough to the source extraction region to properly model the Ni and Cu lines. As for the first method, the energy range is $0.7 - 10$ keV and the results of this procedure are described in Sec. 5.4.2.

5.3.1.3 Quiescent particle background

The quiescent particle background (QPB) is caused by highly energetic particles interacting with the detector and the surrounding material. It is composed of a continuum emission and

fluorescent lines from various elements contained in the assembly of the satellite. XMM-Newton is equipped with a filter wheel system which can be used to measure the level of the QPB. When the filter is closed, only the high energy particles can penetrate the filter and a spectrum of the QPB can be obtained. We use merged event files of the filter-wheel-closed observations which are close to the time of the observation (revolution 2514-2597 for the MOS detectors and 2467-2597 for PN). The continuum part of the spectrum can be described by two power laws while the fluorescent lines are modeled by Gaussians. The QPB varies for all detectors and with the position on the detector. Therefore, we fit the model in two regions – from $0' - 5'$ (the source region, which lies completely on CCD1 for the MOS destectors) and from $7' - 12'$ (the region where we determine the X-ray background, see Sec. 5.3.1.4) – for all detectors independently. For the QPB, diagonal responses are used in the fit and no ancillary response file (ARF) is applied as these particles do not suffer from instrumental effects such as vignetting. The spectra with the best fit models are shown in Fig. 5.2. When fitting the cluster emission, the QPB normalizations of the power-law components and the Gaussian lines are allowed to vary separately by $\pm 20\,\%$ due to possible spatial and temporal variations of the QPB.

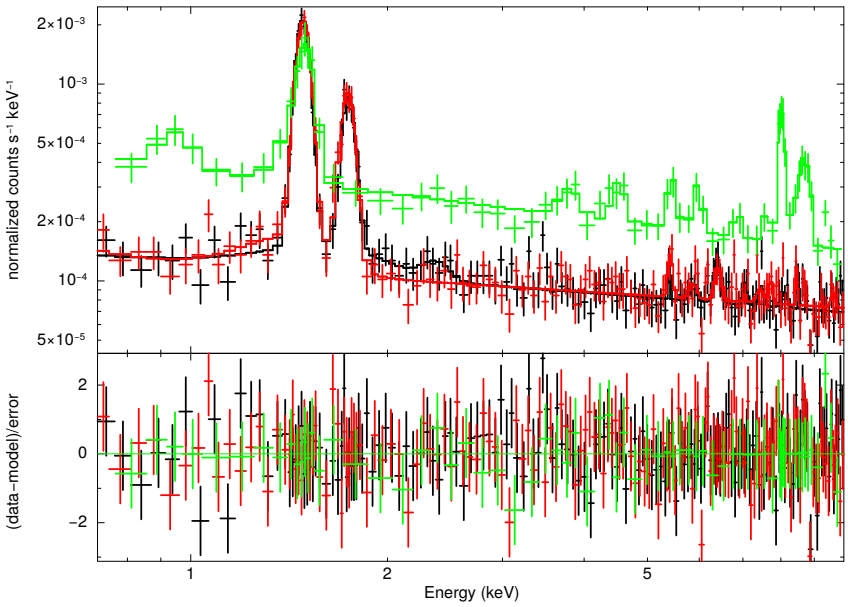

Figure 5.2: Spectra and best fit models of the QPB obtained from the filter-wheel-closed observations and extracted on the central chip in the region $0' - 5'$ for MOS1 (black), MOS2 (red) and PN (green) and normalized to the extraction area.

5.3.1.4 X-ray background

The X-ray background (XRBG) emission is caused by different sources: 1. a local component and solar wind charge exchange (called LHB in the following), 2. a component from the Milky Way halo plasma, and 3. the superposition of the X-ray emission from distant AGNs causing a diffuse background (CXB). To model these background components we extract a spectrum in a region from $7' - 12'$, where no cluster emission is expected. Additionally, ROSAT All-Sky-Survey data[3] are used to support the estimation of the background parameters at energies between $0.1 - 2.0\,\mathrm{keV}$. The first XRBG component can be modeled using an APEC model with

[3] obtained with the HEASARC X-ray background tool `heasarc.gsfc.nasa.gov/cgi-bin/Tools/xraybg/xraybg.pl`

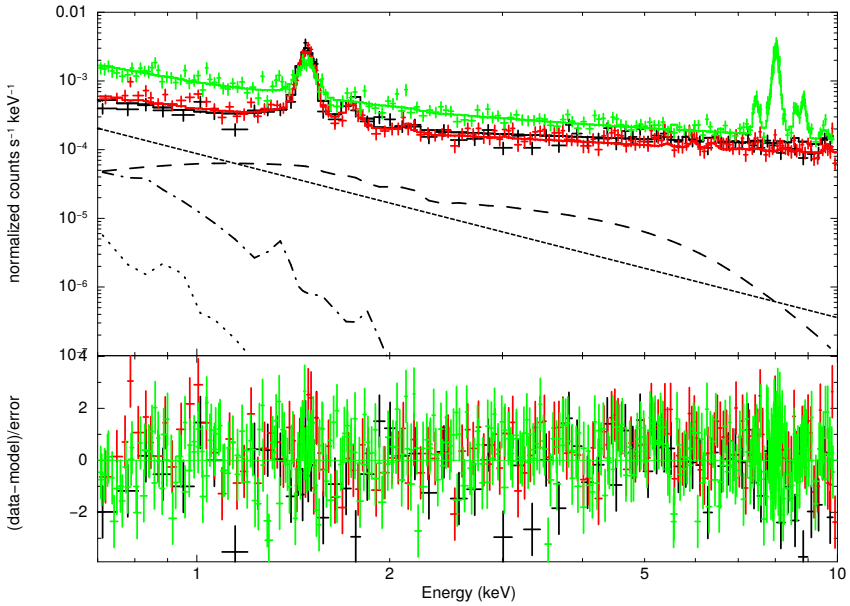

Figure 5.3: Spectra and best fit models for the XRBG + QPB for MOS1 (black), MOS2 (red) and PN (green) in the region $7' - 12'$. The different components of the XRBG are shown as dotted, dash-dotted and dashed lines for the local, halo and CXB component, respectively. The power law component for the residual soft proton emission is shown as short-dashed line. For the spectra and models of the QPB see Fig. 5.2.

temperature and normalization as free fitting parameters. The redshift and the abundance are set to 0 and 1, respectively. The second component can be described by an absorbed APEC model. The superposition of AGN emission was analyzed by De Luca & Molendi (2004) and can be modeled by an absorbed power law with a photon index of 1.41. We accounted for the particle background in this annulus by using the previously determined model in Sec. 5.3.1.3 in the region $7' - 12'$ with two floating multiplicative constants ($\pm 20\%$) for the continuum part and the fluorescent lines, respectively. We additionally introduce a power-law model to account for the residual soft proton emission. Also for this model we use diagonal response matrices.

The XRBG spectra and the best-fit models for the different components are shown in Fig. 5.3 for the off-axis region between $7' - 12'$.

5.3.1.5 PSF correction

The extent of the cluster on the sky is small, therefore we have to choose annular region sizes which suffer from the PSF size of XMM-Newton. This causes "mixing" of photons, i.e. photons originating from a certain region on the sky are detected in another region on the detector. This has an impact on the spectra and influences the measurements, especially the determination of the temperature profile. To avoid this we introduce a PSF correction. The XMM-Newton task *arfgen* allows us to calculate cross-region ARFs. Via these cross-region ARFs the effective area for the emission coming from one particular region, but detected in another, is estimated. These ARFs can then be used in the fitting process to account for the PSF effects. Therefore, we introduced additional absorbed APEC models for each combination of photon mixing (e.g. photons from region 1 on the sky, detected in region 2 on the detector, etc.). These models use the cross-region ARFs and the model parameters are linked to the parameters of the annulus

the emission truly originates from, as described in the corresponding SAS-thread[4]. We neglect the PSF effects for the emission coming from the outermost annulus, which is detected in the two inner annuli as the effective area for those is close to zero.

5.3.2 HST analysis

Here we perform a weak gravitational lensing analysis based on new Hubble Space Telescope observations of Cl $J120958.9+495352$, obtained within the joint XMM-Newton+HST program (HST program ID 13493). Weak lensing measurements require accurate measurements of the shapes of background galaxies well behind the cluster. Given the high redshift of Cl $J120958.9+495352$, typical weak lensing background galaxies are at redshifts $z \gtrsim 1.4$. As most of them are unresolved in ground-based seeing-limited data, HST observations are key for this study. Specifically, we analyze observations obtained with ACS in the F606W filter in a 2×2 mosaic, with integration times of 1.9 ks per pointing, each split into 4 exposures.

The data reduction and analysis is conducted with the same pipeline that was used for the weak lensing analysis of high-redshift galaxy clusters from the South Pole Telescope Sunyaev-Zel'dovich Survey (Bleem et al., 2015b) presented in Schrabback et al. (2016, S16 henceforth). Therefore we only summarize the main analysis steps here and refer the reader to S16 for further details.

For the ACS data reduction we employ basic calibrations from `CALACS`, the correction for charge-transfer inefficiency from Massey et al. (2014), `MultiDrizzle` (Koekemoer et al., 2003) for the cosmic ray removal and stacking, and scripts for the image registration and improvement of masks from Schrabback et al. (2010).

We detect objects using `Source Extractor` (Bertin & Arnouts, 1996) and measure shapes using the KSB+ formalism (Kaiser et al., 1995, Luppino & Kaiser, 1997, Hoekstra et al., 1998) as implemented by Erben et al. (2001) with adaptions for HST measurements described in Schrabback et al. (2007,0). In particular, we apply a model for the temporally and spatially varying HST point-spread function (PSF) constructed from a principal component analysis of ACS stellar field observations. In order to estimate cluster masses from weak lensing, accurate knowledge of the source redshift distribution is required. Here we follow the approach from S16, who first apply a color selection to remove cluster galaxies from the source sample, and then estimate the redshift distribution based on CANDELS photometric redshift catalogs (Skelton et al., 2014), to which they apply consistent selection criteria as used in the cluster fields, as well as statistical corrections for photometric redshift outliers.

For the color selection we make use of additional i-band observations of Cl $J120958.9+495352$ obtained with the Prime Focus Camera PFIP (Prime Focus Imaging Platform) on the 4.2 m William Herschel Telescope (ID: W14AN004, PI: Hoekstra) on March 26, 2014. These observations have been taken with the new red-optimized RED+4 detector, which has an imaging area of 4096×4112 pixels, with a pixel scale of $0\farcs27$ and an $18' \times 18'$ field of view. We reduce these data using `theli` (Erben et al., 2005, Schirmer, 2013), co-adding exposures of a total integration time of 13.5ks and reaching a 5σ limit of $i_{\mathrm{WHT,lim}} \simeq 25.8$ in circular apertures of $2''$, with an image quality of $1\farcs2$. We use SDSS (SDSS Collaboration et al., 2016) for the photometric calibration and convolve the ACS F606W imaging to the ground-based resolution to measure $V_{606,\mathrm{con}} - i_{\mathrm{WHT}}$ colors. For galaxies at the cluster redshift the 4000Å/Balmer break is located within this filter pair. Therefore, by selecting very blue galaxies in this color, we can cleanly remove the cluster galaxies, while selecting the majority of the $z \gtrsim 1.4$ background sources carrying

[4] `cosmos.esa.int/web/xmm-newton/sas-thread-esasspec`

the lensing signal (see S16). To account for the increased scatter at faint magnitudes we apply a magnitude-dependent selection $V_{606,\mathrm{con}} - i_{\mathrm{WHT}} < 0.16$ ($V_{606,\mathrm{con}} - i_{\mathrm{WHT}} < -0.04$) for galaxies with magnitudes $24 < V_{606} < 25.5$ ($25.5 < V_{606} < 26$) measured in $0\farcs7$ diameter apertures from the non-convolved ACS images. These cuts correspond to a color selection in the CANDELS catalogs of $V_{606} - I_{814} < 0.2$ ($V_{606} - I_{814} < 0.0$). In order to select consistent galaxy populations between the cluster field and the CANDELS catalogs we additionally apply consistent lensing shape cuts and add photometric scatter to the deeper CANDELS catalogs as empirically estimated in S16. The depth of our final weak lensing catalog for Cl $J120958.9+495352$ is mostly limited by the mediocre seeing conditions during the WHT observations, which require us to substantially degrade the F606W images in the PSF matching for the color measurements. As a result, we have to apply a rather stringent selection $V_{606,\mathrm{auto}} < 25.8$ based on the `Source Extractor` auto magnitude, which results in a final galaxy number density of $9.6/\mathrm{arcmin}^2$, while the shape catalog extends to $V_{606,\mathrm{auto}} \simeq 26.5$. We therefore recommend that future programs following a similar observing strategy should ensure that complementary ground-based observations are conducted under good seeing conditions, in order to fully exploit the statistical power of the HST weak lensing shape catalogs.

5.4 Results

5.4.1 HST results

In Fig. 5.4 we show contours of the weak lensing-reconstructed mass distribution of Cl $J120958.9+495352$, overlaid onto a color image from the ACS/WFC F606W imaging and WFC3/IR imaging obtained in F105W (1.2 ks) and F140W (0.8 ks). The reconstruction employs a Wiener filter (McInnes et al., 2009, Simon et al., 2009), as further detailed in S16. Divided by the r.m.s. image of the reconstructions of 500 noise fields, the contours indicate the signal-to-noise ratio of the weak lensing mass reconstruction, starting at 2σ in steps of 0.5σ. The reconstruction peaks at R.A. =12:10:00.26, δ =+49:53:48.2, with a positional uncertainty of $23''$ in each direction (estimated by bootstrapping the source catalog), which makes it consistent with the locations of the X-ray peak and the BCG at the 1σ–level.

Fig. 5.5 displays the measured tangential reduced shear profile of Cl $J120958.9+495352$ as function of the projected separation from the X-ray peak, combining measurements from all selected galaxies with $24 < V_{606,\mathrm{aper}} < 26$ as done in S16. Fitting these measurements within the radial range $300\,\mathrm{kpc} \leq r \leq 1.5\,\mathrm{Mpc}$ assuming a model for a spherical NFW density profile according to Wright & Brainerd (2000) and the mass-concentration relation from Diemer & Kravtsov (2015), we constrain the cluster mass to $M_{500}/10^{14}M_{\odot} = 4.4^{+2.2}_{-2.0}(\mathrm{stat.}) \pm 0.6(\mathrm{sys.})$ and $M_{200}/10^{14}M_{\odot} = 6.5^{+3.0}_{-2.9}(\mathrm{stat.}) \pm 0.8(\mathrm{sys.})$.

Here we have corrected for a small expected bias of -7% (-8%) for M_{500} (M_{200}) caused by the simplistic mass model, as estimated by S16 and further detailed in Applegate et al. (in prep.) using the analysis of simulated cluster weak lensing data. Differing from S16 we assume negligible miscentring for the bias correction, justified by the regular morphology of the cluster and precise estimate of the X-ray cluster center. The quoted statistical uncertainty includes shape noise, uncorrelated large-scale structure projections, and line-of-sight variations in the source redshift distribution, while the systematic error estimate takes shear calibration, redshift errors, and mass modeling uncertainties into account (see S16 for details). Here we have doubled the systematic mass modeling uncertainties compared to S16 as we include somewhat smaller scales in the fit. When restricting the radial range in the fit to the more conservative range $500\,\mathrm{kpc} \leq r \leq 1.5\,\mathrm{Mpc}$ from S16, the resulting constraints are

Table 5.2: Global cluster properties between $0' < R < 1.'8$

	background-modeling	background-subtraction
T [keV]	$9.04^{+1.38}_{-1.88}$	$8.84^{+0.97}_{-0.71}$
Z $[Z_\odot]$	$0.35^{+0.20}_{-0.18}$	$0.46^{+0.19}_{-0.17}$
norm[1]	$18.95^{+1.32}_{-1.28}$	$19.09^{+0.72}_{-0.73}$

[1] norm $= \frac{10^{-18}}{4\pi[D_A(1+z)]^2} \int n_e n_H dV \, \mathrm{cm}^{-5}$ with D_A being the angular diameter distance to the source.

$M_{500}/10^{14}M_\odot = 4.2^{+2.6}_{-2.3}(\mathrm{stat.}) \pm 0.4(\mathrm{sys.})$ and $M_{200}/10^{14}M_\odot = 6.3^{+3.6}_{-3.4}(\mathrm{stat.}) \pm 0.6(\mathrm{sys.})$ with smaller expected and corrected biases of 3% (5%) for M_{500} (M_{200}) and smaller systematic uncertainties, but increased statistical errors.

For the comparison to the X-ray measurements we additionally require weak lensing-derived mass estimates for an overdensity $\Delta = 2500$. When assuming the Diemer & Kravtsov (2015) mass-concentration relation and extrapolating the bias corrections[5], the weak lensing mass constraints correspond to $M_{2500}/10^{14}M_\odot = 1.7^{+0.9}_{-0.8}(\mathrm{stat.}) \pm 0.2(\mathrm{sys.})$ when including measurements from scales $300\,\mathrm{kpc} \leq r \leq 1.5\,\mathrm{Mpc}$, and $M_{2500}/10^{14}M_\odot = 1.6^{+1.0}_{-0.9}(\mathrm{stat.}) \pm 0.2(\mathrm{sys.})$ when restricting the analysis to scales $500\,\mathrm{kpc} \leq r \leq 1.5\,\mathrm{Mpc}$.

We expect that our mass estimation procedure is unbiased within the quoted systematic uncertainties for a random population of massive clusters. For an individual cluster as studied here, deviations in the density profile from the assumed NFW profile with a concentration from the Diemer & Kravtsov (2015) mass-concentration relation lead to additional scatter in the mass estimates. To estimate the order of magnitude of this effect we repeat the mass fits for scales $300\,\mathrm{kpc} \leq r \leq 1.5\,\mathrm{Mpc}$ using different concentrations. For fixed concentrations $c_{200} = 3.0$ ($c_{200} = 5.0$), the best-fit mass constraints for $M_{200}, M_{500}, M_{2500}$ change by $+11\%, +6\%, -9\%$ ($-11\%, -5\%, +11\%$) compared to the default analysis using the Diemer & Kravtsov (2015) mass-concentration relation, which corresponds to a concentration $c_{200} = 3.7$ at the best fitting mass. These variations are negligible compared to the statistical uncertainties of the study presented here. Note, that this analysis assumes spherical cluster models which can lead to extra scatter due to triaxiality when comparing to X-ray results.

5.4.2 XMM-Newton results

5.4.2.1 Global cluster properties

The global properties for both methods of the treatment of the background are summarized in Tab. 5.2. The overall properties agree well between both methods.

The luminosity of the cluster in the $0.1 - 2.4\,\mathrm{keV}$ band is $L_X = (18.7^{+1.3}_{-1.2}) \times 10^{44}\,\mathrm{erg/s}$ and $L_X = (19.1^{+0.5}_{-0.6}) \times 10^{44}\,\mathrm{erg/s}$, for background-modeling and background-subtraction method, respectively, estimated from the spectral fit. It is thus comparable to the most X-ray luminous MACS clusters, but at even higher redshift. These values are also in very good agreement with the findings by Buddendiek et al. (2015).

[5] This is necessary given that the analysis from S16 as function of $\log \Delta$ provides bias estimates for $\Delta = 200$ and $\Delta = 500$ only, as masses M_{2500} are not available for the simulations used to derive the bias values. We do propagate the statistical uncertainty of this extrapolation, but note that it is negligible compared to the statistical uncertainty of the mass constraints for Cl $J120958.9{+}495352$.

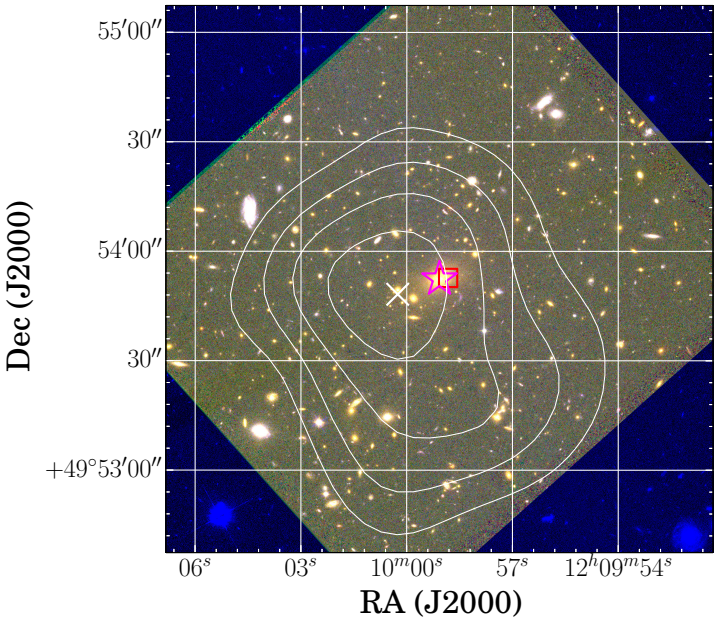

Figure 5.4: HST 2.′5 × 2.′5 color image of Cl J120958.9+495352 based on the ACS/WFC F606W (blue) and WFC3/IR F105W (green) and F140W (red) imaging. The white contours indicate the signal-to-noise ratio of the weak lensing mass reconstruction, starting at 2σ in steps of 0.5σ, with the cross marking the peak position, which is consistent with the X-ray peak (red square) and BCG position (magenta star) within the uncertainty of 23″ in each direction.

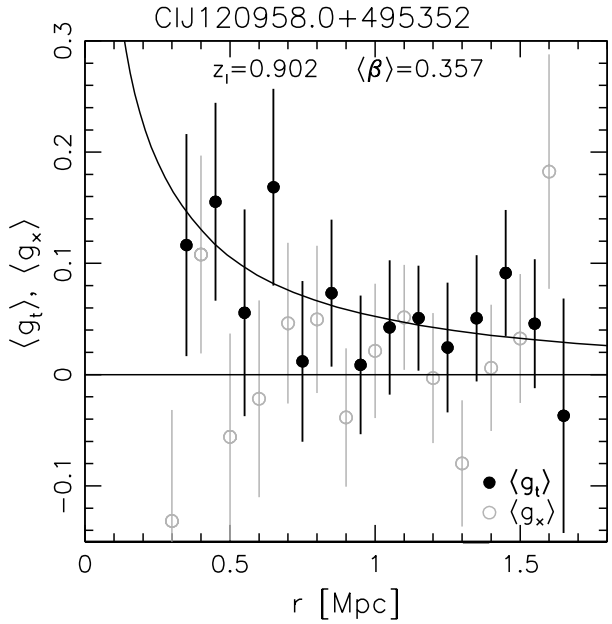

Figure 5.5: Tangential reduced shear profile (black solid circles) of Cl J120958.9+495352, measured around the X-ray peak. Here we combine the profiles of four magnitude bins between $24 < V_{606,\mathrm{aper}} < 26$ as done in S16. The curve shows the corresponding best-fitting NFW model prediction constrained by fitting the data within the range $300\,\mathrm{kpc} \leq r \leq 1.5\,\mathrm{Mpc}$, assuming the mass-concentration relation from Diemer & Kravtsov (2015). The gray open circles indicate the reduced cross-shear component, which has been rotated by 45 degrees and constitutes a test for systematics. These points have been shifted by $dr = -0.05\,\mathrm{Mpc}$ for clarity.

Table 5.3: Fit results for the three radial bins for both methods of background-treatment. The abundance is linked between all annuli.

	$0' - 0.'3$	$0.'3 - 0.'8$	$0.'8 - 1.'3$
background-modeling			
T [keV]	$7.28^{+0.75}_{-0.72}$	$15.13^{+14.04}_{-4.67}$	$4.38^{+5.72}_{-2.13}$
Z $[Z_\odot]$	———	$0.25^{+0.16}_{-0.14}$	———
norm[1]	$11.38^{+0.58}_{-0.49}$	$5.40^{+0.44}_{-0.46}$	$2.08^{+0.86}_{-0.46}$
background-subtraction			
T [keV]	$7.29^{+0.74}_{-0.69}$	$14.61^{+11.55}_{-4.13}$	$8.43^{+7.15}_{-4.42}$
Z $[Z_\odot]$	———	$0.32^{+0.17}_{-0.15}$	———
norm[1]	$11.24^{+0.53}_{-0.51}$	$5.34^{+0.44}_{-0.43}$	$1.82^{+0.47}_{-0.28}$

[1] norm $= \frac{10^{-18}}{4\pi[D_A(1+z)]^2} \int n_e n_H dV \, \mathrm{cm}^{-5}$ with D_A being the angular diameter distance to the source.

5.4.2.2 Temperature and density

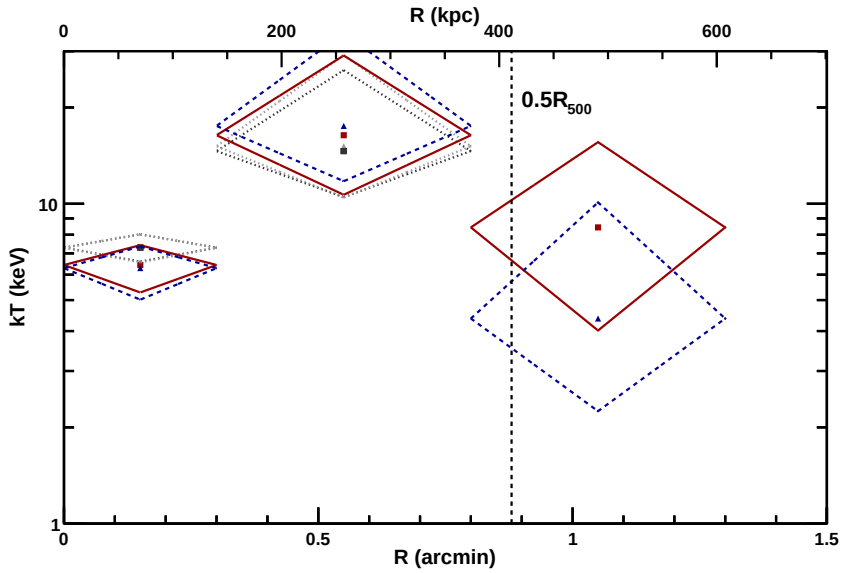

Figure 5.6: Deprojected and PSF-corrected temperature profile of Cl J120958.9+495352. Red (dark gray) solid diamonds show the deprojected (projected) result using the background-subtraction method. Blue (light gray) dashed diamonds corresponds to the background-modeling method.

We compare the results for the two approaches of the background treatment for temperature and density profile. Fig. 5.6 shows the temperature profile of Cl J120958.9+495352 for both approaches and Tab. 5.3 gives the results.

Overall we see a very good agreement between the two different background-methods. The temperature of the central bin is well constrained in both cases and both profiles show a good indication of a cool core. This makes Cl J120958.9+495352 one out of only a few such objects known at high redshifts. The upper uncertainties in the outer two bins are large which is mainly related to the correlation between the parameters due to the PSF correction and the limited

statistics. Even if no PSF correction is applied, the cool core remains and the uncertainty of the second temperature decreases by a factor of ∼5 and of the outermost temperature by a factor of ∼2.

We determine the gas density profile using the PSF-corrected normalizations of the APEC model, which is defined as

$$N_i = \frac{10^{-14}}{4\pi D_{\rm A}^2 (1+z)^2} \int_{V_i} n_{\rm e}(R) n_{\rm H}(R)\, {\rm d}V, \tag{5.1}$$

where i corresponds to the ith annulus from the center and $D_{\rm A}$ is the angular diameter distance to the source. The volume along the line of sight V_i is the corresponding cylindrical cut through a sphere with inner and outer radii of the ith annulus. We adopt $n_{\rm e} = 1.17 n_{\rm H}$. Due to the small extent of the cluster, there is only limited radial resolution. Therefore, we perform a simple deprojection method following Ettori et al. (2002).

The Emission Integral (EI) and temperature (T_i) in ring i is given by

$$EI_i = \sum_{j=i}^{N} n_{\rm e} n_{\rm H} V_{i,j} \tag{5.2}$$

$$T_i = \frac{\sum_{j=i}^{N} \epsilon_j V_{i,j} T_j}{\sum_{j=i}^{N} \epsilon_j V_{i,j}} \tag{5.3}$$

with $V_{i,j}$ being the volume of the cylindrical cut corresponding to ring i through spherical shell j and $n_{\rm e}$, $n_{\rm H}$ being the electron and proton density and ϵ the emissivity. By subtracting the contribution of the overlying shells in each annulus, we determine the deprojected electron density profiles for both background-treatment methods shown in Fig. 5.7. As for the temperature, the two density profiles agree very well showing that our background treatment works well in both cases.

As an additional test for the background-subtraction method we chose an even larger inner radius of the background region (from $4' - 5'$) and repeated the analysis. We find only marginally differences and thus conclude that no significant cluster emission is present in the background-region.

As it can be seen in Fig. 5.1 we detect a point source close to the center of the cluster. To investigate the impact of the point source, we increased the exclusion radius around this source by 50% and repeated the fit. Due to the lowered statistics, the uncertainties clearly increase but we find no significant impact compared to the nominal values.

5.4.2.3 Gas mass fraction

From the gas mass profile and the total mass $M_{\rm tot}(< R)$ inside a given radius R, the gas mass fraction can be obtained

$$f_{\rm gas}(< R) = \frac{M_{\rm gas}(< R)}{M_{\rm tot}(< R)}. \tag{5.4}$$

We note that, given the limited XMM-Newton spatial resolution, a very robust determination of the total mass from the hydrostatic equation is difficult as this would require well spatially resolved measurements of the density and temperature profile. Therefore, we use the total mass based on our weak lensing HST estimates and the corresponding R_{2500} (see Sec. 5.4.1). As a

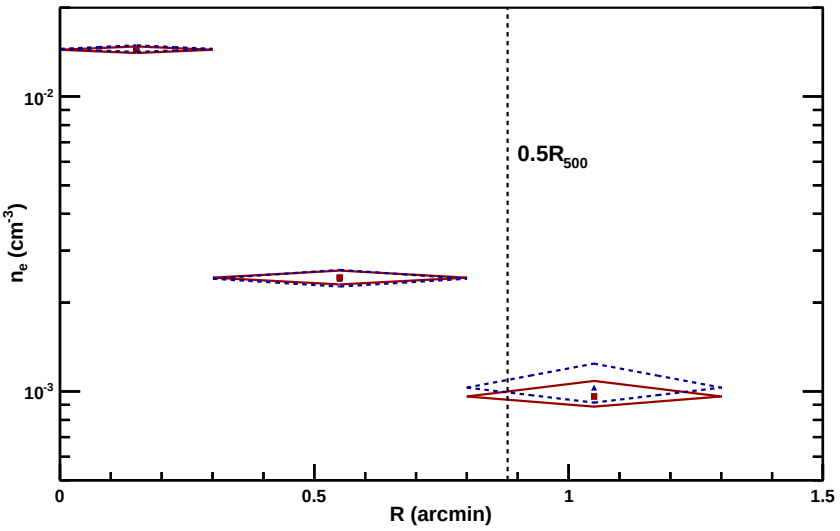

Figure 5.7: Deprojected and PSF-corrected electron density profile of Cl J120958.9+495352. Red solid diamonds show the result using the background-subtraction method. Blue dashed diamonds corresponds to the background-modeling method. The width of the diamonds corresponds to the radial bin size.

cross-check, we also determine the gas-mass fraction using the $L_X - M_{2500}$ relation obtained by Hoekstra (2007) for the total mass.

The HST results yield $M_{2500}/10^{14} M_\odot = 1.7^{+0.9}_{-0.8}(\text{stat.}) \pm 0.2(\text{sys.})$. For the estimation of f_{gas}, we include additional 30% triaxiality/projection uncertainty and 10% uncertainty from the mass-concentration relation on M_{2500}. From 10000 Monte-Carlo (MC) realizations of M_{2500}, we estimate $R_{2500} = 0\farcm75^{+0.13}_{-0.20}$ and for each realization the gas mass within the corresponding R_{2500}, assuming a constant density in each shell. This yields $M_{\text{gas},2500} = (1.64^{+0.53}_{-0.67}) \times 10^{13}\,\text{M}_\odot$ and $M_{\text{gas},2500} = (1.63^{+0.53}_{-0.67}) \times 10^{13}\,\text{M}_\odot$ for the background-subtraction and background-modeling method, respectively, which are in very good agreement. Combining these results, we estimate $f_{\text{gas},2500} = 0.10^{+0.03}_{-0.02}$ for both methods. Note that through this procedure the given uncertainties on M_{2500}, $M_{\text{gas},2500}$ and R_{2500} are, on the one hand, correlated and, on the other hand, the assumption of constant density in each shell is only a rough approximation, which is why the uncertainty on $f_{\text{gas},2500}$ is lower than naively expected. A more general estimate is obtained by using a beta-model for the density profile and following the same procedure as described above. We fix the core radius to a typical value of of $R_c = 0.15 \times R_{500}$ and assume a slope of $\beta = 2/3$ (as e.g. also used in Pacaud et al., 2016) but including 15% scatter on the latter. R_{500} is estimated from our HST results. This yields $f_{\text{gas}} = 0.11^{+0.06}_{-0.03}$ for both background methods. Yet another approach is to estimate f_{gas} and its uncertainties at a *fixed* radius (i.e. assuming the true R_{2500} is known) in which case the uncertainties on M_{2500} and M_{gas} are uncorrelated and directly propagate onto f_{gas} which then yields $f_{\text{gas}} = 0.11^{+0.12}_{-0.05}$. Here, we take the result using the beta-model as default.

Hoekstra (2007) estimated the $L_X - M_{2500}$ relation for a galaxy cluster sample of 20 X-ray luminous objects at intermediate redshifts up to $z{\sim}0.6$. They find a slope consistent with the one from Pratt et al. (2009), which is also used in the redshift evolution study of Reichert et al. (2011) and also consistent with the (inverted) slope of Maughan (2007) who assumed self-similar evolution. Using the relation from Hoekstra (2007) and assuming 30% intrinsic

scatter, we find $M_{2500} = (1.31^{+0.31}_{-0.29}) \times 10^{14}\mathrm{M}_{\odot}$ for the background-subtraction method and $M_{2500} = (1.30^{+0.32}_{-0.30}) \times 10^{14}\mathrm{M}_{\odot}$ for the background-modeling method and (using the corresponding R_{2500}) $M_{\mathrm{gas},2500} = (1.34^{+0.27}_{-0.25}) \times 10^{13}\,\mathrm{M}_{\odot}$ and $M_{\mathrm{gas},2500} = (1.33^{+0.32}_{-0.30}) \times 10^{13}\,\mathrm{M}_{\odot}$, respectively. This yields $f_{\mathrm{gas},2500} = 0.10 \pm 0.02$ for both background-methods and is in very good agreement with our previous findings using the weak lensing mass.

5.4.3 Cooling time

To estimate the cooling time, we further reduced the size of the central region to 0.′2 corresponding to ∼100 kpc and performed the same PSF correction and deprojection method as described above. The cooling time is given by (cf. Hudson et al., 2010)

$$t_{\mathrm{cool}} = \frac{3(n_{\mathrm{e}} + n_{\mathrm{i}})k_{\mathrm{B}}T}{2n_{\mathrm{e}}n_{\mathrm{H}}\Lambda(T, Z)} \tag{5.5}$$

where n_{i} is the ion density and $\Lambda(T, Z)$ the cooling function. Within 100 kpc we find $n_{\mathrm{e}} = (2.09^{+0.10}_{-0.08}) \times 10^{-2}\,\mathrm{cm}^{-3}$ and $T = 4.0^{+1.3}_{-1.5}\,\mathrm{keV}$. This yields a short cooling time for Cl $J120958.9+495352$ within 100 kpc of $t_{\mathrm{cool}} = 2.8 \pm 0.5\,\mathrm{Gyr}$ for the background subtraction method and $t_{\mathrm{cool}} = 2.9 \pm 0.4\,\mathrm{Gyr}$ for the background modeling method. Hudson et al. (2010) studied the cool cores for a local sample of 64 clusters within $0.4\%R_{500}$ with Chandra. According to their findings, Cl $J120958.9+495352$ belongs to the weak cool core clusters, however, it has to be taken into account that the radius, in which they determine the cooling time, is much smaller than what is possible for Cl $J120958.9+495352$ and, presumably, within this radius, the cooling time would be even lower, possibly resulting in a strong cool core classification.

5.5 Discussion and conclusions

Our results show that Cl $J120958.9+495352$, according to Planck Collaboration et al. (2015), belongs to the most luminous galaxy clusters known at z∼0.9. Compared to the total mass estimate from Buddendiek et al. (2015) of $M_{500} = (5.3 \pm 1.5) \times 10^{14}\,h_{70}^{-1}\mathrm{M}_{\odot}$, we find a slightly lower value from our weak lensing analysis of $M_{500}/10^{14}M_{\odot} = 4.4^{+2.2}_{-2.0}(\mathrm{stat.}) \pm 0.6(\mathrm{sys.})$, however, compatible within the uncertainties.

As discussed in e.g. Sanderson et al. (2009) and Semler et al. (2012) there is a tight correlation between the dynamical state of the cluster and the presence and strength of a cool core. We find strong indications for the presence of a cool core and the two different approaches for the background-handling yield similar results which gives us confidence in our treatment of the background. The temperature profile shows a clear drop towards the center and the cooling time within 100 kpc is short with $t_{\mathrm{cool}} = 2.8 \pm 0.5\,\mathrm{Gyr}$ and $t_{\mathrm{cool}} = 2.9 \pm 0.4\,\mathrm{Gyr}$ for the background subtraction and background modeling method, respectively. Another indicator for the morphological state is the offset between the BCG and the X-ray emission peak (see, e.g. Rossetti et al., 2016, Mahdavi et al., 2013, Hudson et al., 2010). Rossetti et al. (2016) defines a relaxed cluster by an offset smaller than $0.02R_{500}$. For Cl $J120958.9+495352$ the offset is about $2''$ (∼15 kpc) corresponding to $0.015R_{500}$ (using the BCG position given in Buddendiek et al., 2015, see also Fig. 5.4) which is another indication for the relaxed nature of the system. Our HST weak lensing study also shows, that the mass reconstruction peak is compatible with the BCG position and the X-ray peak within 1σ.

In a bottom-up scenario for structure formation, massive cool core systems should be extremely rare at high redshifts. Their gas mass fractions should not depend on the cosmological

model. However, the apparent evolution varies for different assumed cosmologies. Previous measurements from Allen et al. (2008) and Mantz et al. (2014) showed that their data are in good agreement with the standard cosmological model, showing a flat behavior of $f_{\rm gas}$ with redshift. However, these data only contain a few objects at very high redshifts. Therefore clusters like Cl $J120958.9{+}495352$ are valuable objects for cosmology.

We obtain a gas mass fraction of $f_{\rm gas,2500} = 0.11^{+0.06}_{-0.03}$ which is consistent with the result from Allen et al. (2008) for their full cluster sample and also consistent with the assumed ΛCDM cosmology ($\Omega_{\rm m} = 0.3$, $h = 0.7$). We performed several tests, i.e. we used an $L_X - M_{2500}$ scaling relation for the total mass and tested the assumption of constant density in each shell, to verify this result and find very good agreement. Mantz et al. (2014) measured the gas mass fraction in an annulus from $0.8R_{2500} < R < 1.2R_{2500}$ excluding the core of the clusters to minimize gas depletion uncertainties and intrinsic scatter in the inner part. They find typical $f_{\rm gas}$ values between $0.10 - 0.12$ and thus consistent with our findings and Allen et al. (2008).

Reichert et al. (2011) studied the evolution of cluster scaling relations up to redshift 1.5. They use the relations from Pratt et al. (2009) for the local clusters and obtain a bias-corrected evolution factor. Testing this $L_X - T$ scaling relations with our estimated global gas temperature yields an about 40% smaller luminosity than our measured value. This results is, at least partially, expected due to the presence of a cool core. However, the uncertainties solely due to the uncertainties of the slope and normalization of the scaling relation (assuming they are uncorrelated) are already large ($\gtrsim 40\%$). Compared to the results from Pratt et al. (2009) we see a good agreement of the luminosities but still within large uncertainties from the scaling relation itself.

The cluster Cl $J120958.9{+}495352$ is not only interesting with respect to cosmology but also in an astrophysical manner. At redshift 0.9 the time span for this massive object to form a cool core is very short. As XMM-Newton is not able to fully resolve the core structure, we aim for higher spatial resolution data in a future project to robustly determine the X-ray hydrostatic mass and perform detailed study of the core properties.

5.6 Acknowledgements

This work is based on joint observations made with the NASA/ESA *Hubble Space Telescope*, using imaging data from program 13493 (PI: Schrabback), and XMM-Newton data (IDs 0722530101 and 0722530201) as well as WHT data (ID W14AN004, PI: Hoekstra). ST and TS acknowledge support from the German Federal Ministry of Economics and Technology (BMWi) provided through DLR under projects 50 OR 1210, 50 OR 1308, 50 OR 1407, and 50 OR 1610. ST and THR acknowledge support by the German Research Association (DFG) through grant RE 1462/6 and the Transregio 33 "The Dark Universe" sub-project B18. ST also acknowledges support from the Bonn-Cologne Graduate School of Physics and Astronomy. LL acknowledge support from the Chandra X-ray Observatory grant GO3-14130B and by the Chandra X-ray Center through NASA contract NAS8-03060. Support for Program number GO-13493 was provided by NASA through a grant from the Space Telescope Science Institute, which is operated by the Association of Universities for Research in Astronomy, Incorporated, under NASA contract NAS5-26555.

CHAPTER 6

X-ray study of shock fronts in Abell 2163 with Suzaku

A relaxed distant cluster, as the one studied in the previous chapter, is rare because merging should take place frequently at early times. However, merging is also observed for lower redshift clusters and such a merger situation is studied in this project in the disturbed cluster A2163 ($z = 0.203$) with the Suzaku satellite. Structure formation "in action" is visible in shocks in the ICM. While galaxies and dark matter pass without interaction in a merging event, the ICM of the merging substructures interacts and forms distinct shock fronts as seen in X-ray observations. Suzaku is able to reveal shocks even in low surface brightness regions far off the center. The data reduction and parts of the spectral fitting in general follow similar steps as in chapter 4 and are thus only briefly summarized here in Sec. 6.3. The content of this chapter is being prepared for submission to *Astronomy & Astrophysics*. Dr. Florian Pacaud kindly provided the XMM-Newton surface brightness profiles (cf. Sec. 6.5.1).

6.1 Introduction

Galaxy clusters – the largest clearly defined building blocks in the universe – form at the intersections of the filamentary large-scale structure (e.g. Borgani & Guzzo, 2001, Springel et al., 2005, Vogelsberger et al., 2014). They grow by merging of smaller substructures and accretion of matter along the direction of the filaments. Such merging events are the most energetic processes in the universe and substantial parts of the energy are dissipated into shocks of the hot ICM. The probably most prominent observational example of a strong shock is the merging Bullet cluster (Markevitch et al., 2002) with a distinct shock front and large Mach number of $M{\sim}3$ (Springel & Farrar, 2007). A shock is in general visible as a discontinuity in the temperature, density and/or surface brightness profile (for a review of shocks see Markevitch & Vikhlinin, 2007). Until now, relatively few shocks have been studied in detail in X-rays. One example is the analysis performed by Simionescu et al. (2009a) for the merging cluster Hydra A using deep XMM-Newton data. They discovered a large scale shock in the surface brightness profile and pressure map with a Mach number of about 1.3. Another example is the cluster A521 studied by Bourdin et al. (2013), also using deep XMM-Newton observations. They find two cores separated by two cold fronts and two shocks propagating in east and south-west direction. The shock heated regions and one of the shock fronts show spatial correlations with a radio halo and a radio relic, respectively, suggesting that the shock might be responsible for the radio emission. Other examples of shocks have been seen by Macario et al. (2011) and Akamatsu

et al. (2012b) for the two nearby mergers A754 and A3376, respectively. Also for these clusters, radio emission is observed and the shocks seen in the X-ray observations seem to be related to radio relics. Akamatsu et al. (2012b) report a high Mach number of $M{\sim}3$ for A3376 estimated from the gas temperature jump.

In this work, we study the disturbed cluster A2163, which is one of the hottest clusters known and also shows prominent radio emission (Feretti et al., 2001). We analyze two Suzaku observations in the north-east (NE) and south-west (SW) direction and investigate the ICM properties with respect to the presence of possible shock fronts. We use archival XMM-Newton data to detect point sources in the field of view.

Sec. 6.2 introduces the cluster A2163 while Sec. 6.3 summarized the analyzed observations and data reduction. In Sec. 6.4 we discuss the spectral analysis and the deduced radial profiles are presented in Sec. 6.5. From these profiles we develop a deprojection strategy and estimate the properties of the shock fronts which are given in Sec. 6.6. Sec. 6.7 discusses the results for the shocks and a short summary and outlook is given in Sec. 6.8. Throughout the analysis we assume $\Omega_\Lambda = 0.7$, $\Omega_\mathrm{m} = 0.3$, $H_0 = 70\,\mathrm{km/s/Mpc}$ and all uncertainties are quoted at the 68% level.

6.2 The cluster Abell 2163

The cluster A2163 at $z = 0.203$ (Struble & Rood, 1999) was part of the first Abell catalog and is an extremely hot and rich irregular cluster. An early study performed by Elbaz et al. (1995) using ROSAT PSPC data found a high ICM temperature of $T = 14.6^{+0.9}_{-0.8}\,\mathrm{keV}$. Later, detailed studies (e.g. Feretti et al., 2001, Maurogordato et al., 2008 and Bourdin et al., 2011) revealed a complex structure, probably due to recent merging of two or more substructures. Ota et al. (2014) looked for hard X-ray emission in A2163 using the Suzaku HXD data from the same observations for which we analyze the XIS data in this project. They find significant emission in the $12 - 60\,\mathrm{keV}$ band and a multi-temperature structure with a high temperature component in the NE direction, but no significant non-thermal emission. In addition, A2163 was one of the three clusters for which the Sunyaev-Zeldovich effect was observed for the first time by Désert et al. (1998).

Fig. 6.1 shows images of A2163 in different wavelengths. The radio image obtained by Feretti et al. (2001) revealed a giant extended radio halo with correlations to the X-ray emission of the ICM. They classify the elongated structure in the NE direction as a radio relic. The projected galaxy density map obtained by Maurogordato et al. (2008) shows an even more pronounced correlation with the radio map and several subclumps can be identified, while the most prominent structure lies north to the main cluster. Bourdin et al. (2011) performed a detailed study of the central region of A2163 using XMM-Newton and Chandra observations. Their findings from spectral imaging show that the ICM is in a highly disturbed status with a hotter region in the NE direction and a cool core located SW of the center. In their interpretation, the cool core was likely separated from its galaxy as there is a galaxy overdensity located close to the cool core bullet. The authors state that it is moving westwards showing a cold front in a sector north-west the bullet. They also state that the prominent structure north of the center is probably not related to the main cluster as the ICM shows no significant indications for an interaction.

A detailed comparison of our work to these findings and the interpretation is given in Sec. 6.7.

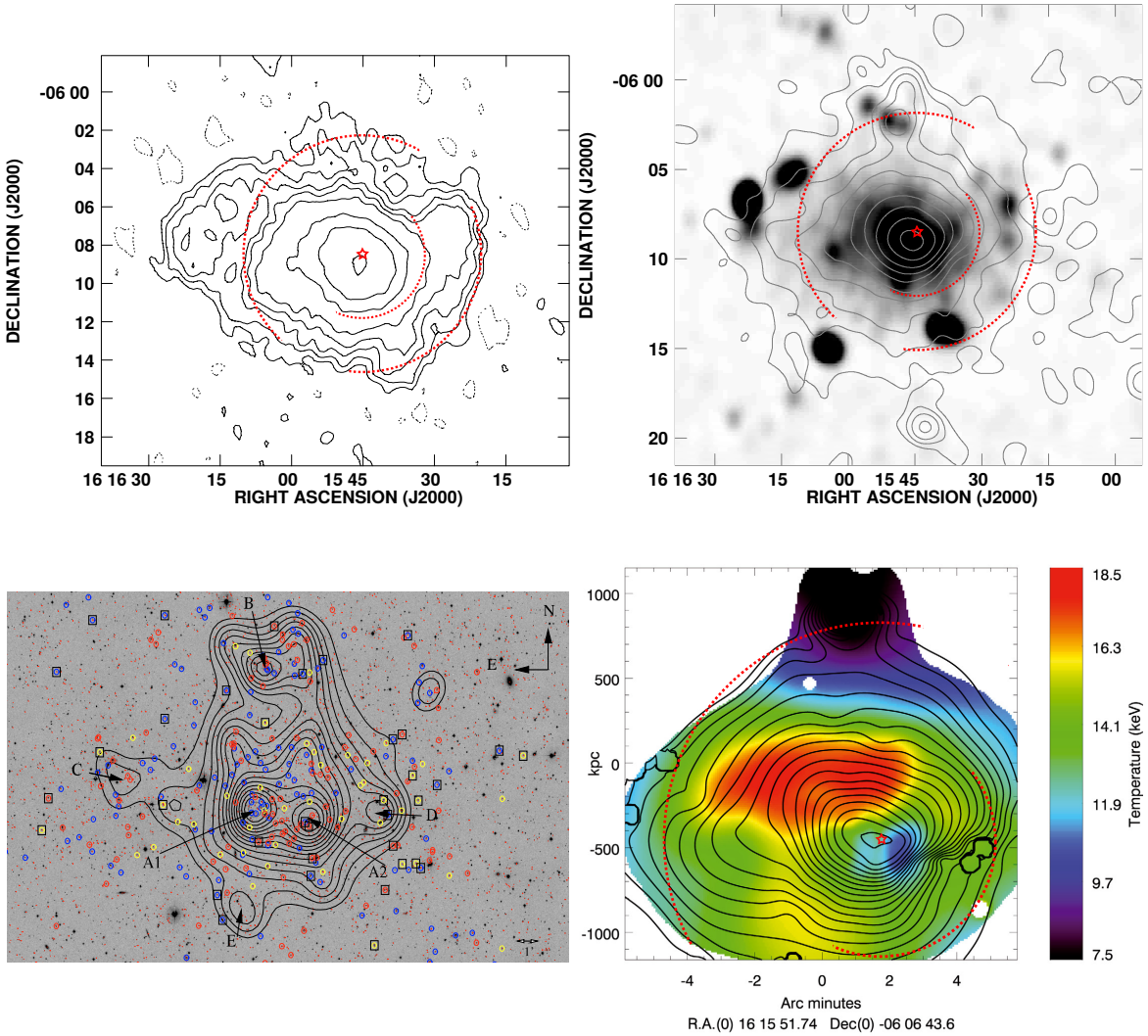

Figure 6.1: *Top left*: Radio map of A2163 at 20 cm after subtraction of unrelated sources obtained by Feretti et al. (2001). Overlaid as red dotted lines and red star are the positions of the temperature jumps obtained in our Suzaku analysis in NE and SW direction (see Sec. 6.6 for details) and the center of our radial analysis, respectively. *Top right*: X-ray contours obtained with ROSAT PSPC overlaid on a radio map and the same jump and center position as in the left figure. The contours show a concentration around $2' - 3'$ from the center. Credit: Feretti et al. (2001). *Bottom left*: Projected galaxy density map overlaid over a Wide Field Imager R-band image. Structures detected with more than 3σ are marked with a letter. Credit: Maurogordato et al. (2008). *Bottom right*: ICM temperature map obtained with XMM-Newton and black surface brightness isocontours obtained from a Chandra observation. The star and the red dashed lines have the same meaning as in the top figures. Credit: Bourdin et al. (2011). *Please note the different scales and centering of the images.*

Table 6.1: Details of the analyzed observations of A2163. The exposure time is the cleaned exposure time after data reduction.

	Date	Pointing (R.A., Dec.)	Exp. Time	Obs-ID	PI
Suzaku NE	2009 Feb	(244.0216, -6.0449)	38.6 ks	803022010	N. Ota
Suzaku SW	2008 Aug	(243.8071, -6.2200)	109.2 ks	803071010	T. H. Reiprich
XMM-Newton	2013 Feb	(243.94167, -6.1500)	90.8 ks	0694500101	H. Bourdin

6.3 Observations and data reduction

In this work, we analyze two Suzaku XIS observations of A2163 in NE and SW direction of 39 ks and 109 ks cleaned exposure time, respectively. Additionally, we use archival XMM-Newton data to detect point sources in the field of view. Details of the observations can be found in Tab. 6.1. We follow the standard data reduction procedure (in detail described in Sec. 4.3) which includes the following steps: Assign coordinates, time and pixel quality flag to each event, apply gain- and charge-transfer-inefficiency correction and identify anomalous pixels. For the geomagnetic cut off rigidity we use a limit of COR2>6 and events falling in the second trailing rows of the charge injection rows are discarded.

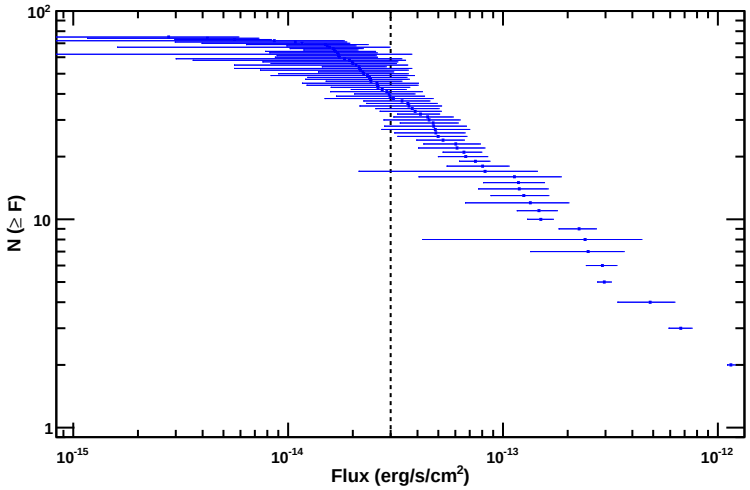

Figure 6.2: Cumulative $\log(N)$–$\log(F)$ plot of all detected point sources in the XMM-Newton observation. N is the number of sources above or equal to a given flux F (cf. also Sec. 4.4.1). The chosen flux limit is $3 \times 10^{-14}\,\mathrm{erg/s/cm^2}$ and all sources above this limit are removed from the Suzaku FOV.

We perform a flare filtering by applying a three-sigma clipping to the light curves and removing the corresponding time intervals. The XMM-Newton observation for the point source detection covers the analyzed area in both Suzaku observations as shown in Fig. 6.3. We reduce the XMM-Newton data by applying the standard steps as described in Sec. 5.3 and cleaned the data for flares. We use the task *emldetect* to detect point sources in two energy bands from $0.5 - 4.5\,\mathrm{keV}$ and $4.5 - 12.0\,\mathrm{keV}$ and apply the energy conversion factors from Rosen et al. (2016) for a power law with spectral index 1.7 to estimate the flux of the sources. Not all of the detected sources can be removed from the Suzaku observation as this would remove a significant amount of area due to Suzaku's larger PSF. Thus, we choose a flux limit of $3 \times 10^{-14}\,\mathrm{erg/s/cm^2}$, motivated by Fig. 6.2. In the north direction we identify the previously mentioned prominent

substructure, which we exclude from the analysis as Bourdin et al. (2011) found no relation to the main cluster. Several sources in the eastern direction are identified which matches the picture of an elongated structure and a merging event in the E–W direction as discussed in Sec. 6.7. All removed sources are shown in Fig. 6.3.

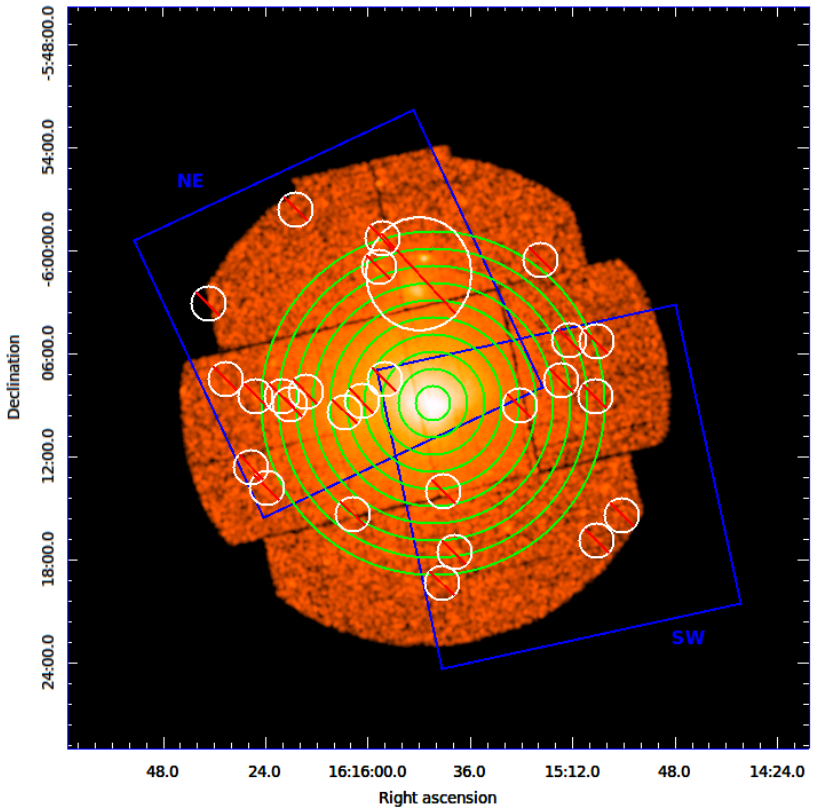

Figure 6.3: Suzaku pointings (blue boxes), extraction regions for the Suzaku analysis (green annuli) and removed (point source) regions (white circles) overlaid on an XMM-Newton MOS2 image. Point sources are removed above a flux limit of 3×10^{-14} erg/s/cm^2. The structure in the north is removed as Bourdin et al. (2011) found it to be unrelated to the main cluster.

6.4 Analysis

6.4.1 Background

The Suzaku non-X-ray background is caused by highly energetic particles hitting the detector and producing continuum and fluorescent line emission. This background is estimated from night earth observations in ±150 days around the observation date and the corresponding spectra are subtracted by the XSPEC analysis software before fitting. For the creation of these NXB spectra, we follow the improved treatment for the flickering pixels[1].

As also described in detail previously (cf. Sec 2.2.1), the X-ray background is mainly composed of three components: A local component (LHB), a Milky Way halo component and the superposition of distant AGNs. We model these components using an apec and absorbed apec

[1] see `heasarc.gsfc.nasa.gov/docs/suzaku/analysis/xisnxbnew.html`

model for the LHB and halo component, respectively, and an absorbed power law for the CXB component with an index of 1.41 (De Luca & Molendi, 2004). The redshift of the apec models is fixed to 0 and the abundance is set to one times the solar abundance using the abundance table obtained by Asplund et al. (2009). In addition to our data, we use ROSAT All-Sky Survey data (obtained with the HEASARC X-ray background tool[2]) to constrain the model parameters in a region far off the center where no cluster emission is expected and at low energies $< 2\,\mathrm{keV}$.

We create ancillary response files for the background spectra using *xissimarfgen* and assuming a uniform distribution.

6.4.2 PSF correction

The limited spatial resolution of Suzaku makes it necessary to correct for the effect of the point-spread function. Therefore, we simulate the mixing of photons between the different annuli for each of the observations separately using *xissim* and background-subtracted surface brightness profiles in each direction to which we fit single-beta models. The profiles were obtained from Suzaku images. From this simulation, we obtain PSF-correction factors which are implemented in the fitting procedure similar to the procedure described in Sec. 4.4.3. To reduce the correlations in the fit, we consider only mixing factors $\geq 10\%$ as we do not expect significant influence from annuli with less mixing. However, significant correlations are still present in the fit which results in "oscillations" of the temperature in neighboring annuli. We thus regularize the temperature and abundance values in the following way: We perform a spectral fit to all annuli without correcting for PSF effects. For the PSF-corrected fit, the parameters of temperature and abundance are allowed to vary by $\pm 2\sigma$ compared to the values of the first (PSF-uncorrected) fit. However, the normalization is not constrained. The effect of the regularization is studied in Sec. 6.6.2.

6.4.3 Fitting procedure

We analyze the two observations in the NE and SW directions separately and extract spectra in 10 and 9 radial bins, respectively, with $1'$ width and centered on the X-ray emission peak estimated with Suzaku. We examine the signal-to-background counts ratio ($N_{\mathrm{source}}/N_{\mathrm{bkg}}$) in each annulus and limit the number of regions such that the ratio is $\gtrsim 1$ in the outermost annulus. The extraction regions are shown in Fig. 6.3.

For the model of the source emission we chose an absorbed apec model with fixed cluster redshift of $z = 0.203$ and the total hydrogen column density from Willingale et al. (2013), which includes molecular hydrogen. The absorption is modeled using the XSPEC phabs model. The abundance table from Asplund et al. (2009) is applied and we use four radial bins for the metallicity, i.e. several abundance parameters are linked across annuli as shown in Fig. 6.6.

Ancillary response files are created using the same beta-model profiles as used previously for the PSF simulation. All spectra are grouped to have at least 25 counts per bin and the χ^2 fit is carried out in the energy range $0.7 - 10.0\,\mathrm{keV}$ except for the outermost three (two) annuli for the NE (SW) direction, for which the fitting range is $0.7 - 7.0\,\mathrm{keV}$ to achieve a sufficient signal-to-background ratio.

[2] `heasarc.gsfc.nasa.gov/cgi-bin/Tools/xraybg/xraybg.pl`

6.5 Radial profiles

6.5.1 Surface brightness

The Suzaku surface brightness profiles determined from the spectral analyses of both observations are shown in Fig. 6.4 (left). Where the two pointings overlap in the center, we see a good agreement between the surface brightness profiles. The NE direction shows a significantly higher surface brightness towards larger radii than the SW profile. The high-resolution XMM-Newton surface brightness profiles shown in Fig. 6.4 (right) are obtained from an imaging analysis (F. Pacaud, priv. comm.) for the Suzaku FOV using the same central coordinates and can thus be directly compared to our findings. Qualitatively, the shapes overall agree with our profiles, showing a higher surface brightness in NE direction. Also, the XMM-Newton surface brightness profiles exhibit a "shoulder" between roughly $4'$ and $5'$, especially in the SW direction.

Already from the surface brightness contours obtained by Feretti et al. (2001) and Bourdin et al. (2011) from ROSAT and Chandra data (shown in Fig. 6.1), respectively, a concentration of the contour lines in SW direction around $3'$ can be seen, which hints at feature (possibly a shock) in this region. We see no clear corresponding feature in the Suzaku profiles, however, XMM-Newton is able to resolve a clear steepening of the profile in the SW direction around $3'$.

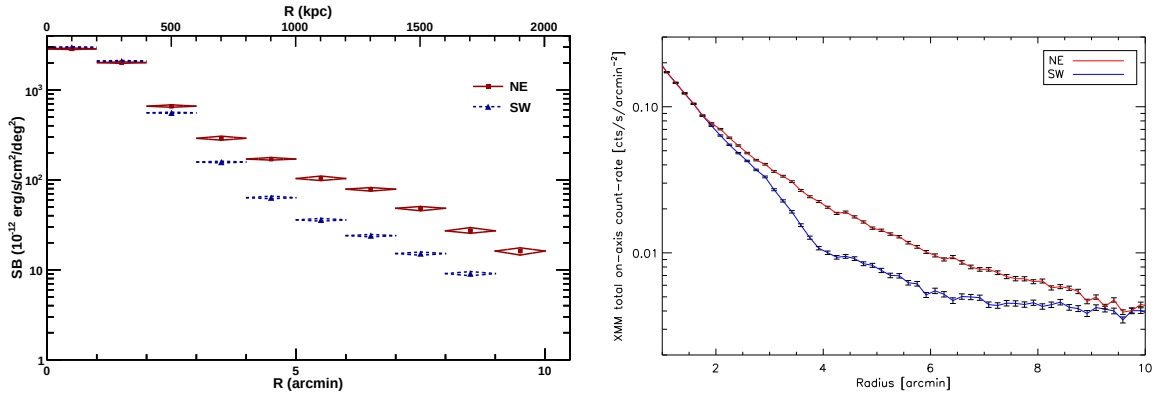

Figure 6.4: *Left:* Suzaku surface brightness profiles of A2163 in NE (solid red) and SW (dashed blue) direction in the $0.5 - 2.0$ keV band. *Right:* XMM-Newton surface brightness profiles measured in the Suzaku FOVs in the same directions (F. Pacaud, priv. comm.) in the $0.4 - 1.25$ keV range (this range is chosen to prevent poor calibration and instrumental lines). Colors have the same meaning as in the left figure. The results show a higher surface brightness in the NE direction and a "shoulder" around $4' - 6'$. The XMM-Newton profile in SW direction steepens around $3'$.

6.5.2 Temperature and metal abundance

The temperature profiles in the NE and SW direction are shown in Fig. 6.5 and the values are given in Tab. 6.3 and 6.4, respectively. The temperature profiles agree in the center as expected while the NE direction shows a higher temperature at large radii than the SW direction, which is qualitatively in agreement with the temperature map shown in Fig. 6.1. The uncertainties in the NE direction are larger due to the lower exposure time. Notably, both profiles show a clear jump in the temperature around $\sim 6'$. In the SW direction, there is an additional slight indication of a temperature drop around $3'$ which approximately coincides with the steepening in the surface brightness profile and the concentration of the X-ray contour lines. The deprojection method as

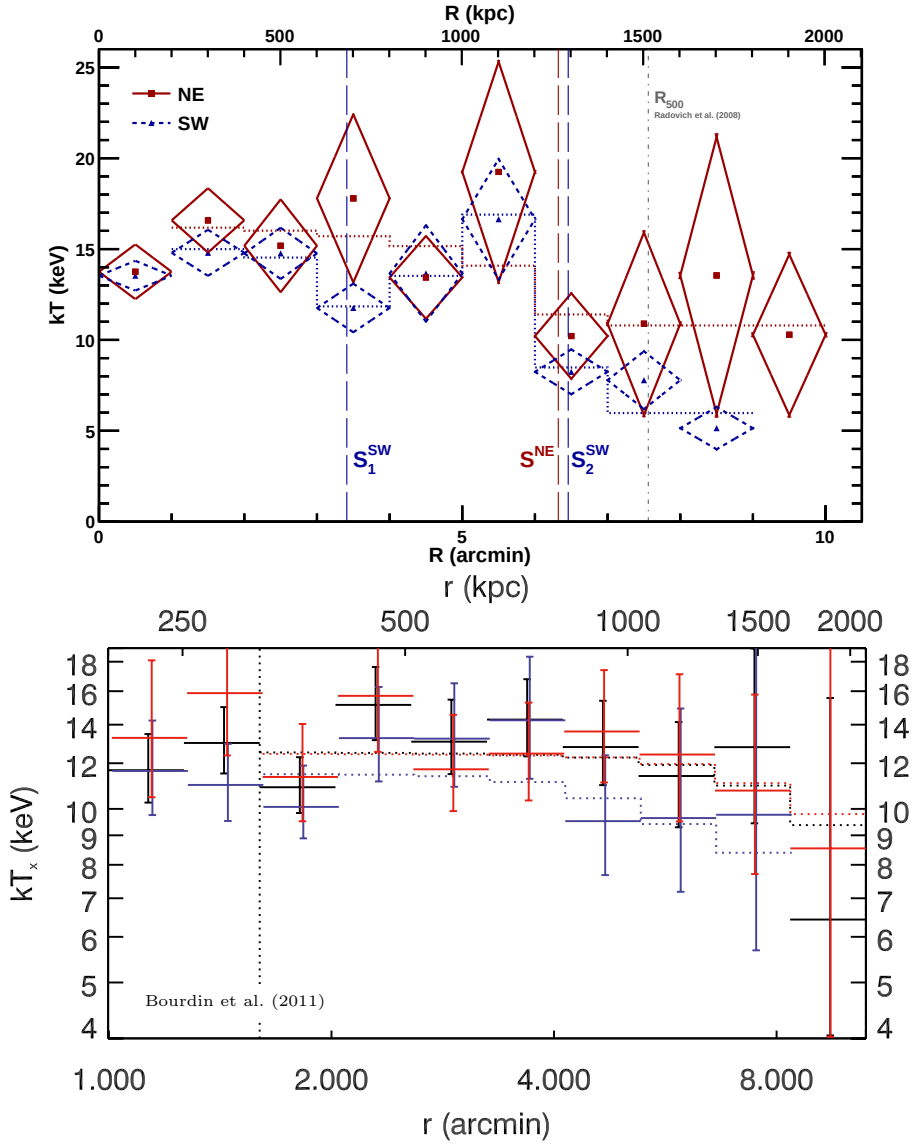

Figure 6.5: *Top:* Temperature profiles of A2163 obtained from our Suzaku analysis in NE (red) and SW (blue) direction. The vertical dashed lines show the jump positions as obtained from our deprojection procedure which described later in this chapter in Sec. 6.6. The gray vertical dot-dashed line corresponds to R_{500} obtained by Radovich et al. (2008) from a weak-lensing analysis. The dotted lines correspond to the projected best-fit temperature models (see Sec. 6.6.1 for details). *Bottom:* The figure is taken from Bourdin et al. (2011) and shows the XMM-Newton temperature profiles in the eastern (red) and western (blue) half of the cluster. Black data points are the temperature extracted in the full annulus. Bourdin et al. (2011) detect a temperature and density jump in their high resolution Chandra data which they overplot as a dotted line in the XMM-Newton profile. *Note that the center of their radial analysis is shifted compared to the center used in this study.* Around 4′ the southern profile shows a drop which roughly coincides with the jump position around 3′ in the Suzaku profile considering the central shift.

well as the quantification of the jump positions and the corresponding shock properties are in detail discussed in Sec. 6.6.

Fig. 6.5 also shows the temperature profiles obtained by Bourdin et al. (2011) with XMM-Newton for the eastern and wester half of the cluster. Their profile towards the western half also shows a jump at $\sim 4'$ which is consistent with our findings around $3'$, considering that the center of their radial analysis is slightly offset from the center used here. The overall high temperature of $12 - 16\,\mathrm{keV}$ is also similar to our and previous findings. Additionally, their profile shows a hint of another temperature drop (albeit with huge uncertainties) in the outermost annulus which roughly agrees with the position of the temperature drop at $6'$ in our measured profiles.

The abundance profiles in both directions are shown in Fig. 6.6. In the central regions, the profiles agree while in SW direction the abundance further decreases and is clearly lower after the first (at $\sim 3'$) and before the second (at $\sim 6'$) temperature jump. Also in the NE direction, we observe a somewhat unusual profile with an increase before the position of the temperature jump followed by a drop after the jump. However, a clear interpretation is difficult because of possible multi-temperature structure that might bias the abundance measurements and because of the coarse spatial resolution. In the future, we plan to improve this by performing an additional spectral analysis of archival XMM-Newton data.

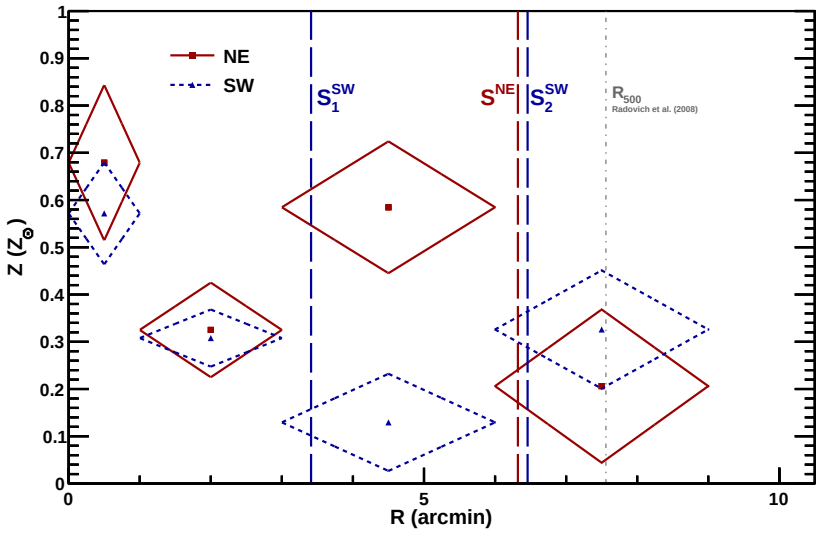

Figure 6.6: Elemental abundance profile of A2163 in NE (solid red) and SW (dashed blue) direction. Vertical lines have the same meaning as in the top panel of Fig. 6.5.

6.6 Study of the shock properties

6.6.1 Deprojection

The estimation of the shock properties, in particular the Mach number, is based on the jumps in the density and temperature profiles at the position of the shock fronts. For this reason, a deprojection is performed in a similar way as described in Sec. 4.4.6 using the emission measure (which itself is directly related to the density and spectral normalization) in each annulus given by Eq. 2.11 and the emission weighted projected temperature given by Eq. 4.2. The models for

the electron density $n_\mathrm{e}(R)$ and the temperature $T(R)$ should include the discontinuities at the shock position. Thus, we choose piecewise functions with the position of the shock being a free parameter as e.g. done in Bourdin et al. (2013). The observations in NE and SW direction are analyzed separately and, due to the differences in both directions, different models are chosen.

The projected temperature profile in the NE direction (Fig. 6.5) suggests a step-function of the following simple form

$$T^\mathrm{NE}(R) = \begin{cases} T_0^\mathrm{NE}, & R \leq R_\mathrm{j} \\ T_1^\mathrm{NE}, & R > R_\mathrm{j} \end{cases} , \tag{6.1}$$

where R_j is the position of the jump. The density profile in this direction is assumed to follow a piecewise power law of the form

$$n_\mathrm{e}^\mathrm{NE}(R) = \begin{cases} n_0^\mathrm{NE} R^{-\alpha}, & R \leq R_\mathrm{j} \\ n_1^\mathrm{NE} R^{-\beta}, & R > R_\mathrm{j} \end{cases} . \tag{6.2}$$

This simplified density model is not able to reproduce the central part of the cluster for which usually a beta-model is needed, which flattens towards the center. Thus, we exclude the central bin in the deprojection.

The above models are used in Eq. 2.11 and 4.2 for the deprojection. The latter is performed as a χ^2 minimization in which the model parameters for the temperature and density models and the jump position are estimated simultaneously to match the measured quantities. The correlations between all density and temperature values (which arises e.g. due to the PSF correction) are taken into account using the covariance matrix obtained in the spectral fit.

The temperature profile in SW direction shows a way more complicated structure. We test the same temperature and density models as for the NE direction but find a very bad description of our measured quantities. However, already these simple single-jump models indicate that a shock position around $\sim 3'$ is preferred instead of the clearly visible jump in the temperature profile at around $6'$. For this reason, we choose a model including two jump positions whereas in the temperature profile the first and second position are smoothly connected via a Sigmoid function. The final temperature model is then given by

$$T^\mathrm{SW}(R) = \begin{cases} T_0^\mathrm{SW}, & R \leq R_\mathrm{j,1} \\ S(R), & R_\mathrm{j,1} < R \leq R_\mathrm{j,2} \\ T_2^\mathrm{SW}, & R > R_\mathrm{j,2} \end{cases} , \tag{6.3}$$

with the Sigmoid function

$$S(R) = \frac{(T_{1,b} - T_{1,a})}{1 + \exp\left(-m[R - 0.5(R_\mathrm{j,2} - R_\mathrm{j,1})]\right)} + T_{1,a}, \tag{6.4}$$

which models the smooth transition between the two temperatures $T_{1,a} < T_{1,b}$ with slope m as illustrated in Fig. 6.7. The turning point is chosen to lie at half distance between the two jumps. We also tested other simple models for the temperature as e.g. a three-constant model and a linear transition between the temperatures instead of a Sigmoid function but found that the above description provides the best fit to our measured values considering the reduced χ^2.

The density is, correspondingly, described by

$$n_{\mathrm{e}}^{\mathrm{SW}}(R) = \begin{cases} n_0^{\mathrm{SW}} R^{-\alpha}, & R \leq R_{\mathrm{j},1} \\ n_1^{\mathrm{SW}} R^{-\beta}, & R_{\mathrm{j},1} < R \leq R_{\mathrm{j},2} \\ n_2^{\mathrm{SW}} R^{-\gamma}, & R > R_{\mathrm{j},2} \end{cases} . \tag{6.5}$$

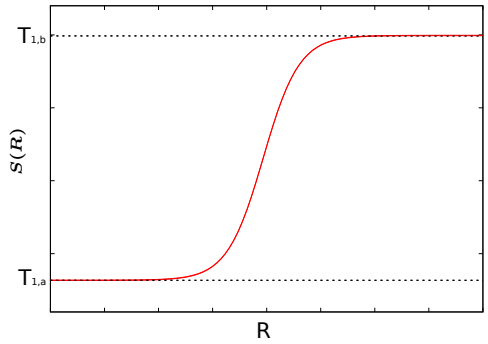

Figure 6.7: The Sigmoid function as a function of radius, used to describe the smooth transition between the temperatures $T_{1,a} < T_{1,b}$ in Eq. 6.4.

For both directions, the deprojected density and temperature profiles around the jump positions are shown in Fig. 6.8. The values of the model parameters are located in Tab. 6.5. The projected quantities reproduced from the best-fit models compared to the measured values are shown in Fig. 6.5 and 6.9 for temperature and emission measure, respectively. Note that the underestimation (overestimation) in the outer bins of the NE (SW) emission measure profile are due to significant positive correlation of the corresponding spectral normalizations. However, we find that our method is generally able to well reproduce the measured profiles. The reduced χ^2 values in NE and SW directions are $\chi^2/\mathrm{d.o.f.} = 0.3$ ($\chi^2 = 2.8$) and $\chi^2/\mathrm{d.o.f.} = 0.8$ ($\chi^2 = 2.5$), respectively. The value in the NE direction is rather low and is affected by the large uncertainties of the spectral fit, which mainly arise due to the PSF correction that introduces significant correlations and increases the uncertainties, especially in the outer lower statistics bins, by almost a factor of two compared to the PSF-uncorrected fit. Additionally, the exposure time is much lower than in SW direction. This also has consequences for the deprojection models in the NE direction which, despite their rather simple form, might still appear too complex for the fit considering the quality of the data. As mentioned previously, we aim for an improvement, also regarding this issue, by adding spectral data of archival XMM-Newton observations which will add additional constraining power.

6.6.2 Mach number

Using the Rankine-Hugoniot jump conditions (cf. Eq. 2.18), the Mach numbers of the shocks in NE and SW direction are estimated from the deprojected density and temperature profiles independently. We find the values given in Tab. 6.2. The uncertainties are estimated from 1000 MC realizations of the measured EM and temperature profiles, taking correlations into account and repeating the deprojection. We reject realizations with unphysical behavior (e.g. negative temperatures) and estimate the 68% confidence interval with respect to the median. We note that the median in some cases is slightly different from the nominal best-fit value, however, we assume the uncertainties to be the same. Using Eq. 2.21 for the speed of sound, we estimate

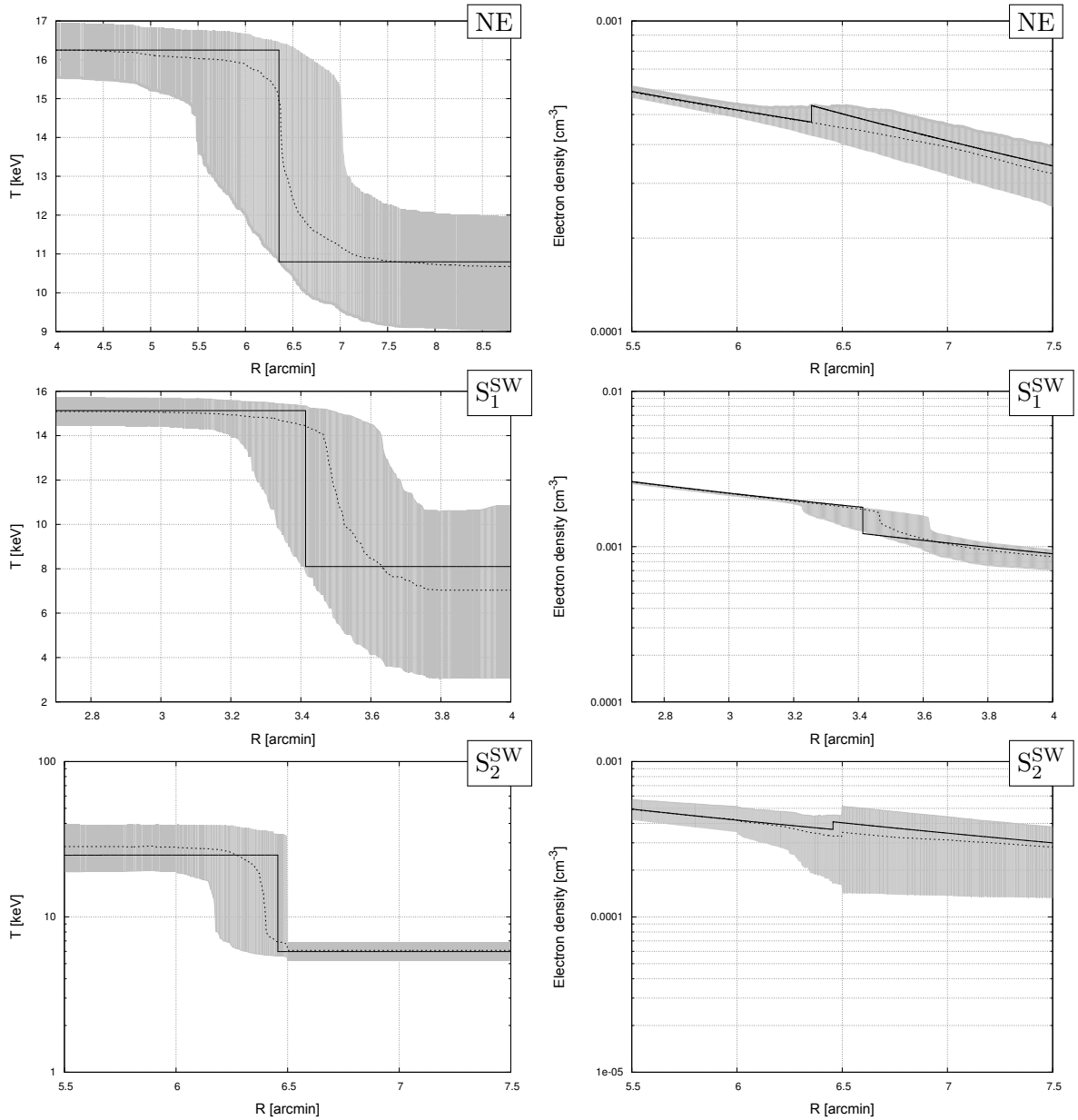

Figure 6.8: Density and temperature jumps in NE and SW direction of the best-fit deprojected models (solid lines). Only the relevant regions around the jump positions are shown. For the values and inferred Mach numbers see Tab. 6.2. The shaded region shows the 68% confidence intervals estimated from 1000 MC realizations. The dashed lines show the median of all realizations. The density jumps in the outer shocks in both directions (top right and bottom right panel) are consistent with one. Note that in case of the first SW density jump, the best-fit model slightly exceeds the 68% interval at the jump position because of the discontinuity which is smeared out in the MC realizations.

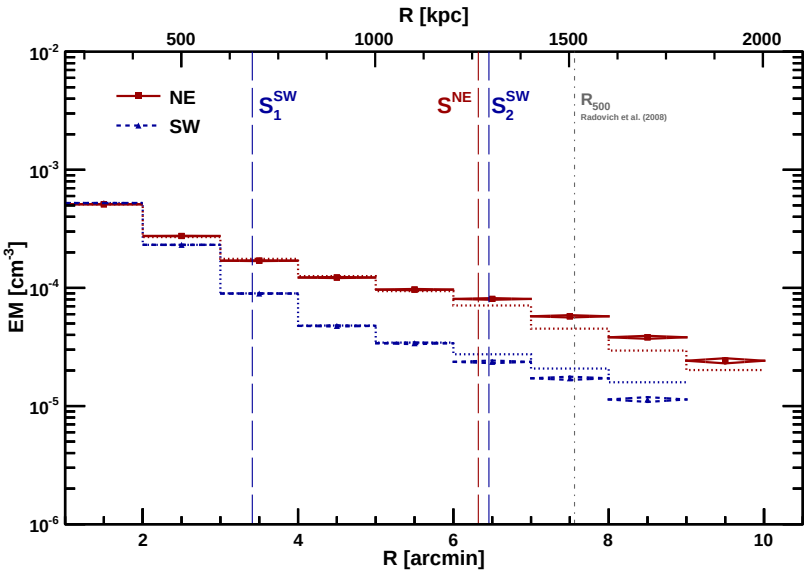

Figure 6.9: Emission measure profile of A2163 obtained from the spectral fit to the Suzaku data for the NE (solid red) and SW (dashed blue) direction. Dashed and dotted lines have the same meaning as in the top panel of Fig. 6.5. The innermost annulus is not shown as it is not considered in the deprojection procedure (see text). The profiles reproduced from the deprojection models (dotted lines) underestimate (overestimate) the EM in the outer parts of the NE (SW) direction due to strong positive correlations in the spectral fit.

Table 6.2: Properties of the shock in NE and the two shocks in SW direction of A2163. A is the jump amplitude, i.e. the ratio of the density/temperature in front of and behind the jump, M is the Mach number and v the shock velocity. Where the jump amplitude is smaller than one, no Mach number and velocity estimates are given.

		Density estimates			Temperature estimates		
	R_j [arcmin]	A	M	v [10^3 km/s]	A	M	v [10^3 km/s]
S_1^{SW}	$3.4^{+0.2}_{-0.2}$	$1.5^{+0.5}_{-0.2}$	$1.3^{+0.3}_{-0.1}$	$1.2^{+0.3}_{-0.1}$	$1.9^{+2.9}_{-0.7}$	$1.8^{+1.7}_{-0.7}$	$1.7^{+1.5}_{-0.6}$
S_2^{SW}	$6.5^{+0.1}_{-0.2}$	$0.9^{+1.8}_{-0.4}$	–	–	$4.2^{+1.8}_{-1.4}$	$3.3^{+0.8}_{-0.7}$	$4.1^{+1.0}_{-0.9}$
S^{NE}	$6.4^{+0.6}_{-1.2}$	$0.9^{+0.4}_{-0.2}$	–	–	$1.5^{+0.3}_{-0.1}$	$1.5^{+0.2}_{-0.1}$	$1.2^{+0.2}_{-0.1}$

the shock velocities v which are also given in Tab. 6.2.

To verify our results, we perform several tests. First, we verified that the regularization procedure described in Sec. 6.4.2 is not affecting the density by performing a fit without regularization, which yields only marginal differences in the density estimates.

As a further test, we repeat the deprojection and estimation of the shock properties without applying the PSF correction and the thereby introduced regularization of the temperature profile. For the shock in NE direction, this results in a slightly higher density jump amplitude of $1.2^{+1.8}_{-0.5}$ (corresponding to $M = 1.1^{+1.9}_{-0.3}$) but is still consistent with one and the nominal value. However, the temperature jump is even less affected with $A = 1.5 \pm 0.2$ and $M = 1.5 \pm 0.2$ which agrees well with the nominal values.

When performing the same test in the SW direction, the properties of the first shock yield Mach numbers of $M = 1.3^{+0.3}_{-0.2}$ and $M = 1.6^{+0.8}_{-0.4}$ for the density and temperature jumps,

respectively, which are well consistent within the uncertainties and also with the nominal values. At the position of the second jump, only a small change in the density estimate is observed ($A = 1.0^{+4.1}_{-0.7}$), however, the upper uncertainty significantly increases and exceeds the validity range of Eq. 2.18 for a monoatomic ideal gas. The temperature jump is slightly lower compared to the nominal value with a Mach number of $2.6^{+0.8}_{-0.5}$ but is still consistent with the nominal result within the uncertainties.

As a last test, we investigate whether our choice of the fitting energy range influences the results. In the previous analysis, the energy range in the outermost annuli was reduced compared to the inner bins (i.e. $0.7 - 7\,\mathrm{keV}$ and to $0.7 - 10\,\mathrm{keV}$, respectively) to achieve a sufficient signal-to-background ratio,. Therefore, we repeat the spectral analysis in both directions using the same energy range for all annuli from $0.7 - 10\,\mathrm{keV}$. However, we find a very good agreement with the nominal results and thus conclude that the influence of the energy range is negligible.

6.7 Discussion

We find that the shocks located at about $6.4'$ ($6.5'$) in NE (SW) directions exhibit clear temperature discontinuities while no significant density jumps are detected. The latter finding might be somewhat related to the shoulders seen in the XMM-Newton surface brightness profiles, however, a connection is not completely obvious from the profiles. Furthermore, from Fig. 6.8 and Tab. 6.2, it is clear that the large uncertainties at these shock positions also allow a larger density jump amplitude. The shock at $6.5'$ in SW direction is stronger with a temperature jump amplitude of $4.2^{+1.8}_{-1.4}$ compared to $1.5^{+0.3}_{-0.1}$ in NE direction. This SW temperature jump is one of the largest observed in galaxy clusters and the resulting Mach number of $M = 3.3^{+0.8}_{-0.7}$ is comparable to the value for the prominent shock in the Bullet cluster. The shock velocity is high with $4.1^{+1.0}_{-0.9} \times 10^3\,\mathrm{km/s}$. The NE temperature jump at $6.4'$ is weaker with $M = 1.5^{+0.2}_{-0.1}$ and $v = (1.2^{+0.2}_{-0.1}) \times 10^3\,\mathrm{km/s}$ and thus compatible with typical merging shocks detected in X-ray observations (cf. Markevitch & Vikhlinin, 2007).

As mentioned before, the SW direction exhibits a second shock at $3.4 \pm 0.2\,\mathrm{arcmin}$. An indication for this is already visible in the steepening of the XMM-Newton surface brightness profile. This shock front is likely related to the moving cool core bullet detected by Bourdin et al. (2011). We find consistent Mach numbers for this shock estimated from the density and temperature jumps ($M = 1.3^{+0.3}_{-0.1}$ and $M = 1.8^{+1.7}_{-0.7}$, respectively) and also here the values are comparable to typical X-ray merging shocks. Note that the cold front detected by Bourdin et al. (2011) using high-resolution Chandra data can not be resolved with Suzaku.

In Fig. 6.1 we show our estimated jump positions overlaid on the radio and X-ray contours obtained by Feretti et al. (2001) as well as the temperature map from Bourdin et al. (2011). The comparison shows that the shock in NE direction lies close to the radio relic which suggests a correlation between the two, likely due to relativistic electrons accelerated in the shock. Also the outer shock in SW direction closely matches the radio contours which is another indication that the radio emission of A2163 is correlated to the X-ray features in the ICM. A correlation was also observed previously by Feretti et al. (2001) but, so far, not associated with a shock front. The inner shock in SW direction lies close to the region where the measurements from Feretti et al. (2001) and Bourdin et al. (2011) show denser X-ray surface brightness contour lines and where the cool core bullet is located (cf. Fig. 6.1). The fact that they do not exactly match could be a result of the finite radial bin size in our Suzaku analysis and slight positional uncertainties due to imperfect calibration of the instruments.

Our findings support the scenario formulated by Maurogordato et al. (2008) and Bourdin et al.

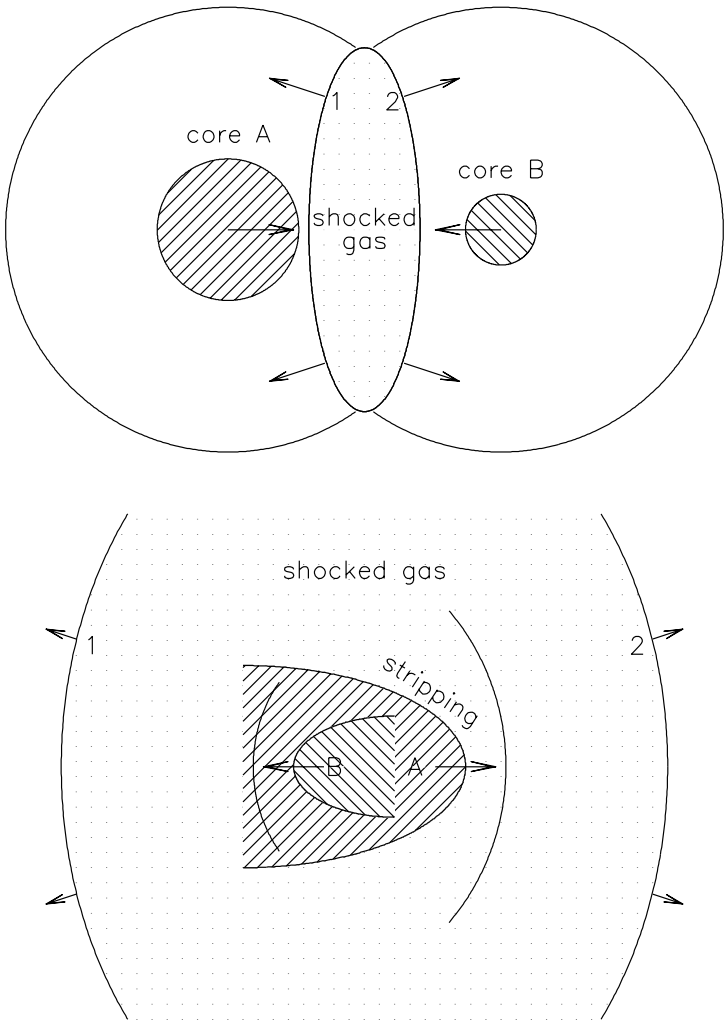

Figure 6.10: Scheme of the shock geometry for the cluster A521, which could also match the situation in A2163. At an early stage of the merger (upper panel), the two substructures develop shock fronts 1 & 2. In the lower panel, a later stage is shown where the cores already merged and the shock waves 1 & 2 propagated farther outwards. Additionally, further shocks can develop in front on the merging cores. Credit: Markevitch & Vikhlinin (2007).

(2011) that A2163 underwent a recent merger in the E-W or NE-SW direction which produced distinct shock fronts. Markevitch & Vikhlinin (2007) describe a merging situation, depicted in Fig. 6.10, for the cluster A521 which is also a conceivable scenario for A2163. The two merging constituents approach each other and develop a shock front at an early stage of the interaction. This shock travels outwards in all directions and, in an ideal case with equal constituents, the shock velocity is the same in all directions. However, A2163 shows a complex merging situation with several substructures beside the moving cool core (cf. Fig. 6.1). The different Mach numbers of the shocks around $6.4'$ and $6.5'$ in NE and SW direction, respectively, suggest that this collision was not symmetric with possibly unequal merging constituents, resulting in different shock velocities. The fact that the shock fronts appear at equal distances to the X-ray emission peak (despite the different velocities) might be due to the fact that the X-ray emission peak does not necessarily coincide with the origin of the initial shock wave. The peak can shift in the merging and gas interaction of the cores. Also, Suzaku's spatial resolution gives rise some uncertainty in the shock positions. In addition to the first shock, further shocks can develop ahead of the merging cores as also depicted in Fig. 6.10. This matches our findings of a second shock in SW direction at $3.4'$ that might be related to the cool core bullet.

6.8 Summary & outlook

We analyzed two Suzaku observations of the merging cluster A2163 in the NE and SW direction. We find shocks at $6.4'$ (NE) and $6.5'$ (SW), with Mach numbers $M = 1.5^{+0.3}_{-0.1}$ and $M = 3.3^{+0.8}_{-0.7}$, respectively, estimated from the temperature jumps. The values and thus the shock velocities significantly differ in both directions suggesting a merging with unequal constituents and/or deviations from a ideal head-on collision. The shock in SW direction is one of the strongest observed in X-rays, comparable to the shock in famous Bullet cluster. Ahead of the moving cool core in SW direction, we detect a second shock around $3.4'$ with a Mach number of $M = 1.8^{+1.7}_{-0.7}$ estimated from the temperature jump amplitude or, consistently, $M = 1.3^{+0.3}_{-0.1}$ from the density estimates. These values are consistent with typical findings for merging shocks detected in X-rays. Our results also show a close correlation to the radio contours obtained by Feretti et al. (2001); in NE direction the shock is located close to a radio relic.

In the future we aim for the analysis of additional spectral data from archival XMM-Newton observations of A2163. We will obtain the temperature profile with a higher spatial resolution than possible with Suzaku and compare it to our findings. Although XMM-Newton might approach its instrumental limits around the position of the outer shocks, we should be able to clearly identify the inner shock front in SW direction and expect an improved measurement of the Mach number. The better resolution of XMM-Newton will also allow us to use advanced models for the deprojection of the temperature and density (as e.g. a (double) beta-model for the latter) and to study their impacts on the jump amplitudes and Mach numbers. In addition, we will study the metal distribution in more detail.

6.9 Appendix

Table 6.3: Fit results in the NE direction.

Annulus [arcmin]	T [keV]	Z [$Z_\odot$]	norm[1]
$0-1$	13.75 ± 1.51	0.68 ± 0.16	65.36 ± 0.61
$1-2$	16.58 ± 1.77	0.33 ± 0.10	146.90 ± 0.73
$2-3$	15.18 ± 2.55		79.12 ± 0.40
$3-4$	17.79 ± 4.63	0.58 ± 0.14	48.88 ± 0.40
$4-5$	13.44 ± 2.28		35.22 ± 0.39
$5-6$	19.24 ± 6.06		27.82 ± 0.37
$6-7$	10.21 ± 2.35	0.21 ± 0.16	23.20 ± 0.38
$7-8$	10.89 ± 5.02		16.54 ± 0.38
$8-9$	13.55 ± 7.61		10.99 ± 0.32
$9-10$	10.28 ± 4.42		6.96 ± 0.35

[1] normalization in the full annulus norm $= \frac{10^{-18}}{4\pi[D_A(1+z)]^2} \int n_e n_H dV \, cm^{-5}$ with D_A being the angular diameter distance to the source.

Table 6.4: Fit results in the SW direction.

Annulus [arcmin]	T [keV]	Z [$Z_\odot$]	norm[1]
$0-1$	13.54 ± 0.82	0.57 ± 0.11	68.60 ± 0.29
$1-2$	14.79 ± 1.27	0.31 ± 0.06	150.43 ± 0.42
$2-3$	14.76 ± 1.41		66.57 ± 0.25
$3-4$	11.76 ± 1.34	0.13 ± 0.10	25.77 ± 0.20
$4-5$	13.66 ± 2.65		13.71 ± 0.17
$5-6$	16.64 ± 3.31		9.79 ± 0.17
$6-7$	8.24 ± 1.23	0.33 ± 0.13	6.81 ± 0.17
$7-8$	7.78 ± 1.59		4.94 ± 0.15
$8-9$	5.14 ± 1.16		3.27 ± 0.15

[1] normalization in the full annulus norm $= \frac{10^{-18}}{4\pi[D_A(1+z)]^2} \int n_e n_H dV \, cm^{-5}$ with D_A being the angular diameter distance to the source.

Table 6.5: Best-fit model parameters from the deprojection in NE (left) and SW (right) direction. See Eq. 6.1 to 6.5. Note that the deprojection is rather insensitive to the slope m of the Sigmoid-function in SW direction, i.e. the uncertainties also allow a step-wise function which is the limit of arbitrarily large slope. However, this does not affect the estimation of the shock properties.

NE	
$R_{\rm j}$ [arcmin]	$6.35^{+0.63}_{-1.18}$
$n_0^{\rm NE}$ [10^{-2} cm^{-3}]	$0.87^{+0.02}_{-0.02}$
$n_1^{\rm NE}$ [10^{-2} cm^{-3}]	$7.81^{+17.96}_{-4.35}$
α	$1.58^{+0.03}_{-0.03}$
β	$2.70^{+0.75}_{-1.09}$
$T_0^{\rm NE}$ [keV]	$16.25^{+0.73}_{-0.67}$
$T_1^{\rm NE}$ [keV]	$10.80^{+1.26}_{-1.58}$

SW	
$R_{\rm j,1}$ [arcmin]	$3.41^{+0.15}_{-0.24}$
$R_{\rm j,2}$ [arcmin]	$6.46^{+0.10}_{-0.22}$
$n_0^{\rm SW}$ [10^{-2} cm^{-3}]	$1.31^{+0.02}_{-0.02}$
$n_1^{\rm SW}$ [10^{-2} cm^{-3}]	$1.22^{+0.69}_{-0.87}$
$n_2^{\rm SW}$ [10^{-2} cm^{-3}]	$1.98^{+1.55}_{-0.81}$
α	$1.62^{+0.03}_{-0.03}$
β	$1.88^{+0.30}_{-0.82}$
γ	$2.08^{+0.36}_{-1.24}$
$T_0^{\rm SW}$ [keV]	$15.13^{+0.66}_{-0.65}$
$T_{\rm 1,a}$ [keV]	$8.10^{+3.17}_{-4.03}$
$T_{\rm 1,b}$ [keV]	$24.99^{+10.67}_{-8.08}$
m	$10.08^{+366.67}_{-34.01}$
$T_2^{\rm SW}$ [keV]	$5.98^{+0.78}_{-0.85}$

CHAPTER 7

Conclusions and outlook

In this work, we studied the X-ray properties of the hot intracluster medium in galaxy clusters and groups, which is their largest baryonic component. In particular, we focused on three interesting individual objects which are different in many respects and therefore cover a variety of topics in galaxy clusters analyses. All projects presented here incorporate aspects which have not been studied intensively before, i.e. the properties of the low surface brightness outskirts of a galaxy group, the study of a rare and distant galaxy cluster at $z = 0.902$ which shows evidence for a cool core and a very high X-ray luminosity, and shock fronts in a merging cluster identified in X-rays through prominent jumps in the radial profiles. The main results of these projects and future prospects are summarized in the following sections.

7.1 X-ray study of UGC 03957

The outskirts of galaxy clusters have been studied in detail in the past years while the outskirts of groups remain widely unexplored. These regions potentially contain valuable information on structure formation effects which imprint on the ICM, such as the breakdown of equilibrium states or clumping and accretion of material. Also, the expected self-similar behavior between clusters and groups up to large radii is a topic of ongoing research and might be violated as found in previous studies.

In the past decade, the Suzaku satellite provided the opportunity to investigate the ICM properties in the outskirts due to its low and stable instrumental background. In this project, we studied the outskirts of a galaxy group out to $1.4R_{200}$ investigating temperature, heavy element abundance, density, entropy and gas mass fraction profiles with very good azimuthal coverage. In contrast to previous results for clusters, we find an entropy profile consistent with the predictions from numerical structure formation simulations after correcting for the gas mass fraction. The latter stays below the cosmic mean value up to large radii. The reason for the entropy modification might be redistribution of gas e.g. due to AGN activity that ranges out to larger radii in groups than in clusters because of the shallower potential well. Also pre-heating of the gas might play a role. However, the overall temperature profile shows a similar behavior compared to galaxy clusters with a temperature drop of a factor of three from the center to the outskirts. From individual abundances of α-elements, we constrained the relative number of core-collapse supernovae that exploded in the past and enriched the ICM. We find a fraction of $N_{\mathrm{SNCC}}/(N_{\mathrm{SNCC}} + N_{\mathrm{SNIa}}) \approx 80 - 100\%$, which is consistent with previous results for groups. The average metal abundance profile points to galactic winds as the primary enrichment process.

7.2 XMM-Newton analysis of Cl J120958.9+495352

In the paradigm of hierarchical structure formation, massive relaxed clusters should be extremely rare at high redshifts. The gas mass fraction of these objects is an important cosmological probe as it, on the one hand, traces the baryon fraction in the universe $\Omega_{\rm baryon}/\Omega_{\rm m}$ and is expected to be constant with time and, on the other hand, it is related to the assumed cluster distance. Whether a cluster is relaxed can be investigated in X-ray observations of the ICM. The presence of a cool core in the cluster center is found to be correlated to the dynamical status. Cool core clusters are characterized by their cooling time and this time span is short for distant clusters which is why only a handful high-z cool cores have been found so far. The cluster Cl J120958.9+495352 has been found by Buddendiek et al. (2015) and was studied in detail in this work with the XMM-Newton satellite. We find strong indications for a cool core such as a short cooling time and a drop of the temperature profile. Using weak lensing data for the total mass, we inferred the gas mas fraction to be $f_{\rm gas,2500} = 0.11^{+0.06}_{-0.03}$ which is consistent with previous findings for local and distant clusters and the standard ΛCDM cosmology.

For a comparison in the future, we aim to estimate cooling times for e.g. the HIFLUGCS cluster sample within the same radius as done for Cl J120958.9+495352 . By this we will assess whether Cl J120958.9+495352 can be classified as a strong cool core. In addition, we aim for higher spatial resolution data using the Chandra satellite. Chandra's point spread function is about $0.5''$ (FWHM) and thus would allow us to well resolve the core of Cl J120958.9+495352 and estimate a detailed temperature profile in this region to confirm the cool core. Chandra observations would also allow us to infer the cooling time within a small radius around the center and compare it to the results of Hudson et al. (2010).

7.3 Shock fronts in Abell 2163

Galaxy clusters form and grow in merging events. The interaction between the gas of the merging constituents can be seen in X-rays. A significant fraction of the energy in such events is going into shocks and heating of the ICM. Shocks are identified through discontinuities in the density, temperature and surface brightness profiles of clusters but only relatively few have been studied in detail. In the last project of this thesis, we analyzed the gas properties of the irregular cluster A2163 using two Suzaku observations in two azimuthal directions. Previous studies of A2163 suggest that it underwent a recent merger and it also shows a prominent radio halo. We find significant differences in the two azimuthal directions concerning e.g. the surface brightness. The temperature profiles in both directions exhibit a jump at $R \sim 1.3\,$Mpc which is a region where the surface brightness already significantly dropped and that can be well studied with Suzaku. The jump in the north-east direction yields a Mach number of $M = 1.5^{+0.3}_{-0.2}$ which is similar to typical values for shocks detected in X-rays. In the south-west direction we find indications for two shock fronts, one ahead of a moving cool core at $R{\sim}700\,$kpc with $M = 1.8^{+1.7}_{-0.7}$ and another one at $\sim$1.3 Mpc. The latter shock seems to be very strong with a Mach number of $M = 3.3^{+0.8}_{-0.7}$ and a high shock velocity of $v = 4.1^{+1.0}_{-0.9} \times 10^3\,$km/s, comparable to the famous Bullet cluster. Furthermore, we find correlations with radio emission that was studied by Feretti et al. (2001). The NE shock lies close to a radio relic and also the outer shock in SW direction closely matches the radio contours, which hints to a connection between the X-ray and radio features.

In the future, we aim for an estimation of the temperature and density profile using archival XMM-Newton data which will allow us to perform a detailed study of the properties of the inner

shock in south-west direction (ahead of the cool core) because of XMM-Newton's better spatial resolution. In addition, we will test whether the instrumental limitations of XMM-Newton (in particular the instrumental background) might still allow us to reach even larger radii and confirm the outer temperature jumps in NE and SW direction. The XMM-Newton data will also give additional constraining power to perform the deprojection, such that we can compare our Suzaku findings to the XMM-Newton results using more advanced temperature and density models. In addition, we might also consider adding Planck data to further investigate the gas properties.

7.4 Final remarks

The projects of this work showed the significance of detailed X-ray analyses of galaxy clusters and groups for both, as laboratories improving the understanding of astrophysical phenomena in the ICM and for cosmology. The ongoing research in this field will benefit from several future X-ray missions as for instance the upcoming eROSITA telescope, which is scheduled for launch in spring 2018. It will detect a large sample of about 100,000 galaxy clusters (Pillepich et al., 2012). Using this large sample, the scientific goal of eROSITA in the upcoming years is to well constrain dark energy and the cosmic evolution. It will perform several all sky surveys followed by 3.5 years of pointed observations of e.g. individual galaxy clusters as analyzed in this thesis.

Another instrument of interest to study low surface brightness regions, especially as a successor to the completed Suzaku mission, is the Hitomi satellite. As Suzaku, Hitomi was planned to be in an low earth orbit and early observations after the launch in February 2016 showed a superior spectral resolution (Hitomi Collaboration et al., 2016). Unfortunately, Hitomi was lost about one month later but already the early results showed the promising capability of the instruments. Lately, there have been prospects of a replacement by a second satellite of similar building technique to be launched in 2020[1].

The long term future will be driven by the Athena mission which is part of the ESA's Cosmic Vision program. The launch is planned for the year 2028. Athena will address the formation and evolution of the large-scale structure using wide-field imaging and high-resolution spectroscopy. It will also push the observations and understanding of the WHIM in the filaments and between clusters as well as high energy astrophysical phenomena including, e.g. black holes and the merging of clusters (e.g. Nandra et al., 2013, Pointecouteau et al., 2013, Ettori et al., 2013, Dovciak et al., 2013, Aird et al., 2013).

[1] http://www.astronomy.com/news/2016/07/jaxa-may-remake-its-x-ray-observatory-hitomi-for-a-2020-launch

APPENDIX A

Cosmological parameters

Parameter	Description	Value
$\Omega_b h^2$	Baryon density	0.02230 ± 0.00014
$\Omega_c h^2$	Dark matter density	0.1188 ± 0.0010
$100\theta_{\mathrm{MC}}$	Sound horizon at last scattering	1.04093 ± 0.00030
τ	Reionization optical depth	0.066 ± 0.012
$\ln 100As$	Primoridal amplitude	3.064 ± 0.023
n_s	Scalar spectral index	0.9667 ± 0.0040
H_0	Hubble constant*	67.74 ± 0.46
Ω_m	Matter density	0.3089 ± 0.0062
Ω_Λ	Dark energy density	0.6911 ± 0.0062
σ_8	Fluctuation amplitude at $8h^{-1}$ Mpc	0.8159 ± 0.0086
z_{eq}	Redshift of matter-radiation equality	3371 ± 23
z_{re}	Redshift of Reionization	$8.8^{+1.2}_{-1.1}$

* in units of km/s/Mpc

Table A.1: Cosmological parameters with 68% confidence limits as determined from Planck Collaboration et al. (2016).

List of Figures

List of Tables

Bibliography

Aaboud, M., Aad, G., Abbott, B., et al., *Search for new phenomena in final states with an energetic jet and large missing transverse momentum in pp collisions at* $\sqrt{s} = 13$ TeV *using the ATLAS detector*. 2016, Phys. Rev. D, 94, 032005

Abell, G. O., *The Distribution of Rich Clusters of Galaxies.* 1958, ApJS, 3, 211

Aird, J., Comastri, A., Brusa, M., et al., *The Hot and Energetic Universe: The formation and growth of the earliest supermassive black holes.* 2013, ArXiv e-prints

Akamatsu, H., de Plaa, J., Kaastra, J., et al., *Properties of the Intracluster Medium of Abell 3667 Observed with Suzaku XIS.* 2012a, PASJ, 64, 49

Akamatsu, H., Hoshino, A., Ishisaki, Y., et al., *X-Ray Study of the Outer Region of Abell 2142 with Suzaku.* 2011, PASJ, 63, 1019

Akamatsu, H., Takizawa, M., Nakazawa, K., et al., *X-Ray View of the Shock Front in the Merging Cluster Abell 3376 with Suzaku.* 2012b, PASJ, 64, 67

Alcock, C., Allsman, R. A., Alves, D. R., et al., *The MACHO Project: Microlensing Results from 5.7 Years of Large Magellanic Cloud Observations.* 2000, ApJ, 542, 281

Allen, S. W., Evrard, A. E., & Mantz, A. B., *Cosmological Parameters from Observations of Galaxy Clusters.* 2011, ARA&A, 49, 409

Allen, S. W., Rapetti, D. A., Schmidt, R. W., et al., *Improved constraints on dark energy from Chandra X-ray observations of the largest relaxed galaxy clusters.* 2008, MNRAS, 383, 879

Anders, E. & Grevesse, N., *Abundances of the elements - Meteoritic and solar.* 1989, Geochim. Cosmochim. Acta, 53, 197

Arida, M. 2012, *The Suzaku Technical Description*, `http://www.astro.isas.jaxa.jp/suzaku/doc/suzaku_td/`, accessed on 2017-02-17

Asplund, M., Grevesse, N., Sauval, A. J., & Scott, P., *The Chemical Composition of the Sun.* 2009, ARA&A, 47, 481

Babyk, I., *A Distant Chandra Galaxy Cluster CL J1415.1+3612: Constraint on Evidence of the Cool-core Phenomenon.* 2014, Baltic Astronomy, 23, 93

Baldi, A., Ettori, S., Molendi, S., & Gastaldello, F., *Self-similarity of temperature profiles in distant galaxy clusters: the quest for a universal law.* 2012, A&A, 545, A41

Banfield, J. K., Andernach, H., Kapińska, A. D., et al., *Radio Galaxy Zoo: discovery of a poor cluster through a giant wide-angle tail radio galaxy.* 2016, MNRAS, 460, 2376

Bartelmann, M. & Schneider, P., *Weak gravitational lensing*. 2001, Phys. Rep., 340, 291

Baumgartner, W. H., Loewenstein, M., Horner, D. J., & Mushotzky, R. F., *Intermediate-Element Abundances in Galaxy Clusters*. 2005, ApJ, 620, 680

Becker, R. H., Fan, X., White, R. L., et al., *Evidence for Reionization at z∼6: Detection of a Gunn-Peterson Trough in a z=6.28 Quasar*. 2001, AJ, 122, 2850

Bennett, C. L., Halpern, M., Hinshaw, G., et al., *First-Year Wilkinson Microwave Anisotropy Probe (WMAP) Observations: Preliminary Maps and Basic Results*. 2003, ApJS, 148, 1

Bertin, E. & Arnouts, S., *SExtractor: Software for source extraction.* 1996, A&AS, 117, 393

Bertschinger, E., *Cosmological dynamics*. 1995, NASA STI/Recon Technical Report N, 96

Bharadwaj, V., Reiprich, T. H., Schellenberger, G., et al., *Intracluster medium cooling, AGN feedback, and brightest cluster galaxy properties of galaxy groups. Five properties where groups differ from clusters*. 2014, A&A, 572, A46

Bleem, L. E., Stalder, B., de Haan, T., et al., *Galaxy Clusters Discovered via the Sunyaev-Zel'dovich Effect in the 2500-Square-Degree SPT-SZ Survey*. 2015a, ApJS, 216, 27

Bleem, L. E., Stalder, B., de Haan, T., et al., *Galaxy Clusters Discovered via the Sunyaev-Zel'dovich Effect in the 2500-Square-Degree SPT-SZ Survey*. 2015b, ApJS, 216, 27

Boehringer, H. & Werner, N., *X-ray Spectroscopy of Galaxy Clusters*. 2009, ArXiv e-prints

Boldt, E., McDonald, F. B., Riegler, G., & Serlemitsos, P., *Extended Source of Energetic Cosmic X Rays*. 1966, Physical Review Letters, 17, 447

Borgani, S. & Guzzo, L., *X-ray clusters of galaxies as tracers of structure in the Universe*. 2001, Nature, 409, 39

Bourdin, H., Arnaud, M., Mazzotta, P., et al., *A2163: Merger events in the hottest Abell galaxy cluster. II. Subcluster accretion with galaxy-gas separation*. 2011, A&A, 527, A21

Bourdin, H., Mazzotta, P., Markevitch, M., Giacintucci, S., & Brunetti, G., *Shock Heating of the Merging Galaxy Cluster A521*. 2013, ApJ, 764, 82

Branchini, E., Camera, S., Cuoco, A., et al., *Cross-correlating the γ-ray Sky with Catalogs of Galaxy Clusters*. 2017, ApJS, 228, 8

Brunetti, G. & Blasi, P., *Alfvénic reacceleration of relativistic particles in galaxy clusters in the presence of secondary electrons and positrons*. 2005, MNRAS, 363, 1173

Bryan, G. L. & Norman, M. L., *Statistical Properties of X-Ray Clusters: Analytic and Numerical Comparisons*. 1998, ApJ, 495, 80

Buddendiek, A., Schrabback, T., Greer, C. H., et al., *Optical and Sunyaev-Zel'dovich observations of a new sample of distant rich galaxy clusters in the ROSAT All Sky*. 2015, MNRAS, 450, 4248

Burrows, D. N. & Mendenhall, J. A., *Soft X-ray shadowing by the Draco cloud*. 1991, Nature, 351, 629

Carlstrom, J. E., Holder, G. P., & Reese, E. D., *Cosmology with the Sunyaev-Zel'dovich Effect.* 2002, ARA&A, 40, 643

Cen, R. & Ostriker, J. P., *Where Are the Baryons?* 1999, ApJ, 514, 1

Chaudhuri, A., Nath, B. B., & Majumdar, S., *Energy Deposition Profiles and Entropy in Galaxy Clusters.* 2012, ApJ, 759, 87

Cox, D. P. & Reynolds, R. J., *The local interstellar medium.* 1987, ARA&A, 25, 303

Croston, J. H., Pratt, G. W., Böhringer, H., et al., *Galaxy-cluster gas-density distributions of the representative XMM-Newton cluster structure survey (REXCESS).* 2008, A&A, 487, 431

Cuciti, V., Cassano, R., Brunetti, G., et al., *Occurrence of radio halos in galaxy clusters. Insight from a mass-selected sample.* 2015, A&A, 580, A97

CXC/SAO. 2009, *Sherpa Deproject package*, `http://cxc.harvard.edu/contrib/deproject/`, 2017-02-23

David, L. P., Jones, C., & Forman, W., *Cosmological implications of ROSAT observations of groups and clusters of galaxies.* 1995, ApJ, 445, 578

de Grandi, S. & Molendi, S., *Metal abundances in the cool cores of galaxy clusters.* 2009, A&A, 508, 565

De Luca, A. & Molendi, S., *The 2-8 keV cosmic X-ray background spectrum as observed with XMM-Newton.* 2004, A&A, 419, 837

de Plaa, J., Werner, N., Bleeker, J. A. M., et al., *Constraining supernova models using the hot gas in clusters of galaxies.* 2007, A&A, 465, 345

Désert, F.-X., Benoit, A., Gaertner, S., et al., *Observations of the Sunyaev-Zel'dovich effect at high angular resolution towards the galaxy clusters A665, A2163 and CL0016+16.* 1998, New A, 3, 655

Diemer, B. & Kravtsov, A. V., *A Universal Model for Halo Concentrations.* 2015, ApJ, 799, 108

Dodelson, S. 2003, *Modern cosmology* (San Diego, CA: Academic Press)

Doe, S. M., Ledlow, M. J., Burns, J. O., & White, R. A., *ROSAT Observations of Five Poor Galaxy Clusters with Extended Radio Sources.* 1995, AJ, 110, 46

Dolag, K. & Schindler, S., *The effect of magnetic fields on the mass determination of clusters of galaxies.* 2000, A&A, 364, 491

Dovciak, M., Matt, G., Bianchi, S., et al., *The Hot and Energetic Universe: The close environments of supermassive black holes.* 2013, ArXiv e-prints

Dressler, A., *The Evolution of Galaxies in Clusters.* 1984, ARA&A, 22, 185

Ebeling, H., Barrett, E., Donovan, D., et al., *A Complete Sample of 12 Very X-Ray Luminous Galaxy Clusters at z ¿ 0.5.* 2007, ApJ, 661, L33

Ebeling, H., Edge, A. C., Mantz, A., et al., *The X-ray brightest clusters of galaxies from the Massive Cluster Survey.* 2010, MNRAS, 407, 83

Eckert, D., Ettori, S., Molendi, S., Vazza, F., & Paltani, S., *The X-ray/SZ view of the virial region. II. Gas mass fraction.* 2013a, A&A, 551, A23

Eckert, D., Molendi, S., Vazza, F., Ettori, S., & Paltani, S., *The X-ray/SZ view of the virial region. I. Thermodynamic properties.* 2013b, A&A, 551, A22

Eckert, D., Roncarelli, M., Ettori, S., et al., *Gas clumping in galaxy clusters.* 2015, MNRAS, 447, 2198

Eckmiller, H. J., Hudson, D. S., & Reiprich, T. H., *Testing the low-mass end of X-ray scaling relations with a sample of Chandra galaxy groups.* 2011, A&A, 535, A105

Eisenstein, D. J., Zehavi, I., Hogg, D. W., et al., *Detection of the Baryon Acoustic Peak in the Large-Scale Correlation Function of SDSS Luminous Red Galaxies.* 2005, ApJ, 633, 560

Elbaz, D., Arnaud, M., & Boehringer, H., *The gas distribution and binding mass in the A 2163 cluster.* 1995, A&A, 293, 337

Erben, T., Schirmer, M., Dietrich, J. P., et al., *GaBoDS: The Garching-Bonn Deep Survey. IV. Methods for the image reduction of multi-chip cameras demonstrated on data from the ESO Wide-Field Imager.* 2005, Astronomische Nachrichten, 326, 432

Erben, T., Van Waerbeke, L., Bertin, E., Mellier, Y., & Schneider, P., *How accurately can we measure weak gravitational shear?* 2001, A&A, 366, 717

ESA. 2017, *The XMM-Newton Technical Description*, `https://www.cosmos.esa.int/web/xmm-newton/technical-details`, accessed on 2017-07-02

ESA and the Planck collaboration. 2013, *Map of the CMB*, `http://www.esa.int/spaceinimages/Images/2013/03/Planck_CMB`, 2017-01-03

ESA/Hubble & NASA. 2011, *Hubble captures a lucky galaxy alignment*, `www.spacetelescope.org/images/potw1151a`, 2017-03-08

Ettori, S., Fabian, A. C., Allen, S. W., & Johnstone, R. M., *Deep inside the core of Abell 1795: the Chandra view.* 2002, MNRAS, 331, 635

Ettori, S., Pratt, G. W., de Plaa, J., et al., *The Hot and Energetic Universe: The astrophysics of galaxy groups and clusters.* 2013, ArXiv e-prints

Fabian, A. C., *Cooling Flows in Clusters of Galaxies.* 1994, ARA&A, 32, 277

Fan, X., White, R. L., Davis, M., et al., *The Discovery of a Luminous Z=5.80 Quasar from the Sloan Digital Sky Survey.* 2000, AJ, 120, 1167

Fang, T., Buote, D. A., Humphrey, P. J., et al., *Confirmation of X-ray Absorption by Warm-Hot Intergalactic Medium in the Sculptor Wall.* 2010, ApJ, 714, 1715

Feretti, L., Fusco-Femiano, R., Giovannini, G., & Govoni, F., *The giant radio halo in Abell 2163.* 2001, A&A, 373, 106

Finoguenov, A., Briel, U. G., & Henry, J. P., *XMM-Newton discovery of an X-ray filament in Coma.* 2003, A&A, 410, 777

Frenk, C. S. & White, S. D. M., *Dark matter and cosmic structure*. 2012, Annalen der Physik, 524, 507

Fujimoto, R., Mitsuda, K., Mccammon, D., et al., *Evidence for Solar-Wind Charge-Exchange X-Ray Emission from the Earth's Magnetosheath*. 2007, PASJ, 59, 133

Fujita, Y., Tawa, N., Hayashida, K., et al., *High Metallicity of the X-Ray Gas Up to the Virial Radius of a Binary Cluster of Galaxies: Evidence of Galactic Superwinds at High-Redshift*. 2008, PASJ, 60, 343

Gaspari, M., Brighenti, F., & Ruszkowski, M., *Solving the cooling flow problem through mechanical AGN feedback*. 2013, Astronomische Nachrichten, 334, 394

Giacintucci, S., Dallacasa, D., Venturi, T., et al., *An unlikely radio halo in the low X-ray luminosity galaxy cluster RXC J1514.9-1523*. 2011, A&A, 534, A57

Giacintucci, S., Kale, R., Wik, D. R., Venturi, T., & Markevitch, M., *Discovery of a Giant Radio Halo in a New Planck Galaxy Cluster PLCKG171.9-40.7*. 2013, ApJ, 766, 18

Giodini, S., Lovisari, L., Pointecouteau, E., et al., *Scaling Relations for Galaxy Clusters: Properties and Evolution*. 2013, Space Sci. Rev., 177, 247

Hayashida, K., Inoue, H., Koyama, K., Awaki, H., & Takano, S., *The origin and behavior of the background in the large area counters on GINGA and its effect on the sensitivity*. 1989, PASJ, 41, 373

Henry, J. P., Gioia, I. M., Huchra, J. P., et al., *Groups of Galaxies in the ROSAT North Ecliptic Pole Survey*. 1995, ApJ, 449, 422

Hitomi Collaboration, Aharonian, F., Akamatsu, H., et al., *The quiescent intracluster medium in the core of the Perseus cluster*. 2016, Nature, 535, 117

Hoekstra, H., *A comparison of weak-lensing masses and X-ray properties of galaxy clusters*. 2007, MNRAS, 379, 317

Hoekstra, H., Bartelmann, M., Dahle, H., et al., *Masses of Galaxy Clusters from Gravitational Lensing*. 2013, Space Sci. Rev., 177, 75

Hoekstra, H., Franx, M., Kuijken, K., & Squires, G., *Weak Lensing Analysis of CL 1358+62 Using Hubble Space Telescope Observations*. 1998, ApJ, 504, 636

Homma, D., Chiba, M., Okamoto, S., et al., *A New Milky Way Satellite Discovered in the Subaru/Hyper Suprime-Cam Survey*. 2016, ApJ, 832, 21

Hoshino, A., Henry, J. P., Sato, K., et al., *X-Ray Temperature and Mass Measurements to the Virial Radius of Abell 1413 with Suzaku*. 2010, PASJ, 62, 371

Hudson, D. S., Mittal, R., Reiprich, T. H., et al., *What is a cool-core cluster? a detailed analysis of the cores of the X-ray flux-limited HIFLUGCS cluster sample*. 2010, A&A, 513, A37

Humphrey, P. J., Buote, D. A., Brighenti, F., et al., *Tracing the Gas to the Virial Radius (R_{100}) in a Fossil Group*. 2012, ApJ, 748, 11

Hwang, U., Mushotzky, R. F., Burns, J. O., Fukazawa, Y., & White, R. A., *Mass and Metallicity of Five X-Ray-bright Galaxy Groups.* 1999, ApJ, 516, 604

Ichikawa, K., Matsushita, K., Okabe, N., et al., *Suzaku Observations of the Outskirts of A1835: Deviation from Hydrostatic Equilibrium.* 2013, ApJ, 766, 90

Ishisaki, Y., Maeda, Y., Fujimoto, R., et al., *Monte Carlo Simulator and Ancillary Response Generator of Suzaku XRT/XIS System for Spatially Extended Source Analysis.* 2007, PASJ, 59, 113

Iwamoto, K., Brachwitz, F., Nomoto, K., et al., *Nucleosynthesis in Chandrasekhar Mass Models for Type IA Supernovae and Constraints on Progenitor Systems and Burning-Front Propagation.* 1999, ApJS, 125, 439

Izotov, Y. I., Thuan, T. X., & Lipovetsky, V. A., *The primordial helium abundance from a new sample of metal-deficient blue compact galaxies.* 1994, ApJ, 435, 647

Izotov, Y. I., Thuan, T. X., & Stasińska, G., *The Primordial Abundance of ^{4}He: A Self-consistent Empirical Analysis of Systematic Effects in a Large Sample of Low-Metallicity H II Regions.* 2007, ApJ, 662, 15

Jaffe, W. J., *Origin and transport of electrons in the halo radio source in the Coma cluster.* 1977, ApJ, 212, 1

Kaiser, N., Squires, G., & Broadhurst, T., *A Method for Weak Lensing Observations.* 1995, ApJ, 449, 460

Kalberla, P. M. W., Burton, W. B., Hartmann, D., et al., *Leiden/Argentine/Bonn (LAB) Survey of Galactic HI (Kalberla+ 2005).* 2005, VizieR Online Data Catalog, 8076, 0

Kapferer, W., Kronberger, T., Weratschnig, J., et al., *Metal enrichment of the intra-cluster medium over a Hubble time for merging and relaxed galaxy clusters.* 2007, A&A, 466, 813

Kawaharada, M., Okabe, N., Umetsu, K., et al., *Suzaku Observation of A1689: Anisotropic Temperature and Entropy Distributions Associated with the Large-scale Structure.* 2010, ApJ, 714, 423

Khosroshahi, H. G., Ponman, T. J., & Jones, L. R., *Scaling relations in fossil galaxy groups.* 2007, MNRAS, 377, 595

King, I., *The structure of star clusters. I. an empirical density law.* 1962, AJ, 67, 471

Klypin, A., Kravtsov, A. V., Valenzuela, O., & Prada, F., *Where Are the Missing Galactic Satellites?* 1999, ApJ, 522, 82

Knowles, K., Intema, H. T., Baker, A. J., et al., *A giant radio halo in a low-mass SZ-selected galaxy cluster: ACT-CL J0256.5+0006.* 2016, MNRAS, 459, 4240

Koekemoer, A. M., Fruchter, A. S., Hook, R. N., & Hack, W. 2003, in HST Calibration Workshop : Hubble after the Installation of the ACS and the NICMOS Cooling System, ed. S. Arribas, A. Koekemoer, & B. Whitmore, 337

Komiyama, M., Sato, K., Nagino, R., Ohashi, T., & Matsushita, K., *Suzaku Observations of Metallicity Distribution in the Intracluster Medium of the NGC 5044 Group*. 2009, PASJ, 61, S337

Komossa, S. & Böhringer, H., *X-ray study of the NGC 383 group of galaxies and the source 1E 0104+3153*. 1999, A&A, 344, 755

Lacey, C. & Cole, S., *Merger rates in hierarchical models of galaxy formation*. 1993, MNRAS, 262, 627

Lee, J. & Komatsu, E., *Bullet Cluster: A Challenge to ΛCDM Cosmology*. 2010, ApJ, 718, 60

Lisse, C. M., Dennerl, K., Englhauser, J., et al., *Discovery of X-ray and Extreme Ultraviolet Emission from Comet C/Hyakutake 1996 B2*. 1996, Science, 274, 205

Lodders, K., *Solar System Abundances and Condensation Temperatures of the Elements*. 2003, ApJ, 591, 1220

Loken, C., Norman, M. L., Nelson, E., et al., *A Universal Temperature Profile for Galaxy Clusters*. 2002, ApJ, 579, 571

Lovisari, L., Kapferer, W., Schindler, S., & Ferrari, C., *Metallicity map of the galaxy cluster A3667*. 2009, A&A, 508, 191

Lovisari, L., Reiprich, T. H., & Schellenberger, G., *Scaling properties of a complete X-ray selected galaxy group sample*. 2015, A&A, 573, A118

Lovisari, L., Schindler, S., & Kapferer, W., *Inhomogeneous metal distribution in the intracluster medium*. 2011, A&A, 528, A60

Lumb, D. H., Warwick, R. S., Page, M., & De Luca, A., *X-ray background measurements with XMM-Newton EPIC*. 2002, A&A, 389, 93

Luppino, G. A. & Kaiser, N., *Detection of Weak Lensing by a Cluster of Galaxies at Z = 0.83*. 1997, ApJ, 475, 20

Macario, G., Markevitch, M., Giacintucci, S., et al., *A Shock Front in the Merging Galaxy Cluster A754: X-ray and Radio Observations*. 2011, ApJ, 728, 82

Mahdavi, A., Hoekstra, H., Babul, A., et al., *Joint Analysis of Cluster Observations. II. Chandra/XMM-Newton X-Ray and Weak Lensing Scaling Relations for a Sample of 50 Rich Clusters of Galaxies*. 2013, ApJ, 767, 116

Mahdavi, A., Hoekstra, H., Babul, A., & Henry, J. P., *Evidence for non-hydrostatic gas from the cluster X-ray to lensing mass ratio*. 2008, MNRAS, 384, 1567

Mantz, A. B., Allen, S. W., Morris, R. G., et al., *Cosmology and astrophysics from relaxed galaxy clusters - II. Cosmological constraints*. 2014, MNRAS, 440, 2077

Mantz, A. B., Allen, S. W., Morris, R. G., et al., *Cosmology and astrophysics from relaxed galaxy clusters - I. Sample selection*. 2015, MNRAS, 449, 199

Markevitch, M., *Intergalactic shock fronts*. 2010, ArXiv e-prints

Markevitch, M., Gonzalez, A. H., David, L., et al., *A Textbook Example of a Bow Shock in the Merging Galaxy Cluster 1E 0657-56*. 2002, ApJ, 567, L27

Markevitch, M., Ponman, T. J., Nulsen, P. E. J., et al., *Chandra Observation of Abell 2142: Survival of Dense Subcluster Cores in a Merger*. 2000, ApJ, 541, 542

Markevitch, M. & Vikhlinin, A., *Shocks and cold fronts in galaxy clusters*. 2007, Phys. Rep., 443, 1

Massey, R., Schrabback, T., Cordes, O., et al., *An improved model of charge transfer inefficiency and correction algorithm for the Hubble Space Telescope*. 2014, MNRAS, 439, 887

Matsushita, K., Fukazawa, Y., Hughes, J. P., et al., *Suzaku Observation of the Metallicity Distribution in the Intracluster Medium of the Fornax Cluster*. 2007, PASJ, 59, 327

Matthew Colless. 2003, *The 2dF Galaxy Redshift Survey*, `http://www.2dfgrs.net/`, accessed on 2017-20-04

Maughan, B. J., *The L_X-Y_X Relation: Using Galaxy Cluster X-Ray Luminosity as a Robust, Low-Scatter Mass Proxy*. 2007, ApJ, 668, 772

Maughan, B. J., Giles, P. A., Randall, S. W., Jones, C., & Forman, W. R., *Self-similar scaling and evolution in the galaxy cluster X-ray luminosity-temperature relation*. 2012, MNRAS, 421, 1583

Maughan, B. J., Jones, L. R., Ebeling, H., & Scharf, C., *An XMM-Newton observation of the massive, relaxed galaxy cluster ClJ1226.9+3332 at z= 0.89*. 2004a, MNRAS, 351, 1193

Maughan, B. J., Jones, L. R., Lumb, D., Ebeling, H., & Gondoin, P., *XMM-Newton observations of the relaxed, high-redshift galaxy cluster ClJ0046.3+8530 at z= 0.62*. 2004b, MNRAS, 354, 1

Maurogordato, S., Cappi, A., Ferrari, C., et al., *A 2163: Merger events in the hottest Abell galaxy cluster. I. Dynamical analysis from optical data*. 2008, A&A, 481, 593

McCarthy, I. G., Schaye, J., Ponman, T. J., et al., *The case for AGN feedback in galaxy groups*. 2010, MNRAS, 406, 822

McDonald, M., Allen, S. W., Bayliss, M., et al., *The Remarkable Similarity of Massive Galaxy Clusters From $z \sim 0$ to $z \sim 1.9$*. 2017, ArXiv e-prints

McInnes, R. N., Menanteau, F., Heavens, A. F., et al., *First lensing measurements of SZ-detected clusters*. 2009, MNRAS, 399, L84

Menanteau, F., Hughes, J. P., Sifón, C., et al., *The Atacama Cosmology Telescope: ACT-CL J0102-4915 "El Gordo," a Massive Merging Cluster at Redshift 0.87*. 2012, ApJ, 748, 7

Merloni, A., Predehl, P., Becker, W., et al., *eROSITA Science Book: Mapping the Structure of the Energetic Universe*. 2012, ArXiv e-prints

Mernier, F., de Plaa, J., Lovisari, L., et al., *Abundance and temperature distributions in the hot intra-cluster gas of Abell 4059*. 2015, A&A, 575, A37

Mittal, R., Hudson, D. S., Reiprich, T. H., & Clarke, T., *AGN heating and ICM cooling in the HIFLUGCS sample of galaxy clusters*. 2009, A&A, 501, 835

Moore, B., Ghigna, S., Governato, F., et al., *Dark Matter Substructure within Galactic Halos.* 1999, ApJ, 524, L19

Morrison, R. & McCammon, D., *Interstellar photoelectric absorption cross sections, 0.03-10 keV.* 1983, ApJ, 270, 119

MPA. 2005, *The Millennium Simulation Project*, `wwwmpa.mpa-garching.mpg.de/galform/virgo/millennium`, accessed on 2017-20-04

Nagai, D. & Lau, E. T., *Gas Clumping in the Outskirts of ΛCDM Clusters.* 2011, ApJ, 731, L10

Nagai, D., Vikhlinin, A., & Kravtsov, A. V., *Testing X-Ray Measurements of Galaxy Clusters with Cosmological Simulations.* 2007, ApJ, 655, 98

Nandra, K., Barret, D., Barcons, X., et al., *The Hot and Energetic Universe: A White Paper presenting the science theme motivating the Athena+ mission.* 2013, ArXiv e-prints

Navarro, J. F., Frenk, C. S., & White, S. D. M., *The Structure of Cold Dark Matter Halos.* 1996, ApJ, 462, 563

Neumann, D. M., *Tracing the X-ray emitting intra-cluster medium of clusters of galaxies beyond r_{200}.* 2005, A&A, 439, 465

Nicastro, F., Mathur, S., & Elvis, M., *Missing Baryons and the Warm-Hot Intergalactic Medium.* 2008, Science, 319, 55

Okabe, N., Smith, G. P., Umetsu, K., Takada, M., & Futamase, T., *LoCuSS: The Mass Density Profile of Massive Galaxy Clusters at z = 0.2.* 2013, ApJ, 769, L35

Ota, N., Nagayoshi, K., Pratt, G. W., et al., *Investigating the hard X-ray emission from the hottest Abell cluster A2163 with Suzaku.* 2014, A&A, 562, A60

Pacaud, F., Clerc, N., Giles, P. A., et al., *The XXL Survey. II. The bright cluster sample: catalogue and luminosity function.* 2016, A&A, 592, A2

Peacock, J. 1999, *Cosmological Physics*, Cambridge Astrophysics (Cambridge University Press)

Peebles, P. 1993, *Principles of Physical Cosmology*, Princeton series in physics (Princeton University Press)

Peimbert, M., Peimbert, A., & Ruiz, M. T., *The Chemical Composition of the Small Magellanic Cloud H II Region NGC 346 and the Primordial Helium Abundance.* 2000, ApJ, 541, 688

Peng, F. & Nagai, D., *Effect of Helium Sedimentation on X-Ray Measurements of Galaxy Clusters.* 2009, ApJ, 693, 839

Perlmutter, S., Aldering, G., Goldhaber, G., et al., *Measurements of Ω and Λ from 42 High-Redshift Supernovae.* 1999, ApJ, 517, 565

Piffaretti, R., Jetzer, P., & Schindler, S., *Aspherical galaxy clusters: Effects on cluster masses and gas mass fractions.* 2003, A&A, 398, 41

Piffaretti, R. & Valdarnini, R., *Total mass biases in X-ray galaxy clusters.* 2008, A&A, 491, 71

Pillepich, A., Porciani, C., & Reiprich, T. H., *The X-ray cluster survey with eRosita: forecasts for cosmology, cluster physics and primordial non-Gaussianity.* 2012, MNRAS, 422, 44

Planck Collaboration, Ade, P. A. R., Aghanim, N., et al., *Planck 2013 results. XXXII. The updated Planck catalogue of Sunyaev-Zeldovich sources.* 2015, A&A, 581, A14

Planck Collaboration, Ade, P. A. R., Aghanim, N., et al., *Planck 2013 results. XV. CMB power spectra and likelihood.* 2014a, A&A, 571, A15

Planck Collaboration, Ade, P. A. R., Aghanim, N., et al., *Planck 2013 results. XVI. Cosmological parameters.* 2014b, A&A, 571, A16

Planck Collaboration, Ade, P. A. R., Aghanim, N., et al., *Planck intermediate results. VIII. Filaments between interacting clusters.* 2013b, A&A, 550, A134

Planck Collaboration, Ade, P. A. R., Aghanim, N., et al., *Planck 2015 results. XIII. Cosmological parameters.* 2016, A&A, 594, A13

Planelles, S., Borgani, S., Dolag, K., et al., *Baryon census in hydrodynamical simulations of galaxy clusters.* 2013, MNRAS, 431, 1487

Pointecouteau, E., Reiprich, T. H., Adami, C., et al., *The Hot and Energetic Universe: The evolution of galaxy groups and clusters.* 2013, ArXiv e-prints

Pratt, G. W., Arnaud, M., Piffaretti, R., et al., *Gas entropy in a representative sample of nearby X-ray galaxy clusters (REXCESS): relationship to gas mass fraction.* 2010, A&A, 511, A85

Pratt, G. W., Croston, J. H., Arnaud, M., & Böhringer, H., *Galaxy cluster X-ray luminosity scaling relations from a representative local sample (REXCESS).* 2009, A&A, 498, 361

Pratt, G. W., Pointecouteau, E., Arnaud, M., & van der Burg, R. F. J., *The hot gas content of fossil galaxy clusters.* 2016, A&A, 590, L1

Press, W. H. & Schechter, P., *Formation of Galaxies and Clusters of Galaxies by Self-Similar Gravitational Condensation.* 1974, ApJ, 187, 425

Radovich, M., Puddu, E., Romano, A., Grado, A., & Getman, F., *A weak-lensing analysis of the Abell 2163 cluster.* 2008, A&A, 487, 55

Rasmussen, J. & Ponman, T. J., *Temperature and abundance profiles of hot gas in galaxy groups - I. Results and statistical analysis.* 2007, MNRAS, 380, 1554

Raymond, J. C. & Smith, B. W., *Soft X-ray spectrum of a hot plasma.* 1977, ApJS, 35, 419

Reichert, A., Böhringer, H., Fassbender, R., & Mühlegger, M., *Observational constraints on the redshift evolution of X-ray scaling relations of galaxy clusters out to z ˜ 1.5.* 2011, A&A, 535, A4

Reiprich, T. H., Basu, K., Ettori, S., et al., *Outskirts of Galaxy Clusters.* 2013, Space Sci. Rev.

Reiprich, T. H. & Böhringer, H., *The Mass Function of an X-Ray Flux-limited Sample of Galaxy Clusters.* 2002, ApJ, 567, 716

Reiprich, T. H. & Zhang, Y.-Y. 2012, *Lecture Notes on 'Multiwavelength Observations of Galaxy Clusters' (Argelander-Institute for Astronomy)*

Ren, B., Fang, T., & Buote, D. A., *X-Ray Absorption by the Warm-hot Intergalactic Medium in the Hercules Supercluster*. 2014, ApJ, 782, L6

Riess, A. G., Filippenko, A. V., Challis, P., et al., *Observational Evidence from Supernovae for an Accelerating Universe and a Cosmological Constant*. 1998, AJ, 116, 1009

Roncarelli, M., Ettori, S., Borgani, S., et al., *Large-scale inhomogeneities of the intracluster medium: improving mass estimates using the observed azimuthal scatter*. 2013, MNRAS, 432, 3030

Rosen, S. R., Webb, N. A., Watson, M. G., et al., *The XMM-Newton serendipitous survey. VII. The third XMM-Newton serendipitous source catalogue*. 2016, A&A, 590, A1

Rossetti, M., Gastaldello, F., Ferioli, G., et al., *Measuring the dynamical state of Planck SZ-selected clusters: X-ray peak - BCG offset*. 2016, MNRAS, 457, 4515

Sanderson, A. J. R., Edge, A. C., & Smith, G. P., *LoCuSS: the connection between brightest cluster galaxy activity, gas cooling and dynamical disturbance of X-ray cluster cores*. 2009, MNRAS, 398, 1698

Santos, J. S., Rosati, P., Tozzi, P., et al., *Searching for cool core clusters at high redshift*. 2008, A&A, 483, 35

Sato, K., Kawaharada, M., Nakazawa, K., et al., *Metallicity of the Fossil Group NGC 1550 Observed with Suzaku*. 2010, PASJ, 62, 1445

Sato, K., Matsushita, K., Yamasaki, N. Y., Sasaki, S., & Ohashi, T., *Temperature and entropy profiles to the virial radius of the Abell 1246 cluster observed with Suzaku*. 2014, PASJ, 66, 85

Sato, K., Tokoi, K., Matsushita, K., et al., *Type Ia and II Supernovae Contributions to Metal Enrichment in the Intracluster Medium Observed with Suzaku*. 2007a, ApJ, 667, L41

Sato, K., Yamasaki, N. Y., Ishida, M., et al., *X-Ray Study of Temperature and Abundance Profiles of the Cluster of Galaxies Abell 1060 with Suzaku*. 2007b, PASJ, 59, 299

Schirmer, M., *THELI: Convenient Reduction of Optical, Near-infrared, and Mid-infrared Imaging Data*. 2013, ApJS, 209, 21

Schmitt, J. H. M. M., Snowden, S. L., Aschenbach, B., et al., *A soft X-ray image of the moon*. 1991, Nature, 349, 583

Schneider, P., *Weak Gravitational Lensing*. 2005, ArXiv Astrophysics e-prints

Schneider, P. 2006, in: *Gravitational Lensing: Strong, Weak & Micro*, Saas-Fee Advanced Course 33, Swiss Society for Astrophysics and Astronomy, G. Meylan, P. Jetzer & P. North (Eds.), Springer-Verlag: Berlin, p. 269

Schneider, P. 2009, *Lecture notes on 'Cosmology' (Argelander-Institute for Astronomy)*

Schneider, P. 2015, *Extragalactic Astronomy and Cosmology - An Introduction* (Springer-Verlag Berlin Heidelberg)

Schrabback, T., Applegate, D., Dietrich, J. P., et al., *Cluster Mass Calibration at High Redshift: HST Weak Lensing Analysis of 13 Distant Galaxy Clusters from the South Pole Telescope Sunyaev-Zel'dovich Survey*. 2016, MNRAS submitted

Schrabback, T., Erben, T., Simon, P., et al., *Cosmic shear analysis of archival HST/ACS data. I. Comparison of early ACS pure parallel data to the HST/GEMS survey.* 2007, A&A, 468, 823

Schrabback, T., Hartlap, J., Joachimi, B., et al., *Evidence of the accelerated expansion of the Universe from weak lensing tomography with COSMOS.* 2010, A&A, 516, A63

SDSS Collaboration, Albareti, F. D., Allende Prieto, C., et al., *The Thirteenth Data Release of the Sloan Digital Sky Survey: First Spectroscopic Data from the SDSS-IV Survey MApping Nearby Galaxies at Apache Point Observatory.* 2016, ApJS submitted (also arXiv:1608.02013)

Semler, D. R., Šuhada, R., Aird, K. A., et al., *High-redshift Cool-core Galaxy Clusters Detected via the Sunyaev-Zel'dovich Effect in the South Pole Telescope Survey.* 2012, ApJ, 761, 183

Shang, C. & Scharf, C., *A Low-Redshift Galaxy Cluster X-Ray Temperature Function Incorporating Suzaku Data.* 2009, ApJ, 690, 879

Shull, J. M., Smith, B. D., & Danforth, C. W., *The Baryon Census in a Multiphase Intergalactic Medium: 30% of the Baryons May Still be Missing.* 2012, ApJ, 759, 23

Siemiginowska, A., Burke, D. J., Aldcroft, T. L., et al., *High-redshift X-ray Cooling-core Cluster Associated with the Luminous Radio-loud Quasar 3C 186.* 2010, ApJ, 722, 102

Simionescu, A., Allen, S. W., Mantz, A., et al., *Baryons at the Edge of the X-ray-Brightest Galaxy Cluster.* 2011, Science, 331, 1576

Simionescu, A., Roediger, E., Nulsen, P. E. J., et al., *The large-scale shock in the cluster of galaxies Hydra A.* 2009a, A&A, 495, 721

Simionescu, A., Werner, N., Böhringer, H., et al., *Chemical enrichment in the cluster of galaxies Hydra A.* 2009b, A&A, 493, 409

Simionescu, A., Werner, N., Urban, O., et al., *A Uniform Contribution of Core-collapse and Type Ia Supernovae to the Chemical Enrichment Pattern in the Outskirts of the Virgo Cluster.* 2015, ApJ, 811, L25

Simon, P., Taylor, A. N., & Hartlap, J., *Unfolding the matter distribution using three-dimensional weak gravitational lensing.* 2009, MNRAS, 399, 48

Skelton, R. E., Whitaker, K. E., Momcheva, I. G., et al., *3D-HST WFC3-selected Photometric Catalogs in the Five CANDELS/3D-HST Fields: Photometry, Photometric Redshifts, and Stellar Masses.* 2014, ApJS, 214, 24

Smith, R. K. & Hughes, J. P., *Ionization Equilibrium Timescales in Collisional Plasmas.* 2010, ApJ, 718, 583

Snowden, S. L., Mebold, U., Hirth, W., Herbstmeier, U., & Schmitt, J. H. M., *ROSAT detection of an X-ray shadow in the 1/4-keV diffuse background in the Draco nebula.* 1991, Science, 252, 1529

Springel, V. & Farrar, G. R., *The speed of the 'bullet' in the merging galaxy cluster 1E0657-56.* 2007, MNRAS, 380, 911

Springel, V., White, S. D. M., Jenkins, A., et al., *Simulations of the formation, evolution and clustering of galaxies and quasars.* 2005, Nature, 435, 629

Struble, M. F. & Rood, H. J., *A Compilation of Redshifts and Velocity Dispersions for ACO Clusters.* 1999, ApJS, 125, 35

Su, Y., Buote, D., Gastaldello, F., & Brighenti, F., *The Entire Virial Radius of the Fossil Cluster RX J1159+5531: I. Gas Properties.* 2015, ApJ, 805, 104

Su, Y., White, III, R. E., & Miller, E. D., *Suzaku Observations of the X-Ray Brightest Fossil Group ESO 3060170.* 2013, ApJ, 775, 89

Sun, M., Voit, G. M., Donahue, M., et al., *Chandra Studies of the X-Ray Gas Properties of Galaxy Groups.* 2009, ApJ, 693, 1142

Tamura, T., Kaastra, J. S., den Herder, J. W. A., Bleeker, J. A. M., & Peterson, J. R., *Elemental abundances in the intracluster medium as observed with XMM-Newton.* 2004, A&A, 420, 135

Tawa, N., Hayashida, K., Nagai, M., et al., *Reproducibility of Non-X-Ray Background for the X-Ray Imaging Spectrometer aboard Suzaku.* 2008, PASJ, 60, 11

Thölken, S., Lovisari, L., Reiprich, T. H., & Hasenbusch, J., *X-ray analysis of the galaxy group UGC 03957 beyond R_{200} with Suzaku.* 2016, A&A, 592, A37

Tinker, J., Kravtsov, A. V., Klypin, A., et al., *Toward a Halo Mass Function for Precision Cosmology: The Limits of Universality.* 2008, ApJ, 688, 709

Tokoi, K., Sato, K., Ishisaki, Y., et al., *Suzaku Observation of HCG 62: Temperature, Abundance, and Extended Hard X-Ray Emission Profiles.* 2008, PASJ, 60, S317

Tsujimoto, T., Nomoto, K., Yoshii, Y., et al., *Relative frequencies of Type Ia and Type II supernovae in the chemical evolution of the Galaxy, LMC and SMC.* 1995, MNRAS, 277, 945

van Weeren, R. J., Brunetti, G., Brüggen, M., et al., *LOFAR, VLA, and Chandra Observations of the Toothbrush Galaxy Cluster.* 2016, ApJ, 818, 204

van Weeren, R. J., Röttgering, H. J. A., Brüggen, M., & Hoeft, M., *Particle Acceleration on Megaparsec Scales in a Merging Galaxy Cluster.* 2010, Science, 330, 347

Vikhlinin, A., Forman, W., & Jones, C., *Outer Regions of the Cluster Gaseous Atmospheres.* 1999, ApJ, 525, 47

Vikhlinin, A., Kravtsov, A., Forman, W., et al., *Chandra Sample of Nearby Relaxed Galaxy Clusters: Mass, Gas Fraction, and Mass-Temperature Relation.* 2006, ApJ, 640, 691

Vikhlinin, A., Kravtsov, A. V., Burenin, R. A., et al., *Chandra Cluster Cosmology Project III: Cosmological Parameter Constraints.* 2009, ApJ, 692, 1060

Vikhlinin, A., Markevitch, M., & Murray, S. S., *A Moving Cold Front in the Intergalactic Medium of A3667.* 2001, ApJ, 551, 160

Viola, M., Cacciato, M., Brouwer, M., et al., *Dark matter halo properties of GAMA galaxy groups from 100 square degrees of KiDS weak lensing data.* 2015, MNRAS, 452, 3529

Vogelsberger, M., Genel, S., Springel, V., et al., *Introducing the Illustris Project: simulating the coevolution of dark and visible matter in the Universe.* 2014, MNRAS, 444, 1518

Voit, G. M., *Tracing cosmic evolution with clusters of galaxies.* 2005, Reviews of Modern Physics, 77, 207

Walker, S. A., Fabian, A. C., Sanders, J. S., & George, M. R., *Further X-ray observations of the galaxy cluster PKS 0745-191 to the virial radius and beyond.* 2012a, MNRAS, 424, 1826

Walker, S. A., Fabian, A. C., Sanders, J. S., & George, M. R., *Galaxy cluster outskirts: a universal entropy profile for relaxed clusters?* 2012b, MNRAS, 427, L45

Walker, S. A., Fabian, A. C., Sanders, J. S., Simionescu, A., & Tawara, Y., *X-ray exploration of the outskirts of the nearby Centaurus cluster using Suzaku and Chandra.* 2013, MNRAS, 432, 554

Wambsganss, J., *Gravitational Lensing in Astronomy.* 1998, Living Reviews in Relativity, 1, 12

Wang, Y., Xu, H.-G., Gu, J.-H., et al., *Central gas entropy excess as direct evidence for AGN feedback in galaxy groups and clusters.* 2010, Research in Astronomy and Astrophysics, 10, 1013

Werner, N., Urban, O., Simionescu, A., & Allen, S. W., *A uniform metal distribution in the intergalactic medium of the Perseus cluster of galaxies.* 2013, Nature, 502, 656

Wesseling, P. 2009, *Principles of Computational Fluid Dynamics*, Springer Series in Computational Mathematics (Springer Berlin Heidelberg)

White, S. D. M., Navarro, J. F., Evrard, A. E., & Frenk, C. S., *The baryon content of galaxy clusters: a challenge to cosmological orthodoxy.* 1993, Nature, 366, 429

Wikimedia Commons. 2008, *Shape distortions due to weak gravitational lensing*, `https://commons.wikimedia.org/wiki/File:Shapenoise.svg`, accessed on 2017-29-04

Willingale, R., Starling, R. L. C., Beardmore, A. P., Tanvir, N. R., & O'Brien, P. T., *Calibration of X-ray absorption in our Galaxy.* 2013, MNRAS, 431, 394

Wright, C. O. & Brainerd, T. G., *Gravitational Lensing by NFW Halos.* 2000, ApJ, 534, 34

Xue, Y.-J. & Wu, X.-P., *Properties of the double β model for intracluster gas.* 2000, MNRAS, 318, 715

Yoshino, T., Mitsuda, K., Yamasaki, N. Y., et al., *Energy Spectra of the Soft X-Ray Diffuse Emission in Fourteen Fields Observed with Suzaku.* 2009, PASJ, 61, 805

Zel'dovich, Y. B., *Gravitational instability: An approximate theory for large density perturbations.* 1970, A&A, 5, 84

Zhang, Y.-Y., Finoguenov, A., Böhringer, H., et al., *Scaling relations and mass calibration of the X-ray luminous galaxy clusters at redshift ~ 0.2: XMM-Newton observations.* 2007, A&A, 467, 437

Zhang, Y.-Y., Finoguenov, A., Böhringer, H., et al., *LoCuSS: comparison of observed X-ray and lensing galaxy cluster scaling relations with simulations.* 2008, A&A, 482, 451

Zhang, Y.-Y., Okabe, N., Finoguenov, A., et al., *LoCuSS: A Comparison of Cluster Mass Measurements from XMM-Newton and Subaru - Testing Deviation from Hydrostatic Equilibrium and Non-thermal Pressure Support*. 2010, ApJ, 711, 1033

Acknowledgements

Over the course of my PhD many people have supported me, for which I want to express my gratitude. Firstly, I would like to thank my supervisor Thomas Reiprich for his professional assistance, his continuous constructive and helpful support and for giving me the opportunity to work and graduate in a field that has fascinated me since my childhood. I also want to thank Tim Schrabback for his advice on the second project of this work, and for the great collaboration, helpful discussions and feedback. I thank Peter Schneider for agreeing to be my second referee and reading my thesis. Furthermore, I would like to express my sincere gratitude to Lorenzo Lovisari and Gerrit Schellenberger for their expertise, for always finding time for discussions and answering all my questions. Many thanks to Brenda Miranda, Floria Pacaud, Katharina Borm, Miriam Ramos Ceja, Bharadwaj Vijaysarathy, Yu-Ying Zhang, Alberto Doria and Axel Buddendiek for their advice and many fruitful discussions. I appreciated the very friendly and cordial atmosphere in our workgroup while working on my master's thesis as well as during my PhD.
I owe thanks to the Bonn Cologne Graduate School of Physic and Astronomy for financial support during the last two years of my PhD.
Many thanks to my office mates Sandra and Hananeh for everyday scientific and moral support. We surely had the best office and I very much enjoyed the time with you.
My deepest thanks go to my family for always supporting, encouraging and motivating me in all my decisions from the very beginning; to my boyfriend Jan for all the endless nights of discussion, for sharing my frustration and joy and for his never-ending patience during this whole time.